

Non-intrusive Measurements of
Microscale Thermal Flow Field by
Spontaneous Raman Imaging

March 2015

Reiko Kuriyama

Non-intrusive Measurements of Microscale Thermal Flow Field by Spontaneous Raman Imaging

March 2015

A thesis submitted in partial fulfilment of the requirements for the degree of
Doctor of Philosophy in Engineering



Keio University

Graduate School of Science and Technology
School of Integrated Design Engineering

Reiko Kuriyama

© Copyright 2014 by Reiko Kuriyama

All Rights Reserved

Abstract

Drastic advances in miniaturized fluidic systems (known as micro-total analysis systems or lab-on-a-chip devices) have stimulated the development of various measurement techniques for monitoring microscale thermal flow fields, since the efficiency and functionality of these microfluidic systems highly depend on the thermofluid behavior in microspace. Currently, micron-resolution particle image velocimetry and micron-resolution laser-induced fluorescence are the most commonly-used methods for the measurement of velocity and scalar (e.g., temperature, concentration) fields, respectively. These fluorescence-based techniques offer high sensitivity and thus yield planar distribution with high spatiotemporal resolution. However, they have an inherent disadvantage of using extrinsic fluorescent labels which can potentially alter the sample properties and flow fields. For instance, they sometimes suffer from electrochemical or spatiotemporal restrictions, such as aggregation, adsorption and photobleaching of fluorescent labels. In order to overcome these problems, label-free techniques are required especially in microfluidic systems dealing with biological samples, electrokinetic flow or surface-related phenomena. One alternative is the usage of Raman spectroscopy, which realizes label-free, chemically-selective, and microscopic analyses. Although some previous studies have demonstrated the compatibility of Raman-based techniques with microfluidic systems, they have usually been limited to point detection through a spectrometer and rarely applied to planar flow imaging. In order to develop non-intrusive and two-dimensional measurement techniques for microfluidic applications, the present study proposes a series of methodologies based on spontaneous Raman imaging, focusing on the visualization of temperature, velocity and near-wall concentration distributions with micron resolution.

A non-intrusive planar temperature measurement technique was developed based on spontaneous Raman imaging utilizing optical bandpass filters and an EM-CCD camera. The measurement principle was based on the unique temperature dependence of the Raman band arising from OH stretching vibration of H₂O molecules, which could be explained by the chemical equilibrium between hydrogen-bonded (HB) and non-hydrogen-bonded (NHB) states. In order to eliminate the influence of non-uniform excitation intensity, water

temperature was determined from the intensity ratio of two Raman signals with contrasting temperature dependencies, i.e., HB and NHB modes. A calibration result showed that the intensity ratio of HB to NHB modes decreased with increasing temperature in the range 293–333 K. By applying the calibration curve, non-uniform steady-state temperature distributions were quantitatively visualized with micron resolution in a milli-channel flow.

In order to extend the applicability of the above measurement technique to unsteady thermal flow fields, two-wavelength Raman imaging technique was developed. The measurement principle was basically the same as the previous one, i.e., it was based on the temperature dependence of OH stretching Raman band. The major difference was the development of a two-wavelength imaging system consisting of two bandpass filters and two EM-CCD cameras. The Raman images of HB and NHB modes were simultaneously captured with this system, and the intensity ratio of these modes was calculated. The simultaneous detection removed the need for manual switching of the filters, and allowed compensation of the spatiotemporal fluctuation of the excitation light. By applying the calibration data, a time-series temperature measurement was realized in a milli-channel. The measurement result agreed well with that obtained by thermocouples.

A non-intrusive methodology for velocity determination was proposed based on thermal tracing by two-wavelength Raman imaging. Although the proposed method has not yet been demonstrated due to the lack of an appropriate heating system, its applicability was investigated focusing on the error in temperature measurement. Raman images were acquired at various measurement conditions (e.g., electron-multiplying gain and spatial averaging process) and the influence of each parameter on measurement error was experimentally investigated. It was observed that the measurable velocity, apparent temperature variance, and spatial resolution were mutually related and significantly varied with the conditions.

A non-intrusive optical measurement technique was developed for planar visualization of near-wall concentration in microchannels, utilizing spontaneous Raman scattering excited by an evanescent wave. This technique is termed total internal reflection (TIR) Raman imaging. The usage of an evanescent wave, which illuminates only the vicinity of the interface with the order of 100 nm, enabled the surface-selective excitation of spontaneous Raman process. The measurement system was developed by combining a two-prism-based TIR microscope with a Raman imaging system, and mixture solutions composed of H₂O and D₂O were selected as sample liquid. The concentration distribution of each species at a glass-solution interface was obtained from the TIR Raman image by exploiting the linear relationship between the spontaneous Raman intensity and the number of illuminated molecules.

The measurement techniques developed in the present study will contribute to the future advance in microfluidic systems as label-free analytical tools which are especially compatible with biological materials and surface-related phenomena.

Contents

Abstract	i
Contents	iii
List of Tables	vii
List of Figures	ix
Nomenclature	xvii
1 Introduction and Objectives	1
1.1 Introduction.....	1
1.2 Literature Survey	4
1.2.1 Conventional Measurement Techniques for Microscale Thermal Flow Field	6
1.2.2 Raman Spectroscopy for Microscopic Measurement	13
1.2.3 Raman Imaging Technique for Two-dimensional Visualization	17
1.3 Motivation and Objectives	19
2 Fundamentals	25
2.1 Theory of Microfluidics	25
2.1.1 Continuum Hypothesis.....	25
2.1.2 Fluid Motion	26
2.1.3 Heat Transport	29
2.1.4 Mass Transport.....	29
2.2 Raman-Based Measurement	30
2.2.1 Introduction to Raman Spectroscopy	30
2.2.2 Classical Theory of Raman Scattering	33

2.2.3	Raman Imaging Techniques	38
2.3	Microscopic Measurement	42
2.3.1	Conventional Microscopy	42
2.3.2	Evanescent Wave	44
2.3.3	Total Internal Reflection Microscopy	49
2.4	Sample Material and Channel Fabrication	51
2.4.1	Sample Material	52
2.4.2	Channel Material	52
2.4.3	Fabrication Process	59
3	Visualization of Steady-State Temperature Distribution by Raman Imaging Technique	63
3.1	Temperature Measurement by Raman Imaging	63
3.1.1	Temperature Dependence of Water Raman Spectra	63
3.1.2	Measurement Principle for Steady-State Temperature Field	69
3.2	Measurement System	71
3.2.1	Experimental Apparatus	71
3.2.2	Filter Selection	75
3.3	Calibration Experiment for Raman Imaging	75
3.3.1	Calibration Curve	75
3.3.2	Consideration for Temperature Uniformity and Stability	80
3.3.3	Correction of Spatial Variance in Intensity Ratio	83
3.4	Visualization of Steady-State Temperature Distributions	86
3.5	Concluding Remarks	90
4	Visualization of Transient Temperature Distribution by Two-Wavelength Raman Imaging Technique	91
4.1	Temperature Measurement by Two-Wavelength Raman Imaging	91
4.2	Measurement System	92
4.2.1	Experimental Apparatus	93
4.2.2	Two-Wavelength Imaging System	94
4.2.3	Image Registration Procedure	96
4.3	Calibration Experiment for Two-Wavelength Raman Imaging	98
4.4	Visualization of Transient Temperature Distributions	101
4.5	Concluding Remarks	105

5	Investigation of Measurement Conditions for Velocity Determination Based on Thermal Tracing by Two-Wavelength Raman Imaging Technique	107
5.1	Concept of Velocity Determination	107
5.2	Experimental Apparatus	109
5.3	Influence of Measurement Conditions	112
5.3.1	Temperature Calibration Experiments	112
5.3.2	Influence of Measurement Conditions	114
5.3.3	Discussion of Applicability	118
5.4	Concluding Remarks	121
6	Visualization of Near-Wall Concentration Distribution by Total Internal Reflection Raman Imaging Technique	123
6.1	Near-Wall Concentration Measurement by Total Internal Reflection Raman Imaging	123
6.1.1	Measurement Principle for Near-Wall Concentration	123
6.1.2	Raman Spectra of H ₂ O/D ₂ O Mixtures	126
6.2	Measurement System	127
6.2.1	Two-Prism-Based Evanescent Wave Illumination System	127
6.2.2	Experimental Apparatus	129
6.2.3	Filter Selection	131
6.3	Calibration Experiment for Total Internal Reflection Raman Imaging	136
6.4	Visualization of Near-Wall Concentration Distributions	141
6.5	Concluding Remarks	145
7	Conclusions and Recommendations	147
7.1	Conclusions	147
7.1.1	Development of Non-intrusive Visualization Techniques for Microscale Temperature Field	148
7.1.2	Investigation of Measurement Conditions of Two-Wavelength Raman Imaging for Velocity Determination	149
7.1.3	Development of Non-intrusive Visualization Technique for Near-Wall Concentration Field	149
7.2	Recommendations for Future Research	151
	Acknowledgements	153
	References	155

List of Tables

1.1	Measurement uncertainties of fluorescence-based techniques	9
1.2	Principles and features of some label-free measurement techniques	11
1.3	Timeline for the evolution of Raman instrumentation (compiled based on the review by Adar <i>et al.</i> (2007))	14
2.1	Intensity ratios of anti-Stokes to Stokes Raman scattering (I_A/I_S) at various Raman shift calculated for different temperatures	34
2.2	Comparison of the parameters for point mapping, line scanning and direct imaging experiments by Schlücker <i>et al.</i> (2003)	41
2.3	Properties of H ₂ O and D ₂ O at 298 K	52
2.4	Comparison of Raman shifts of H ₂ O and D ₂ O in liquid states (Walrafen, 1962)	53
2.5	Typical values of chemical and physical properties of silica glass, borosilicate glass and PDMS. These data are quoted from Tian & Finehout (2008), Newport Corp. (http://www.newport-japan.jp/pdf/technical/1423.pdf , December 8, 2014), and McDonald & Whitesides (2002)	54
2.6	Raman peaks and assignment of pure fused silica (Shibata <i>et al.</i> , 1981)	56
2.7	Raman peaks and assignment of borate groups and silicate units (Konijnendijk & Stevels, 1976)	57
2.8	Borate and silicate groups present in borosilicate glass of each composition (Konijnendijk & Stevels, 1976)	57
2.9	Raman peaks and assignment of PDMS (Julián <i>et al.</i> , 2003)	58
3.1	Specifications of the EM-CCD camera (given by Hamamatsu Photonics K. K.)	73
3.2	Physical properties of water at $T = 298$ K	82
5.1	Measurement conditions for calibration experiments	113
5.2	Measurement conditions for the investigations of temperature variance	115
5.3	Measurable velocity, spatial resolution and Θ calculated for each condition	119
6.1	Properties of H ₂ O/D ₂ O mixtures used for the calibration experiment	132

List of Figures

1.1	Conventional measurement techniques for microscale thermal flow fields and contribution of the present study for the future goal.	5
1.2	Examples of potential disadvantages of the usage of fluorescent labels.	9
1.3	Comparison of the methodologies for obtaining a Raman image.	18
1.4	Previous studies based on Raman imaging technique and the target of each chapter of the present study.	21
1.5	Comparison of spatial and temporal resolutions of the previous studies and those targeted by the present study.	21
1.6	Objective and outline of the present dissertation.	23
2.1	Geometry of a rectangular channel with the width of w_c and the height of h_c	27
2.2	Velocity profiles of pressure-driven flow in the rectangular channel with different aspect ratios. (a) Profiles in the spanwise direction at $z/h_c = 0$, and (b) in the depthwise direction at $y/w_c = 0$	28
2.3	Schematic of the three types of light scattering: Stokes Raman scattering, Rayleigh scattering, and anti-Stokes Raman scattering.	32
2.4	The energy diagrams of molecules showing the origin of (a) Stokes Raman scattering and (b) anti-Stokes Raman scattering.	32
2.5	An example of Raman spectrum obtained from liquid carbon tetrachloride (CCl_4) reported by Hamaguchi & Hirakawa (1988).	34
2.6	Polarizability derivative and Raman activity for each vibrational mode of a linear triatomic molecule such as CO_2	37
2.7	Polarizability derivative and Raman activity for each vibrational mode of a non-linear triatomic molecule such as H_2O	37

List of Figures

2.8 Schematic representations of the methods for obtaining two-dimensional Raman images: (a) point mapping, (b) line scanning and (c) direct imaging approaches. The top row shows the illumination pattern on the sample material and the first gray arrows indicate the set of instruments required for signal detection. The middle row illustrates the information acquired by one measurement. The bottom row shows the resulting data set after the spatial or spectral scanning.40

2.9 Schematic diagram of an inverted fluorescence microscope.....43

2.10 Schematic of the optical imaging system of an inverted microscope.....43

2.11 Schematic of transmission and reflection of an incident light at an interface between two media with different refractive indices ($n_1 > n_2$).45

2.12 (a) Schematic of total internal reflection of light. (b) Enlarged view of the interface where an evanescent wave illumination is generated. The evanescent intensity profile in the z -direction is illustrated in the right-hand side.45

2.13 The intensity profile of the evanescent wave at different incident angles, when an incident light of $\lambda = 532$ nm is totally reflected at an interface between silica glass ($n_1 = 1.461$) and water ($n_2 = 1.333$).46

2.14 Relationship between the incident angle and the penetration depth of the evanescent wave, when an incident light of $\lambda = 532$ nm is totally reflected at an interface between silica glass ($n_1 = 1.461$) and water ($n_2 = 1.333$).46

2.15 Relationship between the incident angle and the absolute values of the Fresnel factors (t_{Px} , t_{Pz} and t_{Sy}) at the silica-water interface ($n_1 = 1.461$, $n_2 = 1.333$).48

2.16 Schematics of configurations for total internal reflection microscopy (TIRM). Typical configurations of (a) an objective-based and (b) a prism-based systems. (c) A two-prism-based TIRM system, in which entry and exit prisms are located in the same side as the objective lens.50

2.17 Typical Raman spectra of H₂O and D₂O in liquid states (Walrafen, 1964). The nomenclatures correspond to those listed in table 2.4.53

2.18 Schematic diagrams of (a) micro- and (b) milli-channels. The left-hand side of the figure shows the cross-sectional views of the channels and the right-hand side illustrates each layer which composes the channel structure.58

2.19 Fabrication processes of a microchannel composed of PDMS and glass. (a) Preparation of a master mold by photolithography. (b) Micro-structuring of PDMS by replica molding. (c) Fabrication of a microchannel used in the experiments.60

3.1	(a) Schematic of the Raman spectroscopy system and (b) the optical layout of the spectrometer.	65
3.2	(a) Raman spectra arising from OH stretching vibration of liquid H ₂ O molecules at different temperatures. The upper horizontal axis shows the corresponding wavelength of the scattered light with 532 nm excitation. (b) Raman difference spectra calculated from the spectra in figure 3.2(a) (the spectrum at 298 K was used as reference).	66
3.3	Relationship between the temperature and the Raman intensity differences at 3200, 3460, and 3600 cm ⁻¹ (derived from figure 3.2(b)).	67
3.4	Schematic views of (a) a water molecule in monomeric (or non-hydrogen-bonded) state and (b) a water molecule forming four hydrogen bonds with nearby molecules (an example of the configuration of water cluster).	67
3.5	Schematic of the direct Raman imaging through the filter which transmits HB mode. The filters were manually switched after the image acquisition.	70
3.6	Schematic of the measurement system for temperature measurement based on Raman imaging.	72
3.7	Spectral response characteristic of the EM-CCD camera (given by Hamamatsu Photonics K. K. (http://www.biovis.com/resources/ccd/e_c910013.pdf , December 8, 2014)).	73
3.8	Sensor characteristics of the EM-CCD camera. (a) Dependence of the signal-to-noise ratio on EM-gain, and (b) dependence of the signal-to-noise ratio on input photon number (given by Hamamatsu Photonics K. K.).	74
3.9	Spectral transmission characteristics of the selected bandpass filters for HB mode and NHB mode (Semrock Inc., FF01-642/10-25 (http://www.semrock.com/FilterDetails.aspx?id=FF01-642/10-25 , December 8, 2014) for HB, and FF01-660/13-25 (http://www.semrock.com/FilterDetails.aspx?id=FF01-660/13-25 , December 8, 2014) for NHB).	76
3.10	Relationship between the temperature and the integrated Raman intensity within the transmission range of each filter, which is calculated from the Raman spectra (shown in figure 3.2(a)).	76
3.11	(a) Top and (b) cross-sectional views of an I-shaped milli-channel used for calibration experiment.	78
3.12	(a) An example of temporally-averaged Raman image obtained through HB filter. Intensity profiles of the Raman image (b) in the horizontal direction (A–A') and (c) in the vertical direction (B–B').	78
3.13	Relationship between the Raman intensities (I_{HB} , I_{NHB}) and the temperature.	79

List of Figures

3.14 Relationship between the temperature and the Raman intensity ratio (I_{HB}/I_{NHB}). ..79

3.15 Temperature rise in a flowing pure water (bulk velocity: 2.0 mm/s) along the x -direction after the initiation of laser irradiation (wavelength: 532 nm, power: 240 mW, diameter: 2.3 mm). The chain line (of $t = 5$ s) and the fine line (of $t = 15$ s) are indistinctive in the figure.82

3.16 (a) Typical Raman images for HB and NHB modes captured at room temperature. (b) Distribution of the intensity ratio (I_{Ratio}) calculated from the HB and NHB images (left-hand side), and the distribution of I_c prepared for the correction (right-hand side). (c) Distributions of I_{Ratio} at different temperature conditions (before correction) and (d) the distributions of I_{Ratio}^* at different temperature conditions (after correction).85

3.17 (a) Top and (b) cross-sectional views of a T-shaped milli-channel.86

3.18 (a) Measurement area positioned at the junction of the T-shaped milli-channel. (b)–(d) temperature distributions obtained with three different heating condition ($T_{hotplate}$). The spatial resolution was calculated to be $12.8 \times 12.8 \mu\text{m}^2$ based on averaging over 8×8 pixels.87

3.19 (a) Measurement area positioned at the junction of the T-shaped milli-channel. (b)–(d) temperature distributions obtained with three different heating condition ($T_{hotplate}$). These temperature maps are calculated from the same Raman images used in figure 3.16, but visualized at spatial resolution of $25.6 \times 25.6 \mu\text{m}^2$ based on averaging over 16×16 pixels.88

3.20 Temperature distributions at $x = 2.0$ mm plotted along the y -direction for three different $T_{hotplate}$. The temperature gradient for each condition is indicated in the figure. (These data are calculated from the result in figure 3.16).89

4.1 Conceptual diagram of the two-wavelength Raman imaging system, which is comprised of a half mirror, two optical filters and two cameras for simultaneous detection of Raman images of different wavelengths.93

4.2 Schematic of the experimental apparatus for temperature measurement by two-wavelength Raman imaging.95

4.3 Arrangement of the components in two-wavelength Raman imaging system.95

4.4 Schematics of (a) the focal position of the objective lens in temperature measurements and (b) the position of the glass plate used for camera calibration.97

4.5 Schematics of the image registration procedure. (a) Images of the grid pattern captured by two different cameras, (b) extraction of the intersections as reference points, and (c) the result of linear transformation.97

4.6	(a) Top and (b) cross-sectional views of an I-shaped milli-channel used for calibration experiment.	99
4.7	Relationship between the temperature and the Raman intensities of HB and NHB modes.	100
4.8	Relationship between the temperature and Raman intensity ratio.	100
4.9	(a) Top and (b) cross-sectional views of the Y-shaped milli-channel. The measurement area is shown in an enlarged view of the junction area.	101
4.10	(a) The measurement area at the junction of the Y-shaped milli-channel. Temperature distribution maps at (b) 25 s, (c) 107 s, (d) 206 s, (e) 305 s, (f) 404 s, (g) 503 s and (h) 602 s after the initiation of heating. These temperature maps are visualized at spatial resolution of $6.0 \times 6.0 \mu\text{m}^2$ based on averaging over 4×4 pixels.	102
4.11	(a) The measurement area at the junction of the Y-shaped milli-channel. Temperature distribution maps at (b) 25 s, (c) 107 s, (d) 206 s, (e) 305 s, (f) 404 s, (g) 503 s and (h) 602 s after the initiation of heating. These are calculated from the same Raman images used in figure 4.10, but visualized at spatial resolution of $24.2 \times 24.2 \mu\text{m}^2$ based on averaging over 16×16 pixels. ..	103
4.12	Comparison of the temporal evolution of the water temperature at $y = 0 \mu\text{m}$ measured by Raman imaging (filled dots), the temperature measured by thermocouples at inlets A and B (dashed lines) and the averaged value of these two temperatures (solid line).	104
5.1	Concept of the velocity measurement based on thermal tracing. (a) Top view of the flow field and (b) the time-series temperature distributions in the streamwise direction.	108
5.2	Conceptual diagrams of the temperature measurement by two-wavelength Raman imaging. (a) Schematic of the imaging system and the transmittance spectra of the filters. (b) Schematic of the procedure for temperature determination from obtained Raman images.	110
5.3	Raman spectra arising from OH stretching vibration of liquid H_2O at three different temperatures. The upper horizontal axis represents the wavelength of the scattered light excited by 488 nm.	110
5.4	Schematic of the experimental apparatus for two-wavelength Raman imaging with an excitation light at 488 nm.	111
5.5	(a) Top and (b) cross-sectional views of the I-shaped milli-channel.	111
5.6	Relationship between the temperature and the Raman intensity ratio at four different measurement conditions listed in table 5.1.	113

List of Figures

5.7	(a) Typical Raman image and the measurement area shown as the red rectangles. Intensity profiles of the Raman image (b) in the horizontal direction (A–A') and (c) in the vertical direction (B–B').	115
5.8	(a) Relationship between the EM gain and the apparent temperature variance (Θ). (b) Relationship between the number of the pixels extracted for measurement area and Θ . (c) Relationship between the number of the pixels integrated for spatial averaging and Θ .	117
5.9	Schematic illustrations of (a) the fluorescent intensity profiles in time series obtained by molecular tagging velocimetry, (b) the temporal evolution of the flow velocity calculated from the displacement of the peak intensity values of the measured profiles, and (c) the velocity profile in the depthwise direction.	120
6.1	Schematic concept of near-wall concentration measurement by TIR Raman imaging. (a) Generation of an evanescent wave in a microchannel by total internal reflection. The enlarged figure illustrates the molecules illuminated by the evanescent wave. (b) Typical example of a raw Raman image and (c) a calculated distribution of near-wall concentration.	125
6.2	Typical Raman spectra of bulk H ₂ O/D ₂ O mixtures in the range 1500–4000cm ⁻¹ , which were measured by the system shown in figure 3.1.	126
6.3	Schematics of (a) the two-prism-based optical system for an evanescent wave illumination in a microchannel and (b) the light path of the excitation laser beam which undergoes total internal reflections.	128
6.4	Schematic of the experimental setup for total internal reflection Raman imaging.	130
6.5	Schematic of the Raman spectroscopy system developed for filter selection.	131
6.6	Total internal reflection (TIR) Raman spectra from the microchannel filled with the H ₂ O/D ₂ O mixtures. The spectrum shown as a red line represents the TIR Raman spectrum from an empty channel (i.e., filled with ambient air). (a) The TIR spectra in the range 0–4000 cm ⁻¹ and (b) the enlarged view of the same spectra in the range 1500–4000 cm ⁻¹ .	133
6.7	(a) Difference Raman spectra of H ₂ O/D ₂ O mixtures which were calculated from the TIR spectra (figure 6.6(b)) by subtracting the spectrum obtained with an empty channel as a reference. (b) Spectral transmittance characteristics of H ₂ O and D ₂ O filters (Semrock Inc., FF01-650/13-25 (http://www.semrock.com/FilterDetails.aspx?id=FF01-650/13-25 , December 8, 2014) for H ₂ O and FF01-615/20-25 (http://www.semrock.com/FilterDetails.aspx?id=FF01-615/20-25 , December 8, 2014) for D ₂ O).	134

6.8	The relationship between the concentration and the integrated intensity in the transmission band of the selected filters (calculated from TIR spectrum shown in figure 6.6).	135
6.9	(a) Top and (b) cross-sectional views of the T-shaped microchannel.	136
6.10	Temporally averaged Raman images obtained from mixtures A, C and E through H ₂ O and D ₂ O filters. A white dashed line represents the position of the evanescent wave spot.	138
6.11	Five points in the evanescent wave spot whose intensities were extracted for calibration.	138
6.12	Relationship between the concentration and the detected Raman intensity (a) detected through H ₂ O filter and (b) D ₂ O filter.	139
6.13	Relationship between the concentration and the normalized Raman intensity calculated from (a) the intensities detected through H ₂ O filter (figure 6.12(a)) and (b) those detected through D ₂ O filter (figure 6.12(b)).	140
6.14	Calibration curves between the normalized Raman intensities and the concentration.	141
6.15	(a) Measurement area at the junction of the T-shaped microchannel (shown in figure 6.9), and two-dimensional distributions of (b) H ₂ O concentration and (c) D ₂ O concentration. The maps represent the ‘initial concentration’ without consideration of isotopic exchange reaction (H ₂ O + D ₂ O ↔ 2HOD).	143
6.16	(a) X-directional concentration profiles of each species at y = 0 μm (calculated from figures 6.15 (b) and (c)). (b) X-directional profile of the sum of the measured H ₂ O and D ₂ O concentrations.	144
7.1	Spatiotemporal resolution achieved in the present study and the characteristic scale of various chemical or biological processes.	150

Nomenclature

Roman Symbols

a	$[\text{m}^{-1}]$	Absorption coefficient
A	$[\text{m}^2]$	Cross-sectional area of channel
c	$[\text{mol}/\text{m}^3]$	Molar concentration
c	$[\text{m}/\text{s}]$	Light speed
C_p	$[\text{J}/\text{kg}\cdot\text{K}]$	Specific heat at constant pressure
d	$[\text{m}]$	Spatial resolution
d_{eva}	$[\text{m}]$	Distance between two adjacent evanescent wave spots
D	$[\text{m}^2/\text{s}]$	Diffusion coefficient
D_h	$[\text{m}]$	Equivalent hydraulic diameter of channel
e	$[\text{m}]$	Smallest distance resolved by imaging device
E	$[\text{V}/\text{m}]$	Electric field
E_0	$[\text{V}/\text{m}]$	Amplitude of electric field
E_a	$[\text{J}]$	Energy of the initial state
E_b	$[\text{J}]$	Energy of the final state
E_x	$[\text{V}/\text{m}]$	Electric field in the X -direction
E_y	$[\text{V}/\text{m}]$	Electric field in the Y -direction
E_z	$[\text{V}/\text{m}]$	Electric field in the Z -direction
f	$[\text{m}/\text{s}^2]$	Acceleration by external body force
G	$[-]$	Green's function
h	$[\text{J}\cdot\text{s}]$	Planck's constant
h_c	$[\text{m}]$	Channel height
H_τ	$[-]$	Heaviside unit step function
I_0	$[\text{photons}/\text{s}\cdot\text{m}^2]$	Excitation laser intensity
I_A	$[\text{photons}/\text{s}\cdot\text{m}^2]$	Intensity of anti-Stokes Raman scattering
I_c	$[-]$	Corrective image

Nomenclature

I_{eva}	[photons/s·m ²]	Evanescent wave intensity
I_i	[photons/s·m ²]	Raman intensity for i -species
I_S	[photons/s·m ²]	Intensity of Stokes Raman scattering
k_B	[J/K]	Boltzmann constant
K	[-]	Constant expressing influencing parameters
K_e	[-]	Equilibrium constant
l	[m]	Length of the probe volume
L	[m]	Characteristic length
M	[-]	Total magnification of the imaging system
n	[-]	Refractive index
n'	[-]	Relative refractive index
n_1	[-]	Refractive index of the first medium
n_2	[-]	Refractive index of the second medium
n_g	[-]	Refractive index of glass slide
n_m	[-]	Refractive index of the medium between objective lens and sample
n_o	[-]	Refractive index of immersion oil
n_p	[-]	Refractive index of prism
n_s	[-]	Refractive index of solution
NA	[-]	Numerical aperture of the objective lens
N_i	[molecules/m ³]	Number density of i -species molecules
p	[Pa]	Pressure
P	[W]	Average power of the laser beam
Pe_D	[-]	Diffusion Peclet number
Pe_T	[-]	Thermal Peclet number
Pr	[-]	Prandtl number
P_{Stokes}	[W/m ²]	Total power of Stokes Raman scattering
Q	[J/s·m ³]	Heat production
Q	[m ³ /s]	Flow rate
Q_k	[m]	Function of the k -th normal coordinate
Q_{k0}	[m]	Maximum vibrational amplitude
r	[m]	$1/e^2$ radius of the laser beam
R	[J/mol·K]	Gas constant
Re	[-]	Reynolds number
S	[m]	Wetted perimeter
Sc	[-]	Schmidt number

t	[s]	Time
t	[-]	Transmission coefficient
t_g	[m]	Thickness of the glass slide
t_{Px}	[-]	Transmission coefficient for the X -component of P-polarized light
t_{Pz}	[-]	Transmission coefficient for the Z -component of P-polarized light
t_{Sy}	[-]	Transmission coefficient for the Y -component of S-polarized light
T	[K]	Absolute temperature
u	[m/s]	Velocity in the X -direction
\mathbf{u}	[m/s]	Velocity
u_{max}	[m/s]	Maximum velocity
U	[m/s]	Characteristic velocity
U_{bulk}	[m/s]	Bulk velocity
v	[m/s]	Velocity in the Y -direction
w	[m/s]	Velocity in the Z -direction
w_c	[m]	Channel width
x	[m]	Cartesian coordinate in the streamwise direction
\mathbf{x}	[m]	Spatial coordinate vector
x_n	[-]	Vertical position of the n -th reference point in image I
x_n'	[-]	Vertical position of the n -th reference point in image II
y	[m]	Cartesian coordinate in the spanwise direction
y_n	[-]	Horizontal position of the n -th reference point in image I
y_n'	[-]	Horizontal position of the n -th reference point in image II
z	[m]	Cartesian coordinate in the depthwise direction
z_p	[m]	Penetration depth of the evanescent wave

Greek Symbols

α	[m ² /s]	Thermal diffusivity
α	[°]	Half-angle of the maximum cone of light
α	[C·m ² /V]	Molecular polarizability
α_0	[C·m ² /V]	Equilibrium value of the polarizability
ΔH	[J/mol]	Reaction enthalpy
ΔS	[J/mol·K]	Reaction entropy

Nomenclature

Δt	[s]	Time interval
ΔT	[K]	Temperature rise induced by instantaneous heating
Δx	[m]	Displacement during the time interval
ε	[-]	Aspect ratio
ε_0	[C/V·m]	Electric permittivity in vacuum
ϕ	[mol%]	Equilibrium concentration of HOD
η	[Pa·s]	Viscosity
λ	[m]	Wavelength
λ_0	[m]	Wavelength of the excitation light
λ_{Raman}	[m]	Wavelength of the Raman scattering
φ	[°]	Inclined angle of laser irradiation
μ	[C·m]	Induced dipole moment
μ_x	[C·m]	Induced dipole moment in the X-direction
μ_y	[C·m]	Induced dipole moment in the Y-direction
μ_z	[C·m]	Induced dipole moment in the Z-direction
μ_{Stokes}	[C·m]	Induced dipole moment which act as the source of Stokes Raman scattering
ν	[m ² /s]	Kinematic viscosity
ν	[Hz]	Frequency
ν_0	[Hz]	Frequency of the incident light
$\tilde{\nu}$	[cm ⁻¹]	Raman shift
θ_c	[°]	Critical angle
θ_i	[°]	Incident angle
θ_p	[°]	Incident angle at the prism-oil interface
θ_t	[°]	Refraction angle
Θ	[K]	Apparent temperature variance
ρ	[kg/m ³]	Fluid density
σ	[cm ² /molecule]	Absolute Raman cross section
ω_0	[rad/s]	Angular frequency
ω_k	[rad/s]	Characteristic frequency
Ω	[sr]	Solid angle of signal detection
ψ	[mol%]	Initial concentration of D ₂ O

Subscripts

0	Reference state
eva	Excited by the evanescent wave
HB	Hydrogen-bonded state
<i>I</i>	<i>i</i> th
NHB	Non-hydrogen-bonded state
Raman	Raman scattering
Ratio	Ratio of two images
ref	Reference value
Stokes	Stokes Raman scattering
<i>w</i>	Known value at wall or surface

Superscripts

*	Dimensionless variable
---	------------------------

Mathematics

$\langle \rangle$	Spatially-averaged value
-------------------	--------------------------

Chapter 1

Introduction and Objectives

1.1 Introduction

Microfluidic technology, i.e., technology for the manipulation and analysis of small amount of fluid, has evolved dramatically over the past few decades, being greatly stimulated by the work by Manz *et al.* (1990) where they demonstrated the microfluidic potential for “micro total analysis systems (μ TAS)”. New concepts and technologies have been introduced for various analytical operations (such as sample preparation, injection, separation, mixing, reaction, detection, etc.) and integrated into a single platform in order to realize mobile automated analytical systems. These integrated systems that perform all the necessary analytical steps are termed μ TAS (Arora *et al.*, 2010) or lab-on-a-chip (LOC) devices (Haeberle & Zengerle, 2007), and offer several advantages; (1) reduction of sample, reagent and waste volume, (3) shorter analysis time with less human involvement, (2) high throughput in parallel or multiplexed processing, (4) low unit cost at mass production and (5) possibility of widespread use as mobile and disposable devices (Bayraktar & Pidugu, 2006). These advantages can offer benefits to various kinds of chemical analyses or syntheses in drug discovery, clinical diagnostics, biotechnology, environmental monitoring, etc. They also open the way for a variety of point-of-care applications, instead of the time-consuming chemical analyses in central laboratories.

When performing chemical analyses on such miniaturized devices, it is imperative to understand the microscale thermofluid behavior, since it determines the efficiency or functionalities of microfluidic devices to a significant extent (Chakraborty, 2010). In case of microscale flow field, the continuum hypothesis is still valid (especially when the working fluid is liquid), and therefore the same governing equations that have been developed for macroscale fluid mechanics can be applied. However, there are several distinctive features in microfluidics which considerably differ from the macroscopic thermofluid behavior. For example, a reduced system size dramatically increases its surface area-to-volume ratio, which

leads to the dominance of surface effects over volumetric effects. Therefore, inertia forces or gravitational forces may often be negligible in comparison with viscous forces, interfacial tension, wettability, or electrostatic forces in microscale flow fields (Chakraborty, 2010). In addition, heat and mass transport phenomena in microscale are generally dominated by heat conduction and molecular diffusion (Sato *et al.*, 2003; Ichiyanagi *et al.*, 2007), while those in macroscale are dominated by convective flow.

These characteristic features in transport phenomena over the microscopic length scale have given rise to a variety of functions in miniaturized systems. For example, different types of flow handling have been developed by utilizing electrical actuation (electroosmotic flows, electro-wetting flows), temperature or concentration gradients (Marangoni flows), and channel patterning (Probstein, 1994; Pollack *et al.*, 2000; Bain, 2001; Takeuchi *et al.*, 2012; Zhao *et al.*, 2002). Electroosmotic flows (EOF) are one of the most widely-used driving forces, which result from the migration of diffused ions in the electric double layer in the applied electric field (typically 100 V/cm). Electroosmotic flows have been utilized in various applications including fluid transport in capillary electrophoresis-based system (Harrison *et al.*, 1993; Polson *et al.*, 2000), mixing (Lin *et al.*, 2004; Leong *et al.*, 2007), and separation (Wu *et al.*, 2007), since they offer several advantages over pressure-driven flows; (1) low sample separation can be achieved by uniform velocity profiles (termed as ‘plug flow’), (2) flows can be controlled by switching voltages without the need of valves, and (3) they obviate the necessity of moving parts in the system (Bayraktar & Pidugu, 2006). For another example, microfluidics-based diagnostic devices have been produced by exploiting laminar diffusion for mixing, separation or detection processes (Hatch *et al.*, 2004; Weigl *et al.*, 2008). These devices perform chemical analyses based on diffusive transport in microchannels which are properly designed to achieve short diffusion lengths or large contacting surface area. Their main advantage is that they can function without any moving parts or external power sources, which is advantageous for non-instrumented, disposable and low-cost diagnostics in home health care, developing-country health care, or emergency situation (Weigl *et al.*, 2008).

As described above, characteristic phenomena in microscale thermal flow fields have played major roles to enhance the efficiency and functionality of microfluidic devices. At the same time, these phenomena sometimes bring the difficulties in the analytical or numerical calculations of thermal flow field. For example, EOF are highly sensitive to ion concentration, temperature, pH, channel materials, and surface contamination, since these factors affect the formation of the electric double layer, namely, zeta-potential (Kirby & Hasselbrink, 2004a, 2004b; Kazoe & Sato, 2007; Pittman *et al.*, 2003). These influencing parameters are treated as external source terms or boundary conditions in governing equations, but these phenomena have not investigated enough to provide the readily available formulation. In addition, as the microchannel size becomes smaller, various factors, such as, surface roughness and textures

of channel wall (Taylor *et al.*, 2006; Guo & Li, 2003), viscosity change due to the surface forces (Ho & Tai, 1998), and dissolved gases in the liquid sample (Guo & Li, 2003) have considerable impact on the transport phenomena inside the devices. Moreover, multiphase flow or non-Newtonian fluids (e.g., human blood) are often encountered in many microfluidic applications, which require the modification or augmentation of governing equations.

Above-mentioned factors are complexly intertwined each other and make the analytical or numerical predictions rather difficult even under the laminar flow condition at low Reynolds number. Therefore, in order to construct the accurate physical model and to provide better guidelines for the optimal design of these devices, it is important to develop microscopic measurement technique which can directly observe flow dynamics and transport phenomena in microfluidic devices.

In addition, such microscale measurements are also required for maximizing their efficiency, reliability and productivity during the operations, as well as for the optimization of their design (Natrajan & Christensen, 2009). For example, measurement of fluid temperature at microscale is of crucial importance for successful control of chemical or biological processes in microfluidic devices, including enzyme-catalysed or exothermal reactions (Antes *et al.*, 2003; Matosevic *et al.*, 2010), cell cultivation and manipulation (Goto *et al.*, 2005; Voldman, 2006; Huang & Lee, 2007), sample transport by thermocapillary pumping (Sammarco & Burns, 1999, 2000) and capillary-electrophoretic separation (Gobie & Ivory, 1990; Knox & McCormack, 1994). Among these, polymerase chain reaction (PCR) (Lee, Kim *et al.*, 2003; Shin *et al.*, 2003) is the most typical example involving thermal management for the amplification of nucleic acid molecules, where the temperature accuracy and uniformity within the thermal cycling dominate the speed, purity and amount of DNA production (Lee *et al.*, 2004; Zhang & Xing, 2007). Since accurate and rapid thermal control is required to operate these systems at high efficiencies, a technique that can realize *in-situ* temperature measurement in microchannels is required to achieve optimal performance. In a similar way, *in-situ* concentration or velocity measurements are also useful for improving the analytical performance of the microfluidic devices by affording quantification of reaction products or providing a record of fluid flow for rapid feedback control and optimization (Leung *et al.*, 2005; Pittman *et al.*, 2003).

From these growing demands stimulated by the recent advance in miniaturized fluidic systems, various measurement techniques have been developed for monitoring microscale thermal flow fields. Currently, the most commonly-used methods are fluorescence-based techniques such as micron-resolution particle image velocimetry (micro-PIV) (Santiago *et al.*, 1998) and micron-resolution laser-induced fluorescence (micro-LIF) (Ross *et al.*, 2001). Since these techniques offer high sensitivity and thus yield planar distributions with high

spatiotemporal resolution, they have been greatly contributed to the analyses or elucidation of microscale transport phenomena, by providing the precise information of velocity and scalar (e.g., temperature, concentration, pH, zeta-potential) fields. However, they have an inherent disadvantage of using extrinsic fluorescent labels which can potentially alter the sample properties and flow fields. In order to overcome these problems, label-free measurement techniques are required.

Figure 1.1 shows the conventional measurement techniques and the contribution of the present study for the future goal. The present study addresses the development of non-intrusive, chemically-selective and two-dimensional measurement techniques for microscale thermal flow fields, which serves as practical and versatile approaches in various microfluidic systems. The physical quantities being dealt with here are temperature, velocity and near-wall concentration. For the above purpose, the present study utilizes vibrational spectroscopy instead of fluorescence-based techniques. The vibrational spectroscopy probes vibrational energy of sample molecule itself, and thus realizes label-free analyses without any sample preparation. Generally, it is classified into infrared (IR) spectroscopy and Raman spectroscopy, but the former is considered to have limited applicability due to the lack of channel material and strong light absorption by water. Therefore, this study employs Raman spectroscopic approach focusing on its compatibility with microfluidic systems. Although Raman spectroscopy has usually been limited to point detection through a spectrometer, this study extends the technique to two-dimensional measurement by introducing direct imaging methodology and applies it to planar imaging of thermal flow fields.

1.2 Literature Survey

At the beginning of this section, conventional measurement techniques for microscale thermal flow fields are summarized. Subsequently, this section examines the previous studies related to Raman-based measurement techniques. These studies are mainly intended for the microfluidic applications, investigations of interfacial phenomena, and non-intrusive microscopic visualization. It should be noted that this study only discusses the techniques based on nonresonant spontaneous Raman scattering, while there are several types of Raman spectroscopy with some signal enhancement strategies (e.g., resonance Raman scattering (RRS), stimulated Raman scattering (SRS), surface-enhanced Raman spectroscopy (SERS), and coherent anti-Stokes Raman scattering (CARS)). These enhanced signals provide higher sensitivity, but some of them require more complicated instrumentation, introduction of nano-structured metal, or sophisticated data analysis due to the contribution of non-resonant background signals (Kneipp, 1999; Day *et al.*, 2011). The usage of the spontaneous Raman

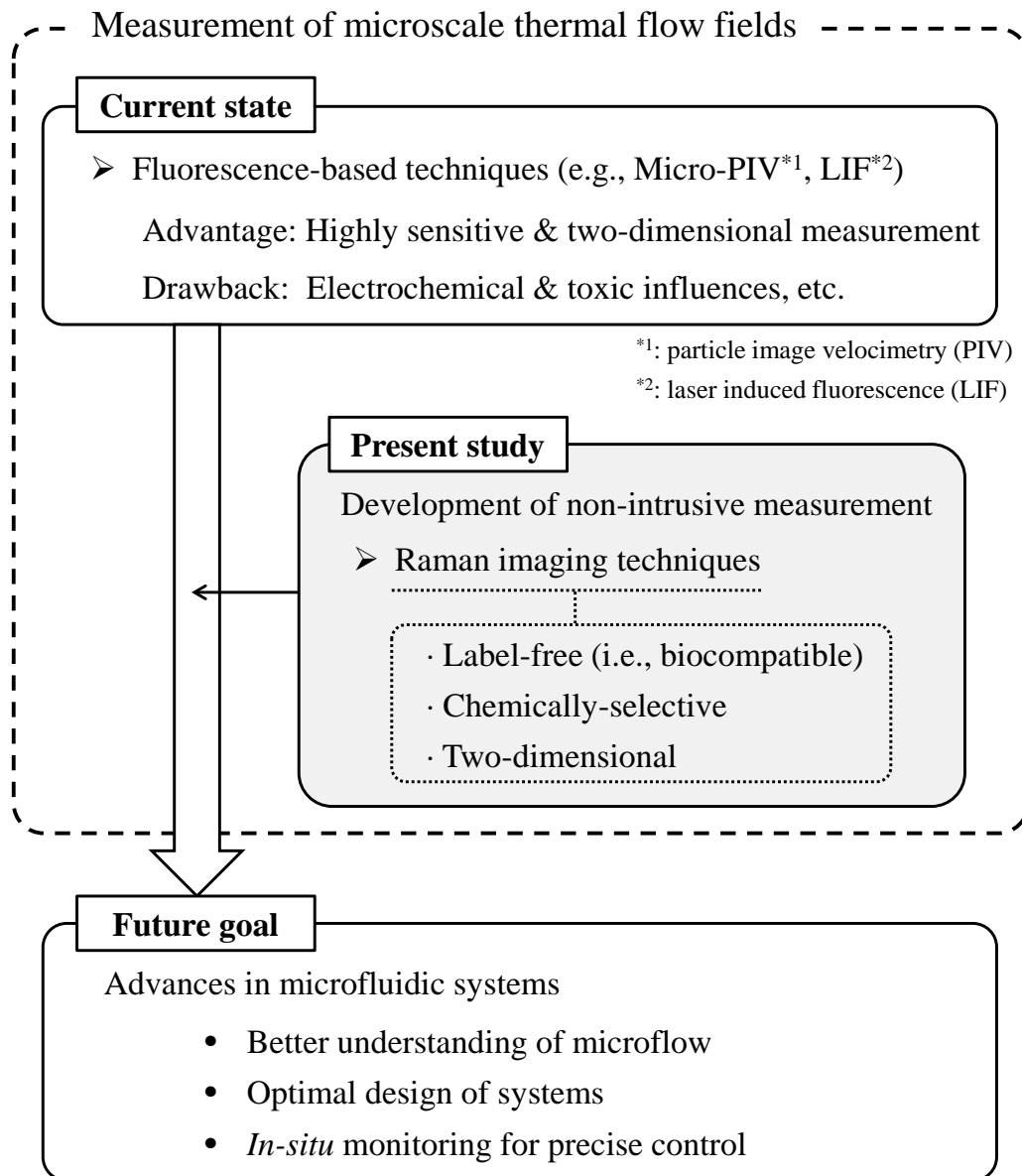


Figure 1.1. Conventional measurement techniques for microscale thermal flow fields and contribution of the present study for the future goal.

scattering allows the experimentally-straightforward measurements, which will lead to the common use in various application fields.

1.2.1 Conventional Measurement Techniques for Microscale Thermal Flow Field

In order to investigate microscale transport phenomena, a variety of measurement methods have been developed for both vector and scalar quantities since the late 1990s. Contact-type sensors such as hot-wire anemometer and thermocouples are commonly used for macroscale measurement, but they can significantly perturb the microscale thermal flow field, which leads to an inaccurate measurement result. Moreover it is generally difficult to achieve sufficient spatial resolution by directly applying these conventional contact-type sensors. Therefore, more elaborate contact-free sensing methods have been intensively studied for microfluidic applications.

Currently, micro-PIV, which was first introduced by Santiago *et al.* (1998), is the most commonly-used technique for spatially-resolved velocimetry in microfluidic devices. In this technique, fluorescently-labeled submicron particles are suspended in the liquid as tracers, and the flow velocity is estimated from the particles' displacement over the time interval. Using this technique, fluid motion can be observed in flow fields whose length scale ranging from 10^{-3} to 10^{-6} m. Thus the micro-PIV technique has been applied to various flow fields; pressure-driven flow (Santiago *et al.*, 1998; Meinhart *et al.*, 1999), near-surface flow with a slip velocity (Tretheway & Meinhart, 2002), and electroosmotic flow (Kim, *et al.*, 2002; Devasenathipathy & Santiago, 2002; Sato & Hishida, 2006). Zettner & Yoda (2003) proposed nano-particle image velocimetry (nano-PIV), which uses an evanescent wave illumination generated by a total internal reflection (TIR) at a glass-solution interface in order to measure near-wall velocities. The evanescent wave decays exponentially with the distance from the interface, and its spatial extent is of the order of 100 nm. Therefore, the nano-PIV technique has been used to investigate the near-wall structure both in pressure-driven flow (Zettner & Yoda, 2003; Jin *et al.*, 2004) and electrokinetically driven flow (Sadr *et al.*, 2006; Kazoe *et al.*, 2010). Other particle-based velocimetries, such as laser Doppler velocimetry and particle streak velocimetry, have been introduced to microscale (Tieu, *et al.*, 1995; Brody *et al.* 1996), but more works have been devoted to PIV-based techniques to date.

Scalar-based flow velocimetry is a different type of technique, where the fluid motion is inferred from the observed velocity of a conserved scalar (Sinton, 2004). For application to microscale flow measurement, light emitting molecules (such as caged-fluorescent dye molecules, fluorescent molecules, and phosphorescent molecules) are typically injected as scalar markers. Molecular tagging velocimetry (MTV) is one type of such scalar-based velocimetry using caged-fluorescent dye. The caged-fluorescent dye molecules are fluoro-

phores with additional chemical groups that render the molecules non-fluorescent, and become uncaged by exposure of ultraviolet (UV) light (Sinton, 2004). In the experiments performed by Paul *et al.* (1998), both pressure-driven and electroosmotic flows in capillaries were investigated. The caged dye in the capillary was locally uncaged by a UV laser sheet, and subsequently excited by second laser beam. The fluid velocity was estimated from the obtained images of the dye transport. More recently, two-dimensional MTV has been developed to measure the flow velocity in a micro-mixing chamber (Roetmann *et al.*, 2008).

For planar measurements of scalar quantities (i.e., concentration, temperature and pH), micro-LIF has been developed by combining LIF technique with fluorescence microscopy. The micro-LIF technique exploits the changes in the emission intensity of a fluorescent dye which is injected into the fluid or sometimes applied onto the channel surface (Sato *et al.*, 2003). For example, Matsumoto *et al.* (2005) realized quantitative measurement of depth-averaged concentration fields in a meander glass microchannel. Hoffmann *et al.* (2006) measured concentration distributions in a T-shaped micro-mixer using confocal laser scanning microscope in order to investigate the three-dimensional mass transfer in microdevices. For microscale temperature measurement, several groups (Ross *et al.* (2001); Sato *et al.* (2003); Natrajan & Christensen (2009); Kim & Yoda (2010)) employed a temperature-sensitive fluorescent dye (sometimes in combination with a temperature-insensitive dye for ratiometric measurement). Kim & Yoda (2010) achieved the experimental uncertainty of ± 0.3 K at a spatial resolution of 30 μm by two-color LIF using two temperature-sensitive dyes. Kazoe & Sato (2007) developed nanoscale LIF (nano-LIF) in their innovative attempt to measure the spatially-distributed wall zeta-potential, which is an important parameter to characterize electrokinetically-driven flows. In nano-LIF, fluorescent markers in the vicinity of channel wall are selectively illuminated by an evanescent wave. The wall zeta-potential distribution was successfully determined from the emission intensity of fluorophore ions which are distributed depending on the surface charge.

Recent years, micro-LIF technique has been often combined with other methods, which has led to the further insight into microscale flow fields. Ichiyanagi *et al.* (2007) first developed simultaneous measurement of velocity and pH distributions by the usage of 1.0 μm fluorescent particles for micro-PIV and pH-sensitive fluorescent dye for micro-LIF. They investigated the mixing processes in microchannel and quantitatively evaluated the convection and diffusion of photons. This simultaneous measurement technique has also been applied to gas dissolution processes (Ichiyanagi *et al.*, 2012a, 2012b).

As summarized above, the fluorescence-based methodologies (including micro/nano-PIV, MTV and LIF) have played important roles in flow analyses in microfluidic devices as well-established techniques over the past decades. The main advantage of these techniques is their high sensitivity. Table 1.1 compiles some examples of previously-reported measurement

Introduction and Objectives

uncertainties of these techniques. As can be seen in table 1.1, they can realize measurements with high spatiotemporal resolution and high accuracy, which has been greatly contributed for the elucidation of various microscale transport phenomena.

On the other hand, the usage of fluorescent particles or dye could be problematic for accurate measurement due to its surface properties and electrochemical characteristics, as illustrated in figure 1.2. For example, fluorescent polystyrene particles, which are generally used as tracers in micro-PIV, are hydrophobic. While various modifications are made to increase the charge and hydrophilicity of the particles, they always retain some hydrophobic characteristics. This leads to the aggregation of particles and adhesion to the microchannel wall (Singh *et al.*, 2001), and therefore it can be a potential cause of the measurement error. It has also been discovered that the charging characteristics of caged fluorescent dye may alter the results of MTV especially in electrokinetic flow, due to the interaction between dye molecules and charged channel wall (Bayraktar & Pidugu, 2006; Ross & Locascio, 2003). Furthermore, some neutral hydrophobic fluorescent dyes which are commonly used in temperature visualizations adsorb onto and diffuse into the PDMS material (Samy *et al.*, 2008). These undesired phenomena result in an artificial change in temperature, alteration of wall zeta-potential, and consequently the change in electroosmotic flow (Erickson *et al.*, 2005; Ross & Locascio, 2003). In order to avoid the dye adsorption and absorption, some special strategy has to be taken; surface coating of channel wall with a positively charged Polybrene solution (Erickson *et al.*, 2005), or addition of sodium dodecyl sulfate to the working fluid (Roman *et al.*, 2006), for example.

Another disadvantage of fluorescent-based techniques is photobleaching, which is a photochemical destruction of fluorophores caused by the light exposure. Photobleaching reduces fluorescent intensity over a short time period, and thus it complicates the quantitative analysis in LIF measurement. This phenomenon is unavoidable, and can only be controlled by limiting the exposure dose or dye concentration (Samy *et al.*, 2008). Additionally, fluorescent labels may exert a toxic effect on biological samples, which makes the techniques less suitable or impractical in biochemical applications. Decreasing of the toxicity has actually been one of major topics in the development of fluorescent probes (Fei & Gu, 2009).

As mentioned above, the fluorescent-based techniques have some drawbacks which are attributed to the properties of fluorescent particles or dyes. Since the usage of these fluorescent labels can potentially affect the sample properties, flow fields, and the measurement results, non-intrusive measurement techniques which do not employ extrinsic tracers or markers are required especially in some applications dealing with biological samples, electrokinetic flow or surface-related phenomena.

In order to realize label-free measurements in microscale, several alternative techniques have been adopted to microfluidic devices: nuclear magnetic resonance (NMR) spectroscopy,

Table 1.1. Measurement uncertainties of fluorescence-based techniques

Target	Technique	Uncertainty	Conditions	Reference
Temperature	Micro-LIF	± 0.3 K	Spatial resolution: $30 \times 30 \mu\text{m}^2$ Temperature range: 293–333 K	Kim & Yoda, 2010
pH (H^+ concentration)	Micro-LIF	± 0.23	Spatial resolution: $5 \times 5 \mu\text{m}^2$ pH range: 5–9	Ichiyanagi <i>et al.</i> , 2007
Zeta-potential	Nano-LIF	± 4.7 mV	Spatial resolution: $7.9 \times 7.9 \mu\text{m}^2$ Potential range: -60 to -90 mV	Kazoe & Sato, 2007
Velocity	Micro-PIV	$\pm 5.5 \mu\text{m/s}$	Spatial resolution: $5 \times 5 \mu\text{m}^2$ Bulk velocity: $\sim 300 \mu\text{m/s}$	Ichiyanagi <i>et al.</i> , 2007

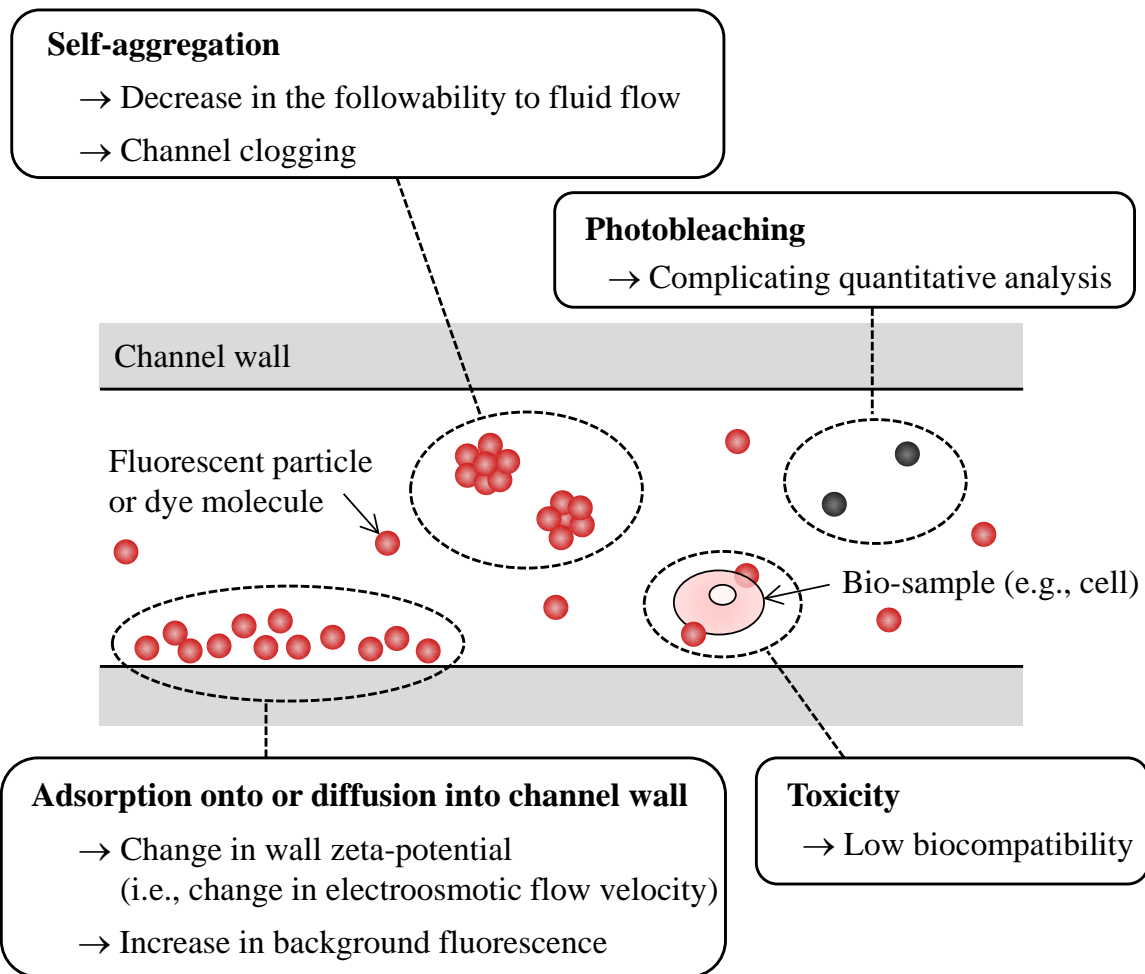


Figure 1.2. Examples of potential disadvantages of the usage of fluorescent labels.

thermal lens microscopy (TLM), infrared (IR) spectroscopy, and Raman spectroscopy, for instance. These are all non-contact methods and require no chemical treatment of the analytes prior to the measurements. Table 1.2 briefly summarizes the measurement principle and some features of these methods.

NMR is a spectroscopic technique based on the interaction of atomic nuclei with an applied external magnetic field oscillating at a particular frequency. Since NMR can derive the physical, chemical, and electron information about molecules by monitoring the radiation, it allows direct determination of molecular structure (Viskari & Landers, 2006). For microscale NMR measurements, several types of microcoils have been introduced and readily integrated with microfluidic devices. For example, Wensink *et al.* (2005) developed a glass-based microfluidic chip with an integrated planar microcoil for the detection of ^1H , and monitored imine formation reaction in real time with probe volumes of less than a microliter. Bart *et al.* (2009) improved the sensitivity of microscale MRI to the 10^{-3} mol/L level with a stripline coils and demonstrated its possibility in monitoring reaction kinetics and metabolomics analysis. Bajaj *et al.* (2010) developed a remotely detected microscale MRI to enhance the applicability to microfluidic systems, and obtained the velocity distributions in microchannel flow. Although these studies have proved the effectiveness of microscale MRI, it requires external instrumentation that can be prohibitively expensive, which has prevented the technique from becoming a universal approach.

Another technique, TLM, offers an ultra-sensitive detection at sub-single-molecule level under optimal condition (Tokeshi *et al.*, 2001) with less expensive instrumentations. This technique detects the photothermally induced lens phenomenon, i.e., the thermal lens effect (TLE), using two coaxial laser beams. One of the lasers serves as an excitation beam whose energy is absorbed by the sample molecules, and the other serves as a probe beam which probes the change in refractive index induced by the heat emitted from the molecules. The degree of TLE, which can be obtained from the change in probe beam power, is in proportion to the number of molecules in the probed region (Kitamori *et al.*, 2004). Hence, quantitative analyses have been successfully carried out in various applications including clinical diagnostics and cell analysis (Sato *et al.*, 2002, 2008). However, the chemical selectivity of TLM is unfortunately poor, i.e., it is unsuitable for the preferential detections, since any kind of absorbing molecule would contribute to the TLE. Therefore, the TLM technique works effectively only when used in combination with an appropriate methodology for the separation of analyte species.

In contrast, IR spectroscopy and Raman spectroscopy are chemically selective, and they are active for almost all the substances encountered in microfluidic systems. These two techniques are classified as vibrational spectroscopy, because their measurement principles are based on the fact that all chemical bonds are associated with a specific vibrational frequency (Viskari & Landers, 2006). Since these techniques can provide information of

Table 1.2. Principles and features of some label-free measurement techniques

Technique	Principle	Advantage	Drawback
NMR	Spectroscopic technique based on the interaction of atomic nuclei with magnetic field	Capable of direct determination of molecular structure	Prohibitively expensive instrumentation
TLM	Detection of absorbing molecules utilizing thermal lens effect	Ultrahigh sensitive detection (at sub-single-molecule level)	Poor chemical selectivity
IR spectroscopy	Vibrational spectroscopy utilizing light absorption in mid-infrared region	Chemically selective and active for most substances	Lack of channel material and strong absorption by water
Raman spectroscopy	Vibrational spectroscopy utilizing inelastic scattering of photons	Chemically selective and active for most substances	Relatively weak signal

molecular constituents and their detailed structure by measuring light absorption or scattering of the sample itself, they have been utilized for non-intrusive chemical analyses such as identification, structure elucidation, and reaction monitoring.

IR spectroscopy acquires molecular and structural information of a sample by measuring the absorption of light in the mid-infrared region (~ 2500 to 20000 nm, which corresponds to ~ 4000 cm^{-1} to 300 cm^{-1}) (Chan & Lieu, 2009). Pan *et al.* (2004) fabricated the micro capillary electrophoretic devices made from CaF_2 substrates which has a broad transmission range of 170 – 7800 nm. They demonstrated the on-chip IR detection of toluene, water, and acetonitrile in the microchannels. Chan & Kazarian (2012) demonstrated the possibility of Fourier transform infrared spectroscopic imaging to study chemical reactions in two-phase microfluidic systems. Using the focal plane array detector, which enables the collection of thousands of spatially resolved IR spectra, they successfully visualized the concentration maps of each component within the microfluidic device through a CaF_2 optical window. Although these IR spectroscopic techniques have already been applied to microfluidic systems, it is likely to have limited applicability due to the lack of channel materials that are transparent for IR region. The most common approaches based on CaF_2 windows have some drawbacks; the difficulties in fabrication, limited device functionality, and higher fabrication costs (Barich & Krunnel, 2013). Even the application range of IR spectroscopic techniques may also be limited by the interference of strong water absorption (Viskari & Landers, 2006).

Raman spectroscopy offers the similar but complementary information to IR spectroscopy. The technique utilizes the inelastic scattering of photons by intrinsic molecular bonds in the sample, which leads to the generation of photons that are shifted in energy by amount equal to the characteristic vibrational energy of the bond (Chan & Lieu, 2009). Since there is a linear dependence of the Raman signals on the number of molecular bonds, quantitative analyses can be achieved with chemical specificity. Unfortunately, Raman-based techniques suffer from some limitations at the same time; (1) relatively long acquisition time is required due to the inherently weak spontaneous Raman process, and (2) careful selection for channel material and thickness is necessary to minimize the background fluorescent signals.

Nevertheless, the Raman-based techniques have come to be regarded as being highly compatible with microfluidics (Chrimes *et al.*, 2013), since the recent improvements in hardware have enabled the Raman spectroscopy to largely overcome the concern for its weak signal (Adar *et al.*, 2007). Table 1.3 shows the timeline of the evolution of Raman instrumentation from the time of the prediction and discovery of the Raman effect. This table and the following passage about the historical development were compiled based on the review by Adar *et al.* (2007). As listed in table 1.3, the earliest system typically consisted of a mercury arc lamp (which was filtered to pass the excitation line), a prism spectrograph, and a photographic plate. The system could measure a wide range of wavelength simultaneously, but the long integration time (tens of hours) were required due to the weakness of the Raman

signal. During the period between the mid-1950s to the late-1970s, most systems were double grating monochromators scanned with photomultiplier tubes (PMTs). In this period, the feasibility of Raman microscopy (i.e., applying Raman technique to micro-sized samples) was proved by the use of a tightly focused laser beam as an excitation light source. In the early 1980s, reliable multichannel detectors were developed, which allowed Raman spectra to be collected in ‘multiplexed’ fashion as had been in the earliest system with a photographic plate. The intensified photodiode array and the imaging PMT were the detector of choice until the maturation of high-sensitive charge-coupled device (CCD) cameras which were advantageous in terms of signal-to-noise ratio, and dynamic range. The performance advances in optical filters also supported the rapid increase in Raman use over the past decade. Especially, the introduction of the holographic notch filters in 1990 greatly reduced the complexity of the conventional spectrometers which had been required to reject strong Rayleigh line, and improved the detection efficiency. Raman spectra could now be recorded in seconds to minutes instead of hours, by the combination use of this filter and CCD camera. In addition, the advent of high-performance filters and two-dimensional detectors has important implications that the direct Raman imaging has become one of the effective choices to obtain Raman images. More recently, highly sensitive cameras (such as image intensified CCD and electron-multiplying (EM) CCD cameras) were developed, which have been largely contributed to faster imaging.

Owing to the above-mentioned evolution of Raman instrumentation, the coupling of Raman spectroscopy and microfluidic systems have found a variety of applications, as seen in a review paper by Chrimes, *et al.* (2013). They are still less sensitive than fluorescence-based techniques (for example, measurement accuracy of Raman-based micro-thermometry is typically several K), but their quantitative nature and unique ability to provide ‘molecular fingerprint’ cannot be replaced by other techniques.

1.2.2 Raman Spectroscopy for Microscopic Measurement

As mentioned in the preceding section (table 1.3), the advent of lasers in the 1960s greatly motivated the birth of Raman micro-spectroscopy, i.e., the coupling of Raman spectroscopy to an optical microscope. This technique enables the determination of chemical and structural properties in sample materials with micrometer resolution in lateral direction. In the 1970s and 1980s, the development of CCD cameras replaced PMTs and enabled multi-channel detection with higher sensitivity in visible and near-infrared regions (Dieing *et al.*, 2011). These improvements in instrumentations brought the development of confocal Raman microscopy around the 1990s. Puppels *et al.* (1990) were among the first to apply the confocal technique to improve spatial resolution along the optical axis.

Table 1.3. Timeline for the evolution of Raman instrumentation (compiled based on the review by Adar *et al.* (2007))

Period	Year(s)	Event	Typical instrumentation
Early	1922–1927	Theoretical predictions of the Raman effect	<u>Components</u> { · Mercury arc lamp · Prism spectrograph · Photographic plate } ⇒ Acquisition time: tens of hours
	1928	Discovery of the Raman effect	
	1939	Development of photomultiplier tube (PMT)	
	1953	Introduction of the first “easy-to-use” Raman system consisting of Hg lamp, double monochromator and PMT	
Middle	1962	First measurement of Raman spectra with ruby laser*1	<u>Components</u> { · Laser · Double grating monochromator · Photomultiplier tube } ⇒ Acquisition time: hours
	1968	First holographic gratings produced	
	1973	First demonstration of Raman microscopy	
	1975	Introduction of concepts for creating Raman images*2 (Raman microprobe and Raman microscope)	
	early 1980s	Development of reliable multichannel detectors (intensified photodiode array, imaging PMT, CCD camera)	
Current	1980	Introduction of triple polychromator	<u>Components</u> { · Laser · Grating polychromator & notch filter · CCD camera } ⇒ Acquisition time: seconds to minutes
	1990	Demonstration of holographic notch filter*3	
	2002	Invention of the electron-multiplying CCD camera	

*1: Porto & Wood, 1962 *2: Delhayre & Dhamelincourt, 1975 *3: Carrabba *et al.*, 1990

Both Raman micro-spectroscopy and confocal Raman microscopy have been routinely utilized as a unique tool for probing ‘molecular fingerprint’ in numerous micro-analytical studies spanning medicine, biotechnology, material science, and forensics (Chrimes *et al.*, 2013). Especially over the last decade, countless studies have introduced these Raman-based techniques to microfluidic fields. Since the techniques realize non-intrusive detection or identification of non-fluorescent samples in microspace, they have been often used as concentration measurement techniques to monitor mixing behavior and chemical reaction in microdevices. For example, some groups (Salmon *et al.*, 2005; Sarrazin *et al.*, 2008; Lin *et al.*, 2010) used confocal Raman microscopy to probe interdiffusion of two liquids in a Y-shaped micro-mixer, and calculated the values of diffusion coefficient from the measured concentration. Fletcher *et al.* (2003) investigated chemical reaction of ethanol and acetic acid in a T-shaped glass micro-reactor. They measured concentration profile of individual species at different mixing stages by focusing on the distinct Raman peaks of the analytes. In a similar manner, Rinke *et al.* (2011) studied the hydrolysis reaction of acetal in a T-shaped micro-mixer. Many more studies have reported on such *in-situ* monitoring applications; such as, monitoring of imine formation reaction in a round-wave glass channel (Lee, Lee *et al.*, 2003), analysis of passive mixing behavior in a serpentine PDMS channel (Park *et al.*, 2004), and detection of gas solubility in aqueous solution in a silicon-Pyrex micro-reactors (Liu *et al.*, 2012).

Such an *in-situ* Raman spectroscopic measurement has been implemented for real-time reaction optimization in a continuous flow micro-reactor by Leung *et al.* (2005). They measured the concentration of the reaction product by confocal Raman microscopy and realized rapid control of product amount by varying the reactants’ flow rate. Moreover, in recent years, optical detection systems for Raman spectroscopy have been integrated into microfluidic devices. A good example for ‘Raman-on-chip device’ is found in the work by Ashok *et al.* (2011), where excitation and detection fibers are integrated into a microfluidic device for on-chip Raman detection of analyte.

Raman-based techniques have been also utilized for microscale thermometry, though the number of studies has been much less compared to concentration measurement. Kim *et al.* (2006) used Raman micro-spectroscopy to measure steady state water temperature inside a microchannel of a polymerase chain reaction (PCR) chip. Pikov & Siegel (2010) developed an original Raman spectrometer system for thermal monitoring of biological samples and performed temperature determination in human lung cells in a thin dish enclosed by transparent membranes. For the purpose of evaluating local temperature distributions inside microchannels, Ewinger *et al.* (2013) investigated the spatial resolution of the measurement. In their experiment, the lateral and depth resolutions were calculated to be approximately 15 μm and 25 μm , respectively. Since these studies aimed at microscale thermometry of water-based materials under relatively low temperature conditions ($< 373 \text{ K}$), they calculated

the temperature by collecting the Raman spectra of temperature-dependent OH vibrational band whose spectral shape is related to the formation of hydrogen bonding.

As for the measurement techniques which are specialized for interfacial regions, total internal reflection (TIR) Raman spectroscopy has been used to study interfacial phenomena. In TIR Raman spectroscopy, near-surface region is selectively excited by an evanescent wave generated by total internal reflection of an incident light, as is the case with well-established techniques like total internal reflection fluorescence (TIRF) (Axelrod, 1981, 2001) and attenuated total reflection infrared spectroscopy (Kazarian & Chan, 2006).

The applicability of TIR to Raman spectroscopy was hinted by Harrick & Loeb in 1973, and was first demonstrated by Ikeshoji *et al.* in 1973. They measured TIR Raman spectra from carbon disulfide (CS₂) liquid in contact with a hemispherical substrate made of flint glass, but the signal was very weak and obscured by the strong background noise from the TIR substrate. In order to overcome this problem, Iwamoto *et al.* (1980) investigated the suitable materials for TIR substrate and improved the signal-to-noise ratio by employing a sapphire substrate. They successfully demonstrated the feasibility of unenhanced TIR Raman spectroscopy to surface analysis by recording spectra from a 1.1 μm-thick polystyrene film without being interrupted by the signal from polyethylene layer coated on the polystyrene film. They also first presented the application of the technique to biological material by recording the spectrum from a thin layer of bovine albumin (Iwamoto *et al.*, 1981). The relationship between the incident angle and TIR Raman intensity was discussed in several studies (Ikeshoji *et al.*, 1973; Iwamoto *et al.*, 1981), and it was confirmed that the TIR Raman signal was maximized with laser irradiation at critical angle. In addition, Ohsawa *et al.* (1984) studied the angular dependence of Raman intensity from thin films deposited on a glass prism. They showed that the sensitivity of TIR Raman signal can be remarkably improved by detecting the signal at a scattering angle near the critical angle of the prism side.

In spite of the above early efforts, TIR Raman spectroscopy has long been overshadowed by surface enhanced Raman spectroscopy (SERS) which can produce highly increased Raman signal from molecules in contact with or in the vicinity of a nano-structured metal surface by excitation of surface-plasmon resonances (Kneipp, 1999). However, modern instrumentation extends its applications especially where SERS is impractical or undesirable (Woods & Bain, 2012). In the more recent works, TIR Raman spectroscopy has been employed in diverse fields to study, for instance, surfactant adsorption and desorption, structure of polymer film, biological interfaces, and lubrication. These are reviewed in some references (Greene & Bain, 2004; Woods & Bain, 2012, 2014). Focusing on solid-liquid interfaces, Nickolov *et al.* (1993) investigated the water structure adjacent to hydrophilic and hydrophobic surfaces by measuring TIR Raman spectra of OH stretching vibrational band of water. Tyrode *et al.* (2008) used TIR Raman to investigate the adsorption amount of a

cationic surfactant from aqueous solutions onto silica glass by measuring the surface concentration of the surfactant using TIR Raman spectroscopy. Their group also extended the technique to study adsorption and desorption kinetics of surfactants in multicomponent systems, and successfully showed that the composition of the adsorbed layer can be followed in real time (Wood *et al.*, 2011a, 2011b).

While these studies demonstrated that TIR Raman spectroscopy has now sufficient ability to probe the composition in a thin liquid layer in contact with solid surface, it has not been applied to near-wall flow analysis in microfluidic devices. Moreover, with regard to two-dimensional visualization using TIR Raman scattering, there has only been one example to date. Michaels (2010) obtained the Raman images of a micro-patterned polymer film by plotting the peak area of TIR spectrum collected at each point in the sample.

1.2.3 Raman Imaging Technique for Two-dimensional Visualization

There have been various methodologies for obtaining two-dimensional lateral Raman images, and these are generally classified into two major groups; image reconstruction and direct imaging (Puppels *et al.*, 1993). Their procedures are illustrated in figure 1.3. The image reconstruction technique records a whole spectrum at each point of measurement area using a spectrometer and a scanning system, and subsequently reconstructs a Raman image at a specific wavenumber. In contrast, direct imaging technique does not record Raman spectra. In this technique, Raman scattering arising from globally-illuminated sample is collected thorough an optical filter and imaged onto a two-dimensional detector. This means that a Raman image at specific wavenumber (transmitted by the filter) can be obtained by a single measurement. Since the present study aims at measurements of thermal flow fields which are generally accompanied by temporal changes, the latter technique is considered to be more suitable in terms of data acquisition time. Hence, this section deals with the previous works related to direct Raman imaging.

The concept of direct Raman imaging was first introduced by Hartley in 1974 (by the name of ‘Ramanography’) in the field of combustion research. Soon after that, Delhaye & Dhamelincourt (1975) introduced the system termed ‘Raman microscope’ where direct Raman imaging technique was coupled to an optical microscope. Since then, direct Raman imaging has been used in the wide range of areas including both macroscopic and microscopic aspects. Its application fields cover biology (cell or tissue analyses (Schaeberle *et al.*, 1996; Otto *et al.*, 1997; Maier *et al.*, 2006)), medicine (visualization of drug distributions in living cells (Ling *et al.*, 2002)), material science (analysis of polymer structure (Batchelder *et al.*, 1991)), and thermofluid mechanics.

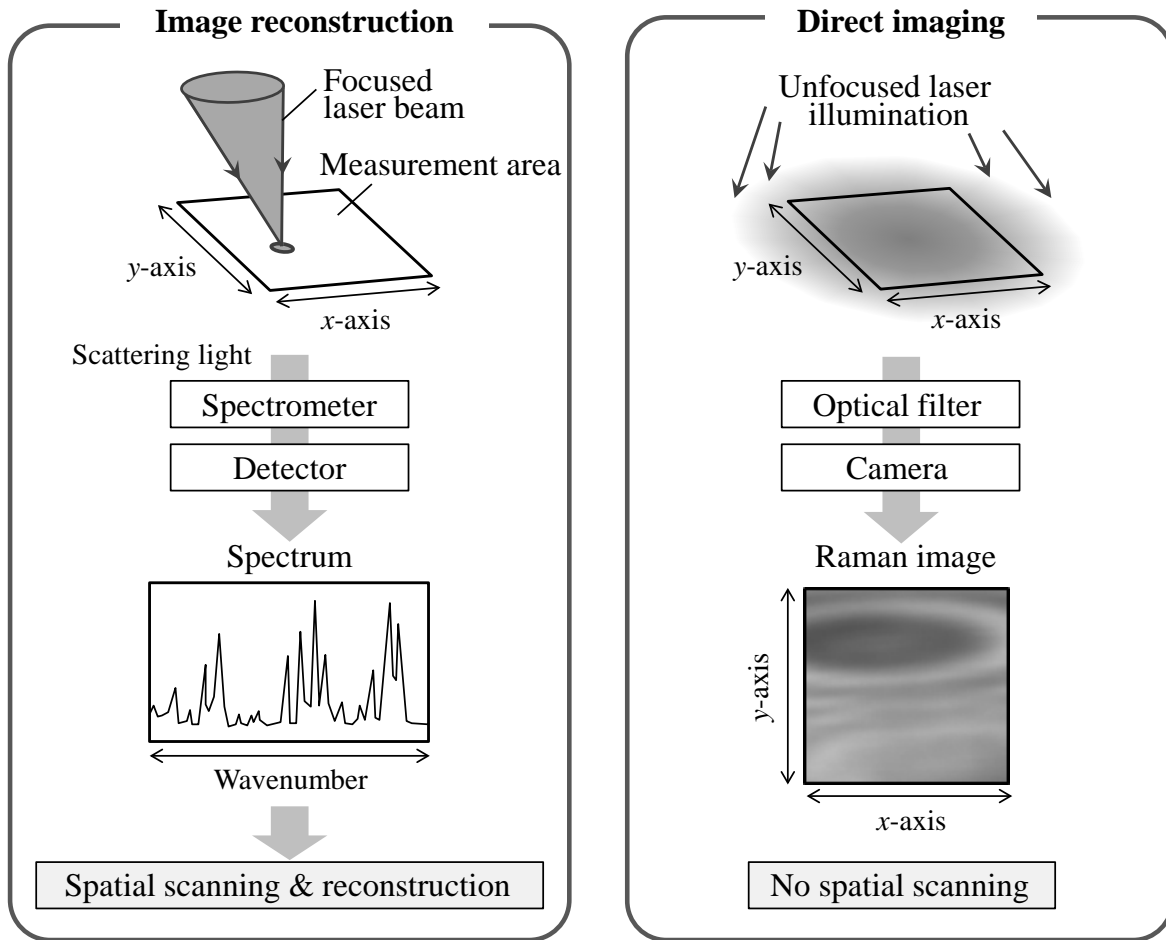


Figure 1.3. Comparison of the methodologies for obtaining a Raman image.

Focusing on the applications to macro-scale thermal flow fields, direct Raman imaging has been often used for quantitative visualization of fluid composition, namely, concentration imaging of specific species. Mayer *et al.* (2003) applied the imaging technique to investigate jet behavior in a pressurized chamber under cryogenic conditions. They determined the density distribution of liquid N₂ and jet spreading angle from the obtained Raman images. Malarski *et al.* (2006) reported the simultaneous measurement of concentration and velocity fields in a turbulent mixing flow of liquid water and ethanol, by using Raman imaging in combination with PIV technique. Leipertz's group has been published a series of papers on measurements in gaseous or supercritical environments. They performed H₂ mole-fraction measurement in a combustion chamber (Braeuer *et al.*, 2009), and CO₂ density imaging in supercritical environments (Dowy *et al.*, 2009a, 2009b). In addition to concentration measurement, temperature visualization techniques have been developed based on direct

Raman imaging. Rabenstein & Leipertz (1997) demonstrated planar thermometry in a burner flame by exploiting the temperature dependence of the intensity ratio of Stokes to anti-Stokes Raman signals. Braeuer & Leipertz (2009) performed simultaneous imaging of temperature and concentration fields in a flow chamber. They acquired Raman images of three different wavelengths using three EM-CCD cameras in order to probe the population numbers of the specific rotational and vibrational energy levels of N_2 and H_2 gases.

Owing to these previous studies, direct Raman imaging technique has been proved to be a promising approach for macro-scale flow measurements. On the other hand, only a few studies have performed Raman imaging technique for microscale flow analysis. Roetmann *et al.* (2008) developed a Raman imaging system with a laser sheet illumination to monitor concentration fields in micro-mixers. They successfully visualized the spatial distributions of different components (water and methanol) with extremely short integration time (6 ns). Using a similar setup, Rinke *et al.* (2012) measured the concentration distributions of several planes in the micro-mixer by traversing the laser sheet and compared the measured concentration with CFD calculations. In addition, the setup has been combined with PIV system by Wellhausen *et al.* (2012). Another group, Takahashi *et al.* (2012) demonstrated a fluorescence-free velocity measurement in channel flow using Raman imaging. They injected a drop of electrolyte solution into flowing water and measured the time-series distributions of ion concentration in the downstream area with frame interval of 91 ms. Subsequently, they calculated the fluid velocity from the displacement of the peak position in the obtained distributions. The technique requires an injection of electrolyte solution as tracer for velocity determination, and thus it has only limited applicability.

1.3 Motivation and Objectives

The motivation of the present study is to develop a series of techniques which can realize non-intrusive, chemically-selective, and two-dimensional measurements of microscale thermal flow fields based on spontaneous Raman imaging. Non-intrusive approaches, which do not employ any extrinsic markers or labels, are advantageous especially to measurements in interfacial region, in electrokinetic flow, or in flow containing biological materials. Chemical specificity achieves measurements in multicomponent systems such as reaction fields. Furthermore, two-dimensional measurements would greatly aid in achieving accurate flow control in microdevices due to the much better understanding that a full-field view provides. In the present study, the target physical quantities are bulk temperature, bulk velocity, and near-wall concentration.

There have been only a few examples of studies which employed Raman imaging technique for flow analyses in the current state. Figure 1.4 briefly summarizes the previous studies based on Raman imaging and the target of each chapter in the present study. These are classified according to their target physical quantity and characteristic length scale. Figure 1.5 presents the comparison of spatiotemporal resolutions of the previous studies which are listed in figure 1.4, and those targeted by the present study. The red and blue circles represent the previous studies on temperature and concentration measurements, respectively, and a number for each circle corresponds to the number assigned to each reference in figure 1.4. Here, the temporal resolution is defined as the time required for obtaining a single Raman image, which is generally determined by the frame interval of the camera or the laser repetition rate. It should be noted that the above-defined temporal resolution is sometimes much longer than the integration time for a single image, since the integration time generally represents the laser pulse duration when a pulsed laser is used as an excitation light source. (Actually, most previous studies (except for Takahashi, *et al.* (2012)) employed pulsed lasers with duration of several nanoseconds.) It is also noted that the total acquisition time will be much longer than the above-defined resolution, when image accumulation is required. The spatial resolution is generally defined as the size of the area which is imaged onto one binned pixel (i.e., the lateral spatial resolution). However, only for the target of the near-wall concentration measurement in chapter 6, it is defined by that in the depthwise direction which is characterized by the penetration depth of the evanescent illumination.

For temperature measurements, a couple of examples have been reported in macroscale, but not yet in microscale. In addition, the methodologies in macroscale were developed especially for combustion analyses. These techniques rely on the measurement of anti-Stokes Raman scattering whose intensity is considerably weak below 1000 K (Rabenstein & Leipertz, 1997) or rotational Raman signals which can be observed only from molecules in gaseous phase (Braeuer & Leipertz, 2009). Hence, these cannot be applied directly to microfluidic systems where liquid phase samples are intensively examined at relatively low temperature conditions. This challenge will be addressed in chapters 3 and 4 in this study.

As for concentration measurements, there have been several studies employing Raman imaging both for macro- and microscale flow analyses exploiting the linear proportional nature of Raman scattering intensity with concentration. However, the imaging technique has not yet been applied to interfacial phenomena occurring in sub-microscale, where the addition of external fluorescent labels has the most noticeable influence (such as adsorption and absorption). Therefore, chapter 6 in the present study will deal with the concentration measurement in the vicinity of the surface.

For velocity measurements, Takahashi *et al.* (2012) proposed a scalar-based methodology using Raman imaging, where the fluid velocity was estimated from the displacement of the peak position in the time-series concentration distributions. (Thus it is represented by a blue

	Characteristic length scale			
	nm	μm	mm	m
Temperature measurement		Chapters 3 & 4		Rabenstein & Leipertz (1997) ^{*1} Braeuer & Leipertz (2009) ^{*2}
Concentration measurement		Chapter 6	Roetmann <i>et al.</i> (2008) ^{*7} Rinke <i>et al.</i> (2012) ^{*8} Wellhausen <i>et al.</i> (2012) ^{*9}	Malarski <i>et al.</i> (2006) ^{*3} Braeuer <i>et al.</i> (2009) ^{*4} Dowy <i>et al.</i> (2009a) ^{*5} , b ^{*6}
Velocity measurement		Chapter 5		Takahashi <i>et al.</i> (2012) ^{*10}

Figure 1.4. Previous studies based on Raman imaging technique and the target of each chapter of the present study.

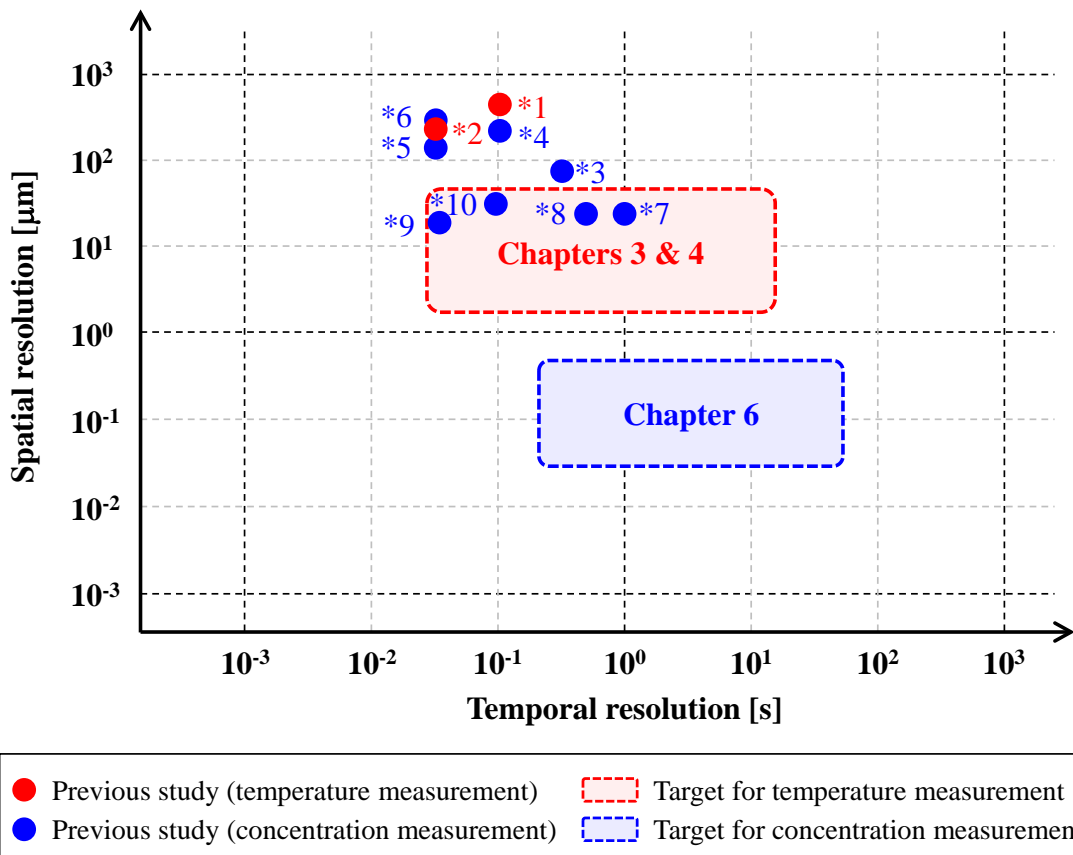


Figure 1.5. Comparison of spatial and temporal resolutions of the previous studies and those targeted by the present study.

circle in figure 1.5.) This technique was surely fluorescence-free, but required the additional injection of electrolyte solution as a tracer, which makes it less suitable for practical use. A more versatile approach based on Raman imaging will be proposed in chapter 5.

Figure 1.6 depicts the objectives of the present study and outline of the dissertation.

Chapter 2 summarizes the fundamental of microfluidics, and introduction to optics sufficient to explain microscopic measurement based on Raman imaging. The material and fabrication techniques of milli- and microchannels are also described.

Chapter 3 details the development of a non-intrusive planar temperature measurement technique using Raman imaging. The conventional fluorescence-based techniques require extrinsic labels to be added to measure fluid temperature. On the other hand, the present technique exploits the temperature dependence of the Raman intensity from the fluid itself, especially focusing on the chemical equilibrium between hydrogen-bonded (HB) and non-hydrogen-bonded (NHB) states of liquid H₂O molecules. This chapter experimentally examines the temperature dependence of the OH stretching Raman band whose shape is closely related to the intermolecular hydrogen bonds. Subsequently, a Raman imaging system is developed using a camera and optical filters instead of a spectrometer. A relationship between the temperature and the Raman intensity of HB to NHB modes is investigated, and visualization of steady-state temperature field in channel flow is demonstrated according to the obtained relationship.

Chapter 4 presents the development of two-wavelength Raman imaging technique for non-intrusive and two-dimensional monitoring of transient temperature field. The present technique is based on the same principle as the technique described in chapter 3, but a two-wavelength imaging system is newly developed by incorporating two cameras and two optical filters. This system enables the simultaneous detection of two Raman signals with contrasting temperature dependencies (i.e., HB and HNB modes), and thus allows the measurement in unsteady temperature field. Moreover, the two-wavelength methodology has another advantage that it is immune to the temporal fluctuation of an excitation light. This section details the configuration of the developed imaging system, and assesses the applicability of the technique for monitoring the non-uniform and transient temperature distributions in channel flow.

Chapter 5 contains the proposal of a concept of fluorescent-free velocity measurement based on thermal tracing by two-wavelength Raman imaging technique, and the investigation of its possibility focusing on the error in temperature measurement with short acquisition time. Raman images are acquired at various measurement conditions (such as electron-multiplying gain and spatial averaging process) and the influence of each parameter on measurement error is experimentally investigated. The velocity determination by the proposed method has not yet been demonstrated, but a measurable velocity range and a

temperature rise required for thermal tracing are roughly estimated as the preliminary step towards the establishment of a non-intrusive microscale velocimetry.

Chapter 6 describes the development of a novel measurement technique for near-wall concentration, which is termed total internal reflection (TIR) Raman imaging. This technique utilize the Raman scattering excited by an evanescent wave which illuminates only the vicinity of an interface (within 100 nm). Since the spontaneous Raman signal is linearly proportional to the number of molecules present, the obtained Raman images can be interpreted into concentration distributions. An optical measurement system is newly developed by combining a two-prism-based TIR microscopy system with a Raman imaging system in order to realize chemically-specific, surface-selective, and two-dimensional concentration measurements at the glass-solution interface in a microchannel. Mixtures of H₂O and D₂O are prepared as sample solutions, and the distribution of each component is separately visualized in a non-uniform mixing field.

Chapter 7 summarizes the conclusions of the present study. In addition, future issues and the potential applications of the developed measurement techniques are discussed.

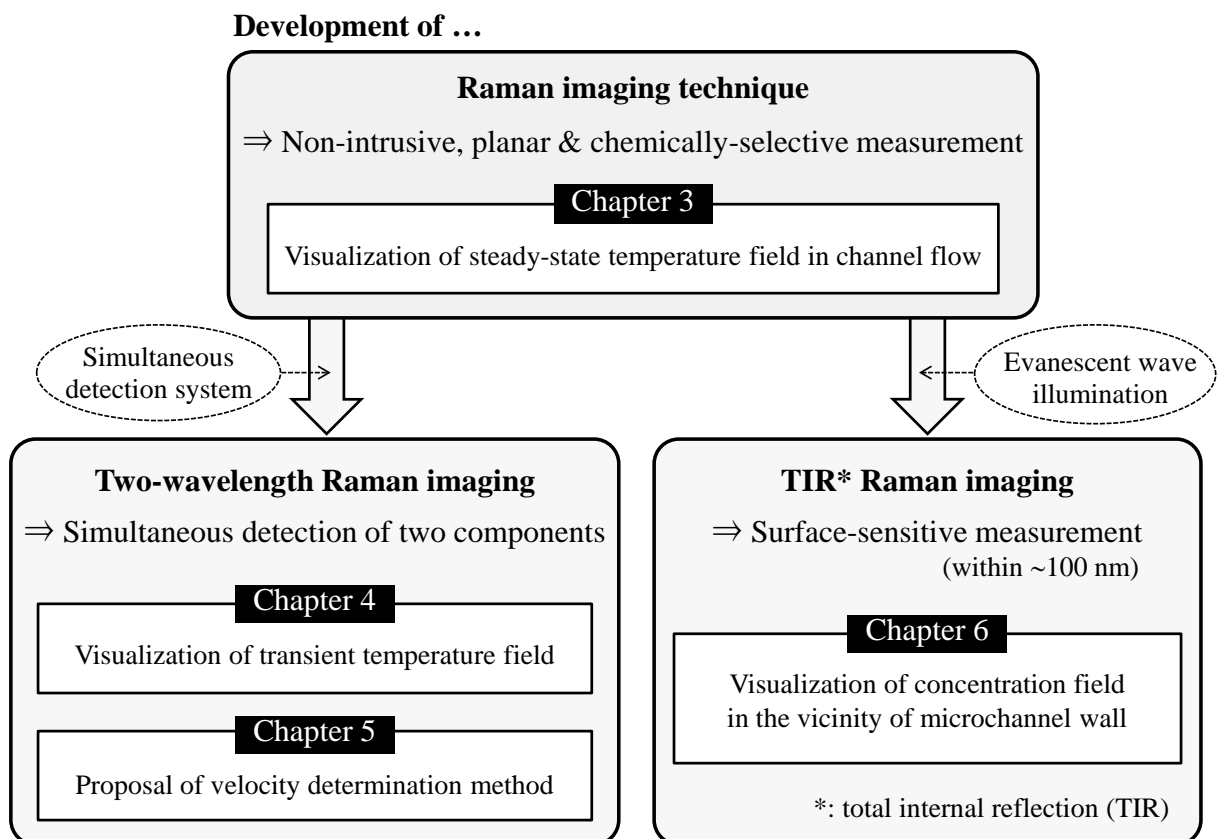


Figure 1.6. Objective and outline of the present dissertation.

Chapter 2

Fundamentals

This chapter describes the background necessary to understand the Raman-based microscopic measurement techniques developed in the present study. The first section summarizes the fundamental of microfluidics, including theory of fluid motion, thermal transport and mass transport. The second and third sections give introduction to optics sufficient to explain microscopic measurement based on Raman imaging. It contains fundamental of Raman scattering, conventional microscopy and total internal reflection. The last section describes the sample preparation and channel fabrication.

2.1 Theory of Microfluidics

2.1.1 Continuum Hypothesis

Microfluidics deals with the fluid flows over micron or sub-micron length scales, pertaining to the actuation, precise control and manipulation of liquids or gases commonly in femto-liter to micro-liter precision (Chakraborty, 2010). The continuum approximation still holds for such flow scales encountered in microfluidics (of the order of 10 μm and more), since fluids are quantized on the much smaller length scale, i.e., intermolecular distances (of the order of 0.3 nm for liquids and 3 nm for gases) (Bruus, 2008). Therefore, the fluid is regarded as ‘continuous’ in microfluidics, and its ‘average’ behavior is considered rather than the individual molecular behavior (Tian & Finehout, 2008). This means that microfluidic flows are typically governed with the same fundamental equations developed for macroscale fluid mechanics. However the continuum approximation breaks down in the nanofluidics, where the system under consideration approaches molecular scale, e.g., in liquid transport through nano-porus or in nano-channels (Bruus, 2008).

2.1.2 Fluid Motion

Under the continuum approximation, the governing equations for incompressible Newtonian fluids are given by,

$$\nabla \cdot \mathbf{u} = 0 \quad (2.1)$$

$$\frac{\partial \mathbf{u}}{\partial t} + (\mathbf{u} \cdot \nabla) \mathbf{u} = -\frac{1}{\rho} \nabla p + \nu \nabla^2 \mathbf{u} + \mathbf{f} \quad (2.2)$$

where $\mathbf{u} = (u, v, w)$ is the fluid velocity [m/s], ρ is the fluid density [kg/m^3], t is the time [s], p is the pressure [Pa], and ν is the kinematic viscosity [m^2/s]. The last term in the right-hand side, \mathbf{f} [m/s^2], represents the acceleration by external body forces acting on the fluid, such as gravity and electric body force which induces electrokinetic flow. Equations (2.1) and (2.2) correspond to the equation of continuity and the momentum equation (i.e., the Navier-Stokes equation) at the position $\mathbf{x} = (x, y, z)$, respectively.

In order to normalize equation (2.2), the variables were nondimensionalized as follows:

$$\mathbf{x} = L\mathbf{x}^*, \quad \mathbf{u} = U\mathbf{u}^* \quad (2.3)$$

where the starred quantities represent the dimensionless variables. Here L is a characteristic length scale and U is a characteristic velocity of the fluid. A characteristic pressure and a characteristic time scale were also set to be as follows:

$$p = \frac{\rho \nu U}{L} p^*, \quad t = \frac{L^2}{\nu} t^* \quad (2.4)$$

The time L^2/ν corresponds to the time required for viscous diffusion to traverse the distance L (Currie, 2003). In terms of the above dimensionless variables, the Navier-Stokes equation can be rewritten as,

$$\frac{\nu U}{L^2} \frac{\partial \mathbf{u}^*}{\partial t^*} + \frac{U^2}{L} (\mathbf{u}^* \cdot \nabla^*) \mathbf{u}^* = -\frac{\nu U}{L^2} \nabla^* p^* + \frac{\nu U}{L^2} \nabla^{*2} \mathbf{u}^* \quad (2.5)$$

Here the external force term is omitted for simplicity. Multiplying equation (2.5) by $L^2/\nu U$ and introducing the Reynolds number, $Re (= UL/\nu)$ gives,

$$\frac{\partial \mathbf{u}^*}{\partial t^*} + Re (\mathbf{u}^* \cdot \nabla^*) \mathbf{u}^* = -\nabla^* p^* + \nabla^{*2} \mathbf{u}^* \quad (2.6)$$

In equation (2.6), the Reynolds number Re represents the ratio of inertial forces to viscous forces. For most microfluidic systems the Reynolds number is very low (typically, $Re < 1$), which means that the viscous forces rather than inertial forces dominate the fluid dynamics. This results in a laminar flow, i.e., a smooth and predictable flow (Brody *et al.* 1996). By taking the limit $Re \rightarrow 0$ (i.e., ignoring the inertial term), it is evident that the Navier-Stokes equation, which is a non-linear partial differential equation, can be transformed into a simple linear one. The resulting equation is,

$$\frac{\partial \mathbf{u}}{\partial t} = -\frac{1}{\rho} \nabla p + \nu \nabla^2 \mathbf{u} \quad (2.7)$$

Equation (2.7) is referred to as the time-dependent Stokes equation. In addition, when the flow is in the steady state, the time derivative term can be negligible. This approximation derives the Stokes equation,

$$\nabla p = \eta \nabla^2 \mathbf{u} \quad (2.8)$$

where $\eta (= \rho \nu)$ is the viscosity [Pa·s]. This type of fluid flow, which is known by ‘Stokes flow’ or ‘low Reynolds number flow’, is determined entirely by the pressure distribution, the incompressibility constraint (equation (2.1)), and the boundary conditions (Brody *et al.* 1996).

By solving equation (2.8), the velocity profile in a rectangular microchannel with width w_c and height h_c , with the origin of coordinates on the centerline (figure 2.1) is obtained with the boundary conditions of $\mathbf{u} = 0$ at $y = \pm w_c/2$ and $z = \pm h_c/2$ (Brody *et al.* 1996; Ichikawa *et al.* 2004) as follows:

$$u(y, z) = \frac{4h_c^2}{\eta\pi^3} \left(-\frac{\partial p}{\partial x} \right) \sum_{n=0}^{\infty} \frac{(-1)^n}{(2n+1)^3} \times \left\{ 1 - \frac{\cosh[(2n+1)\pi y / h_c]}{\cosh[(2n+1)\pi w_c / 2h_c]} \right\} \cos[(2l+1)\pi z / h_c] \quad (2.9)$$

Figure 2.2(a) shows the velocity profiles in the spanwise direction at $z = 0$ in rectangular microchannels with three different aspect ratios $\varepsilon (= h_c / w_c)$. It is clearly observed that the velocity in the microchannel with small aspect ratio shows plug like profile in the y -direction. In contrast, the velocity profiles in the depthwise direction at $y = 0$ become parabolic for all the aspect ratios (figure 2.2(b)).

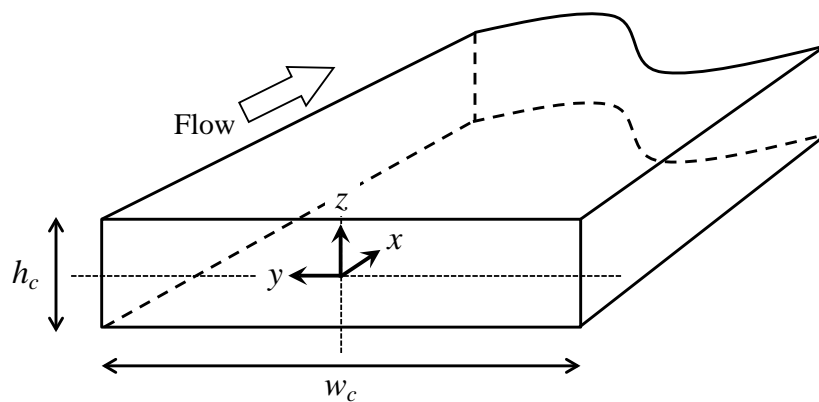


Figure 2.1. Geometry of a rectangular channel with the width of w_c and the height of h_c .

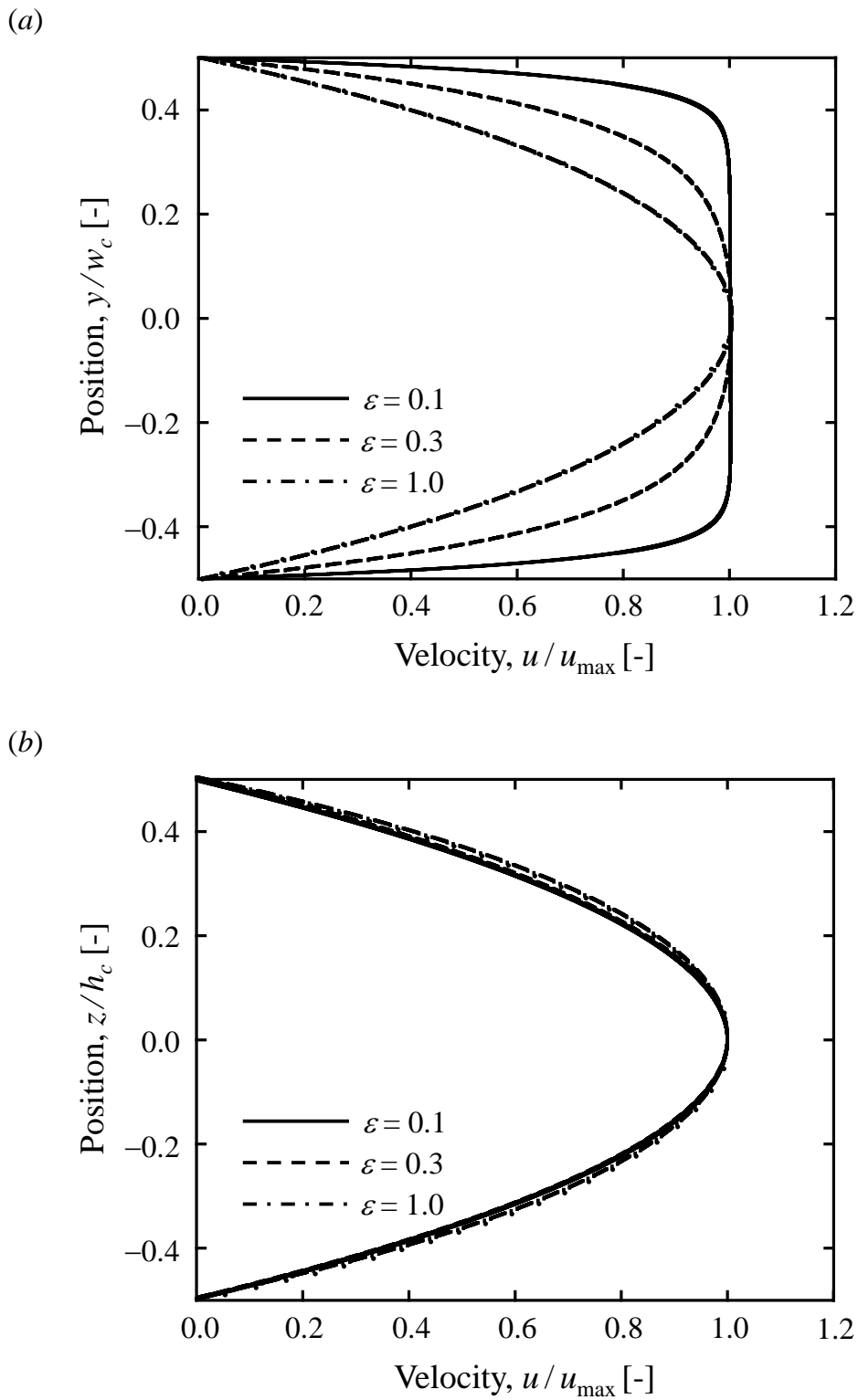


Figure 2.2 Velocity profiles of pressure-driven flow in the rectangular channel with different aspect ratios. (a) Profiles in the spanwise direction at $z / h_c = 0$, and (b) in the depthwise direction at $y / w_c = 0$.

2.1.3 Heat Transport

The energy equation is derived by application of the law of conservation of energy. For a fluid of constant physical properties under moderate flow conditions, the energy equation can be expressed as,

$$\frac{\partial T}{\partial t} + \mathbf{u} \cdot \nabla T = \alpha \nabla^2 T \quad (2.10)$$

where T is the absolute temperature [K], α is the thermal diffusivity [m^2/s]. In equation (2.10), sometimes referred to as the heat conduction equation, heat flux due to interdiffusion and due to viscous dissipation are neglected as small, and heat sources are absent (Probstein, 1994).

As is the case with the momentum equation (equation (2.2)), the energy equation can be converted into a dimensionless expression using equation (2.3) and

$$(T - T_0) = (T_0 - T_w) T^*, \quad t = \frac{L^2}{\alpha} t^* \quad (2.11)$$

where $(T_0 - T_w)$ is the characteristic driving temperature difference and L^2/α corresponds to the time required for thermal diffusion to traverse the distance L . The subscription 0 denotes a reference state, such as an initial or free stream value, and w may, for example, represent a known value of the temperature at a wall or surface in the flow (Probstein, 1994). In terms of the reduced variables, equation (2.10) becomes

$$\frac{\partial T^*}{\partial t^*} + Pe_T (\mathbf{u}^* \cdot \nabla^* T^*) = \nabla^{*2} T^* \quad (2.12)$$

where $Pe_T (=UL/\alpha)$ is the thermal Peclet number, which represents the ratio of the heat transported by convection to that transported by conduction. The thermal Peclet number plays a similar role in heat transport as the Reynolds number in momentum transport, and it can be written as,

$$Pe_T = \frac{UL}{\alpha} = \frac{UL}{\nu} \cdot \frac{\nu}{\alpha} = Re \cdot Pr \quad (2.13)$$

where a new dimensionless parameter ($Pr = \nu/\alpha$), which is termed as Prandtl number, is introduced. It should be noted that the Prandtl number is a property of the fluid, while the Reynolds number represents a property of the flow (Probstein, 1994). The order of magnitude of the Prandtl number for common liquids (except for liquid metals) is $10 < Pr < 10^2$ (Asano, 2006). For example, the Prandtl number for water at 300 K is $Pr = 5.65$, which leads to the consequence that conductive heat transfer can be dominant at low Reynolds number frequently encountered in microfluidics ($Re \approx 10^{-2}$) as reported by Sato *et al.* (2003).

2.1.4 Mass Transport

The governing equation for mass transport is derived by application of the law of

conservation of mass. Assuming a fluid of constant physical properties under moderate flow conditions without chemical reaction, the equation is termed the convective diffusion equation and expressed as,

$$\frac{\partial c}{\partial t} + \mathbf{u} \cdot \nabla c = D \nabla^2 c \quad (2.14)$$

where c is the molar concentration [mol/m^3], and D can be the binary diffusion coefficient or the diffusion coefficient of i -th species [m^2/s]. When $\mathbf{u} = 0$, equation (2.14) reduced to the ordinary diffusion equation, i.e., Fick's second law of diffusion (Probstein, 1994). It is important to note that equation (2.14) is an approximate one and is only valid in the dilute concentration range (Asano, 2006).

In analogy with the case of thermal transport, equation (2.14) can be normalized by applying equation (2.3) and the parameters,

$$(c - c_0) = (c_0 - c_w) c^*, \quad t = \frac{L^2}{D} t^* \quad (2.15)$$

as follows:

$$\frac{\partial c^*}{\partial t^*} + Pe_D (\mathbf{u}^* \cdot \nabla^* c^*) = \nabla^{*2} c^* \quad (2.16)$$

where $Pe_D (=UL/D)$ is the diffusion Peclet number, which represents the ratio of the mass transported by convection to that transported by diffusion. The diffusion Peclet number can be rewritten by,

$$Pe_D = \frac{UL}{D} = \frac{UL}{\nu} \cdot \frac{\nu}{D} = Re \cdot Sc \quad (2.17)$$

where $Sc (= \nu/D)$ is the Schmidt number. The order of magnitude of the Schmidt number for common liquids is $400 < Sc < 10^4$ (Asano, 2006). For instance, the Schmidt number for dilute solutions at 293 K is $Sc \approx 10^3$. The consequence of such a large Schmidt number is that convection dominates over diffusion at moderate and even relatively low Reynolds numbers (Probstein, 1994).

2.2 Raman-Based Measurement

2.2.1 Introduction to Raman Spectroscopy

The well-known fundamentals of spontaneous Raman scattering can be found in many publications. Therefore only a brief summary is given here. References (Long, 1977; Tu, 1982; Nakamoto, 2009) all cover the most of the material in the following subsection.

When monochromatic light is incident on a sample, it is partially transmitted, absorbed and scattered. Most part of the scattered radiation has the same frequency as the incident light,

ν_0 [Hz], due to the elastic process; this is called Rayleigh scattering. A small fraction of the scattered radiation occurs however, as a result of inelastic collisions of photons and molecules, and thus is observed as a frequency-shifted emission ($\nu_0 \pm \Delta\nu$), as shown in figure 2.3. This inelastic scattering event, which is much weaker than the Rayleigh scattering by a factor of 10^{-3} – 10^{-5} (Nakamoto, 2009), is known as Raman scattering or Raman effect. Raman scattering was discovered by C. V. Raman and K. S. Krishnan in 1928, although it had been predicted theoretically a few years earlier by Smekal (1923). The scattered radiation at lower frequency ($\nu_0 - \Delta\nu$) is called Stokes Raman scattering, whereas that at higher frequency ($\nu_0 + \Delta\nu$) is termed anti-Stokes Raman scattering. These frequency-shifted signals arise when the irradiated material absorbs or loses a portion of the incident energy, and their processes are illustrated as energy diagrams in figure 2.4. E_a and E_b [J], represent the energy of the initial state and that of the final state, respectively, and their energy difference can be expressed by,

$$|E_b - E_a| = h\Delta\nu \quad (2.18)$$

where h is Planck's constant [J·s]. This energy difference corresponds to the increase or decrease in the vibrational- and/or rotational-energy level of an irradiated molecule. The frequency difference ($\pm \Delta\nu$) between the incident and the scattered light is referred to as Raman shift, and it is independent of the frequency of incident photons.

When the scattered light is dispersed according to its frequency shift, a Raman spectrum can be obtained. Figure 2.5 gives an example of a Raman spectrum which was obtained from liquid carbon tetrachloride (CCl_4) by Hamaguchi and Hirakawa (1988). The vertical axis is scattering intensity and the horizontal axis is Raman shift expressed as a wavenumber [cm^{-1}], which is calculated as,

$$\tilde{\nu} = \frac{\Delta\nu}{c} = \frac{1}{\lambda_0} - \frac{1}{\lambda_{\text{Raman}}} \quad (2.19)$$

where c is light speed [m/s], and λ_0 and λ_{Raman} are the wavelengths of the excitation light and that of the Raman scattering [m], respectively. As shown in figure 2.4, the Raman shift is determined by the energy difference between the initial and final states of the material and it is equal to the vibrational or rotational frequency of a molecule involved. Therefore the Raman spectrum is unique for an individual species and provides an effective tool for the identification or qualitative analysis of samples, which makes it being described as 'molecular fingerprint'.

Quantitative evaluation is also realized by measuring the Raman scattering intensity, exploiting its linear dependence with the number of molecules being excited. The expression for the measured Raman intensity for i -species, I_i [photons/s·m²], is

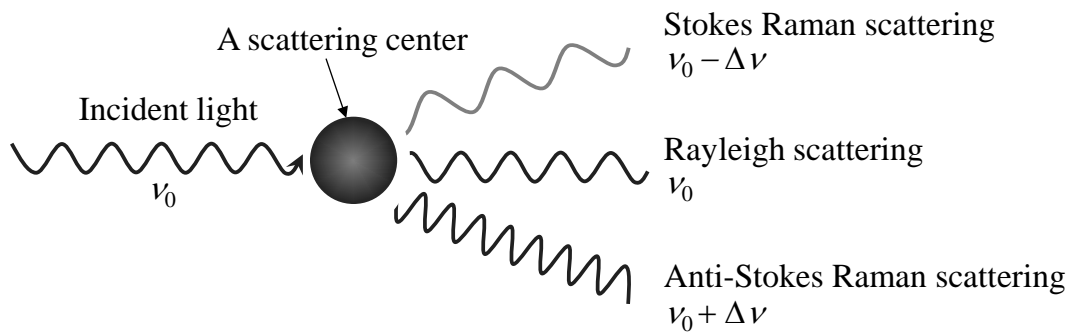


Figure 2.3. Schematic of the three types of light scattering: Stokes Raman scattering, Rayleigh scattering, and anti-Stokes Raman scattering.

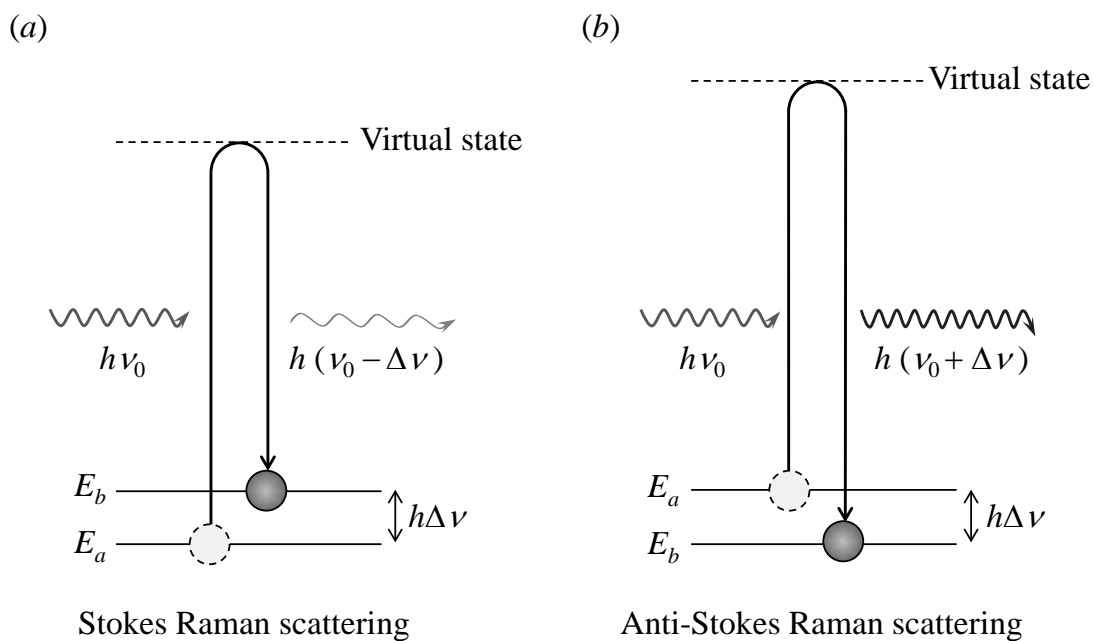


Figure 2.4. The energy diagrams of molecules showing the origin of (a) Stokes Raman scattering and (b) anti-Stokes Raman scattering.

$$I_i = K \cdot I_0 \cdot \Omega \cdot \left(\frac{d\sigma}{d\Omega} \right)_i \cdot l \cdot N_i \quad (2.20)$$

where I_0 [photons/s·m²] is the excitation laser intensity, Ω [sr] is the solid angle of signal detection, $d\sigma/d\Omega$ [cm²/molecule·sr] is the absolute differential Raman cross section, l [m] is the length of the probe volume and N_i [molecules/m³] is the number density of i -species molecules being illuminated inside the probe volume (Kiefer *et al.*, 2008). The constant K [-] is introduced to express influencing parameters such as transmission of the optical components and collection efficiency of the detector. Typical cross sections of Raman scattering are about 10⁻³⁰ cm²/molecule, and smaller than those of fluorescent dyes (~ 10⁻¹⁶ cm²/molecule) by about 14 orders of magnitude (Nie & Emory, 1997).

The Stokes and anti-Stokes signals possess the same information in quality, but the intensity of anti-Stokes scattering (I_A) is generally much lower than that of Stokes scattering (I_S) as shown in figure 2.5. This is because their intensities depend on the populations of the initial states which are determined by Boltzmann distribution law, i.e., depending on temperature. The intensity ratio of anti-Stokes to Stokes signals is expressed as,

$$\frac{I_A}{I_S} = \frac{(\nu_0 + \Delta\nu)^4}{(\nu_0 - \Delta\nu)^4} \exp\left\{-\frac{E_b - E_a}{k_B T}\right\} = \frac{(\nu_0 + \Delta\nu)^4}{(\nu_0 - \Delta\nu)^4} \exp\left(-\frac{h\Delta\nu}{k_B T}\right) \quad (2.21)$$

where k_B is Boltzmann constant [J/K] and T is absolute temperature [K]. It must be noted that the correction term which is related to the forth power of the scattering frequency should be replaced by the cube of the frequency in the case of measuring scattering intensity as photon number. According to equation (2.21), the intensity ratio was calculated for different Raman shifts and various temperatures as listed in table 2.1. In this calculation, an excitation wavelength was set to be 532 nm (i.e., $\nu_0 = 5.64 \times 10^{14}$ Hz). Since the present study focuses on relatively large Raman shift (2500–4000 cm⁻¹) at low temperature range (300–350 K) where the anti-Stokes signal is almost imperceptible compared to Stokes signal, only the Stokes Raman scattering is measured throughout the experiments.

2.2.2 Classical Theory of Raman Scattering

In this section, the classical treatment of Raman scattering is discussed in order to yield an understanding of interaction between electromagnetic field and molecular systems. Since the following classical description is based on the non-quantized approach, it has some severe shortfalls; it does not provide any description for rotational Raman scattering, and moreover it does not offer any explanation for a resonance effect that is found in resonance Raman scattering and surface-enhanced Raman scattering (Dieing *et al.*, 2011). The present study, however, focuses on the spontaneous Raman scattering arising from condensed phase (such

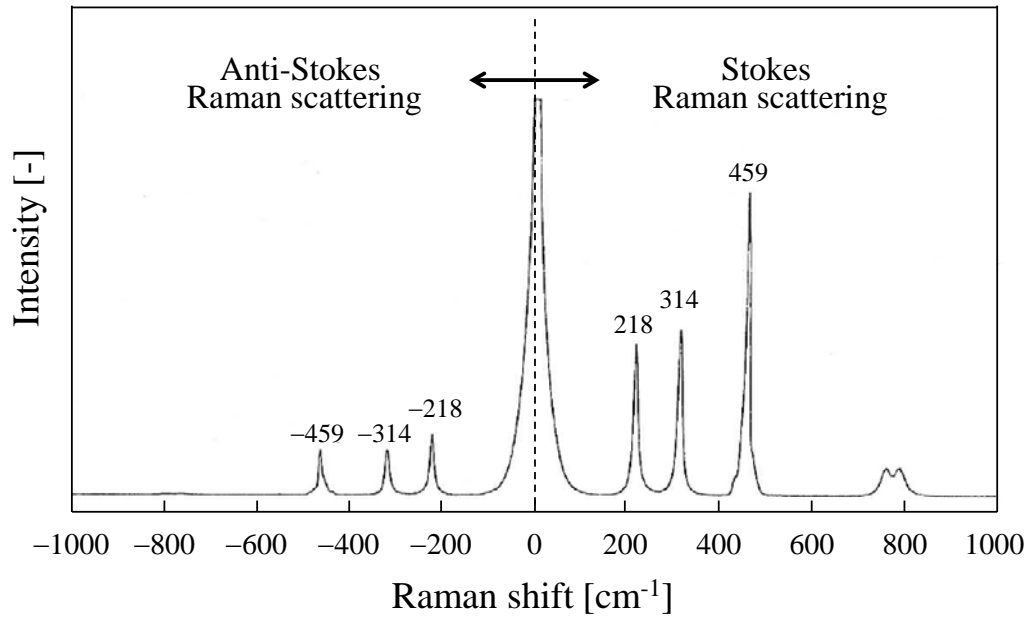


Figure 2.5. An example of Raman spectrum obtained from liquid carbon tetrachloride (CCl_4) reported by Hamaguchi & Hirakawa (1988).

Table 2.1. Intensity ratios of anti-Stokes to Stokes Raman scattering (I_A/I_S) at various Raman shift calculated for different temperatures

Raman shift [cm^{-1}]	Temperature [K]					
	100	300	500	700	900	1100
200	0.052	0.352	0.517	0.601	0.667	0.707
400	0.003	0.124	0.267	0.371	0.445	0.500
800	0.000	0.015	0.071	0.137	0.198	0.250
1600	0.000	0.000	0.005	0.019	0.039	0.062
3200	0.000	0.000	0.000	0.000	0.002	0.004

as liquid H₂O and D₂O), where the rotational Raman scattering cannot be observed due to the line broadening by molecular collisions. Hence, only the classical theory is provided below for an intuitive understanding of the Raman effect.

Generally, the primary incident electric field disturbs the electronic charge distribution in the molecule and thereby induces a dipole moment even in the case of an unpolar molecular system. The sum of the induced dipole moments acts as the source of a secondary electric field, i.e., the scattered light (Dieing *et al.*, 2011). When the incident electric field \mathbf{E} is sufficiently small and expressed as,

$$\mathbf{E} = \mathbf{E}_0 \cos(\omega_0 t) \quad (2.22)$$

where \mathbf{E}_0 is its amplitude [V/m] and ω_0 is its angular frequency ($\omega_0 = 2\pi\nu_0$) [rad/s], the induced dipole moment $\boldsymbol{\mu}$ [C·m] can be written by,

$$\boldsymbol{\mu} = \alpha \mathbf{E} = \alpha \mathbf{E}_0 \cos(\omega_0 t) \quad (2.23)$$

Here α is the molecular polarizability [C·m²/V], which represents the extent to which the driving field is able to disturb the electron density of the sample out of its equilibrium configuration, i.e., the configuration in the absence of an external field (Dieing *et al.*, 2011). In equation (2.23), $\boldsymbol{\mu}$ and \mathbf{E} are vector quantities and α is a second-rank tensor comprised of 3 × 3 components, which can be detailed as follows;

$$\begin{pmatrix} \mu_x \\ \mu_y \\ \mu_z \end{pmatrix} = \begin{pmatrix} \alpha_{xx} & \alpha_{xy} & \alpha_{xz} \\ \alpha_{yx} & \alpha_{yy} & \alpha_{yz} \\ \alpha_{zx} & \alpha_{zy} & \alpha_{zz} \end{pmatrix} \begin{pmatrix} E_x \\ E_y \\ E_z \end{pmatrix} \quad (2.24)$$

The component α_{xy} determines the magnitude of dipole moment along y-direction induced by the electric field in x-direction, and is equal to α_{yx} .

Assuming that the irradiated molecule is oscillating with a characteristic frequency ω_k , the molecular polarizability has a time-dependent component which changes periodically due to the nuclear oscillation, and therefore it is not a steady value. Since the polarizability changes depending on the nuclear position relative to its equilibrium position, it can be described as a function of the k -th normal coordinate Q_k by using a series expansion around the equilibrium nuclear geometry ($Q_k = 0$);

$$\alpha = \alpha_0 + \sum_k \left[\left(\frac{\partial \alpha}{\partial Q_k} \right)_0 \cdot Q_k + \frac{1}{2} \left(\frac{\partial^2 \alpha}{\partial Q_k^2} \right)_0 \cdot Q_k^2 + \frac{1}{3!} \left(\frac{\partial^3 \alpha}{\partial Q_k^3} \right)_0 \cdot Q_k^3 \dots \right] \quad (2.25)$$

where α_0 represents the equilibrium value of the polarizability. For a polyatomic molecule containing N atoms, there are $3N - 6$ vibrational modes ($3N - 5$ modes for a linear molecule); $k = 1, 2, \dots, 3N - 6$. The instantaneous position of the nuclei vibrating along the normal coordinate is given by,

$$Q_k = Q_{k0} \cos(\omega_k t) \quad (2.26)$$

where Q_{k0} is the maximum vibrational amplitude.

Substituting equations (2.25) and (2.26) into equation (2.23) yields,

$$\mu(t) = \left[\alpha_0 + \sum_k \left(\frac{\partial \alpha}{\partial Q_k} \right)_0 \cdot Q_{k0} \cos(\omega_k t) \right] \cdot E_0 \cos(\omega_0 t) \quad (2.27)$$

where the series expansion (equation (2.25)) is truncated after the term that is linearly related to the displacement. By utilizing a trigonometric identity, equation (2.27) can be rewritten by,

$$\begin{aligned} \mu(t) = & \alpha_0 E_0 \cos(\omega_0 t) \\ & + \frac{1}{2} \sum_k \left(\frac{\partial \alpha}{\partial Q_k} \right)_0 \cdot Q_{k0} \cdot E_0 \cos[(\omega_0 - \omega_k)t] \\ & + \frac{1}{2} \sum_k \left(\frac{\partial \alpha}{\partial Q_k} \right)_0 \cdot Q_{k0} \cdot E_0 \cos[(\omega_0 + \omega_k)t]. \end{aligned} \quad (2.28)$$

It is clearly seen that the induced dipole moment contains three components oscillating at different angular frequencies, ω_0 , $(\omega_0 - \omega_k)$, and $(\omega_0 + \omega_k)$, which lead to a radiation of the secondary electromagnetic waves (i.e., scattered light) at the same frequencies as themselves. That is to say, the first term of equation (2.28) acts as the source of the scattered light oscillating at the same frequency (ω_0) as the incident field, i.e., the Rayleigh scattering, while the second and third terms are responsible for the inelastic scattering events, the Stokes and anti-Stokes Raman scatterings, respectively. It can be intuitively understood that the Raman scattering provides molecular information through its frequency shifted by $\pm\omega_k$.

In addition, equation (2.28) offers a comprehensible explanation about so-called ‘selection rule’ for Raman scattering; this inelastic scattering requires a non-zero derivative of the polarizability at the equilibrium position along the normal coordinate, i.e.,

$$\left(\frac{\partial \alpha}{\partial Q_k} \right)_0 \neq 0 \quad (2.29)$$

The above relation is often compared with the selection rule for infrared absorption, which is described as $(\partial\mu / \partial Q_k)_0 \neq 0$. According to the above classical selection rule, the Raman and activities of different vibration modes were assessed and summarized for linear and non-linear triatomic molecules (CO_2 and H_2O) in figures 2.6 and 2.7, respectively. From figure 2.7, it is confirmed that three different vibration modes of water molecule (H_2O), which is used as sample liquid in the present study, are all Raman active.

Subsequently, the expression for the Raman intensity is discussed focusing on the induced dipole moment oscillating at $(\omega_0 - \omega_k)$, which act as the source of the Stokes Raman

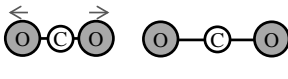
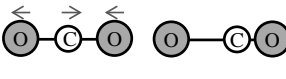
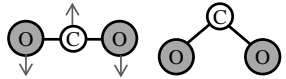
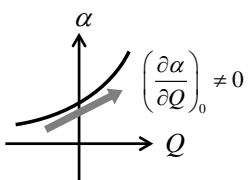
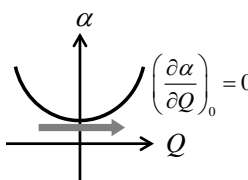
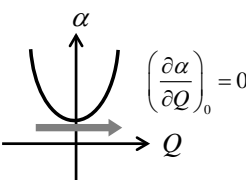
	Symmetric stretching	Antisymmetric stretching	Bending
Vibrational mode			
Polarizability derivative			
Raman activity	Raman active ν_1 (1340 cm^{-1})	Raman inactive	Raman inactive

Figure 2.6. Polarizability derivative and Raman activity for each vibrational mode of a linear triatomic molecule such as CO_2 .

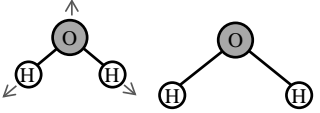
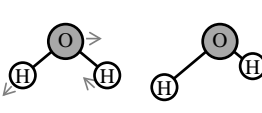
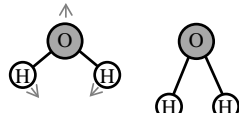
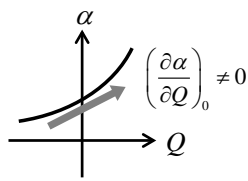
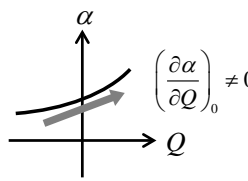
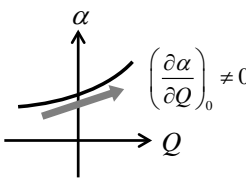
	Symmetric stretching	Antisymmetric stretching	Bending
Vibrational mode			
Polarizability derivative			
Raman activity	Raman active ν_1 (3650 cm^{-1})	Raman active ν_3 (3756 cm^{-1})	Raman active ν_2 (1595 cm^{-1})

Figure 2.7. Polarizability derivative and Raman activity for each vibrational mode of a non-linear triatomic molecule such as H_2O .

Fundamentals

scattering, shown in equation (2.28):

$$\mu_{\text{Stokes}}(t) = \frac{1}{2} \left(\frac{\partial \alpha}{\partial Q_k} \right)_0 \cdot Q_{k0} \cdot E_0 \cos[(\omega_0 - \omega_k)t] \quad (2.30)$$

Here, the summation notation for all normal modes is reduced for simplicity. The oscillating induced dipole moment serves as a Hertzian dipole, i.e., as an antenna emitting the secondary oscillation (Dieing *et al.*, 2011). The total power emitted by the dipole is given by,

$$P_{\text{Stokes}} = \frac{1}{6\pi \cdot \varepsilon_0 \cdot c^3} \left| \frac{\partial^2 \mu_{\text{Stokes}}}{\partial t^2} \right|^2 = \frac{Q_{k0}^2}{48\pi \cdot \varepsilon_0 \cdot c^3} \cdot \left(\frac{\partial \alpha}{\partial Q_k} \right)_0^2 \cdot (\omega_0 - \omega_k)^4 \cdot E_0^2 \quad (2.31)$$

where ε_0 is the electric permittivity in vacuum [C/V·m]. In the second identity, the oscillating part of

$$\left| \frac{\partial^2 \mu_{\text{Stokes}}}{\partial t^2} \right|^2 \propto \cos^2[(\omega_0 - \omega_k)t] \quad (2.32)$$

was temporally averaged as follows;

$$\lim_{T_1 \rightarrow \infty} \frac{1}{T_1} \int_0^{T_1} \cos^2[(\omega_0 - \omega_k)t] dt = \frac{1}{2} \quad (2.33)$$

Therefore the intensity of Stokes Raman scattering, which is proportional to the total power P_{Stokes} , is expressed as,

$$I_{\text{Stokes}} \propto \left(\frac{\partial \alpha}{\partial Q_k} \right)_0^2 \cdot (\omega_0 - \omega_k)^4 \cdot E_0^2 \quad (2.34)$$

From equation (2.34), the Raman intensity is influenced by the derivative of the polarizability and the molecular frequency, which are individual for each molecular system. It is also obvious that the Raman intensity increases with the intensity of the incident light as well as its frequency. Especially, a proportional relationship between the scattering intensity and the forth power of the scattering frequency is known as the ν^4 law, which has already appeared in equation (2.21). Thus, the laser power and its wavelength are important experimental parameters to observe Raman scattering.

2.2.3 Raman Imaging Techniques

The development of the laser in 1960s greatly motivated the birth of Raman micro-spectroscopy, i.e., the coupling of Raman spectroscopy to an optical microscope, which enables the determination of chemical composition in material at micrometer-scale. Following the early studies which reported optical arrangements to obtain Raman spectra from micro-sized samples (Freeman & Landon, 1969; Rosasco *et al.*, 1975), some studies

described the methods to obtain not only the spectra but also their lateral positions, i.e., Raman images. For example, Delhaye and Dhamelincourt (1975) introduced the systems termed ‘Raman microprobe’ and ‘Raman microscope’ and outlined several approaches for obtaining Raman images. These methods have been compared in terms of their advantages and limitations both theoretically (Puppels *et al.*, 1993) and experimentally (Markwort *et al.*, 1995; Schlücker *et al.*, 2003), and utilized in incredibly wide range of applications, from semiconductors to the pharmaceuticals, from biology to geology (Zoubir, 2012).

Figure 2.8 illustrates the concepts of some major methodologies for obtaining two-dimensional lateral Raman images. They can be classified into two main groups according to their approach for sample illumination and signal detection; image reconstruction and direct imaging. Point mapping (figure 2.8(a)) and line scanning (figure 2.8(b)) are typical examples of image reconstruction approach, in which numerous spectra are need to be recorded with a scanning system in order to reconstruct a Raman image at a specific wavenumber. In contrast, direct (or global) Raman imaging technique (figure 2.8(c)) does not record a Raman spectrum but provides a two-dimensional intensity distribution at a specific wavenumber by a single measurement of a globally-illuminated sample. The difference and characteristics of these methodologies are briefly summarized below.

In the point mapping approach (figure 2.8(a)), an excitation laser beam is focused to a small point and a Raman spectrum is obtained from each point within the measurement area. Since it is a point-by-point approach, it is required to move the sample using a micromotion stage or traverse the laser spot by mirrors along two spatial axes (x - and y -axes). The Raman signal from the individual point is collected through a spectrometer and sent to a detector. In this case, a two-dimensional detector is not necessarily required. Although the point mapping approach requires relatively long acquisition time to map an area point-by-point, it is the most flexible and popular method for recording three-dimensional information: two spatial dimensions and one spectral dimension. Its spectral quality is comparable to that of the conventionally recorded spectra. Moreover its axial resolution can be improved by using a confocal pinhole which removes out-of-focus signal (Dieing *et al.*, 2011).

In the line scanning approach, the sample is illuminated in a line as shown in figure 2.8(b). The Raman signal from all the points along the illuminated line can be simultaneously focused on the entrance slit of the spectrometer and imaged onto the two-dimensional detector (e.g., CCD camera). Therefore the resultant image projected onto the detector provides spectral information for one axis and spatial information along the line illumination for the other axis. A second spatial dimension is recorded by scanning the laser line (or the sample) along the spatial axis which is perpendicular to the illuminated line. This approach has an advantage in speed compared to a point mapping approach, because the line scanning can reduce the number of measurements required to map an area. However, a confocal pinhole cannot be used for line mapping approach, since the signal propagates from the

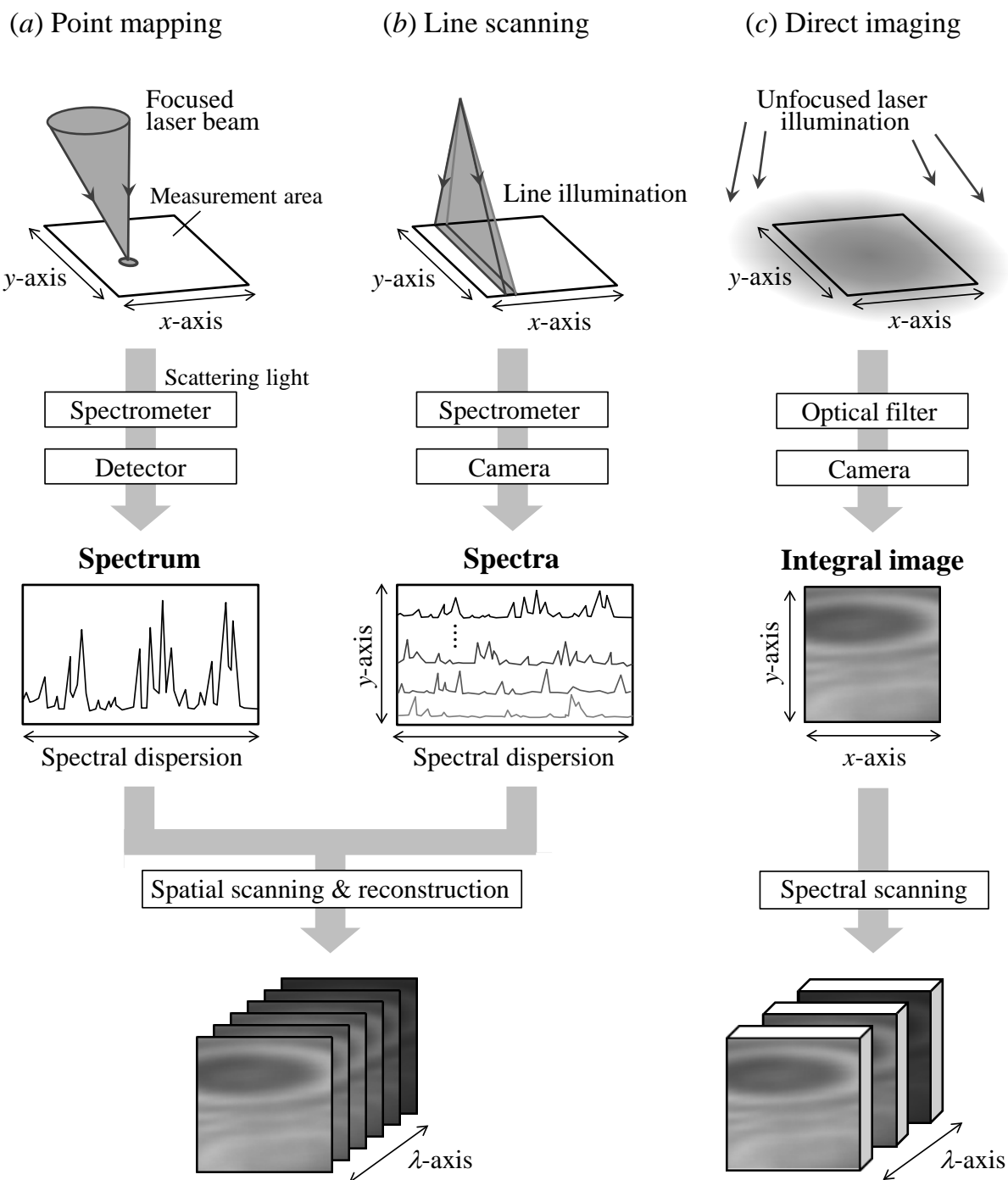


Figure 2.8. Schematic representations of the methods for obtaining two-dimensional Raman images: (a) point mapping, (b) line scanning and (c) direct imaging approaches. The top row shows the illumination pattern on the sample material and the first gray arrows indicate the set of instruments required for signal detection. The middle row illustrates the information acquired by one measurement. The bottom row shows the resulting data set after the spatial or spectral scanning.

sample to the detector in a line shape (Zoubir, 2012).

In the direct imaging technique (figure 2.8(c)), the whole measurement area is illuminated by an unfocused laser beam and the Raman signal is projected onto a two-dimensional detector through an optical filter which is used for wavelength selection. Therefore both x - and y -axes of the obtained image represent lateral positions, as those of images formed by a conventional microscope. This takes much shorter time than recording a full Raman spectrum for each location within the area. In addition, this approach can generally suppress the excitation power density (i.e., laser power per unit area) at a moderate level, while the point mapping and the line scanning approaches can achieve high-speed imaging only by increasing power density. For obtaining multispectral information, Raman images are required to be recorded at several characteristic wavelengths which should be determined from a pre-obtained full range spectrum. Therefore, the total measurement time depends on the number of wavelength positions at which a Raman image is recorded. The spectral resolution is defined by the transmittance wavelength range of the filters. As a result, unlike a point mapping and a line scanning approaches, fine spectral features cannot be observed in the direct imaging method. Additionally, this approach is prone to a non-uniform illumination, especially between the circumference and the center of the illuminated area (Zoubir, 2012).

In order to compare the above three methodologies, the measurement results reported by Schlücker *et al.* (2003) is quoted and listed in table 2.2, where the spatial resolution, signal-to-noise ratio and total acquisition time to map 61×61 points are quantitatively summarized. The excitation power densities were adjusted to be the equivalent value for all the methodologies, which allows direct comparisons between them. The relatively large value of 0.008 MW/cm^2 was the damage threshold which represents the maximum power density that can be applied to the sample (silicon substrate).

Table 2.2. Comparison of the parameters for point mapping, line scanning and direct imaging experiments by Schlücker *et al.* (2003)

Properties	Point mapping	Line scanning	Direct imaging
Power density	0.008 MW/cm^2	0.008 MW/cm^2	0.008 MW/cm^2
Spectral resolution	4 cm^{-1}	4 cm^{-1}	–
Spectral band-pass	–	–	7 cm^{-1} (fwhm)
Spatial resolution	$1.1 \mu\text{m}$	$1.1 \mu\text{m}$	$0.313 \mu\text{m}$
Signal-to-noise ratio	29	77	14
Total acquisition time	11 h 24 min	12 min 34 s	46 min 22 s
Exposure time only	$(61 \times 61) \text{ points} \times 10 \text{ s}$ = 10 h 20 min	$61 \text{ lines} \times 10 \text{ s}$ = 10 min 10 s	$194 \text{ s} \times 10 \text{ frames}$ = 32 min 20 s

In the present study, the direct imaging approach is employed to measure planar distributions of temperature or concentration in channel flow, taking advantage of its relatively short acquisition time with high spatial resolution and moderate power density.

2.3 Microscopic Measurement

2.3.1 Conventional Microscopy

The present study describes the development of micro- and nano-scale optical measurement techniques based on Raman microscopy. Conventional and commercially available fluorescent microscopes are utilized or partially altered to construct measurement systems. Figure 2.9 shows a fundamental setup of an inverted fluorescence microscope, which is mainly composed of a light source, a filter block and an objective lens. A continuous mercury lamp is generally equipped as a light source for fluorescence excitation. The filter block is composed of an excitation filter, a dichroic mirror and a barrier filter, whose wavelength characteristics are determined in consideration of the excitation and emission wavelengths of fluorescence. The light from the mercury lamp is spectrally filtered by the excitation filter to provide excitation wavelength, reflected by the dichroic mirror and introduced through the objective lens to a sample positioned on a microscope stage. The resultant signal is collected by the same objective lens and captured by a detector after passing through the dichroic mirror and the barrier filter which remove the excitation wavelength. In the present study, an excitation light source of Raman process is externally provided by a continuous laser instead of using the previously-installed mercury lamp, and thus the excitation filter is not used. Furthermore, the combination of the dichroic mirror and the barrier filter is determined with consideration for the wavelengths of excitation light, undesired fluorescence and desired Raman signal.

Figure 2.10 illustrates an optical imaging system of the inverted microscope. If the imaging system employs a completely aberration-free objective lens with a uniform circular aperture, its resolving power is determined by diffraction effect which arises from the wave nature of light. In this case, the spatial resolution or the minimum resolvable separation of two adjacent equal points, d [m], can be estimated based on the Rayleigh criterion;

$$d = 1.22 \frac{\lambda}{2NA} \quad (2.35)$$

where λ [m] is the signal wavelength in vacuum and NA [-] is the numerical aperture of the objective lens. Note that the distance d is equal to the radius of a ring-shaped diffraction pattern, so-called an Airy disk (Inoué 1986). The numerical aperture NA can be expressed as,

$$NA = n_m \sin \alpha \quad (2.36)$$

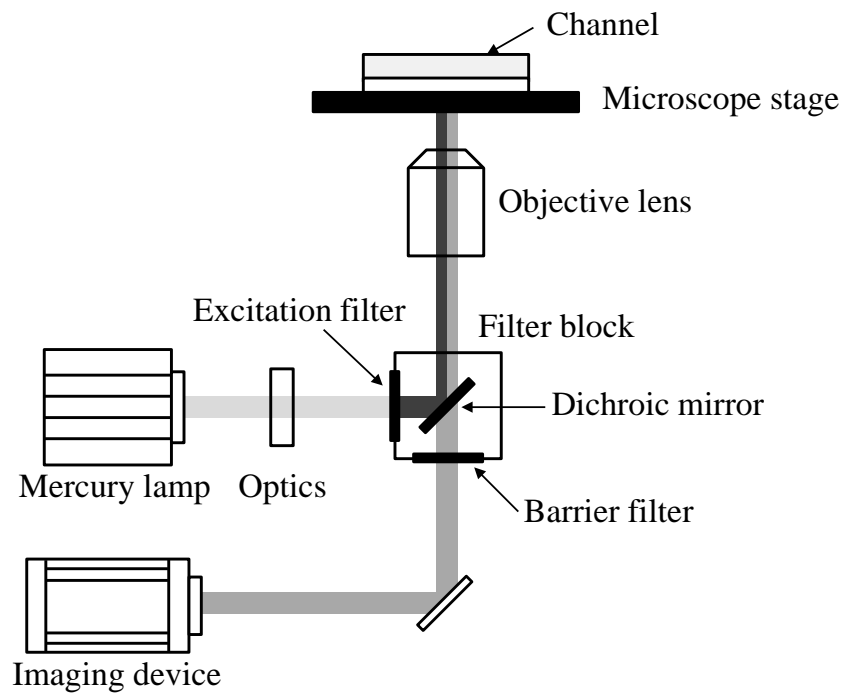


Figure 2.9. Schematic diagram of an inverted fluorescence microscope.

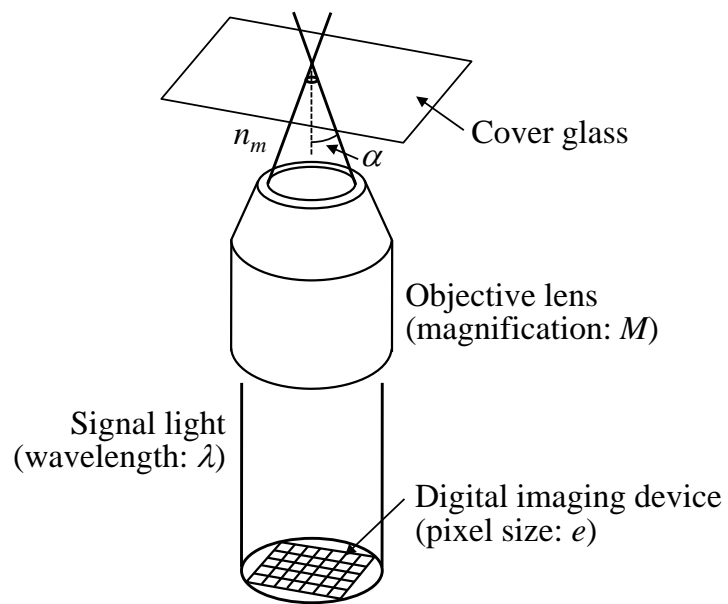


Figure 2.10. Schematic of the optical imaging system of an inverted microscope.

where n_m is the refractive index of the medium between the objective lens and sample, and α is the half-angle of the maximum cone of light that can enter the lens. The lateral spatial resolution can be improved by the usage of a water- or oil-immersion objective lens ($n_m = 1.33$ or 1.52 , respectively), since it is inversely related to NA as shown in equation (2.35).

On the other hand, the depthwise resolution is characterized depending on the illumination system and the characteristics of the recording optics. In the present study, a volume illumination and evanescent wave illumination are employed for temperature and near-wall concentration measurements, respectively. In the case for volume illumination, whereby the test section is illuminated by a volume of light (Meinhart *et al.*, 2000), the depthwise resolution is characterized by the depth of field. This is the depth over which the fine-focusing knob of the microscope can be controlled without diminishing the sharpness of the image of an infinitely thin specimen (Inoué 1986). The depth of field of a standard microscope, which can be expressed as the summation of the depth of field due to the diffraction and the geometrical effects, is given by Inoué & Spring (1997),

$$d = \frac{\lambda n_m}{NA^2} + \frac{n_m e}{NA \cdot M} \quad (2.37)$$

where M is total magnification of the system [-] and e is the smallest distance [m] that can be resolved by an imaging device located in the image plane of the microscope objective lens. For the case of a digital imaging device, e is the spacing between pixels, i.e., the pixel size. The depth of field resulting from the diffraction effect (the first term on the right-hand side in equation (2.37)) decreases inversely with the square of NA , while the lateral resolution decreases in inverse proportion to NA (equation (2.35)).

2.3.2 Evanescent Wave

An evanescent field is a thin layer of illumination which exponentially decays in intensity with increasing distance normal to the surface (Axelrod, 2001). The evanescent field is generated by total internal reflection of an excitation beam and utilized for optical sectioning at interfacial region. The basic optical theory of the evanescent field is summarized below.

When light passes from one medium with higher refractive index (e.g., glass) to another with lower refractive index (e.g., water), some is reflected back into the first medium and the other is transmitted into the second medium (figure 2.11). If the incident angle θ_i is smaller than the critical angle θ_c , most of the light propagates into the lower index medium at a refraction angle θ_t which is given by Snell's law,

$$n_1 \sin \theta_i = n_2 \sin \theta_t \quad (2.38)$$

where n_1 and n_2 are the refractive indices of the first and the second medium, respectively. For supercritical condition ($\theta_i > \theta_c$), all of the light is reflected, i.e., it undergoes total

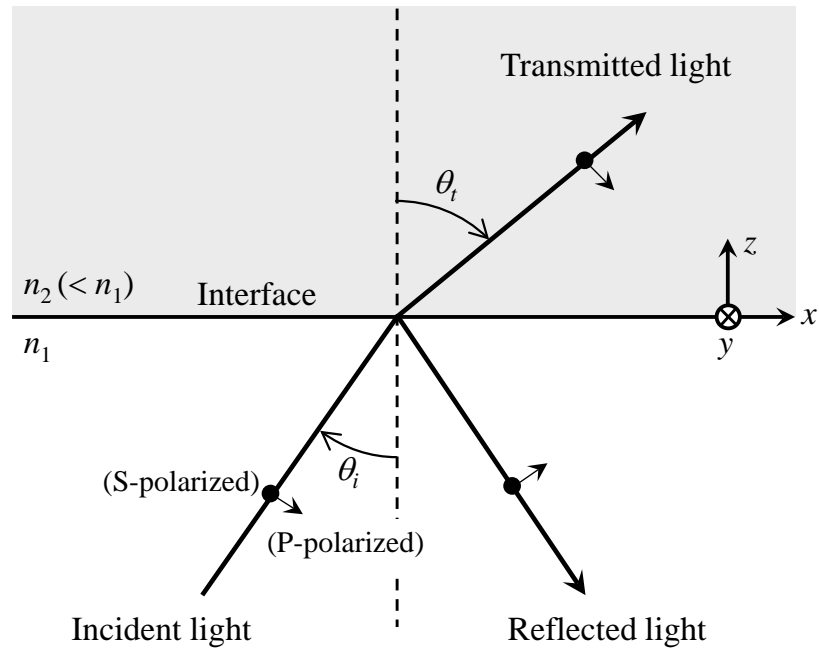


Figure 2.11. Schematic of transmission and reflection of an incident light at an interface between two media with different refractive indices ($n_1 > n_2$).

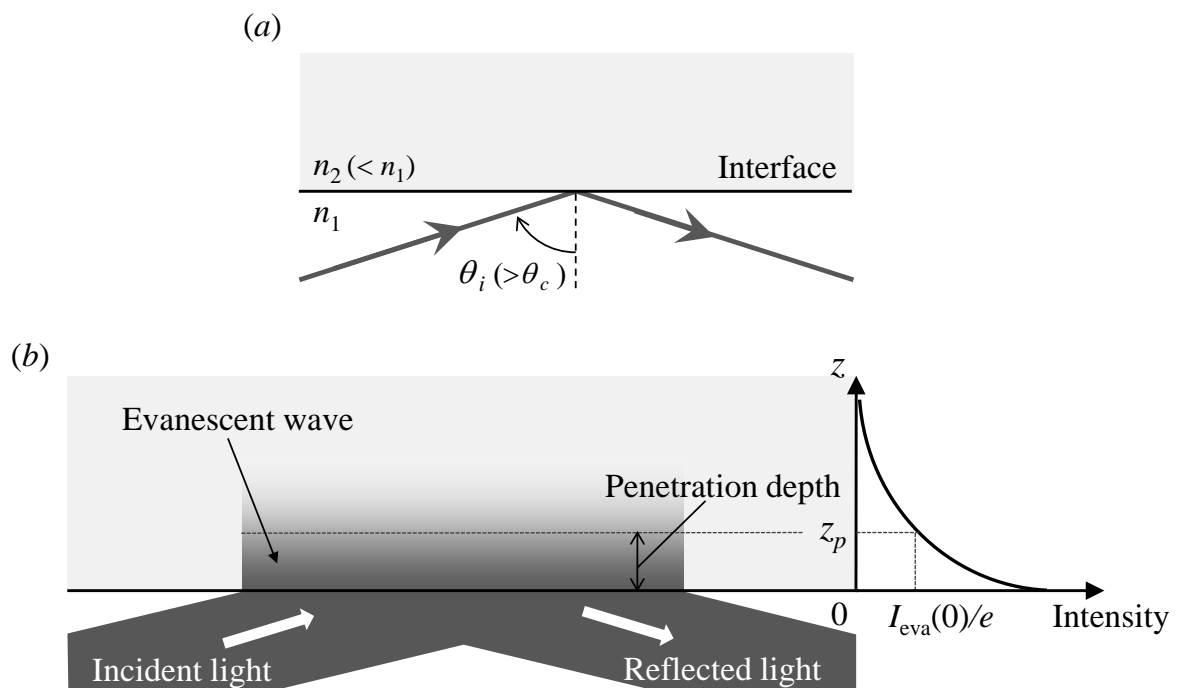


Figure 2.12. (a) Schematic of total internal reflection of light. (b) Enlarged view of the interface where an evanescent wave illumination is generated. The evanescent intensity profile in the z -direction is illustrated in the right-hand side.

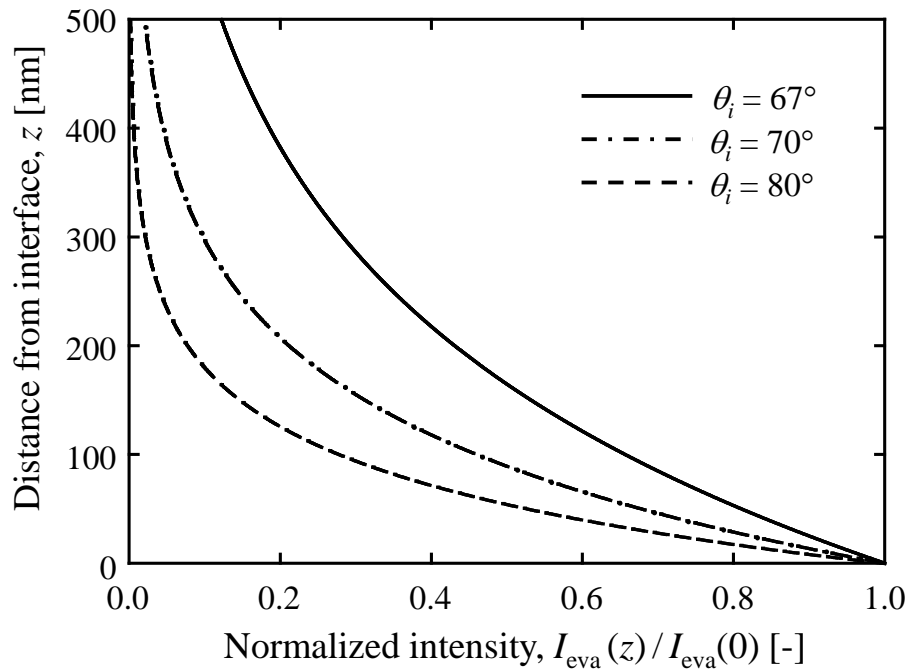


Figure 2.13. The intensity profile of the evanescent wave at different incident angles, when an incident light of $\lambda = 532$ nm is totally reflected at an interface between silica glass ($n_1 = 1.461$) and water ($n_2 = 1.333$).

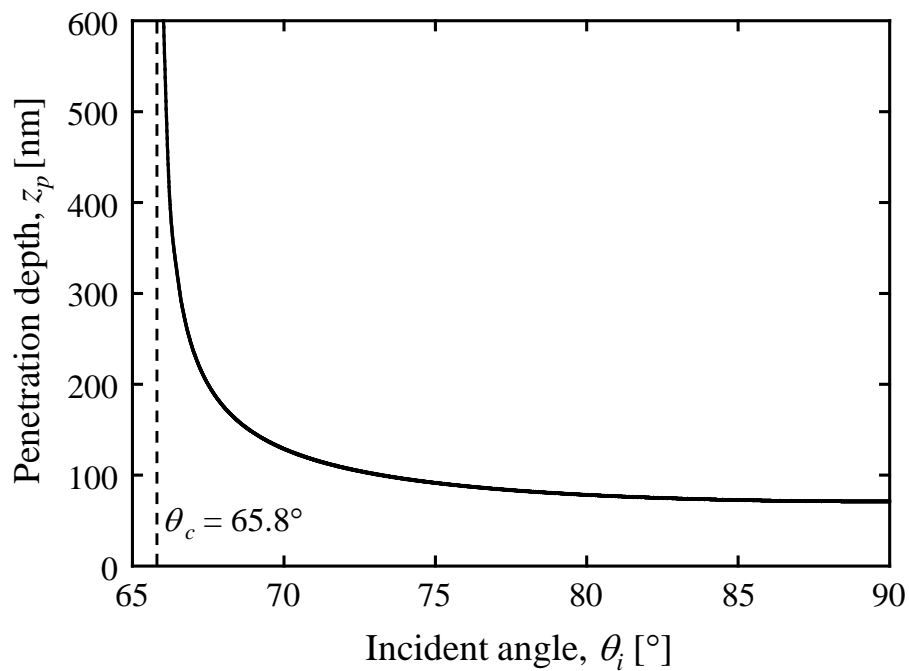


Figure 2.14. Relationship between the incident angle and the penetration depth of the evanescent wave, when an incident light of $\lambda = 532$ nm is totally reflected at an interface between silica glass ($n_1 = 1.461$) and water ($n_2 = 1.333$).

internal reflection (TIR) as illustrated in figure 2.12(a)). The critical angle θ_c for TIR is defined as the angle of incidence where the refraction angle reaches 90° , and thus derived by:

$$\theta_c = \sin^{-1} \frac{n_1}{n_2} \quad (2.39)$$

Even in this case, however, the electromagnetic field penetrates through the interface and propagates parallel to the surface (figure 2.12(b)). This electromagnetic field is termed evanescent wave and its intensity, I_{eva} [photons/s·m²], decays exponentially with the perpendicular distance z [m] from the interface, as expressed by

$$I_{\text{eva}}(z) = I_{\text{eva}}(0) \exp\left(-\frac{z}{z_p}\right) \quad (2.40)$$

where

$$z_p = \frac{\lambda}{4\pi\sqrt{n_1^2 \sin^2 \theta_i - n_2^2}} \quad (2.41)$$

The characteristic length z_p [m] is called the penetration depth. Figure 2.13 shows the intensity profile of the evanescent wave at different incident angles, when an incident light of $\lambda = 532$ nm is totally reflected at an interface between silica glass ($n_1 = 1.461$) and water ($n_2 = 1.333$). The evanescent wave intensity decays faster at larger incident angle. Figure 2.14 illustrates the relationship between the incident angle and the penetration depth at the silica-water interface where the critical angle is calculated to be 65.8° .

Since z_p is generally of the order of λ or smaller, except for supercritical $\theta_i \rightarrow \theta_c$ (where $z_p \rightarrow \infty$), the evanescent wave can selectively excite the molecules in the vicinity of the interface without exciting the region farther from the interface (Axelrod, 1981). The thickness of the evanescent wave layer is considered to be within a few hundred nanometers, or $3z_p$ – $4z_p$ from equation (2.40), since $e^{-3} = 5.0\%$ and $e^{-4} = 1.8\%$ (Yoda & Kim, 2013). According to the previous report by Zettner & Yoda (2003), where they experimentally investigated the thickness of the evanescent illumination, it was estimated to be approximately $2.3z_p$. They used a stainless steel pin mounted on a lever and a micrometer-driven translation stage, and estimated the thickness from the vertical distance where the pin completely left from the illuminated region when raising it above the glass surface.

The polarization of the evanescent wave depends on that of incident light, which can be either S polarized (polarized normal to the plane of incidence, i.e., y-direction in figure 2.11) or P polarized (polarized parallel to the plane of incidence, i.e., xz-plane). Above the critical angle, the transmission coefficient t (also known as Fresnel factor), which represents the electric field amplitude of the transmitted light relative to that of the incident light, is given for each polarization as (Woods & Bain, 2012, 2014),

$$\left. \begin{aligned}
 t_{Px} &= \frac{2 \cos \theta_i (\sin^2 \theta_i - n'^2) + 2n'^2 i \cos^2 \theta_i \sqrt{\sin^2 \theta_i - n'^2}}{n'^4 \cos^2 \theta_i + \sin^2 \theta_i - n'^2} \\
 t_{Pz} &= \frac{2n'^2 \cos^2 \theta_i \sin \theta_i - 2i \cos \theta_i \sin \theta_i \sqrt{\sin^2 \theta_i - n'^2}}{n'^4 \cos^2 \theta_i + \sin^2 \theta_i - n'^2} \\
 t_{Sy} &= \frac{2 \cos^2 \theta_i - 2i \cos \theta_i \sqrt{\sin^2 \theta_i - n'^2}}{1 - n'^2}
 \end{aligned} \right\} \text{for } \theta_i \geq \theta_c \quad (2.42)$$

where $n' = n_2 / n_1$. It must be noted that the above set of equations can be applied only in the supercritical condition and the transmission coefficients are defined for the subcritical conditions as follows:

$$\left. \begin{aligned}
 t_{Px} &= \frac{2 \sin \theta_i \cos \theta_i \cos \theta_t}{\sin(\theta_i + \theta_t) \cos(\theta_i - \theta_t)} \\
 t_{Pz} &= \frac{2 \sin \theta_i \cos \theta_i \sin \theta_t}{\sin(\theta_i + \theta_t) \cos(\theta_i - \theta_t)} \\
 t_{Sy} &= \frac{2 \sin \theta_i \cos \theta_i}{\sin(\theta_i + \theta_t)}
 \end{aligned} \right\} \text{for } \theta_i \leq \theta_c \quad (2.43)$$

According to equations (2.42) and (2.43), the absolute values of the Fresnel factors calculated for the silica-water interface are plotted versus incident angle (figure 2.15).

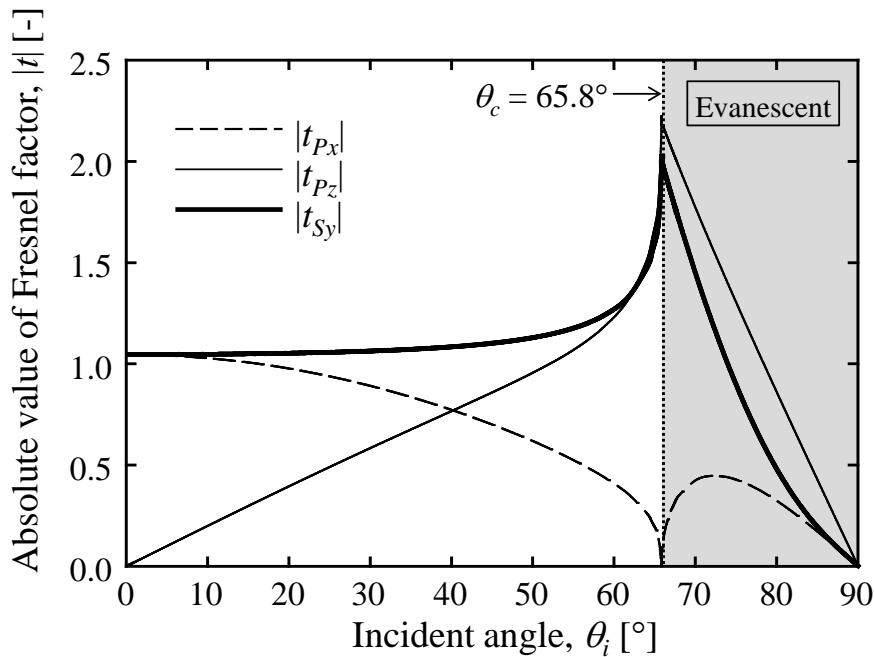


Figure 2.15. Relationship between the incident angle and the absolute values of the Fresnel factors (t_{Px} , t_{Pz} and t_{Sy}) at the silica-water interface ($n_1 = 1.461$, $n_2 = 1.333$).

Regardless of polarization, the absolute values decay to zero as the incident angle approaches to 90° . At the critical angle, $|t_{Sy}|$ and $|t_{Pz}|$ are maximized and are almost twice as the values for normal incidence, which means that the evanescent intensity at the interface is greater than the incident light intensity. On the other hand, $|t_{Px}|$ vanishes at the critical angle. Consequently the P-polarized beam produces an evanescent field oscillating purely in the z -direction when it is incident at the critical angle. In the present study, the incident angle is set to be about 10° away from the critical angle, because the evanescent wave intensity and the penetration depth are considered to be significantly influenced by the slight change in the incident angle around the critical angle.

2.3.3 Total Internal Reflection Microscopy

In total internal reflection microscopy (TIRM), or evanescent-wave microscopy, the sample is illuminated by an evanescent wave and imaged by a microscope (Kazoe & Yoda, 2013). The first application of total internal reflection to microscopy was reported in 1961 (Ambrose, 1961), and became widely used in combination with fluorophores in 1990s. Since TIRM enables the surface-selective observation, it is often used to study cell adhesion, colloid-wall interaction, and flow structure in miniaturized fluidic systems, as reviewed previously (Axelrod *et al.*, 1984; Axelrod, 2001; Prieve, 1999; Kazoe & Yoda, 2013). In this section, optical configurations of TIRM and their features are briefly summarized.

Figure 2.16 shows two typical configurations of TIRM; objective lens-based and prism-based systems. The most popular configuration is the objective lens-based TIRM shown in figure 2.16(a), which uses a microscope objective lens with high numerical aperture (NA) for both illumination and observation (Török & Kao, 2007). An excitation laser beam is focused off-axis in the back focal plane of the objective lens, emitted from the lens in a collimated form and introduced into a cover glass through immersion oil. The evanescent wave is generated by total internal reflection of the beam at the interface between the glass-solution interface. The maximum angle at which the beam can emerge into the oil is determined by NA of the objective lens defined by equation (2.36). Since $n\sin\theta$ is conserved by the Snell's law as shown in equation (2.38), for TIR to occur at the interface between silica glass ($n_1 = 1.461$) and water ($n_2 = 1.333$), the NA must be larger than $n_1\sin\theta_c = n_2\sin 90^\circ = 1.333$. The advantages of this configuration are (1) ease of alignment (because the illumination and the imaging optical paths coincide), (2) high accessibility to the sample (which makes sample manipulation easier), and (3) good signal-to-noise ratio (due to the large NA and magnification of the objective lens). The main disadvantage of the system is that the optical properties of the objective lens limit the selectivity of coverslip used for TIR substrate. In a typical objective-based TIRM system equipped with an objective lens with NA of 1.45, the choice of the substrate is limited to a 170- μm -thick coverslip made of

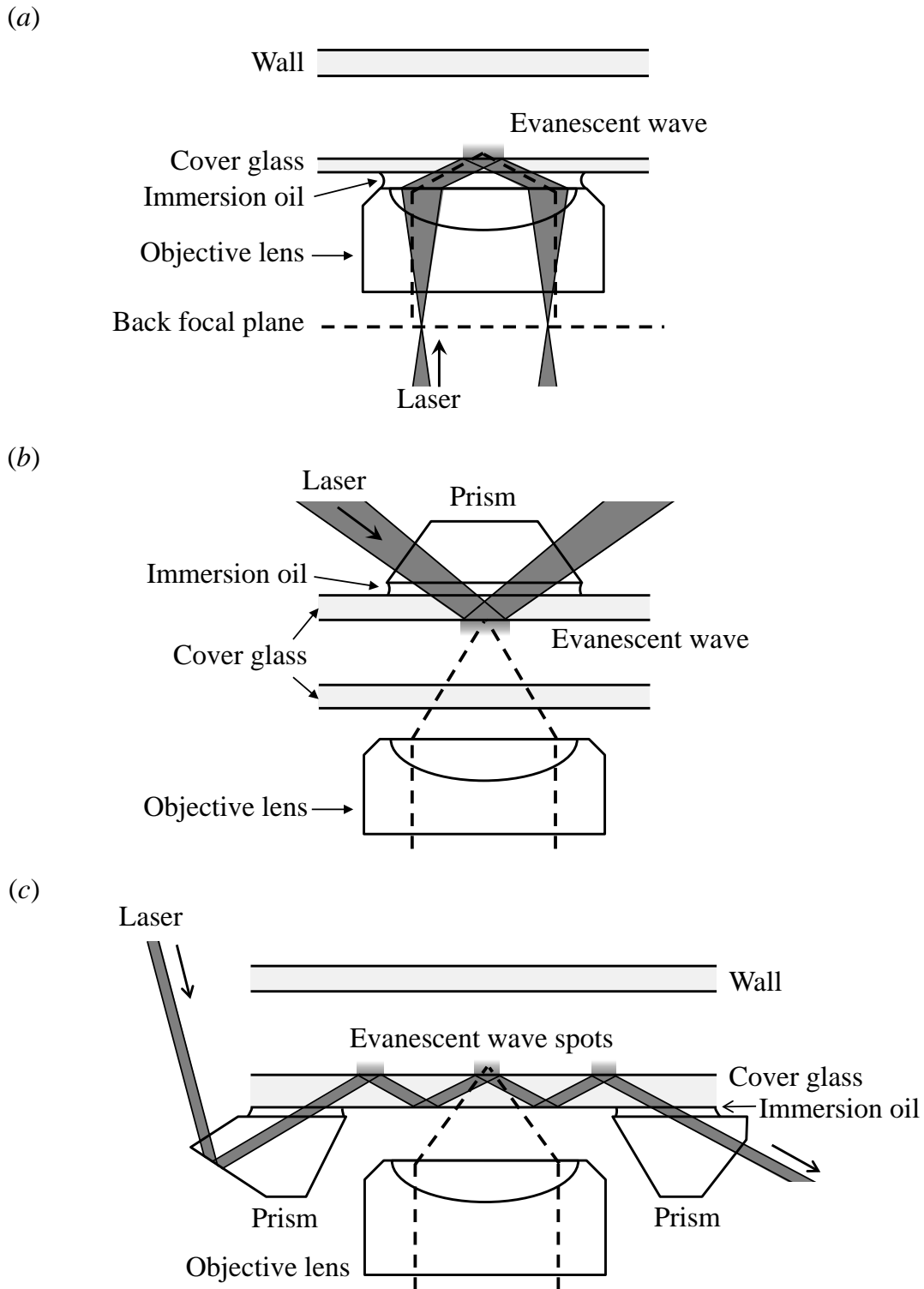


Figure 2.16. Schematics of configurations for total internal reflection microscopy (TIRM). Typical configurations of (a) an objective-based and (b) a prism-based systems. (c) A two-prism-based TIRM system, in which entry and exit prisms are located in the same side as the objective lens.

borosilicate glass ($n = 1.52$), whose fragility and autofluorescence are sometimes problematic in experiments. Another disadvantage is that the observed signal can suffer from the luminescence of the internal elements of the objective lens (Török & Kao, 2007).

On the other hand, the prism-based TIRM shown in figure 2.16(b) uses a prism to direct the light towards the TIR interface with a separate objective lens for observation (Török & Kao, 2007). In the conventional configuration (in figure 2.16(b)) the prism is positioned above the sample with a layer of immersion oil. This configuration has advantages that (1) it has wide selectivity of the thickness and material of substrate (such as borosilicate glass and silica glass), (2) larger field of view can be achieved by using an objective lens with low magnification, and (3) ‘cleaner’ signal can be obtained compared to objective-based system (Török & Kao, 2007). However, the usage of a prism can impose geometrical constraints on sample manipulation and restrict the choice of objective lens to low- or medium-power lens in some cases, because the prism is positioned in the opposite side of the objective lens. Moreover this configuration makes the optical alignment more difficult.

For TIR Raman imaging, the present study employs a two-prism-based TIRM system (figure 2.16(c)) which was proposed by Kazoe & Sato (2007). This configuration is another type of prism-based arrangements but two prisms are positioned in the same side of an objective lens; a laser beam is introduced into a cover glass through a prism and thrown out from the other prism after undergoing multiple total internal reflections. Therefore this configuration has an advantage in accessibility to the sample compared to the conventional prism-based system (figure 2.16(b)), which enables the free space above the sample to be used for flow controlling devices or other optical methods, while the signal-to-noise ratio can be worse because of scattering from the adjacent reflections which occurs close to the objective lens (Conibear & Bagshaw, 2000).

2.4 Sample Material and Channel Fabrication

This section first deals with the properties and Raman spectra of liquid H₂O and D₂O, which are used as sample materials in the present study, and subsequently outlines the materials and fabrication processes of micro- and milli-channels. The characteristic properties of glass and polymeric materials, which are utilized to construct miniaturized flow channels in this study, are summarized especially focusing on the availability for microfluidic systems and for Raman-based optical measurements. The Raman spectra of these materials will also be provided in the discussion. Afterwards the microfabrication processes based on two well-established techniques, photolithography and soft lithography (Ziaie *et al.*, 2004), are explained. A simpler method for milli-channel fabrication is shortly described at the end.

2.4.1 Sample Material

In the present study, water (H₂O) and heavy water (D₂O) are selected as working fluids for the development of measurement techniques based on Raman imaging in anticipation of application for various water-based medium including biological solutions and tissues. H₂O (prepared by ultrapure water system of Merk Millipore) is used throughout all the sets of experiments, and D₂O (99.9%, Wako Pure Chemical Industries, Ltd.) is used in the experiments for concentration measurement in chapter 6. The properties of these liquids are summarized in table 2.3. In addition, examples of their Raman spectra and the list of characteristic Raman shifts are shown in figure 2.17 and table 2.4., respectively (Walrafen, 1962, 1964). While the spectral shapes of these liquids are very similar, the Raman shifts of D₂O are lower than the corresponding shifts of H₂O due to the weight difference of isotope deuterium and hydrogen.

For the present set of experiments, H₂O and D₂O are used without a degassing operation (i.e., in saturated condition). The dissolved air is considered to have little influence on the Raman signals of these samples, since the air solubility is sufficiently low (24.6 mg/mL or 1.5×10^{-5} mole per mole of water at 293 K). In addition, some gas species have substantially lower Raman shifts (O₂: 1555 cm⁻¹, CO₂: 1285 cm⁻¹ and 1388 cm⁻¹) compared to the target Raman shift of the present study (2000–4000 cm⁻¹).

2.4.2 Channel Material

There is a variety of materials which have been used for construction of micro-fabricated devices, including silicon, glass, polymer, metal, ceramic, paper, and fabric thread. An appropriate material (or combination of materials) must be chosen for an intended application

Table 2.3. Properties of H₂O and D₂O at 298 K

Properties	Unit	H ₂ O	D ₂ O
Molar mass	[g/mol]	18.0	20.0
Density	[g/cm ³]	0.997	1.104
Viscosity	[Pa·s]	0.891×10^{-3}	1.095×10^{-3}
Kinematic viscosity	[m ² /s]	0.893×10^{-6}	0.992×10^{-6}
Surface tension	[N/m]	0.0720	0.0719
Refractive index (at 589 nm)	[-]	1.333	1.328

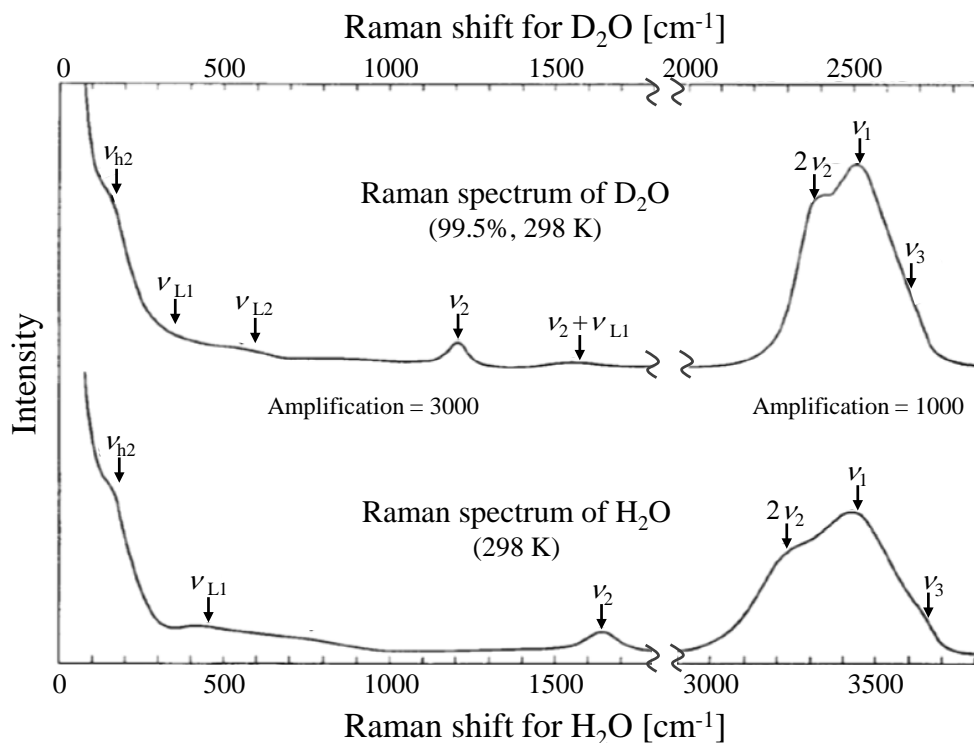


Figure 2.17. Typical Raman spectra of H₂O and D₂O in liquid states (Walrafen, 1964). The nomenclatures correspond to those listed in table 2.4.

Table 2.4. Comparison of Raman shifts of H₂O and D₂O in liquid states (Walrafen, 1962)

Raman shift [cm ⁻¹]		Nomenclature	Assignment
H ₂ O	D ₂ O		
175	175	ν_{h1}	Hydrogen bond O-O stretching
450	350	ν_{L1}	Libration, arising from hydrogen bonding
780	500	ν_{L2}	Libration, arising from hydrogen bonding
1645	1235	ν_2	Bending
2115	1600	$\nu_{L1} + \nu_2$	Combination
3225	2363	$2\nu_2$	Fermi resonance
3450	2515	ν_1	Symmetric stretching lowered from frequency of gas (3650 cm ⁻¹) by hydrogen bonding
3630	2662	ν_3	Antisymmetric stretching lowered from frequency of gas (3756 cm ⁻¹) by hydrogen bonding
3990	—	$2\nu_2 + \nu_{L2}$	Combination

considering some characteristics: cost, robustness, surface chemistry, optical and electrical properties, biocompatibility, ease of fabrication and integration, and feasibility of large-scale production (Kovarik *et al.*, 2012). The most widely-used materials for microfluidic devices are silicon and glass primarily because there are well-established fabrication techniques that have historically been developed in the semiconductor industry (Tian & Finehout, 2008). Also various kinds of polymers (such as para-xylylene, polydimethylsiloxane (PDMS), polymethyl methacrylate and so on) are available and its use is rapidly growing. Paper and thread are relatively new materials and have been exploited as the substrates for disposable microfluidic platforms (Carrilho *et al.*, 2009; Li *et al.*, 2010). Among these materials, this study uses two kinds of glasses (silica and borosilicate glasses) and a polymer (PDMS) for channel fabrication, whose characteristics are detailed below. Typical values of chemical and physical properties are summarized in table 2.5 (quoted from Tian & Finehout, 2008; Newport Corp. (<http://www.newport-japan.jp/pdf/technical/1423.pdf>, December 8, 2014); McDonald & Whitesides, 2002).

Table 2.5. Typical values of chemical and physical properties of silica glass, borosilicate glass and PDMS. These data are quoted from Tian & Finehout (2008), Newport Corp. (<http://www.newport-japan.jp/pdf/technical/1423.pdf>, December 8, 2014), and McDonald & Whitesides (2002)

Properties	Silica glass	Borosilicate glass	PDMS
Optical			
Refractive index [-]	1.47	1.52	1.41
Transparency	200–2400 nm	380–2100 nm	240–1100 nm
Electrical			
Dielectric strength [MV/m]	8	–	20
Mechanical			
Young's module [MPa]	86.7×10^3	81.5×10^3	0.75
Density [g/cm ³]	2.2	2.5	–
Thermal			
Thermal conductivity [W/m·K]	1.4	1.1	0.2
Thermal expansion [$10^{-6}/K$]	0.54	7.1	310

Glass is an amorphous solid made of inorganic materials such as silica sand, sodium, calcium carbonates, borates and so on (Doremus, 1994). Among a virtually infinite variety of glasses, soda lime, silica (or quartz) and borosilicate glasses are commonly used in microfluidics (Tian & Finehout, 2008). The major advantages of these glasses arise from their favorable material properties: chemically inert, electrically insulating, optically transparent, and low auto-fluorescence (Tian & Finehout, 2008). For example, their chemical inertness allows the usage of most chemical agents and their excellent insulation properties enables electrokinetic manipulations inside a microchannel. Moreover their transparency and low fluorescence emission are desirable for optical measurements. However, fabrication techniques for glass materials (e.g., lithography and chemical etching) are expensive and time-consuming (McDonald & Whitesides, 2002), and it is difficult to machine into complex 3-D structures due to their amorphous nature (Tian & Finehout, 2008).

In contrast, an elastomeric polymer like PDMS can be molded into complex 3-D shapes with simple fabrication process called soft lithography (Xia & Whitesides, 1998; McDonald & Whitesides, 2002; Ng *et al.*, 2002). PDMS belongs to a class of polymers called silicones containing a Si-O backbone, and is comprised of repeating units of $(\text{CH}_3)_2\text{SiO}$ groups. Since PDMS was first introduced for micropatterning (Kumar and Whitesides, 1993), it has been the most popular polymer material for microfluidic applications because of its attractive characteristics: inexpensive, reversibly deformable, electrically insulating, compatible to biological materials, suitable for surface modification, and optically transparent down to 240 nm (McDonald & Whitesides, 2002). However, the usage of PDMS can be problematic in some applications. Its low thermal conductivity results in the diminished heat dissipation. This can lead to a significant temperature rise in microchannel when an electric field is applied or a strong light absorption is expected to occur. In addition, PDMS has a critical problem of swelling in common organic solvents like toluene, which makes it difficult to perform many organic reactions and solvent-based syntheses (Lee, Park *et al.*, 2003; Kim *et al.*, 2009).

Next, the Raman scattering from these channel materials is investigated. Tables 2.6, 2.7 and 2.9 compile the representative Raman peaks and their assignments for silica glass, borosilicate glass and PDMS, respectively. From table 2.6 (reported by Shibata *et al.* (1981)), silica glass has strong peaks at 440 cm^{-1} , 485 cm^{-1} and 800 cm^{-1} , but shows only weak signals above 900 cm^{-1} . Compared to silica glass which is made of simple oxide (SiO_2), borosilicate glass which is mainly composed of SiO_2 , B_2O_3 and Na_2O shows different peak positions depending on its composition. As listed in table 2.8 (from work by Konijnendijk & Stevels (1976)), it is obvious that the peak positions are influenced by the SiO_2 content and the alkali/boron ratio. Generally, borosilicate glasses produced for optical use have high SiO_2 content. For example, BK7, which is the most popular type of borosilicate glass for optical use, is typically composed of SiO_2 (69%), B_2O_3 (10%), Na_2O (9%), K_2O (8%), BaO (3%)

and As₂O₃ (1%) (Izumiya, 1984). According to tables 2.7 and 2.8, this type of borosilicate glass is considered to have peaks at 435 cm⁻¹, 495 cm⁻¹, 540 cm⁻¹, 630 cm⁻¹ and 1090 cm⁻¹. In the case of PDMS, strong Raman peaks appear in the relatively high wavelength region (around 2900–3000 cm⁻¹) as well as in the low wavelength range (below 800 cm⁻¹), as seen in table 2.9 (reported by Julián *et al.* (2003)). Especially the Raman peak arising from symmetric C-H stretching vibration (at 2904 cm⁻¹) is prominent in the whole spectrum. The Raman scattering from these channel materials is usually regarded as undesired light since it can hinder the detection of the signal from sample inside the channel. The channel material should be carefully selected to avoid spectral overlap between the desired signal from sample and other undesired light.

In the present study, micro- and milli-channels are made of combination of glass and PDMS as shown in figure 2.18. PDMS is used to construct channel structures because it can be easily shaped into the desired figure. On the other hand, glass is used to enclose the channel as top and/or bottom walls and therefore it works as an optical window for microscope observation or as a TIR substrate. This is mainly because of its optical properties: transparency, low auto-fluorescence and weak Raman signals in 2000–4000 cm⁻¹ (i.e., almost no overlap with the signal from aqueous solution used in this study). In addition, the hybrid PDMS/glass channel is considered to suppress the temperature rise in the sample solutions (Erickson *et al.*, 2003) caused by photothermal effect of laser irradiation since glass material has a relatively high thermal conductivity.

Table 2.6. Raman peaks and assignment of pure fused silica (Shibata *et al.*, 1981)

Raman shift [cm ⁻¹]		Assignment
440	(vs)*	Si–O–Si bond-bending vibration
485	(vs)	Si–O–Si bond-bending vibration
605	(m)	Si ⁺ ...O ⁻ –Si
800	(s)	Si–O–Si bond-stretching vibration
900	(vw)	Overtone of ν_4
1060	(w)	Si–O–Si bond-stretching vibration
1200	(w)	Si–O–Si bond-stretching vibration
1600	(vw)	Overtone of Si–O–Si bond-stretching vibration, and combination of Si–O–Si bond-stretching and bending vibrations

* s = strong, m = medium, w = weak, and v = very

Table 2.7. Raman peaks and assignment of borate groups and silicate units (Konijnendijk & Stevels, 1976)

Raman shift [cm^{-1}]	Assignment
435, 495	SiO_4 tetrahedra with four bridging oxygen ions
540	SiO_4 tetrahedra with one non-bridging oxygen ion
590	SiO_4 tetrahedra with two non-bridging oxygen ions
630	Ring-type metaborate groups
760	Six-membered borate ring with one BO_4 tetrahedron
770	Six-membered borate ring with two BO_4 tetrahedron
806	Boroxol groups
950	SiO_4 tetrahedra with two non-bridging oxygen ions
1050	SiO_4 tetrahedra with one non-bridging oxygen ion

Table 2.8. Borate and silicate groups present in borosilicate glass of each composition (Konijnendijk & Stevels, 1976)

	Alkali/boron ratio < 0.5	Alkali/boron ratio > 0.5
35 mol% SiO_2	Boroxol	Diborate
	Tetraborate	Metaborate
	Diborate	SiO_4 (four bridging oxygen ions)
	SiO_4 (four bridging oxygen ions)	SiO_4 (one non-bridging oxygen ion)
65 mol% SiO_2	Boroxol	Metaborate
	Tetraborate	SiO_4 (four bridging oxygen ions)
	(Diborate)	SiO_4 (one non-bridging oxygen ion)
	Metaborate	
	SiO_4 (four bridging oxygen ions)	

Table 2.9. Raman peaks and assignment of PDMS (Julián *et al.*, 2003)

Raman shift [cm ⁻¹]	Assignment
490 (s)*	(Si–O–Si) symmetric stretching
709 (s)	(C–Si–C) symmetric stretching
790 (w)	(C–Si–C) antisymmetric stretching + (CH ₃) antisymmetric rocking
862 (vw)	(CH ₃) symmetric rocking
1256 (w)	(C–H) symmetric bending
1410 (m)	(C–H) antisymmetric bending
2904 (vs)	(C–H) symmetric stretching
2964 (s)	(C–H) antisymmetric stretching

* s = strong, m = medium, w = weak, and v = very

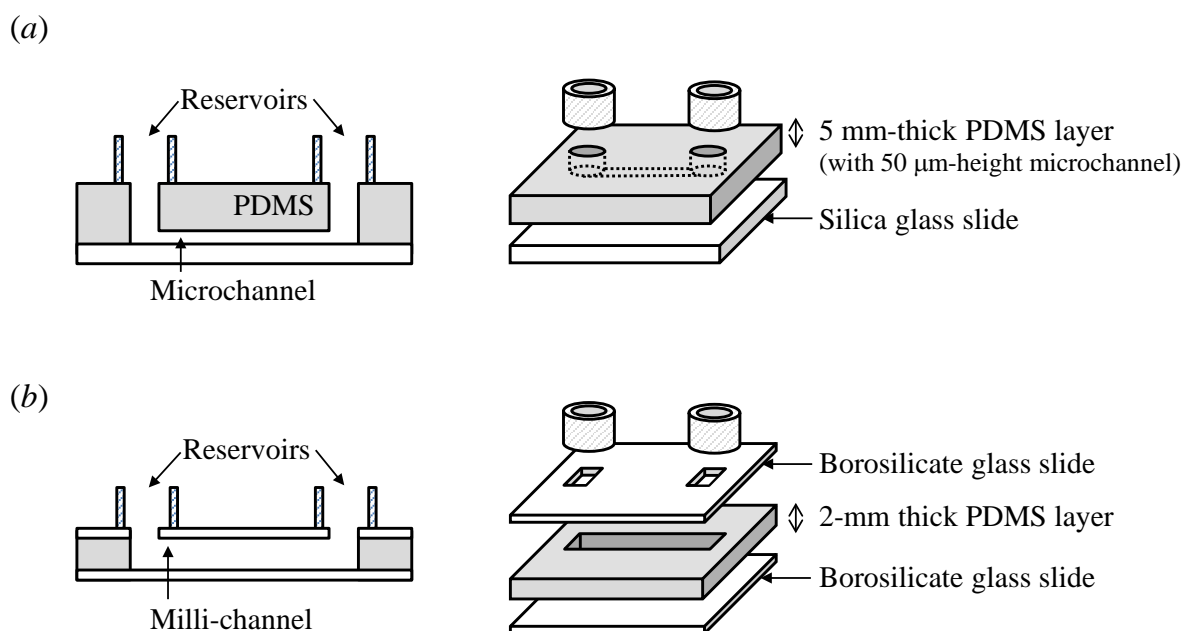


Figure 2.18. Schematic diagrams of (a) micro- and (b) milli-channels. The left-hand side of the figure shows the cross-sectional views of the channels and the right-hand side illustrates each layer which composes the channel structure.

2.4.3 Fabrication Process

The microchannel used in the present study is composed of a glass slide and a PDMS layer with microstructures which are formed by a method called replica molding or cast molding (Xia & Whitesides, 1998). This method is classified as one of the soft lithographic techniques and commonly used due to its easy duplication process. The master mold for replica molding is created by photolithography using a photoresist material, SU-8, in this study.

Figure 2.19(a) illustrates the fabrication process of the master mold by photolithography, which proceeds as follows: spin coating, soft baking, exposure, post baking, and development. A glass wafer (Matsunami Glass Inc., Ltd., Micro Slide Glass) is carefully cleaned in an ultrasonic bath sonicator with a detergent surfactant (AR BROWN Co. Ltd., DCN90), acetone, ethanol and ultrapure water, and then dried on a hotplate at 100 °C. After that a photosensitive resist material is coated on the glass wafer by spinning. Following the spin-coating process, the wafer is soft-baked on the hotplate to remove solvents from the resist and improve adhesion (Ziaie *et al.*, 2004). Subsequently, the photoresist is exposed to a UV light through a photomask, which is a glass plate having the desired micropatterns generated by photographic processes. The exposed wafer is baked again on the hotplate in order to selectively cross-link the UV-exposed region of the resist (post-exposure baking). The resist is subsequently developed by washing off the unexposed regions in a developer (MicroChem Corp., SU-8 Developer) and rinsed with isopropyl alcohol. Detailed parameters in the above process (such as spin speed, temperature and time for baking, UV exposure time and develop time) are required to be properly set depending on the desired thickness of the photoresist film (i.e., the channel height).

Figure 2.19(b) shows the process of replica molding. In this process, a material is introduced into a mold in its liquid state and allowed to solidify in the shape inside the mold (Tian & Finehout, 2008). In the present study, the pre-polymer mixture of PDMS, which is prepared by mixing PDMS base and its curing agent (Dow Corning Toray Co., Ltd., SILPOT 184) in 10:1 ratio by mass, is cast over the master mold. Following the sufficient degassing in a vacuum desiccator, the pre-polymer is cured for 2 h at 65 °C on a hotplate. After the polymer is solidified into an elastic layer, the PDMS replica is peeled off from the master. Since the master can be repeatedly used for several times, this technique enables replicating micro and nanoscale features without the use of expensive clean room processes (Tian & Finehout, 2008). In order to form the PDMS replica into a microchannel that can be used in experiments, access holes to reservoirs are prepared by punching through the PDMS material with a sharp needle. Subsequently the PDMS chip is attached on a cover glass by exploiting its self-adhesion, and reservoirs are bonded as illustrated in figure 2.19(c).

In the case of making a relatively large milli-scale channel, the starting point is making a PDMS layer of a desired thickness which is controlled by the weight of the pre-polymer to be

Fundamentals

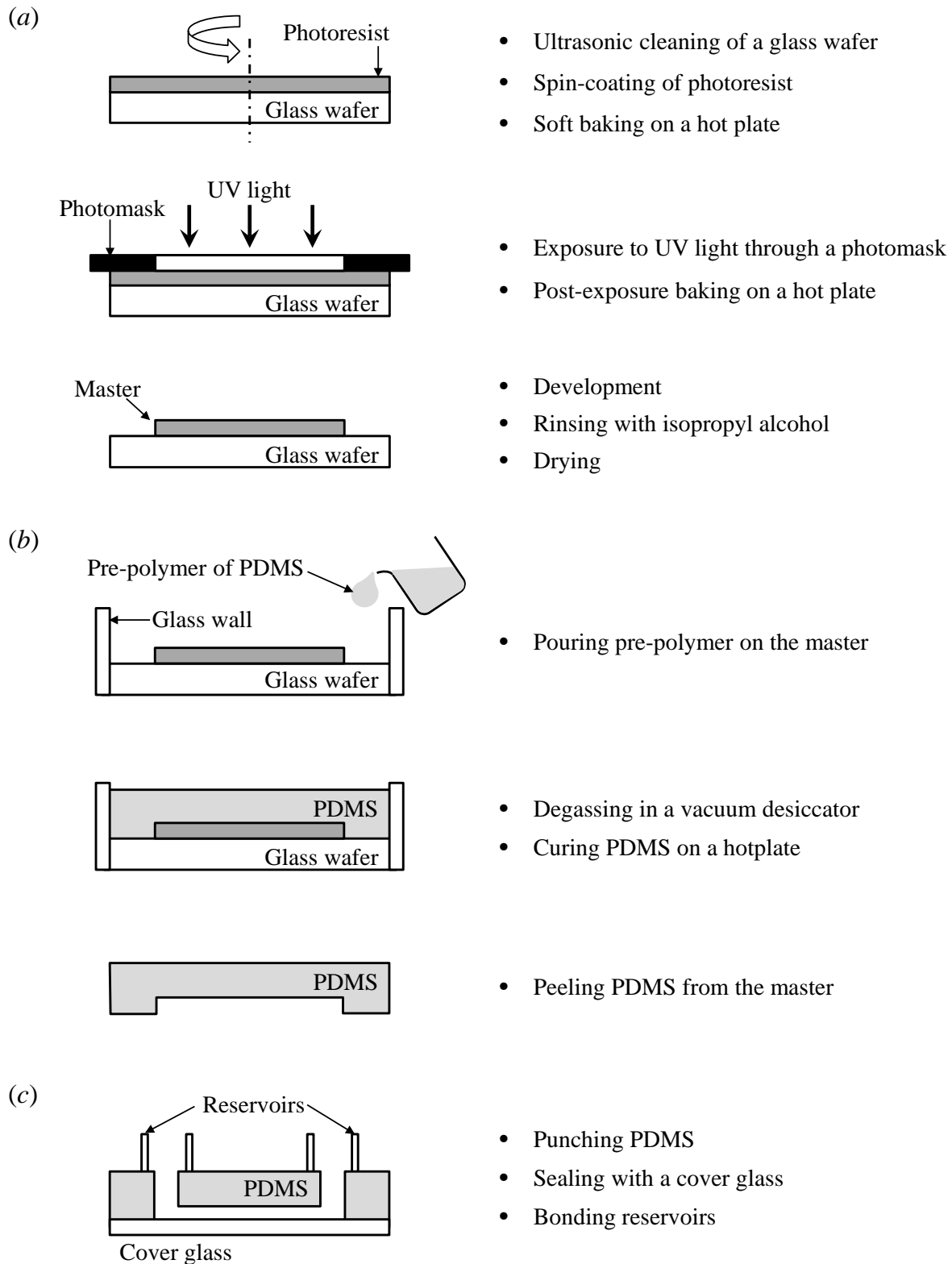


Figure 2.19. Fabrication processes of a microchannel composed of PDMS and glass. (a) Preparation of a master mold by photolithography. (b) Micro-structuring of PDMS by replica molding. (c) Fabrication of a microchannel used in the experiments.

used. The mixed pre-polymer is cast over a flat substrate (such as glass plate and plastic petri dish) and cured in the same way as replica molding. The resultant PDMS layer is peeled off from the substrate and the desired channel shape is cut off from the layer. Subsequently, the channel structure is enclosed with two pieces of glass slides which serve as the top and bottom walls of the channel. Thus the thickness of PDMS defines the channel height. Finally reservoirs are bonded on the chip. The fabrication process of milli-channel is much simpler but less reproducible and less accurate compared to the above replica molding.

Chapter 3

Visualization of Steady-State Temperature Distribution by Raman Imaging Technique

This chapter proposes a label-free planar temperature measurement technique based on direct Raman imaging. The present technique focuses on the temperature-sensitive Raman band of liquid H₂O molecules, whose spectral shape is closely related to the formation of intermolecular hydrogen bonds. Temperature distributions are determined from the intensity ratio of two Raman images at different wavelengths in order to compensate the influence of the non-uniform excitation light. Microscale visualization of water temperature is achieved in steady-state channel flow using the previously-obtained calibration data.

3.1 Temperature Measurement by Raman Imaging

This section concentrates on the observation of water Raman spectra at the beginning. The temperature-dependent spectral change is related to the frequency shift of intramolecular vibrations due to the hydrogen bonds formed between liquid water molecules. Subsequently, the measurement principle of the present imaging technique is described including the methodology for correction of the influence of non-uniform illumination.

3.1.1 Temperature Dependence of Water Raman Spectra

In the present study, water temperature is determined by measuring the Raman scattering from OH vibration of liquid H₂O molecules, whose intensity is known to be highly sensitive to temperature change due to the influence of hydrogen bonds. In order to examine the temperature dependence of water Raman spectra, a spectroscopic measurement was conducted at different temperatures. Pure water was introduced into a milli-channel

fabricated from PDMS and borosilicate glass slides (as shown in figure 2.18(b)). The spectra were acquired using a measurement system shown in figure 3.1(a). The system mainly consists of a continuous-wave (CW) Nd:YVO₄ laser (Coherent Inc., Verdi V-6, $\lambda = 532$ nm), an objective lens (Nikon Corp., 10 \times , $NA = 0.25$, $WD = 7.0$ mm), and a grating spectrometer (Solar TII Ltd., SL100M) which is mounted on an electron-multiplying charge-coupled device (EM-CCD) camera (Hamamatsu Photonics K. K., C9100-13, 512×512 pixels, $16 \times 16 \mu\text{m}^2/\text{pixel}$, 16 bits). The electron-multiplying (EM) gain was set to be 500, and the total acquisition time per spectrum was 45 s. The optical layout of the grating spectrometer is illustrated in figure 3.1(b). A 400 groove/mm grating provided a reciprocal linear dispersion of 17.7 nm/mm, and a spectral window of approximately 4100 cm^{-1} on the detector. The spectral resolution of the system was calculated to be less than 0.57 nm which approximately corresponds to 10 cm^{-1} . The wavelength calibration was conducted by utilizing emission lines of commercially available mercury and neon lamps with a second-order polynomial interpolation.

Figure 3.2 shows water Raman spectra in the $2800\text{--}4000 \text{ cm}^{-1}$ region at various temperatures. For noise reduction, the measured spectra were smoothed with a 11-points, 3rd-order Savitzky-Golay filter (Savitzky & Golay, 1964). The bottom horizontal axis is the Raman shift expressed in wavenumbers, and the upper horizontal axis represents the corresponding wavelength of the scattered light with 532 nm excitation. The vertical axis is the intensity in arbitrary unit. As seen in figure 2.17 and table 2.4, the Raman scattering of this region mainly arises from symmetric and antisymmetric stretching intramolecular vibrations of H₂O molecules. Figure 3.2(a) indicates that the Raman intensity in lower frequency range (left-hand side of the band) decreases with a temperature rise, while the intensity in higher frequency range (right-hand side) slightly increases in contrast. In addition, it is clearly seen from the enlarged view of $3400\text{--}3500 \text{ cm}^{-1}$ that all the spectra intersect in a point around 3460 cm^{-1} . It is comparable to previously-reported values for isosbestic point, which refers to the wavenumber where the Raman intensity is independent of temperature (Walrafen, 1967; Walrafen *et al.*, 1986).

In order to present the temperature-dependent spectral change more clearly, Raman difference spectra were calculated from figure 3.2(a), by subtracting the reference spectrum at 298 K from the other spectra. Figure 3.2(b) shows the obtained difference spectra, where it is evident that the OH stretching Raman band has two parts with contrasting temperature dependencies; one with a negative peak at 3200 cm^{-1} , and the other with a relatively small positive peak around 3600 cm^{-1} . For further insight, the Raman intensity differences at 3200 , 3460 and 3600 cm^{-1} (figure 3.2(b)) are plotted against the temperature in figure 3.3. It clearly indicates that the intensity variations at 3200 cm^{-1} and 3600 cm^{-1} are opposite in sign and both are almost proportional to temperature change, while that at 3460 cm^{-1} (i.e., isosbestic point) is negligibly small over the range of $298\text{--}328 \text{ K}$.

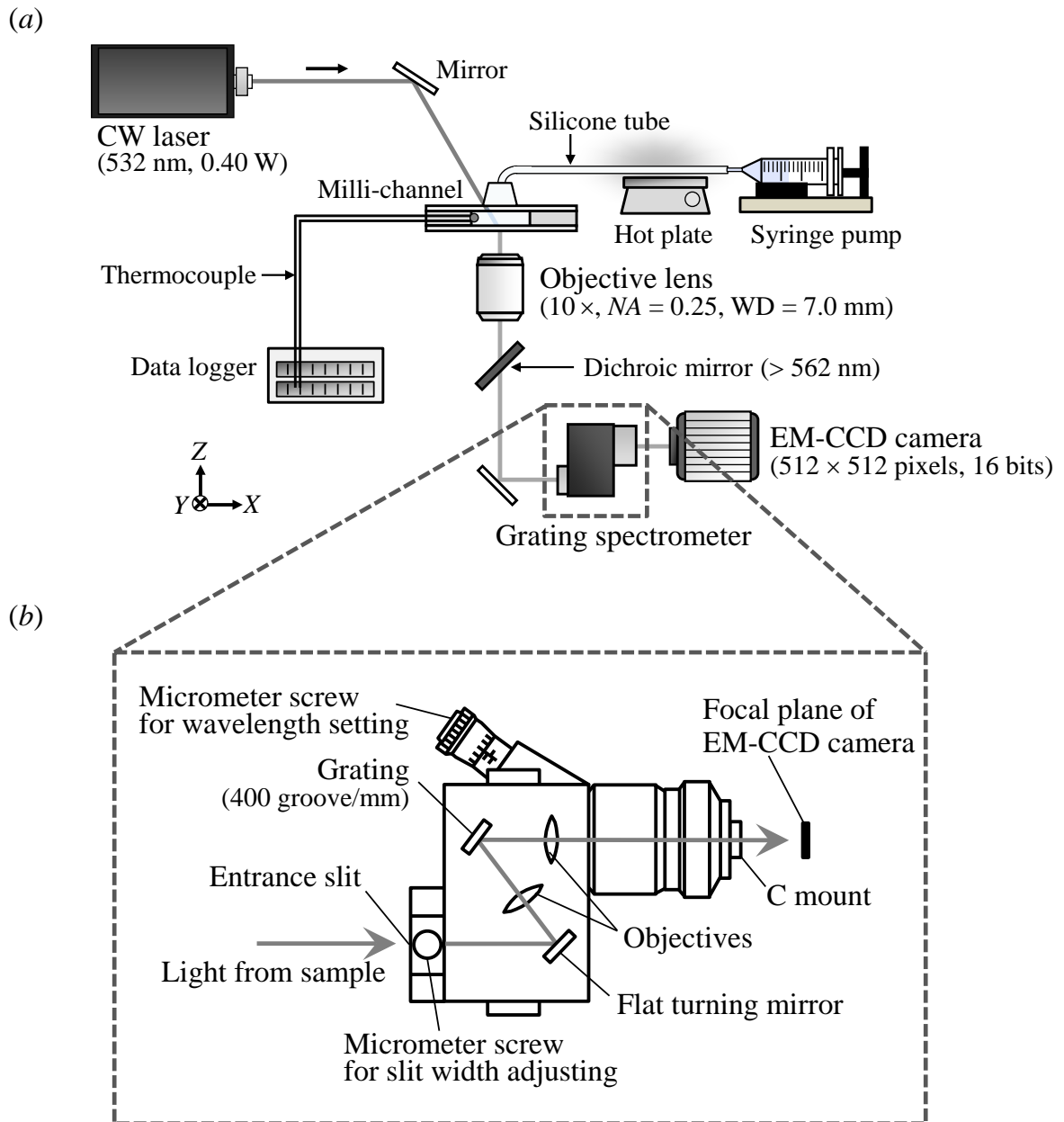
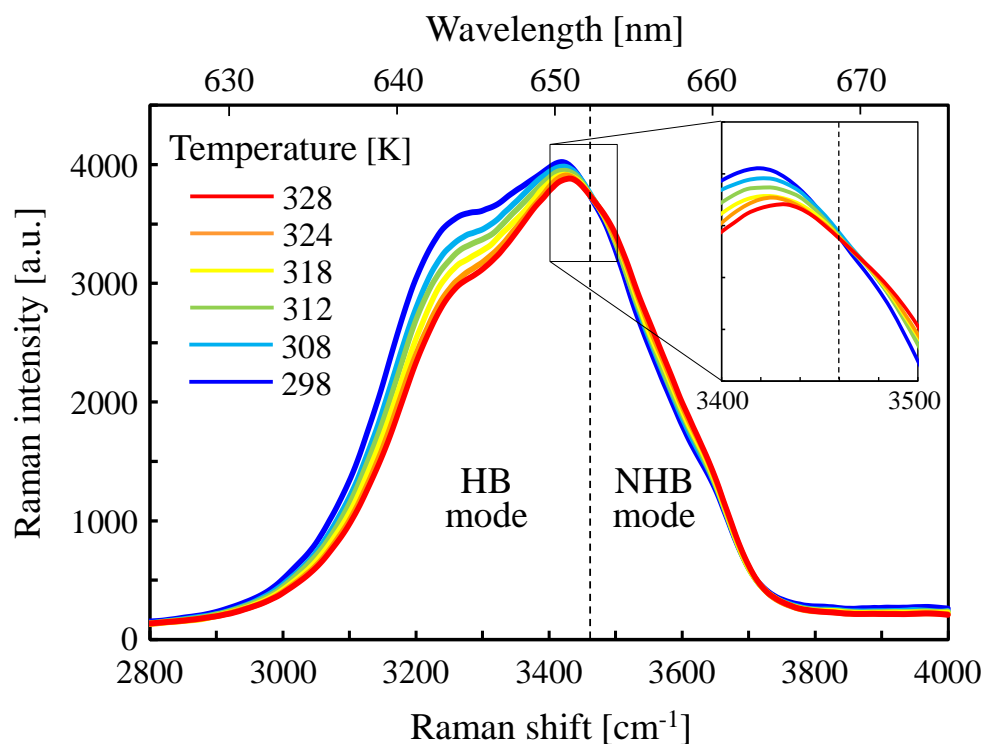


Figure 3.1. (a) Schematic of the Raman spectroscopy system and (b) the optical layout of the spectrometer.

(a)



(b)

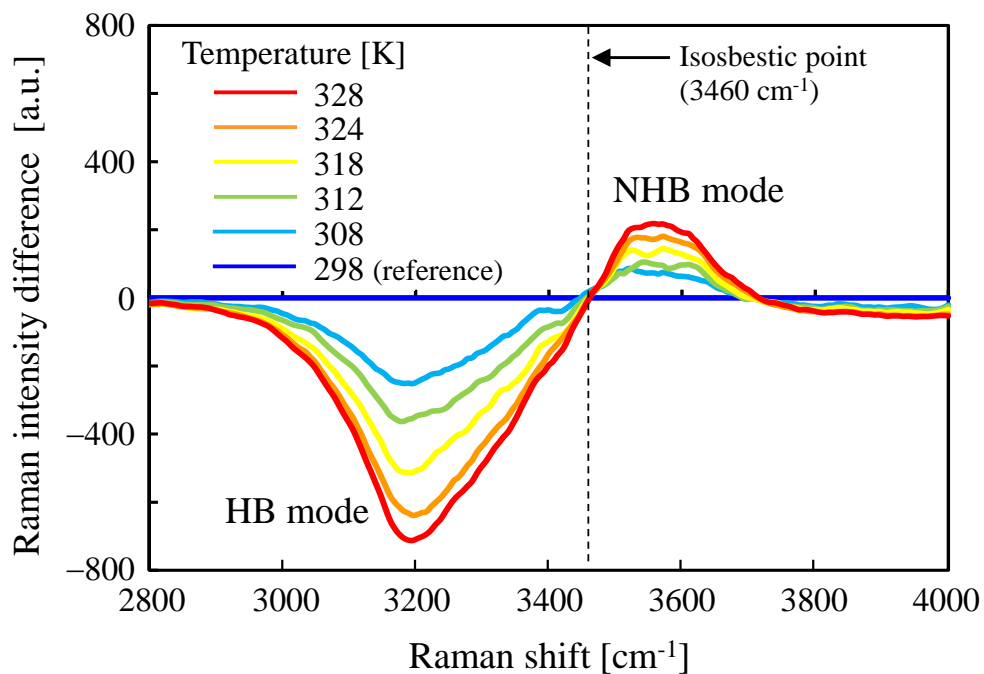


Figure 3.2. (a) Raman spectra arising from OH stretching vibration of liquid H₂O molecules at different temperatures. The upper horizontal axis shows the corresponding wavelength of the scattered light with 532 nm excitation. (b) Raman difference spectra calculated from the spectra in figure 3.2(a) (the spectrum at 298 K was used as reference).

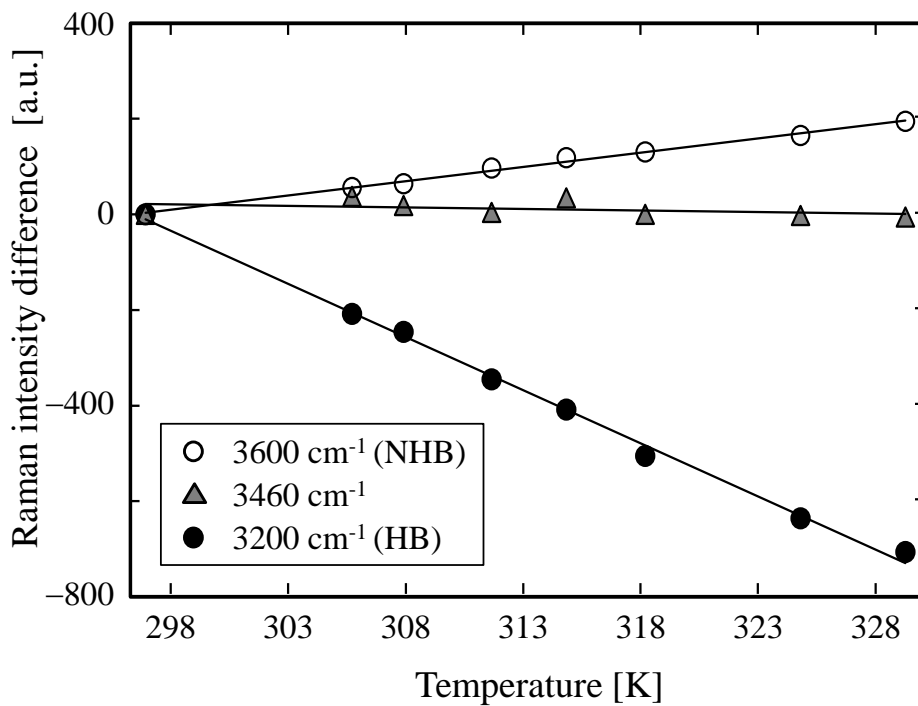


Figure 3.3. Relationship between the temperature and the Raman intensity differences at 3200, 3460, and 3600 cm^{-1} (derived from figure 3.2(b)).

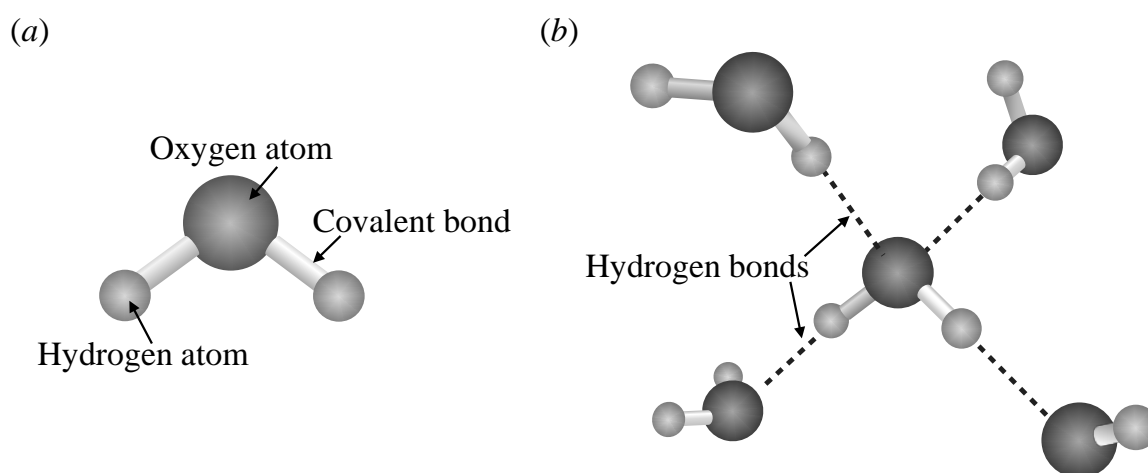


Figure 3.4. Schematic views of (a) a water molecule in monomeric (or non-hydrogen-bonded) state and (b) a water molecule forming four hydrogen bonds with nearby molecules (an example of the configuration of water cluster).

The contrasting temperature dependencies observed above and below the isosbestic point can be explained in terms of the chemical equilibrium between the cluster (or hydrogen-bonded: HB) and monomeric (or non-hydrogen-bonded: NHB) states of H₂O molecules, which are illustrated in figure 3.4. A hydrogen bond represents the intermolecular attraction between the hydrogen atom of one water molecule and the lone-pair electrons on another (Ludwig, 2001). In liquid water, H₂O molecules can exist as ‘water clusters’, i.e., groups of molecules held together with hydrogen bonds (Maheshwary *et al.*, 2001). Since hydrogen bonds lower the frequency of intramolecular vibration of H₂O molecules as indicated in table 2.17, the Raman scattering from HB molecules appears in a lower Raman shift compared to NHB ones. Therefore, a temperature rise, which weakens hydrogen bonds and increases the number of NHB molecules, results in the intensity increase of the high-frequency range and causes the intensity decrease of the low-frequency range. In other words, the spectral change shown in figure 3.2 was observed as a result of the equilibrium shift between HB and NHB states by temperature change. The following passage provides explanation about the above intensity change in theoretical aspect.

In an equilibrium represented by NHB \leftrightarrow HB, the equilibrium constant K_e is expressed as,

$$K_e = \frac{N_{\text{HB}}}{N_{\text{NHB}}} \quad (3.1)$$

where N_{HB} and N_{NHB} [molecules/m³] are the concentration (or the number density) of HB and NHB water molecules, respectively. Using the van't Hoff equation for relating K_e to absolute temperature T , the following equation can be obtained:

$$\ln K_e = \ln \left(\frac{N_{\text{HB}}}{N_{\text{NHB}}} \right) = -\frac{\Delta H}{RT} + \frac{\Delta S}{R} \quad (3.2)$$

where R is the gas constant [J/mol·K], ΔH is the enthalpy change for the reaction [J/mol], and ΔS is the reaction entropy [J/mol·K]. Here, ΔH represents the enthalpy change for the formation of a mole of hydrogen bonds in water (i.e., energy of hydrogen bonds per mole), and its typical value is approximately -20 kJ/mol. A rearrangement of equation (3.2) leads to

$$\frac{N_{\text{HB}}}{N_{\text{NHB}}} = \exp \left(-\frac{\Delta H}{RT} + \frac{\Delta S}{R} \right) = A \exp \left(\frac{B}{T} \right) \quad (3.3)$$

where $A = \exp(\Delta S/R)$, and $B = -\Delta H/R$. Assuming that ΔS and ΔH are constant, the ratio of N_{HB} to N_{NHB} decays exponentially with increasing temperature, while the total amount of water molecules (i.e., the sum of N_{HB} and N_{NHB}) is constant. Consequently, the Raman intensities from HB and NHB water molecules exhibit contrasting temperature dependencies as shown in figure 3.2, since the Raman intensity is proportional to the concentration N (equation (2.20)).

3.1.2 Measurement Principle for Steady-State Temperature Field

The present study realizes temperature measurements by focusing on the Raman intensities arising from HB and NHB molecules, i.e., the temperature determination is carried out by probing the number of H₂O molecules at each state. According to the spectral measurement result in figure 3.2, the range of 3000–3460 cm⁻¹ and that of 3460–3800 cm⁻¹ are roughly defined as HB and NHB modes, respectively, although there might be some spectral overlap between actual Raman bands of HB and NHB molecules. Direct Raman imaging technique is employed to measure temperature distributions in channel flow because it can provide two-dimensional Raman images in a specific spectral region (see figure 2.8(c)). The whole measurement area is illuminated by an unfocused laser beam, and Raman images of each mode (HB or NHB modes) are captured by the EM-CCD camera through an optical filter which selectively transmits the wavelength range corresponding to HB or NHB modes. After the image acquisition of one mode, the filter is manually switched to the other one and the image acquisition is repeated. This measurement procedure is illustrated in figure 3.5.

According to equation (2.20), the detected Raman intensity of the HB region, I_{HB} , can be represented by the following equation:

$$I_{\text{HB}} = K_{\text{HB}} \cdot I_0 \cdot \Omega \cdot \left(\frac{d\sigma}{d\Omega} \right)_{\text{HB}} \cdot l \cdot N_{\text{HB}} \quad (3.4)$$

where I_0 [photons/s·m²] is the excitation laser intensity, Ω [sr] is the solid angle of signal detection, $d\sigma/d\Omega$ [cm²/molecule·sr] is the absolute differential Raman cross-section and l [m] is the length of the probe volume. N_{HB} [molecules/m³] is the number density of hydrogen-bonded water molecules inside the probe volume, which reflects temperature change. The constant K_{HB} [-] is introduced to express influencing parameters such as transmission of the optical components and collection efficiency of the detector. In the same manner, the Raman intensity of the NHB region, I_{NHB} , can be expressed as,

$$I_{\text{NHB}} = K_{\text{NHB}} \cdot I_0 \cdot \Omega \cdot \left(\frac{d\sigma}{d\Omega} \right)_{\text{NHB}} \cdot l \cdot N_{\text{NHB}} \quad (3.5)$$

In order to calculate a temperature distribution from the measured Raman image, the influence of the non-uniformity of excitation intensity, which would linearly affect the calculated temperature, is required to be eliminated. In the present study, this is overcome thorough determining the intensity ratio of two modes:

$$I_{\text{Ratio}} = \frac{I_{\text{HB}}}{I_{\text{NHB}}} = \frac{K_{\text{HB}} \cdot I_0 \cdot \Omega \cdot \left(\frac{d\sigma}{d\Omega} \right)_{\text{HB}} \cdot l \cdot N_{\text{HB}}}{K_{\text{NHB}} \cdot I_0 \cdot \Omega \cdot \left(\frac{d\sigma}{d\Omega} \right)_{\text{NHB}} \cdot l \cdot N_{\text{NHB}}} = K_{\text{Ratio}} \cdot \frac{N_{\text{HB}}}{N_{\text{NHB}}} \quad (3.6)$$

By calculating this Raman intensity ratio, common factors (such as I_0 , Ω and l) are cancelled

out and all the temperature-independent factors are integrated into a constant K_{Ratio} . When the sample is pure liquid water under normal atmospheric pressure, i.e., there is no other influencing factors such as pressure change and impurity like electrolyte ions, the ratio of the number densities of HB and NHB molecules ($N_{\text{HB}}/N_{\text{NHB}}$) is determined by absolute temperature (T), as predicted by equation (3.3). Thus, the intensity ratio can be expressed as a function of temperature, by combining equations (3.3) and (3.6):

$$I_{\text{Ratio}} = K_{\text{Ratio}} \cdot A \exp\left(\frac{B}{T}\right) = K_{\text{Ratio}} \cdot f(T) \quad (3.7)$$

If the constant K_{Ratio} is uniformly distributed over the measurement area, the temperature distribution can be simply determined from the distribution of the intensity ratio (I_{Ratio}). On the other hand, in the case where K_{Ratio} has significantly different values depending on the location in the measurement area, its spatial distribution should be corrected by using some reference image. The correction methodology will be detailed in section 3.3.3.

The advantages of considering intensity ratio of HB to HNB modes are that (1) the influence of the spatial non-uniformity of excitation intensity is cancelled out (i.e., planar temperature measurement can be realized for any excitation intensity profile) and (2) higher sensitivity is expected for temperature determination by utilizing the opposite temperature dependencies of the two modes.

It should be noted that the present study employs volume illumination for excitation of Raman process, that is, the entire test section is illuminated by a volume of light as shown in figure 3.1(a). This means that the detected intensity represents the Raman intensity integrated along the optical light path (i.e., along the channel height), and consequently the proposed technique provides the two-dimensional temperature map which is averaged over the depthwise direction. Therefore, when one needs a temperature distribution at arbitrary depth

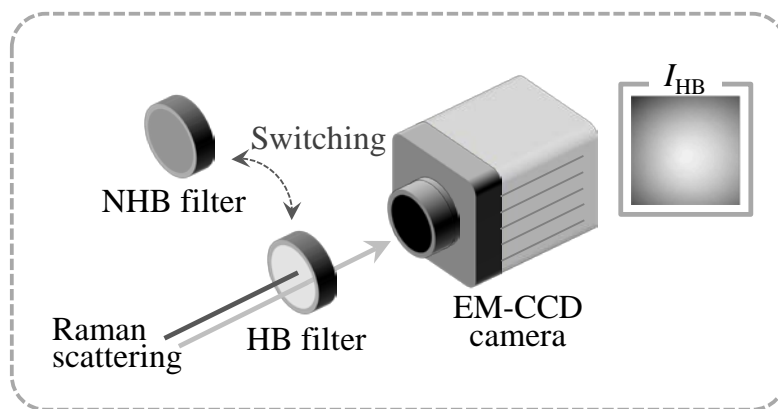


Figure 3.5. Schematic of the direct Raman imaging through the filter which transmits HB mode. The filters were manually switched after the image acquisition.

position in the channel, point mapping approach using confocal Raman micro-spectroscopy is suitable rather than the present imaging technique. It is also noted that the present methodology is not applicable to the temperature field which changes quickly during the set of image acquisitions, since it requires temporal switching of the optical filters manually and thus cannot acquire the images of HB and NHB modes simultaneously. Therefore, this chapter focuses on the visualization of steady-state temperature fields as a primary step. The application of Raman imaging technique to the transient temperature measurement will be detailed in chapter 4.

3.2 Measurement System

3.2.1 Experimental Apparatus

Figure 3.6 shows a schematic of the measurement system for steady-state temperature imaging. The system consists of an inverted microscope (Nikon Corp., Ti-U), an objective lens (Nikon Corp., $\times 10$, $NA = 0.25$, $WD = 7.0$ mm), a filter block for separating a specific Raman signal, and the same CW laser ($\lambda = 532$ nm) and the EM-CCD camera that were used for the above spectral measurement. The excitation wavelength for Raman process was selected with consideration for the photothermal effect in the sample material; in this case the absorption coefficient of water is extremely low at 532 nm (about 0.05 m^{-1}) according to the work by Smith & Baker (1981). Furthermore, excitation light in visible range has an advantage in that high-performance optical filters and detectors are commercially available compared to light in UV range. The specifications of the camera are listed in table 3.1. The present setup gives a measurement area of $819 \times 819 \text{ }\mu\text{m}^2$ and a depth of field of $14.9 \text{ }\mu\text{m}$.

The laser beam was used to irradiate pure water flowing in a milli-channel on the microscope stage. The laser power was 240 mW at the measurement point with an ellipsoidal spot (major axis: 2.5 mm, minor axis: 2.3 mm). In order to prevent the laser beam from directly entering the objective lens, the beam was introduced to the channel with an incident angle of 28° . Moreover the objective lens with long working distance was selected as noted above. The Raman signal from the irradiated water was imaged by the EM-CCD camera after passing through the objective lens and the filter block. The filter block is equipped with a dichroic mirror (Semrock, Inc., transmission wavelength: > 562 nm) that removes the excitation light (i.e., the Rayleigh scattered light) and a bandpass filter that transmits the HB or NHB mode. The EM-CCD camera has a quantum efficiency of approximately 90% at 630–670 nm as indicated in figure 3.7; therefore it is sufficiently sensitive to detect the OH stretching band in $3000\text{--}3800 \text{ cm}^{-1}$ excited by the 532 nm laser (see figure 3.2(a)). Figure 3.8 shows the sensor characteristics of the EM-CCD camera, where the signal-to-noise ratio

(SNR) is plotted versus EM-gain (figure 3.8(a)) and input photon number (figure 3.8(b)). Here the input photon number is defined as the photon number detected by a single pixel during a single frame. It is observed from figure 3.8(a) that the SNR is significantly improved by increasing EM gain when the input photon number is small, while it is almost constant when the input photon number is over 1000. Figure 3.8(b) also shows that the SNR exhibits little dependence on the EM-gain when it is set at over 200 with the condition of sufficiently large photon number. In this experiment, the typical number of input photon is estimated to be approximately 180 from the typical intensity value (20000 counts at the gain of 700), the typical conversion coefficient (5.8 electrons/count) and the quantum efficiency (90%). Therefore, the EM-gain of 700 is considered to be large enough to obtain good SNR.

For controlling water temperature, an inlet of the milli-channel was connected to a syringe pump (KD Scientific Inc., KDS-200) by a silicone tube and water heated on a hotplate was injected into the channel at a constant flow rate. The water temperature inside the channel was controlled between room temperature (approximately 296 K) and 333 K by adjusting the hotplate temperature (T_{hotplate}). A T-typed thermocouple (diameter: 76 μm) was inserted in the channel and the water temperature was recorded by a data logger (Keyence Corp., NR-250) at a sampling rate of 1 Hz. The data logger was synchronized with the EM-CCD camera using a pulse generator to enable the water temperature and Raman images to be simultaneously detected.

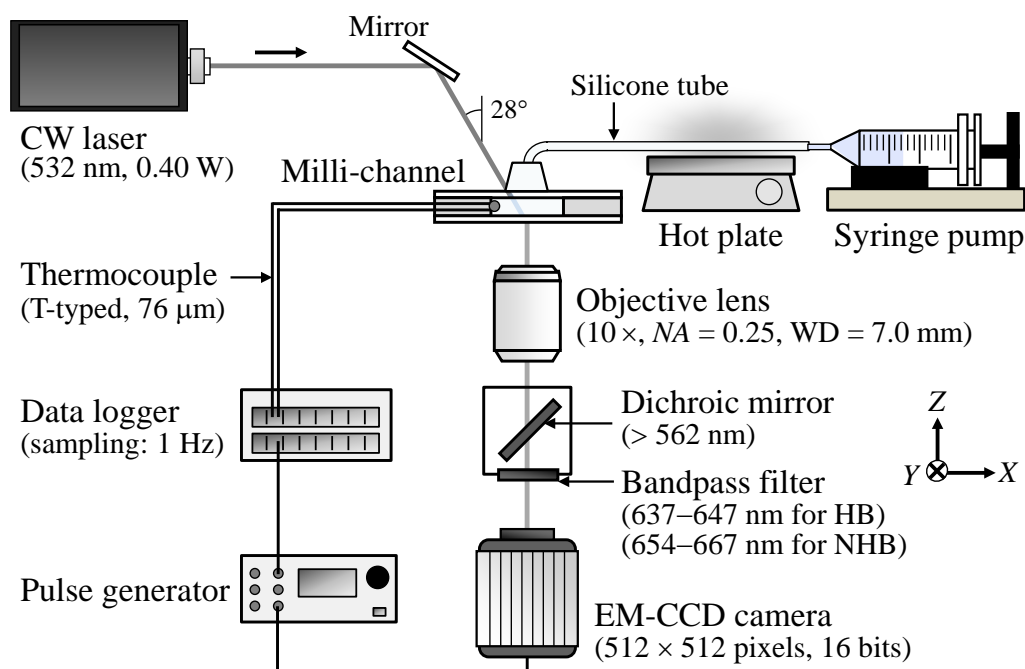


Figure 3.6. Schematic of the measurement system for temperature measurement based on Raman imaging.

Table 3.1. Specifications of the EM-CCD camera (given by Hamamatsu Photonics K. K.)

Number of pixels	512 (H) × 512 (V)
Cell size	16 μm (H) × 16 μm (V)
Effective area	8.192 mm (H) × 8.192 mm (V)
Maximum frame rate	31.9 frames/s
A/D converter	16 bits
Exposure time	30.5 ms to 2 h
Electron multiplier gain	From 4 × to 2000 ×
Readout noise (r.m.s.) (typ.)	25 electrons at EM gain min.
Full well capacity (typ.)	370000 electrons
Conversion coefficient (typ.)	5.8 electrons/count
Cooling method	Forced-air peltier cooling
Cooling temperature	-65 °C

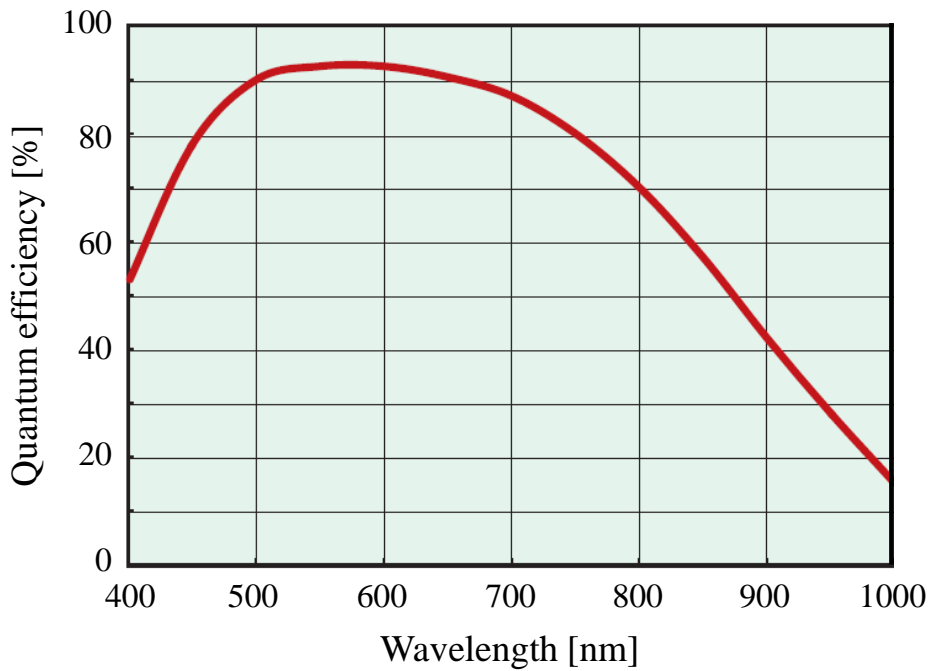
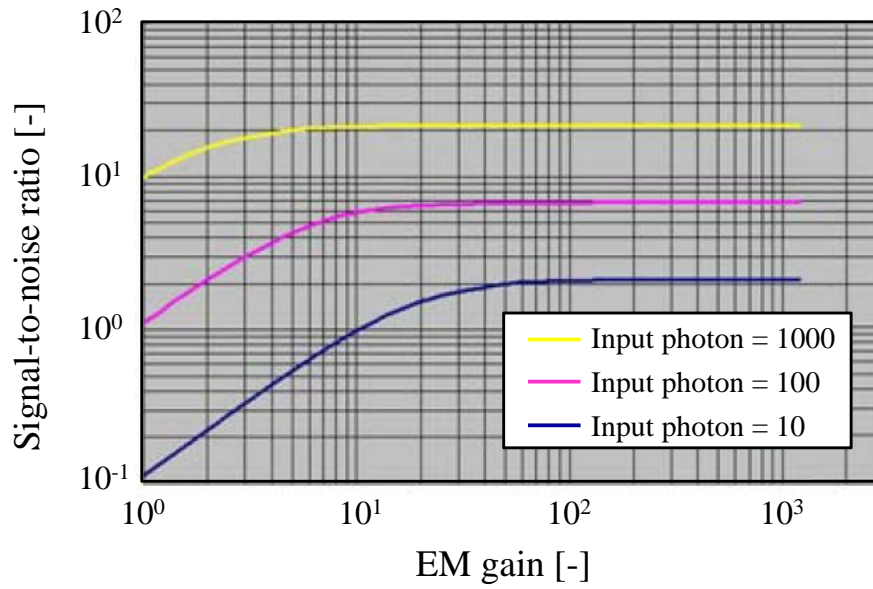


Figure 3.7. Spectral response characteristic of the EM-CCD camera (given by Hamamatsu Photonics K. K. (http://www.biovis.com/resources/ccd/e_c910013.pdf, December 8, 2014)).

(a)



(b)

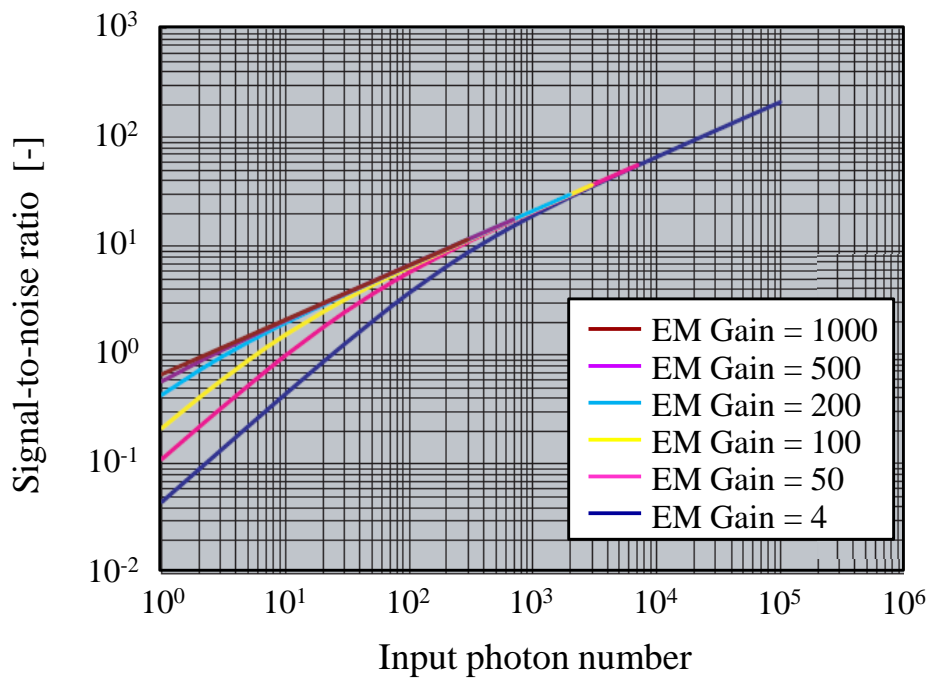


Figure 3.8. Sensor characteristics of the EM-CCD camera. (a) Dependence of the signal-to-noise ratio on EM-gain, and (b) dependence of the signal-to-noise ratio on input photon number (given by Hamamatsu Photonics K. K.).

3.2.2 Filter Selection

As is the case for other optical sensing techniques, it is important to separate the signal from the noise. In this technique, it is critical to select appropriate optical bandpass filters in order to detect only the spectral regions of HB and NHB modes, which are sensitive to temperature change. Hence, bandpass filters were chosen for the HB and NHB modes based on the spectral measurement result in figure 3.2(a). Figure 3.9 shows the spectral properties of the selected filters (Semrock Inc., FF01-642/10-25 for HB and FF01-660/13-25 for NHB). This figure clearly shows that the transmission wavelengths of the two bandpass filters correspond to the spectral regions of the HB and NHB modes, although the transmission range of the NHB filter partially overlaps the HB region. The optical densities of these filters are higher than 5 at 532 nm. Therefore, the excitation wavelength (i.e., the Rayleigh scattered light) is adequately removed by using them in combination with the aforementioned dichroic mirror. The transmission range (with transmission over 90%) is 634–648 nm for HB filter and 649–668 nm for NHB filter. In order to examine the availability of the selected filters, the Raman intensities of the water Raman spectra (in figure 3.2(a)) are integrated within the above transmission ranges, and plotted against the temperature in figure 3.10. The integrated intensity calculated for each filter exhibits the temperature sensitivity, which supports availability of the selected filters for the following Raman imaging.

The Raman images of HB and NHB modes were obtained by inserting the corresponding filters in the detection path. I_{HB} and I_{NHB} are defined as the intensity value detected through each bandpass filter and then substituted into equation (3.6).

3.3 Calibration Experiment for Raman Imaging

3.3.1 Calibration Curve

In order to correlate the Raman intensity ratio and the water temperature, a calibration experiment was performed under uniform temperature condition. An I-shaped milli-channel (in figure 3.11) consisting of poly(dimethylsiloxane) (PDMS) sheet and borosilicate glass slides was used for the experiment. The channels were fabricated by the process described in section 2.4.3. A 2-mm-thick PDMS sheet was prepared by curing the pre-polymer solution and the channel pattern was cut from the sheet. Then the sheet was sealed with two 0.15 mm-thick borosilicate glass slides, which served as the top and bottom walls of the channel. The inlet was connected to the syringe pump by a silicone tube as illustrated in figure 3.6. For monitoring the water temperature, an insulated thermocouple was placed at

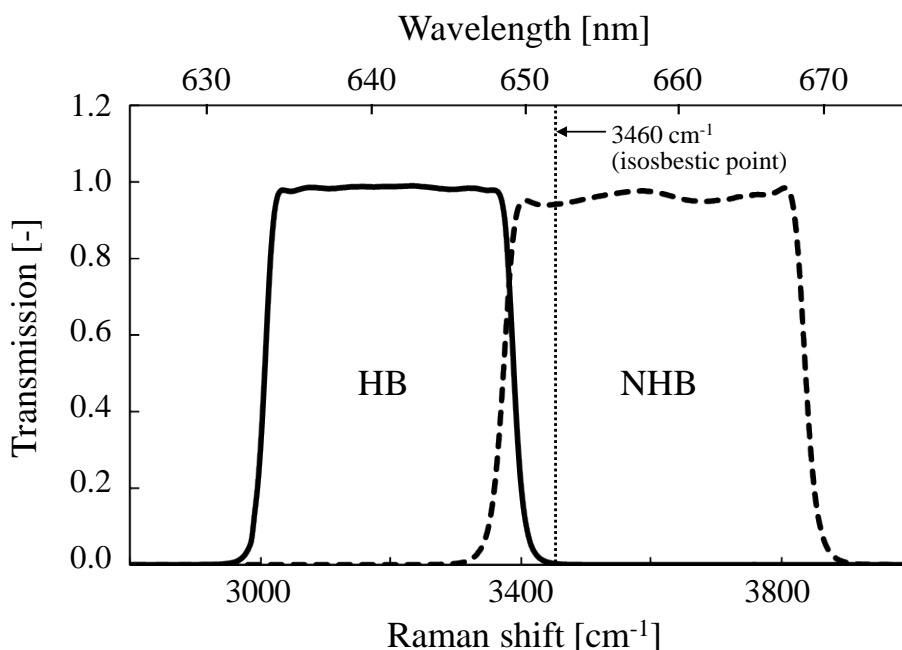


Figure 3.9. Spectral transmission characteristics of the selected bandpass filters for HB mode and NHB mode (Semrock Inc., FF01-642/10-25 (<http://www.semrock.com/FilterDetails.aspx?id=FF01-642/10-25>, December 8, 2014) for HB, and FF01-660/13-25 (<http://www.semrock.com/FilterDetails.aspx?id=FF01-660/13-25>, December 8, 2014) for NHB).

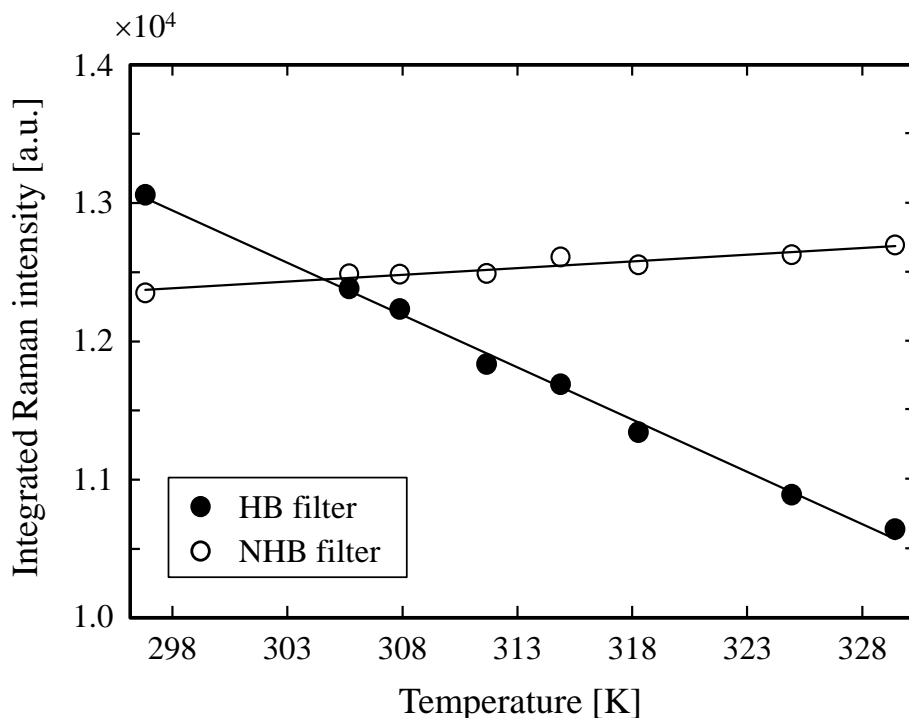


Figure 3.10. Relationship between the temperature and the integrated Raman intensity within the transmission range of each filter, which is calculated from the Raman spectra (shown in figure 3.2(a)).

the middle of the PDMS sheet, which was moved about 0.5 mm into the water from the channel sidewall. During the experiment, small bubbles were generated from the air-saturated water and PDMS wall, and sometimes hindered the temperature measurement by covering the thermocouple tip. The experimental data clearly influenced by the bubbles were excluded from the following results.

At each temperature, Raman image acquisition was started with HB filter. Subsequently, the filter was manually switched to NHB filter, and Raman images were acquired again. These image acquisitions were conducted after the water temperature had reached a steady state. To ensure the stability of the temperature field during the measurement, the water flow rate was maintained at 2 mL/min by the syringe pump. The excitation light path was set at the central region of the channel and kept away from the PDMS side wall in order to avoid the generation of scattered light at PDMS channel wall, since PDMS emits intense Raman signal of C-H stretching modes around 2900–3000 cm^{-1} (in table 2.9) The focal plane of the objective lens was positioned at the center of the channel in the depthwise direction in order to ensure that the bulk temperature was obtained. The depth of field was calculated to be 14.9 μm from equation (2.37). Throughout the present set of experiments, the exposure time and frame interval of the EM-CCD camera were set to be 465 and 500 ms, respectively, and 30 images were collected for each measurement. This resulted in a total acquisition time of 15 s. After the measurement, the obtained 30 Raman images were temporally averaged. The EM-gain was set to be 700, which is considered to be sufficiently large according to figure 3.8.

A typical Raman image which was obtained thorough HB filter is shown in figure 3.12(a). A Gaussian-like intensity profile can be observed over the whole image, since the Raman intensity linearly increases with the excitation intensity according to equation (3.4). Figures 3.12(b) and (c) depict the intensity profiles plotted along the horizontal and vertical axes, respectively. As the laser spot size (major axis: 2.5 mm, minor axis: 2.3 mm) was sufficiently large compared to the measurement area ($819 \times 819 \mu\text{m}^2$), it is considered that adequate signal quality was obtained even at the edge region of the measurement area. (The intensity at the corner of the area was approximately 75% of that at the central region.) Therefore, the difference in signal-to-noise ratio due to the non-uniform excitation intensity was not taken into consideration (i.e., the whole imaging area was used for temperature measurement).

Figure 3.13 shows the Raman intensity values obtained through HB and NHB filters (I_{HB} , I_{NHB}) at various temperatures. Each plot represents the mean intensity value of the temporally-averaged Raman image, and the horizontal axis is the water temperature measured by the thermocouple (figure 3.11). It shows that I_{HB} decreases with increasing temperature, whereas I_{NHB} increases slightly with increasing temperature. These contrasting temperature dependencies are consistent with the spectral measurement result (figures 3.2 and 3.10), which implies that temperature measurement of channel flow can be realized by Raman imaging through these filters.

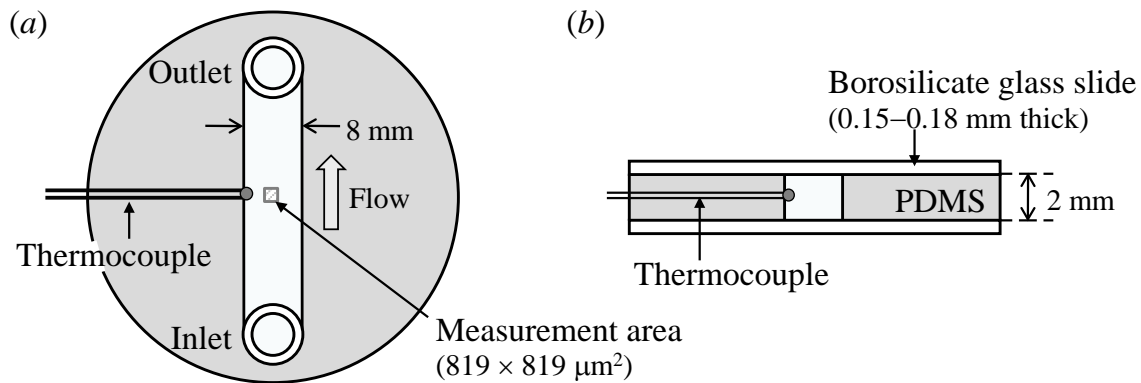


Figure 3.11. (a) Top and (b) cross-sectional views of an I-shaped milli-channel used for calibration experiment.

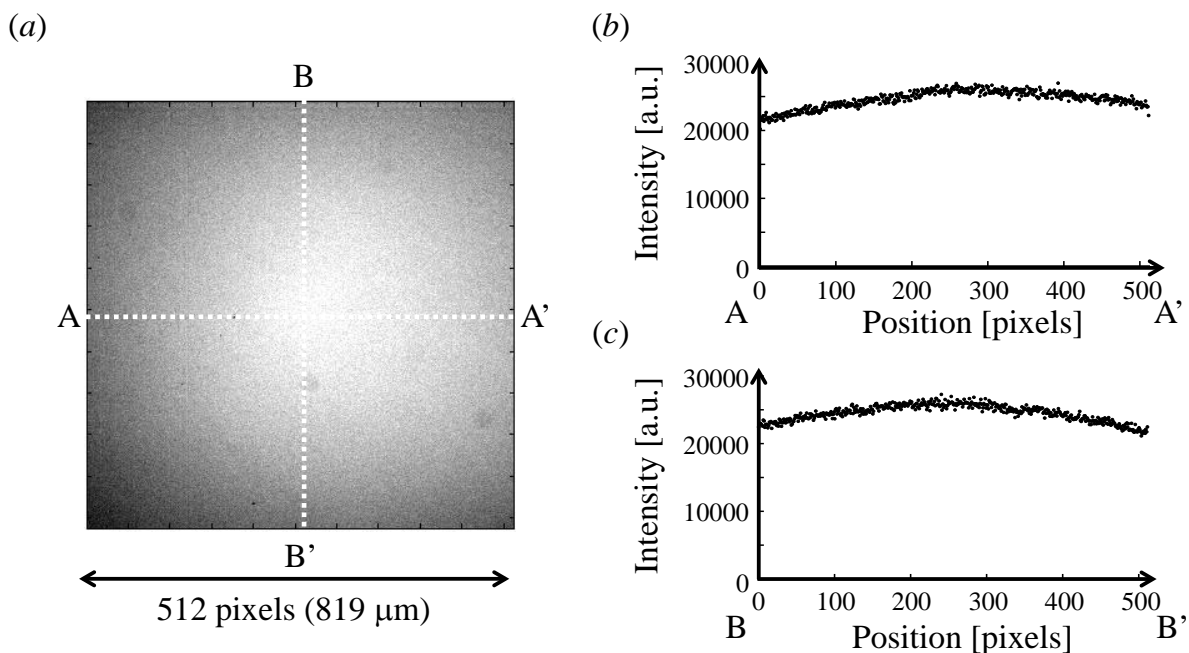


Figure 3.12. (a) An example of temporally-averaged Raman image obtained through HB filter. Intensity profiles of the Raman image (b) in the horizontal direction (A–A') and (c) in the vertical direction (B–B').

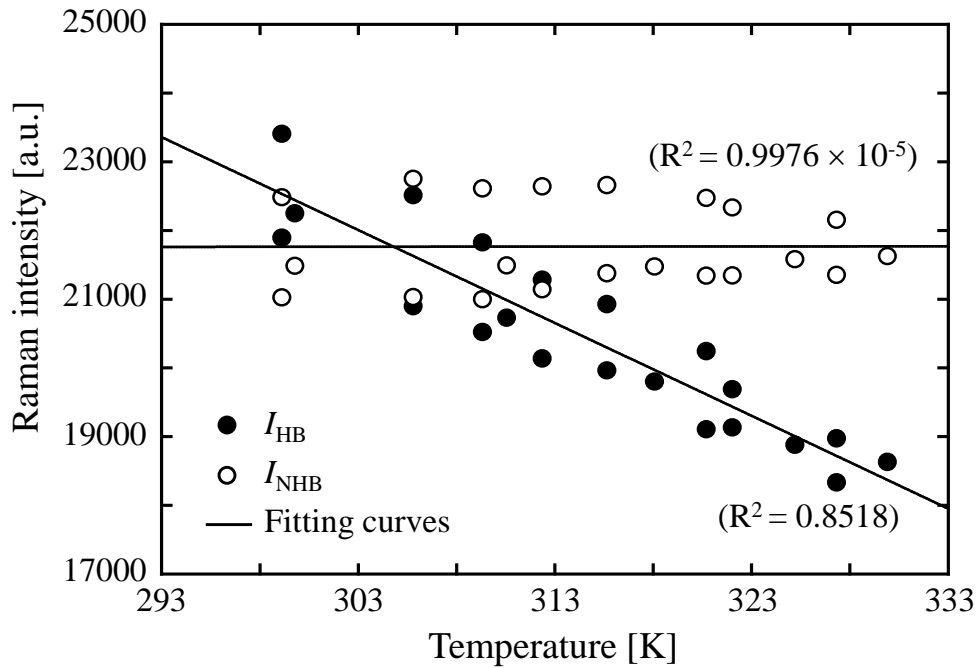


Figure 3.13. Relationship between the Raman intensities (I_{HB} , I_{NHB}) and the temperature.

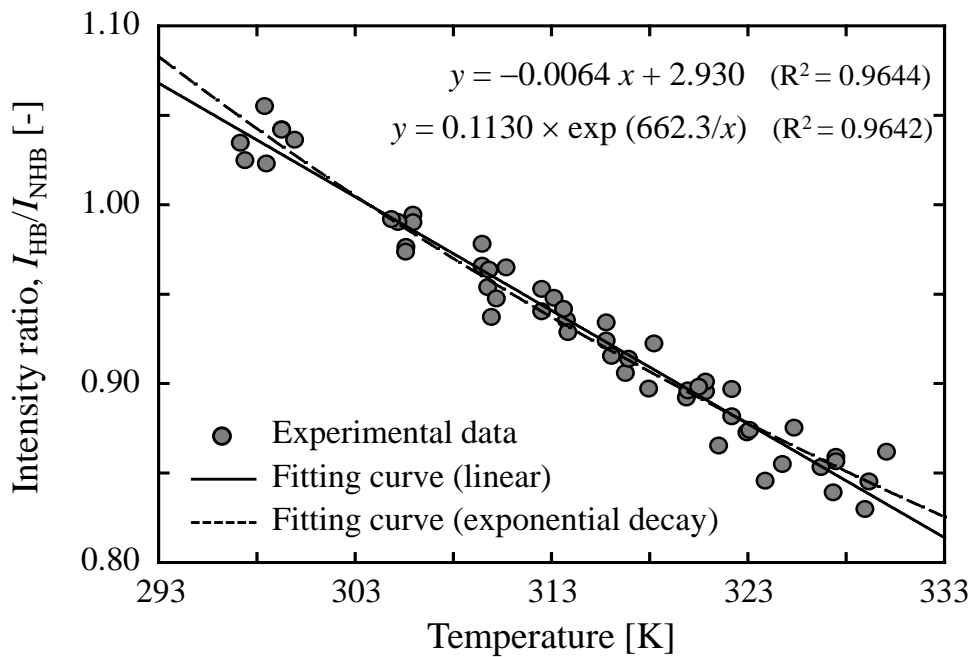


Figure 3.14. Relationship between the temperature and the Raman intensity ratio (I_{HB}/I_{NHB}).

Subsequently, a distribution of the intensity ratio ($I_{\text{HB}}/I_{\text{NHB}}$) was calculated from the temporally-averaged Raman images. The mean intensity ratio in the distribution is plotted against the temperature in figure 3.14. It is clearly observed that the mean intensity ratio decreases with increasing temperature in the range 293–333 K. Solid and dashed lines in figure 3.14 are the fitting curves obtained by least-squares regression analyses using linear and exponentially-decaying functions, respectively. Although the exponential-type fitting is considered to be more reasonable than the linear one according to equation (3.7), there is little difference (about 0.7%) between the two curves in the temperature range of this study. Hence, the present study employed the simple linear one (slope: -0.0064 ; intercept: 2.930 ; $R^2 = 0.9644$) as a calibration curve between the temperature and the intensity ratio in subsequent experiments, according to previous studies (Kim *et al.*, 2006; Ewinger *et al.*, 2013). The uncertainty associated with the regression was estimated to be 3.7 K at a 95% confidence level, and the temperature sensitivity was calculated to be approximately $-0.59\% \text{ K}^{-1}$.

3.3.2 Consideration for Temperature Uniformity and Stability

In this section, the temperature uniformity and stability in the I-shaped milli-channel used for the calibration experiment are investigated especially focusing on the heat dissipation and photothermal effect

First, the temperature decrease along the flow direction is estimated using thermocouples. In the present study, water was heated by a hotplate before it was introduced into a channel (as shown in figure 3.6), which is considered to result in the temperature decrease along the streamwise direction. Therefore, three thermocouples were arranged at intervals of 5 mm in an I-shaped milli-channel which was similar to that used in the calibration experiment. According to the measurement result, the temperature decay in the measurement area of $819 \times 819 \mu\text{m}^2$ was estimated. The maximum temperature decay in the streamwise direction was roughly calculated to be less than 0.3 K. In addition, the temporal fluctuation of the measured temperature was approximately $\pm 0.2 \text{ K}$ throughout the experiments.

Subsequently, the temperature increase in channel water caused by the absorption of the excitation laser beam, i.e., the influence of the photothermal effect, is investigated according to the theoretical treatment (Rose *et al.*, 1986; Vyas *et al.*, 1988). When a laser beam propagates in the z -direction through the medium which is flowing in the x -direction with velocity u [m/s], the temperature above the ambient, $T(x, y, t)$ [K], is given by the solution of the energy equation (equation (2.10)):

$$\frac{\partial T(x, y, t)}{\partial t} = \alpha \nabla^2 T(x, y, t) - u \frac{\partial T(x, y, t)}{\partial x} + \frac{1}{\rho C_p} Q(x, y, t) \quad (3.8)$$

where α is the thermal diffusivity [m^2/s], ρ is the fluid density [kg/m^3], and C_p [J/kg·K] is the

specific heat of the fluid at constant pressure. The two-dimensional differential equation implies that any inhomogeneity in the fluid along the laser beam is assumed to be negligible. The first, second, and third terms on the right-hand side of equation (3.8) represent the effects of thermal diffusion, fluid flow, and heating due to the laser absorption (i.e., source term which was neglected in equation (2.10)), respectively. Assuming that the flowing medium is weakly absorbing, the heat production, $Q(x, y, t)$ [$\text{J/s}\cdot\text{m}^3$], produced by the continuous-wave (CW) laser with a Gaussian spatial profile is written as,

$$Q(x, y, t) = \frac{2aP}{\pi r^2} \exp\left[-2(x^2 + y^2)/r^2\right] \quad (3.9)$$

where a [m^{-1}] is the absorption coefficient of the fluid, r [m] is a $1/e^2$ radius of the laser beam, and P [W] is the average power of the laser beam. The beam is set to be centered to be origin of the coordinate system, and turned on at $t = 0$.

The equation (3.8) has been solved in two dimensions assuming the boundary conditions:

$$\begin{aligned} T(x, y, t)|_{t=0} &= 0, & T'(x, y, t)|_{t=0} &= 0 \\ T(x, y, t)|_{x=\pm\infty} &= 0, & T(x, y, t)|_{y=\pm\infty} &= 0 \end{aligned} \quad (3.10)$$

where T' is the spatial gradient of the temperature. The solution of equation (3.8) is given by introducing the Green's function, G , as follows:

$$T(x, y, t) = \int_{-\infty}^{+\infty} \int_{-\infty}^{+\infty} \int_0^{\infty} Q(\zeta, \eta, \tau) G(x|\zeta; y|\eta; t|\tau) d\zeta d\eta d\tau \quad (3.11)$$

where functional form of $Q(\zeta, \eta, \tau)$ is given by equation (3.9). The Green's function satisfied the differential equation

$$-\alpha \nabla_{xy}^2 G + u \frac{\partial G}{\partial x} + \frac{\partial G}{\partial t} = \frac{1}{\rho C_p} \delta(x - \zeta) \delta(y - \eta) \delta(t - \tau) \quad (3.12)$$

with appropriate boundary conditions. According to the study by Rose *et al.* (1986), the Green's function for equation (3.12) can be expressed as,

$$\begin{aligned} G &= \frac{H_{\tau}(t)}{4\pi\rho C_p \alpha (t - \tau)} \exp\left(-\left\{x - [\zeta + u(t - \tau)]\right\}^2 / 4\alpha (t - \tau)\right) \\ &\times \exp\left[-(y - \eta)^2 / 4\alpha (t - \tau)\right] \end{aligned} \quad (3.13)$$

where $H_{\tau}(t)$ is the Heaviside unit step function. Since the Green's function is independent of the source term (equation (3.9)), the same function (equation (3.13)) is valid for any type of source function, e.g., a pulsed laser, a CW laser or a laser with elliptical Gaussian profile etc. Finally, substituting equations (3.9) and (3.13) into equation (3.11) leads to the result:

Table 3.2. Physical properties of water at $T = 298$ K

Density	ρ	[kg/m ³]	997
Specific heat	C_p	[J/kg·K]	4179.3
Thermal diffusivity	α	[m ² /s]	1.43×10^{-7}
Absorption coefficient	a	[m ⁻¹]	0.0196 (at 490 nm) 0.0507 (at 530 nm)

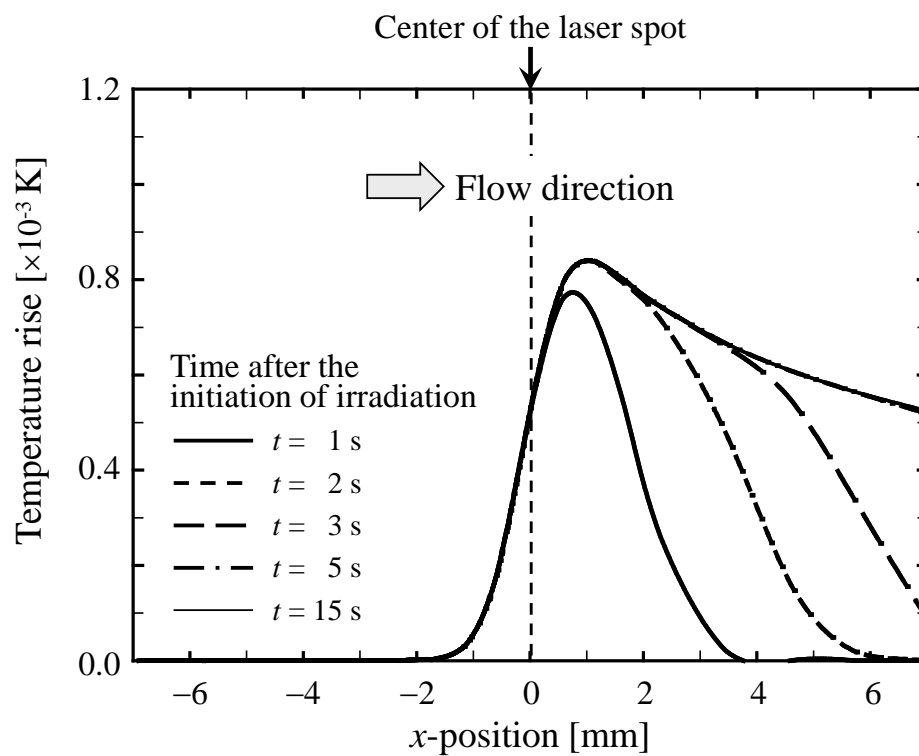


Figure 3.15. Temperature rise in a flowing pure water (bulk velocity: 2 mm/s) along the x -direction after the initiation of laser irradiation (wavelength: 532 nm, power: 240 mW, diameter: 2.3 mm). The chain line (of $t = 5$ s) and the fine line (of $t = 15$ s) are indistinctive in the figure.

$$T(x, y, t) = \frac{2aP}{\pi\rho C_p} \int_0^t \frac{1}{\left[r^2 + 8\alpha(t-\tau)\right]} \times \exp\left(-2\left\{\left[x-u(t-\tau)\right]^2 + y^2\right\}/\left[r^2 + 8\alpha(t-\tau)\right]\right) d\tau \quad (3.14)$$

where the integration over τ must be performed numerically.

Utilizing the above theoretical approach, the temperature rise produced by the photothermal effect was calculated based on the measurement conditions in section 3.3.1. The laser power and beam diameter was taken to be 240 mW, and 2.3 mm, respectively. The physical properties of water were as listed in table 3.2. The integration in equation (3.14) was performed by the method of 70-point Gaussian quadrature. The temporal evolution of the water temperature distribution at $y = 0$ is plotted along the flow direction (i.e., x -direction) in figure 3.15. The water temperature rise was calculated to be negligibly small ($< 1.0 \times 10^{-3}$ K), and it reached a quasi-steady state after 5 seconds. This is because water has an extremely low absorption coefficient of about 0.05 m^{-1} at 532 nm (Smith & Baker, 1981) and because the measurement was performed in the flow field (bulk velocity: 2.1 mm/s).

According to the above estimations, the non-uniformity and the instability of the temperature field in the calibration experiment is considered to be sufficiently small. This implies that the uncertainty of the temperature calibration (approximately 3.7 K) is attributed to the fluctuation of the illumination light or other causes rather than the temperature non-uniformity or instability.

3.3.3 Correction of Spatial Variance in Intensity Ratio

This section describes the correction procedure for spatial variance in intensity ratio. Figure 3.16(a) shows examples of Raman images of the two modes (I_{HB} and I_{NHB}) obtained at room temperature condition. These images offer a resolution of 64×64 binned pixels, since raw Raman images of 512×512 pixels were temporally averaged and spatially smoothed by binning of 8×8 pixels. Consequently, the area of the binned pixel corresponds to an area of $12.8 \times 12.8 \text{ }\mu\text{m}^2$. Despite the almost uniform temperature field, the Raman intensities in figure 3.16(a) significantly vary depending on the location due to the non-uniformity of the excitation intensity, I_0 . In order to eliminate this influence, the intensity ratio of the two images, I_{Ratio} , was calculated as explained in section 3.1.2 (from equations (3.6) and (3.7)):

$$I_{\text{Ratio}} = \frac{I_{\text{HB}}}{I_{\text{NHB}}} = \frac{K_{\text{HB}} \cdot I_0 \cdot \Omega \cdot \left(\frac{d\sigma}{d\Omega}\right)_{\text{HB}} \cdot l \cdot N_{\text{HB}}}{K_{\text{NHB}} \cdot I_0 \cdot \Omega \cdot \left(\frac{d\sigma}{d\Omega}\right)_{\text{NHB}} \cdot l \cdot N_{\text{NHB}}} = K_{\text{Ratio}} \cdot f(T) \quad (3.15)$$

where I_{HB} and I_{NHB} are the Raman intensities of HB and NHB modes, respectively, and the K_{Ratio} includes all the temperature-independent factors such as signal losses due to collection geometry. The resultant distribution is shown in the left-hand image of figure 3.16(b). It is

clearly seen that I_{Ratio} at room temperature still exhibits non-uniform distribution in the measurement area. The typical standard deviation of the intensity ratio within the measurement area was calculated to be 2.8%, which corresponds to 4.0 K according to the temperature sensitivity of the calibration curve (figure 3.14). The intensity ratios obtained at three different temperature conditions are also shown in Figure 3.16(c). They seem to have similar distributions irrespective of the water temperature, which indicates that the spatial variance in I_{Ratio} is attributed to the temperature-independent factor included in K_{Ratio} .

In order to reduce the measurement error due to the non-uniform distribution of I_{Ratio} , its spatial distribution is corrected by the following procedure. The distribution of the intensity ratio obtained at room temperature (left-hand side of figure 3.16(b)) is selected for a reference image ($I_{\text{Ratio,ref}}$), and the mean value of the intensity ratio ($\langle I_{\text{Ratio,ref}} \rangle$) is calculated. Assuming that the temperature field is perfectly homogeneous, i.e., the spatial variance in I_{Ratio} arises only from K_{Ratio} , a corrective image, I_c , is prepared as follows:

$$I_c = \frac{\langle I_{\text{Ratio,ref}} \rangle}{I_{\text{Ratio,ref}}} = \frac{\langle K_{\text{Ratio}} \rangle \cdot f(T_{\text{ref}})}{K_{\text{Ratio}} \cdot f(T_{\text{ref}})} = \frac{\langle K_{\text{Ratio}} \rangle}{K_{\text{Ratio}}} \quad (3.16)$$

The right-hand side of figure 3.16(b) shows the distribution of I_c calculated from I_{Ratio} at room temperature (left-hand side of figure 3.16(b)). By multiplying the intensity ratio at each temperature (I_{Ratio}) by this corrective image (I_c), the spatial distribution in K_{Ratio} can be compensated:

$$I_{\text{Ratio}}^* = I_{\text{Ratio}} \cdot I_c = K_{\text{Ratio}} \cdot f(T) \cdot \frac{\langle K_{\text{Ratio}} \rangle}{K_{\text{Ratio}}} = \langle K_{\text{Ratio}} \rangle \cdot f(T) \quad (3.17)$$

Applying the above procedure, the distributions of the intensity ratio were converted into the corrected intensity ratio (I_{Ratio}^*) as shown in figure 3.16(d). The distributions in figure 3.16(d) clearly exhibit the improvement in the spatial uniformity compared to those in figure 3.16(c). The spatial variance was considerably reduced to 0.65% (corresponding to 0.9 K) after the correction. According to these results, above correction procedure is employed for the calculation of planar temperature distribution in the following experiments.

There may be some system-related cause for the non-uniformity in I_{Ratio} (or K_{Ratio}), but it has not been experimentally ascertained. It should be emphasized that the switch of optical filters (HB to NHB filters) did not cause difference in the image location between HB and NHB Raman images. As detailed in section 3.2.2, HB and NHB images were captured through different bandpass filters with different substrate thickness (HB: 3.5 mm, NHB: 2.0 mm) and transmission ranges (HB: 634–648 nm, NHB: 649–668 nm). However, there was no detectable difference in image location due to these differences, which was experimentally confirmed by comparing the positions of fluorescent particles scattered on a glass slide whose fluorescent images were captured through HB and NHB filters.

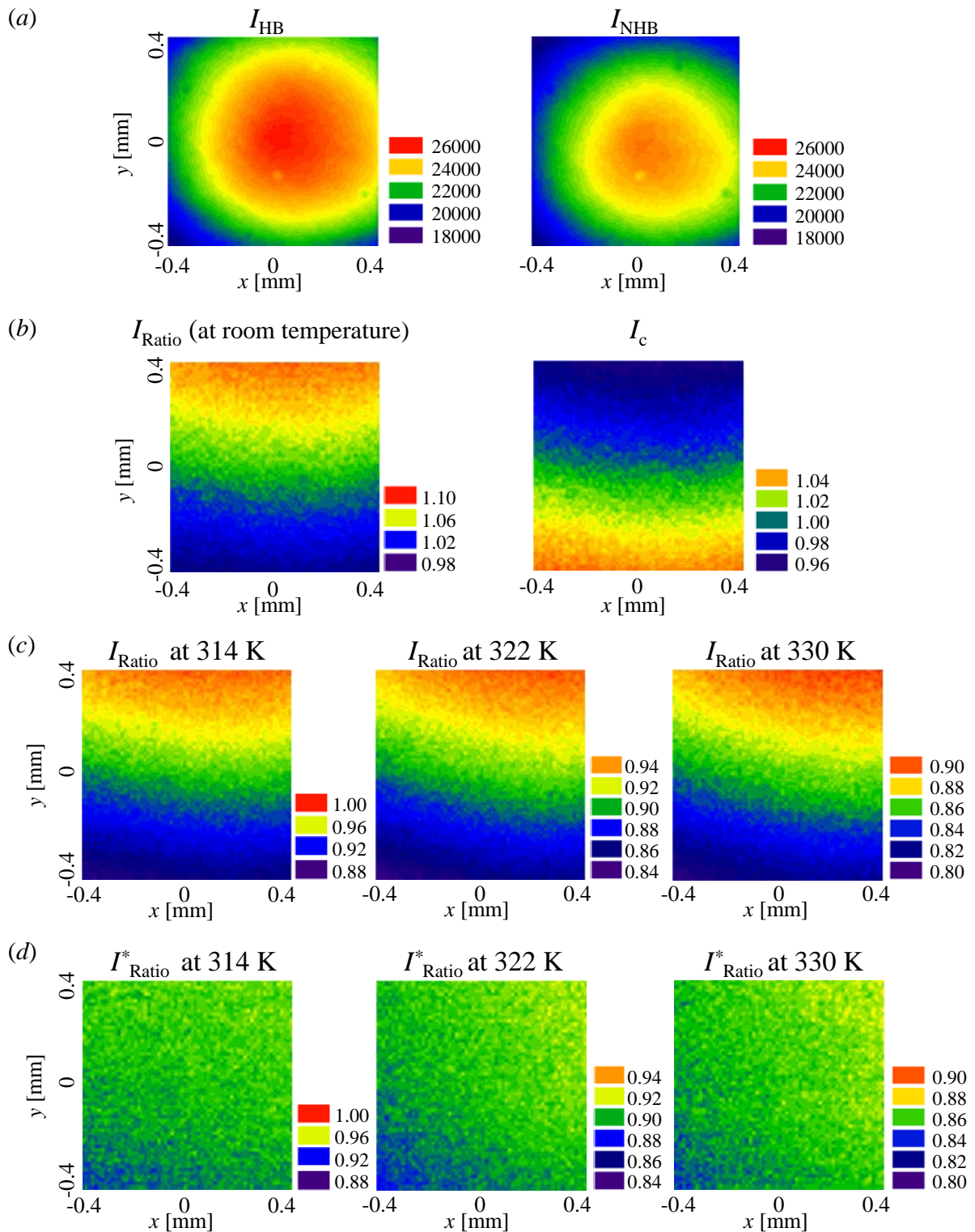


Figure 3.16. (a) Typical Raman images for HB and NHB modes captured at room temperature. (b) Distribution of the intensity ratio (I_{Ratio}) calculated from the HB and NHB images (left-hand side), and the distribution of I_c prepared for the correction (right-hand side). (c) Distributions of I_{Ratio} at different temperature conditions (before correction) and (d) the distributions of I_{Ratio}^* at different temperature conditions (after correction).

3.4 Visualization of Steady-State Temperature Distributions

The temperature distribution in a mixing flow field was visualized using the present measurement technique by applying the calibration curve (a solid straight line in figure 3.14). A non-uniform temperature distribution was realized in the junction area of a T-shaped channel (in figure 3.17) by flowing water at different temperatures from the two inlets. Water at room temperature and water heated on the hotplate were injected at a flow rate of 1 mL/min from inlets A and B, respectively. The Reynolds number ($Re = UL/\nu$) and the thermal Peclet number ($Pe_T = UL/\alpha$) were calculated to be of 7.5 and 46.6, respectively, according to the definition in section 2.1. These relatively large values indicate that the convective heat transport dominated the thermal flow field in this experimental condition. In the above calculations, the equivalent hydraulic diameter of the channel $D_h = 3.2 \text{ mm}$ ($= 4A/S$) was selected as the characteristic length L , and the bulk velocity $U_{\text{bulk}} = 2.1 \text{ mm/s}$ ($= Q/A$) was used as the characteristic velocity U , where A is the cross-sectional area [m^2], S is the wetted perimeter [m], and Q is the flow rate [m^3/s]. Measurements were performed for three different hotplate temperatures, T_{hotplate} , of 323, 343, and 363 K. Raman images were obtained over the measurement area of $819 \times 819 \mu\text{m}^2$, as shown in figure 3.17(a). The data acquisition conditions were set to be the same as those of the calibration experiment.

Figure 3.18 shows the measurement results. They quantitatively visualize the non-uniform temperature distributions at the junction area at spatial resolution of $12.8 \times 12.8 \mu\text{m}^2$ based on averaging over 8×8 pixels. Although the spatial resolution can be improved by using an objective lens with higher magnification, the $\times 10$ objective was selected in this study to obtain a sufficiently large measurement area in our millimeter-scale channel. It is

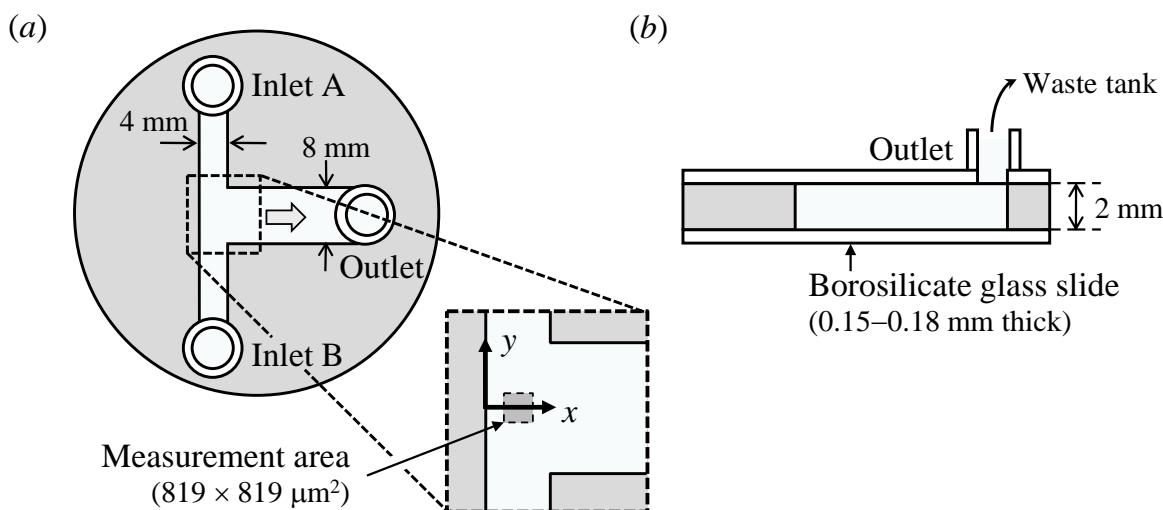


Figure 3.17. (a) Top and (b) cross-sectional views of a T-shaped milli-channel.

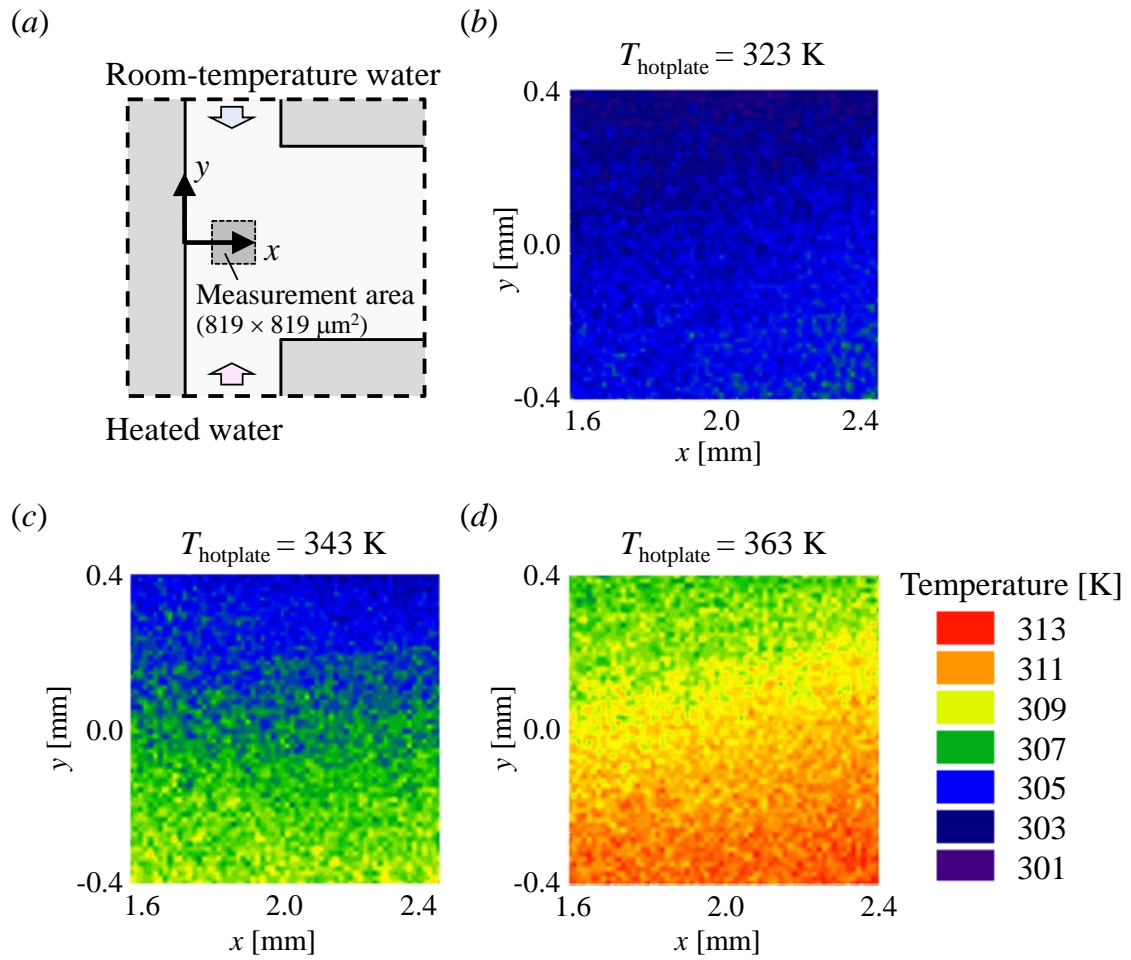


Figure 3.18. (a) Measurement area positioned at the junction of the T-shaped milli-channel. (b)–(d) temperature distributions obtained with three different heating condition (T_{hotplate}). The spatial resolution was calculated to be $12.8 \times 12.8 \mu\text{m}^2$ based on averaging over 8×8 pixels.

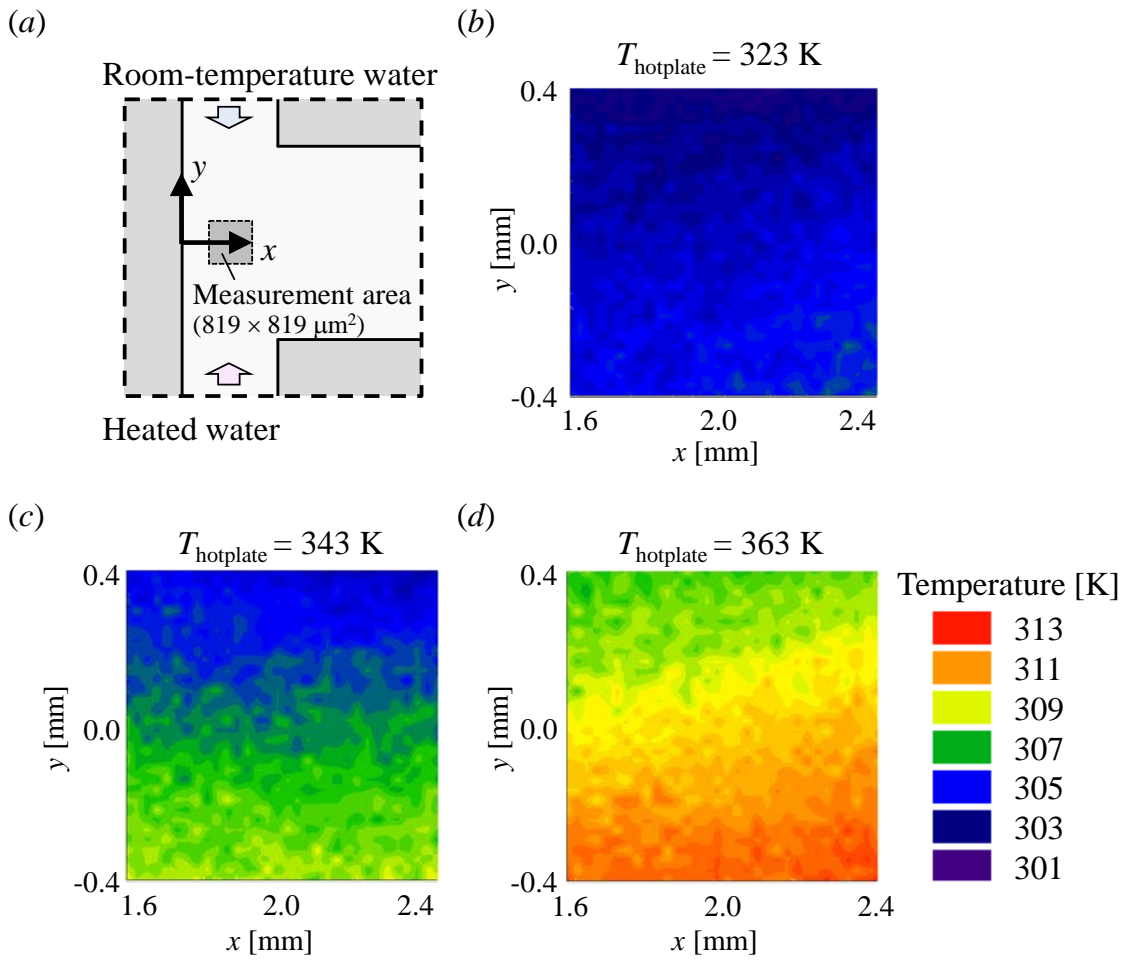


Figure 3.19. (a) Measurement area positioned at the junction of the T-shaped milli-channel. (b)–(d) temperature distributions obtained with three different heating condition (T_{hotplate}). These temperature maps are calculated from the same Raman images used in figure 3.18, but visualized at spatial resolution of $25.6 \times 25.6 \mu\text{m}^2$ based on averaging over 16×16 pixels.

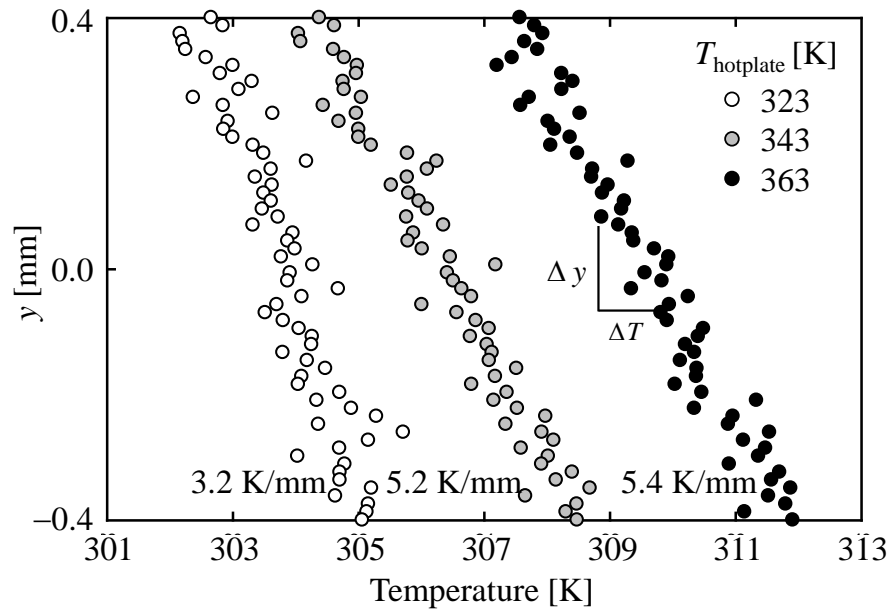


Figure 3.20. Temperature distributions at $x = 2.0$ mm plotted along the y -direction for three different T_{hotplate} . The temperature gradient for each condition is indicated in the figure. (These data are calculated from the result in figure 3.18).

observed from figure 3.18 that hot water from inlet B flowed into the junction and increased the temperature of the upper side of the measurement area. In addition, the overall temperature increased with increasing T_{hotplate} . These temperature maps exhibit rather ‘spotty’ patterns containing unnaturally high or low temperature data over the whole measurement area. These spotty distributions are due to the measurement error (arising from shot noise, for example) and can be smoothed by increasing the binning factor for spatial averaging. Figure 3.19 gives the measurement result, which are calculated from the same Raman images used in figure 3.18 and visualized at spatial resolution of $25.6 \times 25.6 \mu\text{m}^2$ based on integrating 16×16 pixels. These maps display less spotty patterns compared to those in figure 3.18. The standard deviation of the measured temperature within the measurement area was typically 0.9 K for 8×8 pixels binning, and 0.7 K for 16×16 pixels binning, under a uniform temperature condition.

In order to obtain further insight into the temperature distributions, the measurement result at $x = 2.0$ mm (in figure 3.18) was plotted against the position in the y -direction (see figure 3.20). Each data point represents the temperature which is spatially averaged within an area of $51.2 \mu\text{m}$ around $x = 2.0$ mm. The results show that there is a temperature gradient in the y -direction due to merging of fluids at different temperatures. Figure 3.20 also indicates the average temperature gradient for each condition. The measured temperature gradient increased with increasing T_{hotplate} , which suggests that the present technique is effective for measuring temperature distributions.

3.5 Concluding Remarks

A non-intrusive planar temperature measurement technique was developed based on spontaneous Raman imaging utilizing optical bandpass filters and an EM-CCD camera. Raman scattering arising from OH stretching vibration of liquid H₂O molecule was used to determine the local temperature in channel flow. In order to compensate the influence of non-uniform excitation intensity, the ratiometric procedure was employed where the intensity ratio of two Raman images were calculated for temperature visualization.

Water Raman spectra were measured at various temperatures and the spectral change of the OH stretching vibrational band (in 3000–3800 cm⁻¹) was examined in detail. The contrasting temperature dependencies were observed above and below the isosbestic point (3460 cm⁻¹), which could be explained in terms of the chemical equilibrium between the cluster (or hydrogen-bonded: HB) and monomeric (or non-hydrogen-bonded: NHB) states of H₂O molecules. The spectral regions of 3000–3460 cm⁻¹ and 3460–3800 cm⁻¹ were termed HB and NHB modes, respectively, and bandpass filters which transmit only the wavelength range of HB or NHB modes were carefully selected.

A calibration experiment was conducted in order to quantify the relationship between the water temperature and the Raman intensity. The Raman images of HB and NHB modes were separately captured through the corresponding filters, and the intensity ratio of HB to NHB images was calculated at each temperature. The intensity ratio decreased with increasing temperature in the range 293–333 K with temperature sensitivity of approximately -0.59% K⁻¹. The linear least-squares regression gave a calibration curve with an uncertainty of 3.7 K at a 95% confidence level. The major advantage of considering the ratio of HB to NHB images is that the influence of the spatial non-uniformity in excitation intensity is cancelled out, i.e., two-dimensional temperature measurement can be realized for any excitation intensity profile. At the same time, it is noted that the procedure is only applicable to steady-state temperature fields, since the present system requires manual switching of the filters and repetition of image acquisition.

Finally, temperature distribution measurements were performed at the junction of a T-shaped milli-channel where warm water and room-temperature water mixed. By applying the calibration curve, non-uniform temperature distributions were quantitatively visualized at a spatial resolution of 12.8 × 12.8 μm² (based on averaging per 8 × 8 pixels), and 25.6 × 25.6 μm² (based on averaging per 16 × 16 pixels) with total acquisition time of approximately 30 s. A temperature gradient was clearly observed for each heating condition, which implies that the proposed technique is effective for measuring temperature distributions with micron resolution.

Chapter 4

Visualization of Transient Temperature Distribution by Two-Wavelength Raman Imaging Technique

This chapter describes the development of two-wavelength Raman imaging technique which realizes simultaneous detection of two different vibrational Raman signals, and assess its applicability for non-intrusive and two-dimensional monitoring of transient temperature distributions. The measurement principle is based on the chemical equilibrium between hydrogen-bonded (HB) and non-hydrogen-bonded (NHB) OH stretching motions of water molecules, as already explained in chapter 3. Raman images of HB and NHB modes are simultaneously acquired using the developed imaging system and the planar temperature distribution is determined for each instant of time from the intensity ratio of these images.

4.1 Temperature Measurement by Two-Wavelength Raman Imaging

In chapter 3, water temperature measurements were realized based on direct Raman imaging technique by using a single camera and two different optical filters (see figure 3.5). Using the system shown in figure 3.6, water Raman images of HB and NHB modes were successively obtained through the selected filters, and the temperature distribution was visualized from the intensity ratio of these two images. However, this methodology cannot be applied for measurements of unsteady temperature fields since it would require temporal switching of the optical filters manually and thus could not acquire the intensity ratio instantaneously. Moreover, it can be easily affected by instantaneous laser beam fluctuations, which might

have contributed to the large uncertainty (about 3.7 K) in temperature calibration.

In order to overcome these problems and realize transient measurements of planar temperature distributions, a two-wavelength Raman imaging system is developed. Figure 4.1 illustrates a concept of the imaging system, which is comprised of a half mirror, two different optical filters and two EM-CCD cameras. By using this optical system, Raman signal arising from water is divided into two paths, spectrally filtered by the filters which transmit the desired signals (HB or NHB modes) and simultaneously detected by the two cameras. The theory and the procedure for temperature determination are essentially the same as those described in section 3.1. The ratio of the simultaneously detected intensities, I_{Ratio} , can be written as a function of temperature (from equations (3.6) and (3.7)):

$$I_{\text{Ratio}} = \frac{I_{\text{HB}}}{I_{\text{NHB}}} = \frac{K_{\text{HB}} \cdot I_0 \cdot \Omega \cdot \left(\frac{d\sigma}{d\Omega}\right)_{\text{HB}} \cdot l \cdot N_{\text{HB}}}{K_{\text{NHB}} \cdot I_0 \cdot \Omega \cdot \left(\frac{d\sigma}{d\Omega}\right)_{\text{NHB}} \cdot l \cdot N_{\text{NHB}}} = K_{\text{Ratio}} \cdot A \exp\left(\frac{B}{T}\right) \quad (4.1)$$

where I_0 [photons/s · m²] is the excitation intensity, Ω [sr] is the solid angle of signal detection, $d\sigma/d\Omega$ [cm²/molecule · sr] is the absolute differential Raman cross-section, l [m] is the length of the probe volume, and N_i [molecules/m³] is the number density of i -species molecules. The constant K_{Ratio} includes all the temperature-independent factors such as transmission of the optical components and collection efficiency of the detector. As explained in section 3.3.3, the inhomogeneous distribution of K_{Ratio} can be compensated by calculating the corrected intensity ratio I_{Ratio}^* using a reference image. Since the volume illumination is employed for excitation, the resultant temperature distribution represents the temperature information averaged over the whole channel height, as described in section 3.1.2.

The most important advantage of considering intensity ratios of simultaneously-acquired images is that not only the spatial non-uniformity but also the temporal fluctuation of the excitation light can be compensated. The methodology described here is considered to be also effective for compensating the pulse-to-pulse fluctuation of the excitation intensity in the case of using a pulsed laser for Raman imaging.

4.2 Measurement System

This section covers the development of the measurement system of two-wavelength Raman imaging. Most components (such as the illumination system, channel configuration, and heating system) are the same as those used in chapter 3. Therefore, this section mainly focuses on the newly-developed setup for simultaneous imaging of Raman signals with different wavelengths, and the procedure for the registration of two cameras.

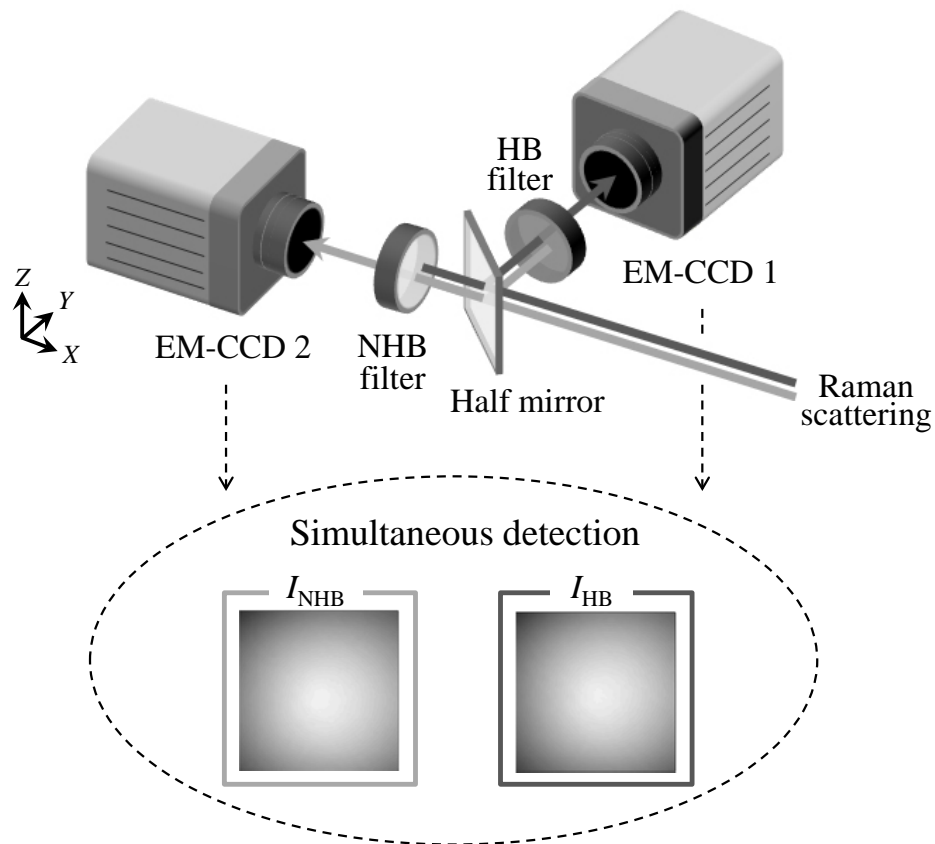


Figure 4.1. Conceptual diagram of the two-wavelength Raman imaging system, which is comprised of a half mirror, two optical filters and two cameras for simultaneous detection of Raman images of different wavelengths.

4.2.1 Experimental Apparatus

Figure 4.2 shows a schematic of the experimental setup. This setup is nearly identical to that developed for steady-state temperature measurement in chapter 3 (as shown in figure 3.6) except for an additional EM-CCD camera and additional optical components for two-wavelength Raman imaging. An unfocused laser beam at 532 nm was introduced into a water-filled milli-channel positioned on a microscope stage and Raman scattering arising from the irradiated water was collected by an objective lens. The nominal power at the laser head was set at 400 mW, which resulted in decaying to 380 mW at the sample stage with an ellipsoidal spot (major axis: 3.4 mm, minor axis: 2.8 mm). To prevent the excitation light from directly entering the objective lens and damaging the detector, the beam was delivered at an incident angle of 42° . Raman scattering, passing through a dichroic mirror and an

achromatic lens ($f = 50$ mm, diameter: 25 mm), was split into two optical paths by a half mirror and recorded by two EM-CCD cameras. Each camera was equipped with an optical filter, which was selected for HB or NHB modes in order to ensure the detection of only the desired Raman signals for temperature measurement. The characteristics of the filters are detailed in section 3.2.2. This setup resulted in a total magnification of 10.6, which translates to a whole imaging area of $773 \times 773 \mu\text{m}^2$ captured by the above EM-CCD cameras. The excitation laser spot is considered to be large enough to provide adequate signal quality even at the circumference of the imaging area. (The intensity at the corner of the area was typically more than 80% of that at the central region.) Therefore, the whole imaging area of $773 \times 773 \mu\text{m}^2$ was used for temperature measurement.

Also the configuration and fabrication process of the channel were same as those described in section 3.2.1. For controlling the water temperature, a channel inlet was connected to a syringe pump (KD scientific Inc., Legato 210P) and water heated on a hotplate was introduced. T-typed thermocouples with diameter of $76 \mu\text{m}$ were inserted into the channel and the water temperature was recorded by a data logger (Keyence Corp., NR-1000) at sampling rate of 5 Hz. The data logger was synchronized with the two EM-CCD cameras by a pulse generator (Quantum Composers Inc., 9618+).

4.2.2 Two-Wavelength Imaging System

This section details the arrangement of the key components for two-wavelength Raman imaging. In order to provide a HB or NHB Raman image on each camera, a relay system which can split and filter the light from the microscope is necessary. In addition, it is required to completely cover the light path between the microscope port and each camera to avoid signal degradation by external noise. In the present study, a relay lens system shown in figure 4.3 was constructed by utilizing commercially available C-mount compatible components (Edmund Optics Inc.) such as lens holder, mirror holder and two filter holders. These components have threaded rings or holes which can be used to secure them to each other or to C-Mount compatible systems (e.g., EM-CCD cameras used in this study). The achromatic lens ($f = 50$ mm, diameter: 25 mm), half mirror ($35 \times 35 \times 1$ mm) and two bandpass filters (ϕ $25 \text{ mm} \times 5 \text{ mm}$) were installed into them as illustrated in figure 4.3. The lens holder and filter holders are tube-shaped component with outer diameter of 30 mm, and equipped with length-adjusting barrels. By adjusting the length of these barrels, the optical path length leading to the two cameras were set to be identical so that the cameras had identical magnification.

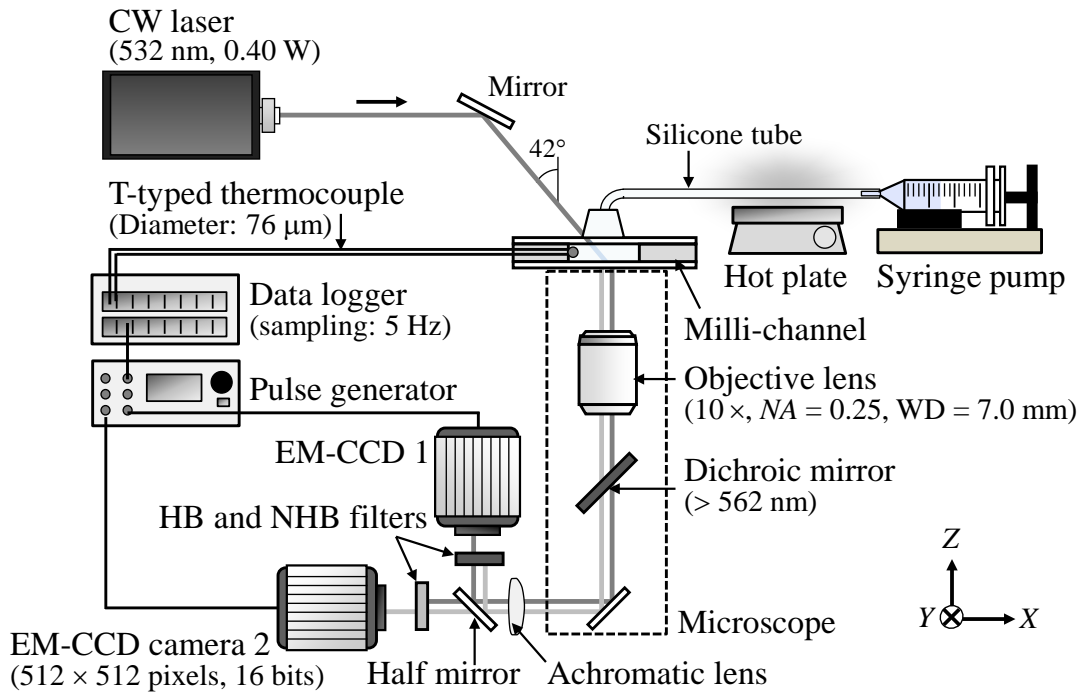
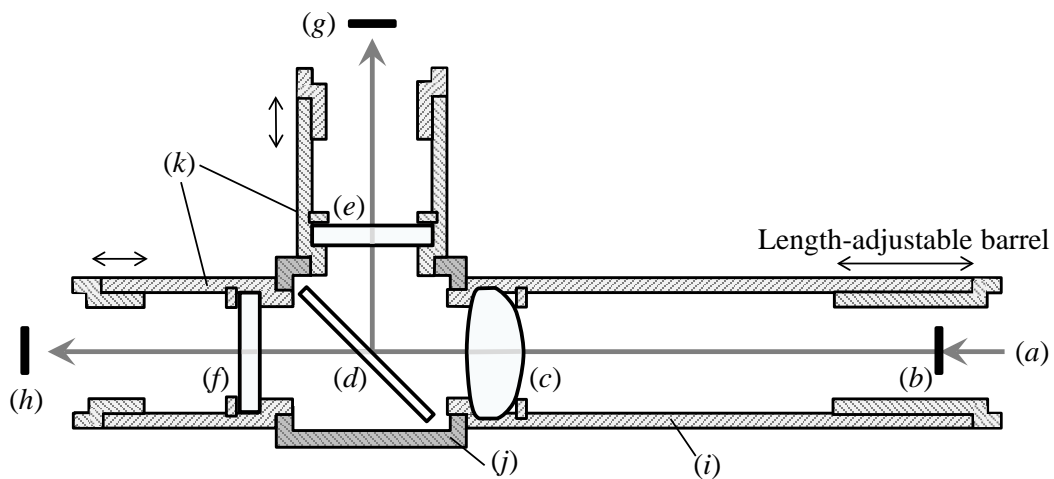


Figure 4.2. Schematic of the experimental apparatus for temperature measurement by two-wavelength Raman imaging.



- (a) Scattered light
- (b) Image plane of microscope
- (c) Achromatic lens
- (d) Half mirror
- (e) HB filter
- (f) NHB filter
- (g) Image plane of EM-CCD camera 1
- (h) Image plane of EM-CCD camera 2
- (i) Lens holder with adjustable barrel
- (j) Half mirror holder
- (k) Filter holder with adjustable barrel

Figure 4.3. Arrangement of the components in two-wavelength Raman imaging system.

4.2.3 Image Registration Procedure

A calibration of the image coordinates of the two cameras was required prior to the experiments, because the two-wavelength methodology requires calculations of the Raman intensity ratio pixel-by-pixel for planar temperature determination according to equation (4.1). For this purpose, a glass plate with a grid pattern (line width: 10 μm , spacing: 100 μm) was used as a calibration target. In temperature measurements, the focal plane of the objective lens was set at the center of the milli-channel in the depthwise direction, as illustrated in figure 4.4(a). Therefore a channel with half the height was prepared for image registration using the glass plate (figure 4.4(b)), in order to position the grid pattern at the same focal plane as subsequent experiments.

Using this calibration channel, the orientation of the cameras was manually adjusted so that the two cameras had nearly identical measurement area and magnification. Besides the above mechanical procedure, image processing was employed to precisely register the images detected by two cameras relative to one another. Figure 4.5 illustrates the present registration methodology. First, the images of the grid pattern were captured simultaneously by two cameras via LED illumination (figure 4.5(a)) and then intersections of the grid lines were extracted as reference points (figure 4.6(b)). The coordinates of each image plane was calibrated to one another using the linear transformation (also called affine transformation), which can describe image deformations including scaling, rotation, shear, translation and reflection. The transformation can be expressed by using so-called homogeneous coordinates and matrix notation as:

$$\begin{bmatrix} x'_n & y'_n & 1 \end{bmatrix} = \begin{bmatrix} x_n & y_n & 1 \end{bmatrix} \begin{bmatrix} a & b & 0 \\ c & d & 0 \\ e & f & 1 \end{bmatrix} \quad (4.2)$$

where (x_n, y_n) is the position of the n -th reference point in image I and (x'_n, y'_n) is the position of the corresponding point in image II (Dreier *et al.*, 2000; Russ, 2007). Equation (4.2) can be rewritten by,

$$\begin{aligned} x'_n &= ax_n + cy_n + e \\ y'_n &= bx_n + dy_n + f \end{aligned} \quad (4.3)$$

From these equations, it is obvious that the a, b, c, d terms are the stretching and rotation coefficient, and the e and f terms are the translation shift values. By substituting the positions of the reference points (figure 4.5(b)) into equation (4.2), the affine matrix with the six coefficients can be obtained. Figure 4.5(c) shows an example of result of this registration methodology applied to the images in figure 4.5(a). The difference in positions between the intersection points in image I and those in transformed image II was calculated to be within

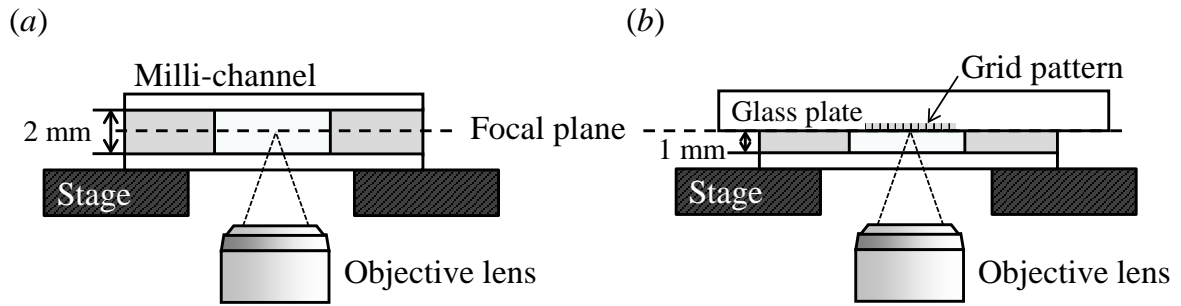


Figure 4.4. Schematics of (a) the focal position of the objective lens in temperature measurements and (b) the position of the glass plate used for camera calibration.

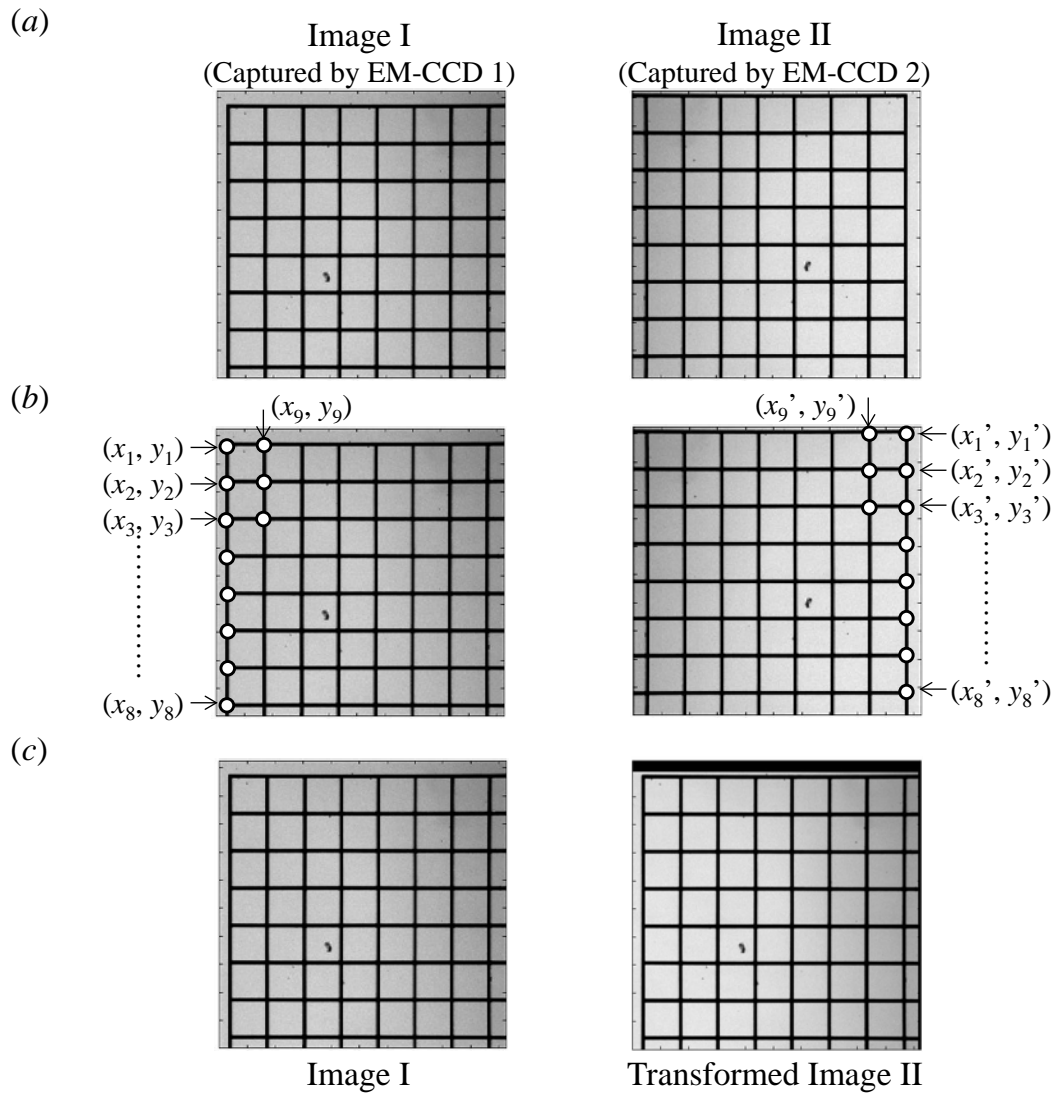


Figure 4.5. Schematics of the image registration procedure. (a) Images of the grid pattern captured by two different cameras, (b) extraction of the intersections as reference points, and (c) the result of linear transformation.

1 pixel, which approximately corresponds to 1.5 μm in the object plane. This result shows the good spatial correspondence between the two images. Utilizing the obtained affine matrix as a mapping function, the HB and NHB Raman images were registered to one another in temperature determination.

Since the affine transformation cannot produce curvature or twisting, a more elaborate calibration methodology using non-linear terms should be employed when the image distortion is non-negligible (Russ, 2007; Soloff *et al.*, 1997).

4.3 Calibration Experiment for Two-Wavelength Raman Imaging

In order to correlate the temperature and the Raman intensity ratio, a calibration experiment was performed under uniform temperature conditions in the central region of an I-shaped milli-channel (figure 4.6). The exposure time, frame interval and EM-gain of the cameras were set at 500 ms, 550 ms, and 330, respectively, and 30 images were collected and temporally averaged for each measurement. The input photon number was estimated to be around 200 from the typical intensity of 10000 counts. In order to insure the stability of the temperature field during measurements, the flow rate was maintained at 2 mL/min, which is equivalent to Reynolds number of 7.5. Figure 4.7 shows the intensity values of HB and NHB modes at each temperature acquired simultaneously by the two cameras (50 data points for each mode). Every data point indicates the averaged value over 456×456 pixels ($688 \times 688 \mu\text{m}^2$) in a temporally-averaged Raman image of each mode and straight lines are obtained by least-square regressions. Although figure 4.7 displays considerable variation in intensity, it can be observed that I_{HB} tends to decrease with temperature and that I_{NHB} tends to increase in contrast. These contrasting temperature dependencies are consistent with the spectral measurement result (figures 3.2 and 3.10), which implies the possibility of temperature measurements by two-wavelength Raman imaging through the filters shown in figure 3.9. The standard error of estimate in the regressions were 3.9% for I_{HB} and 4.6% for I_{NHB} , and these were mainly attributed to variation in intensity and beam position of excitation light.

Subsequently, the ratio of I_{HB} to I_{NHB} images was calculated for each pair of individual measurement. The correction procedure described in section 3.3.3 was also employed here in order to compensate the variance in intensity ratio arising from the distribution of K_{Ratio} (in equation (4.1)), i.e., the corrected intensity ratio I_{Ratio}^* was calculated from I_{Ratio} using a reference image. The mean value in each I_{Ratio}^* image was plotted against the temperature in figure 4.8. The mean intensity ratio decreases with temperature in the range of 293–343K and linear least-squares fit gives a solid line (slope: -0.0056 , intercept: 2.631, R^2 : 0.9961). It is

obvious that the Raman intensity ratio in figure 4.8 exhibits a notable improvement in scattering compared to the raw intensity values in figure 4.7. The standard error of estimate in the regression was decreased to approximately 0.5%, which indicates that the intensity variation due to the laser fluctuations could be effectively compensated by this ratiometric approach through equation (4.1). This result clearly demonstrates the advantage of the two-wavelength Raman imaging technique.

In the present set of experiments, 4×4 pixels were integrated by software binning in each distribution of I_{Ratio}^* for temperature visualization. Thus, for the measurement area of 456×456 pixels, a smoothed image with 114×114 binned pixels was created. The error bar which are shown for each point in figure 4.8 indicates the standard deviation of the intensity ratio in each smoothed image with 114×114 binned pixels. A typical value for the standard deviation was 8.15×10^{-3} , which approximately corresponds to 1.46 K in temperature according to the slope of the linear fitting (-0.0056). It is noted that the standard deviation decreased with increasing the binning factor (i.e., the number of pixels integrated for spatial averaging). For example, it was typically 15.2×10^{-3} (corresponds to 2.72 K) for 2×2 pixels binning and 2.55×10^{-3} (corresponds to 0.46 K) for 16×16 pixels binning.

Since the size of the error bar was almost constant for the whole temperature range, the above regression analysis was carried out in unweighted manner. Although a nonlinear fitting curve using an exponential function (a dashed line in figure 4.8) is expected to provide reasonable prediction in a broader temperature range according to equation (4.1), little difference (about 0.9%) was found between the linear and nonlinear fits in the temperature range of this study. The solid straight line in figure 4.8 was therefore used as the calibration curve in subsequent temperature imaging, as is the case in chapter 3. The uncertainty associated with the linear regression was estimated to be 1.43 K at a 95% confidence level, and the temperature sensitivity was calculated to be approximately $-0.58\% \text{ K}^{-1}$, which was nearly identical to that reported in section 3.3.1.

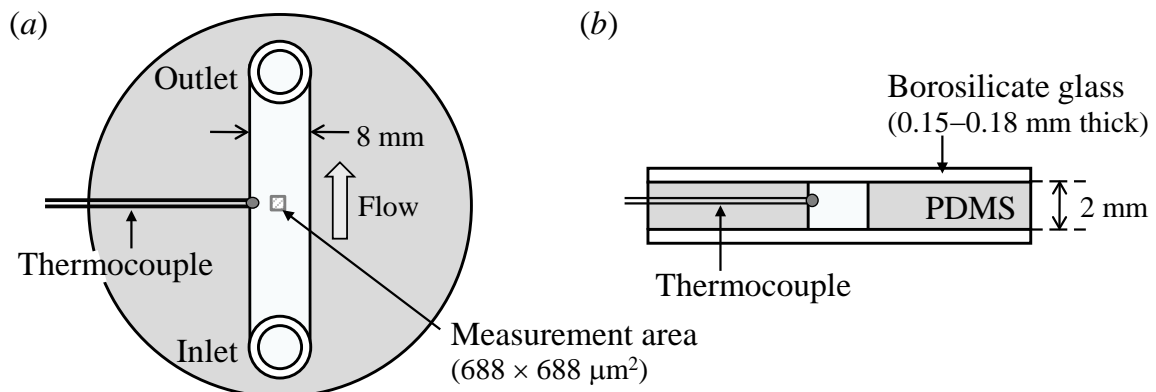


Figure 4.6. (a) Top and (b) cross-sectional views of an I-shaped milli-channel used for calibration experiment.

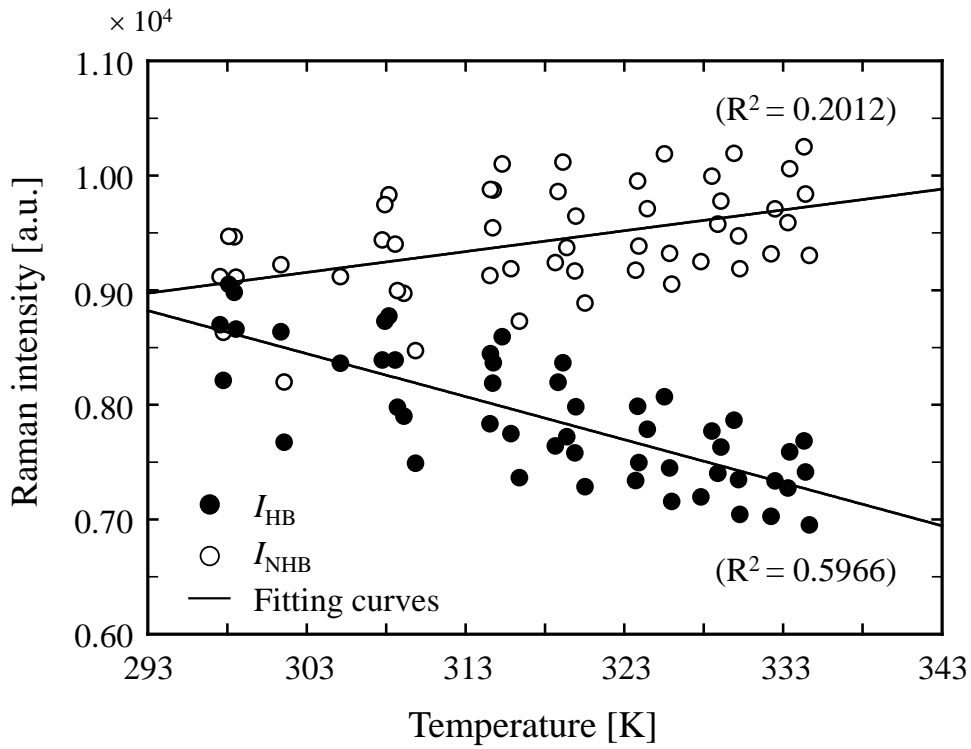


Figure 4.7. Relationship between the temperature and the Raman intensities of HB and NHB modes.

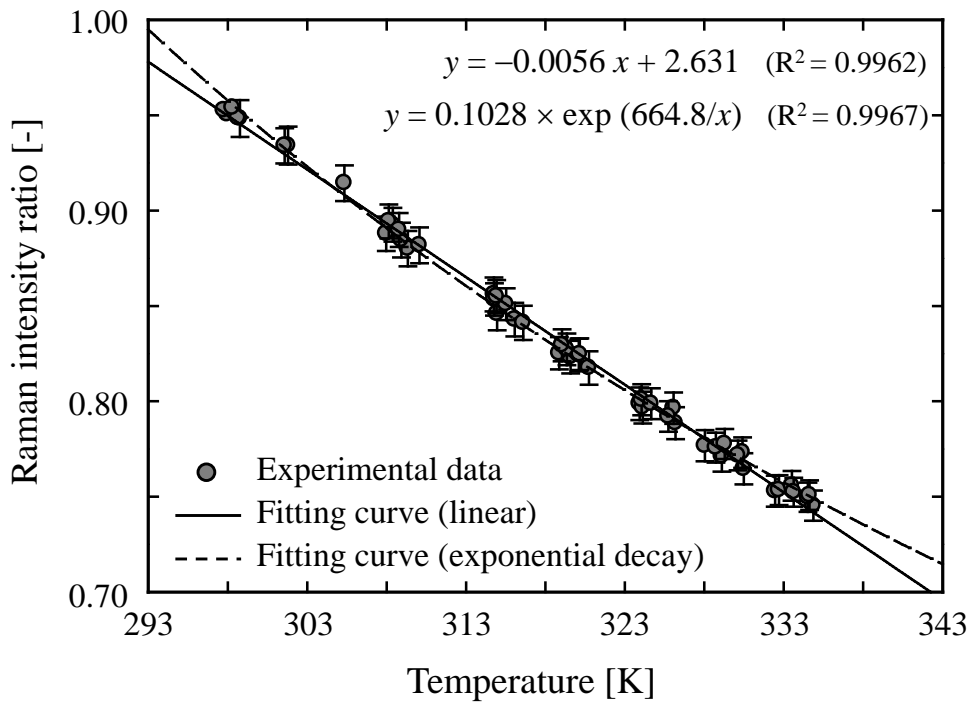


Figure 4.8. Relationship between the temperature and Raman intensity ratio.

4.4 Visualization of Transient Temperature Distributions

Using the above calibration result, two-wavelength Raman imaging was performed to measure the unsteady and non-uniform temperature distribution in Y-shaped milli-channel (figure 4.9). Water heated on a hotplate and room-temperature water were injected into the channel from Inlets A and B, respectively. The flow rate from each inlet was kept at 1 mL/min which corresponds to the bulk velocity of 2.1 mm/s, Reynolds number of 7.5, and thermal Peclet number of 46.6. These values indicate that the heat transport by the convection had larger effect on the temperature field rather than that by the conduction. The above calculations were conducted in a manner similar to that explained in section 3.4.

The measurement area was positioned at the junction of the channel where water at different temperatures merged (figure 4.9 (a)). The hotplate was switched on at $t = 0$ s in order to heat the water towards inlet A. The image acquisition and data sampling of the thermocouples were also started at $t = 0$ s and continued for 650 s. Figure 4.10 gives a series of temperature distributions measured by the present technique after initiation of heating the hotplate. These are visualized with a spatial resolution of $6.0 \times 6.0 \mu\text{m}^2$ which was calculated based on the pixel size of the cameras ($16 \times 16 \mu\text{m}^2/\text{pixel}$), the total magnification of the system ($M = 10.6$) and number of binned pixels (4×4 pixels). The total acquisition

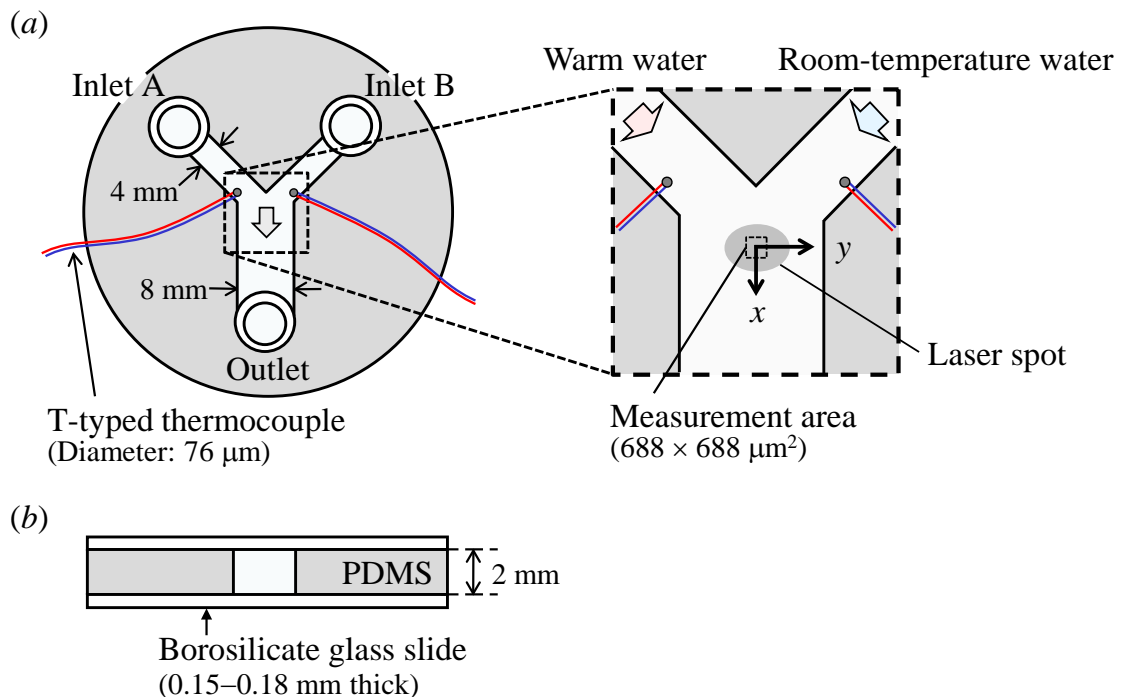


Figure 4.9. (a) Top and (b) cross-sectional views of the Y-shaped milli-channel. The measurement area is shown in an enlarged view of the junction area.

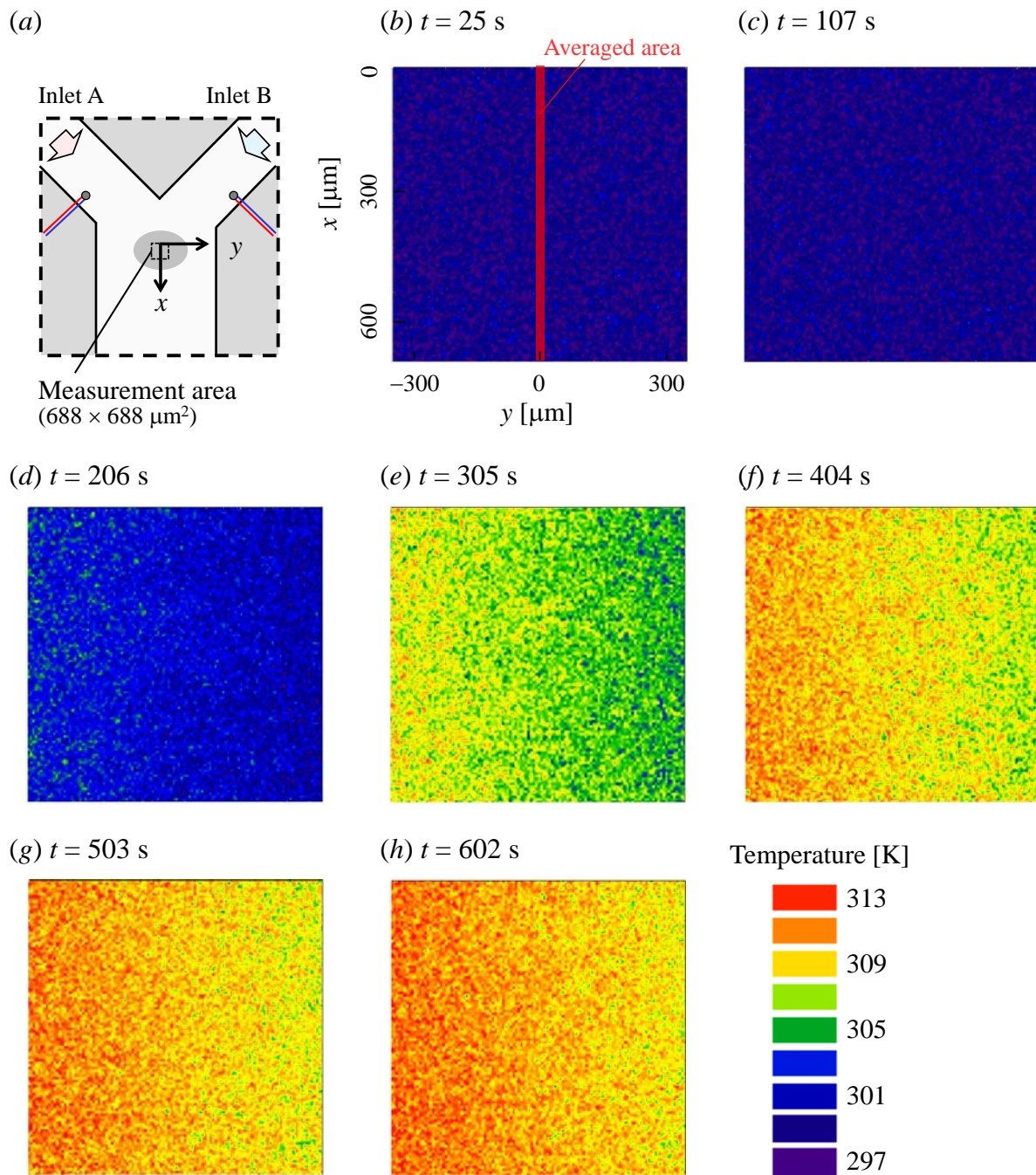


Figure 4.10. (a) The measurement area at the junction of the Y-shaped milli-channel. Temperature distribution maps at (b) 25 s, (c) 107 s, (d) 206 s, (e) 305 s, (f) 404 s, (g) 503 s and (h) 602 s after the initiation of heating. These temperature maps are visualized at spatial resolution of $6.0 \times 6.0 \mu\text{m}^2$ based on averaging over 4×4 pixels.

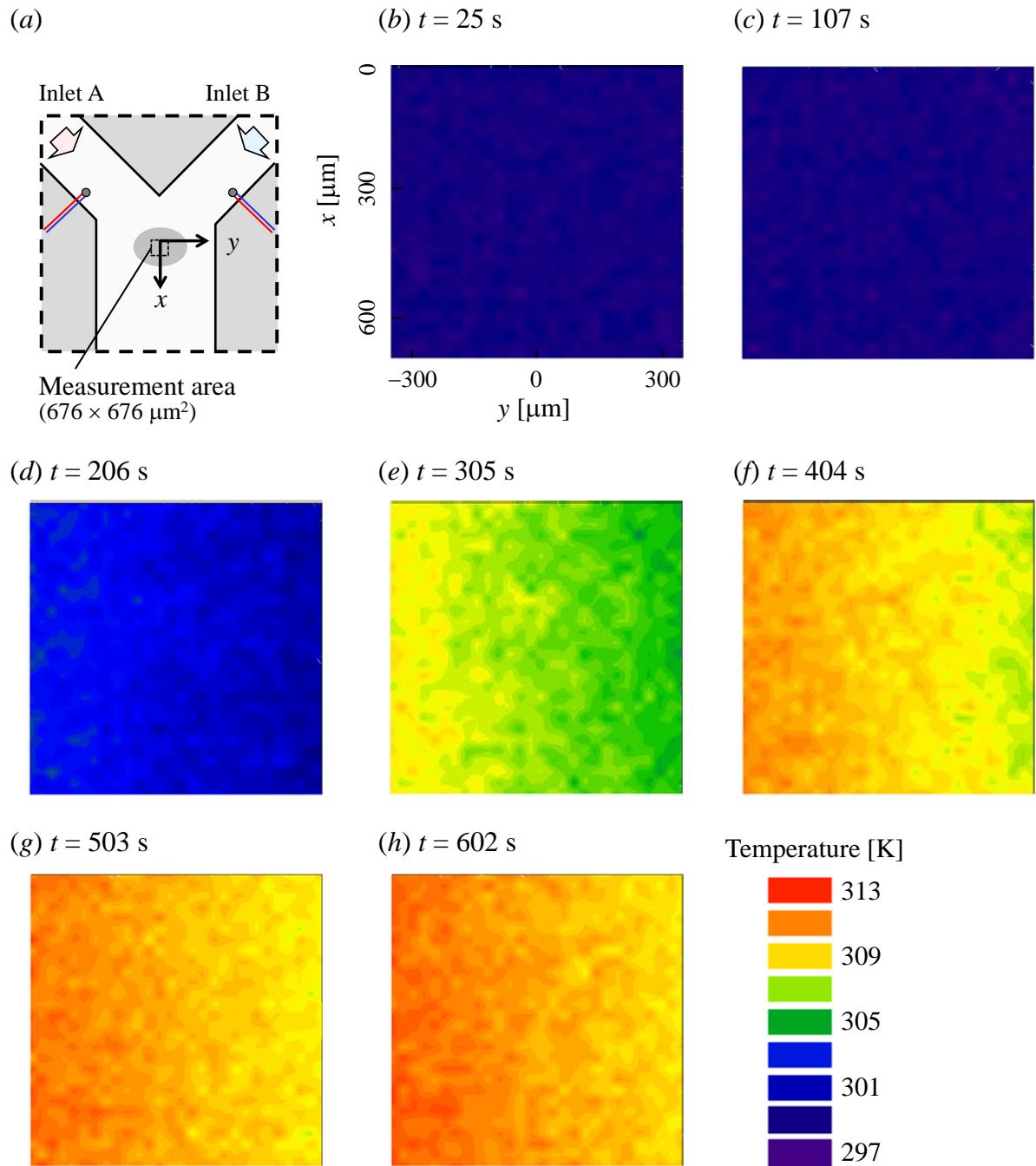


Figure 4.11. (a) The measurement area at the junction of the Y-shaped milli-channel. Temperature distribution maps at (b) 25 s, (c) 107 s, (d) 206 s, (e) 305 s, (f) 404 s, (g) 503 s and (h) 602 s after the initiation of heating. These are calculated from the same Raman images used in figure 4.10, but visualized at spatial resolution of $24.2 \times 24.2 \mu\text{m}^2$ based on averaging over 16×16 pixels.

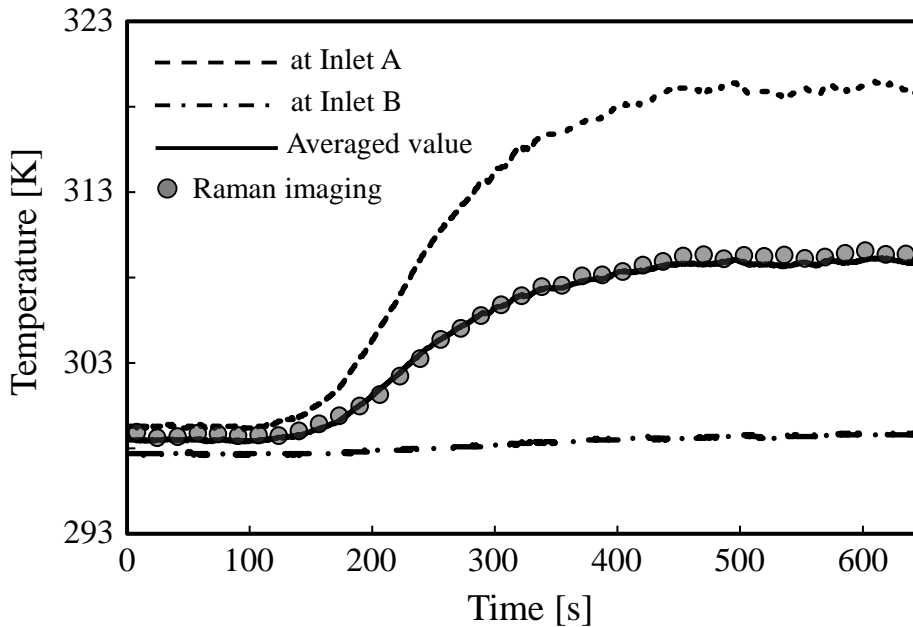


Figure 4.12. Comparison of the temporal evolution of the water temperature at $y = 0 \mu\text{m}$ measured by Raman imaging (filled dots), the temperature measured by thermocouples at inlets A and B (dashed lines) and the averaged value of these two temperatures (solid line).

time per temperature map was 16.5 s based on averaging over 30 successive Raman images. More smoothed temperature maps are also shown in figure 4.11 for reference, where the temperature distributions are visualized at spatial resolution of $24.2 \times 24.2 \mu\text{m}^2$ based on averaging over 16×16 pixels. It is obvious that the spotty patterns in figure 4.10 are diminished to some extent by increasing the binning factor.

As shown in figure 4.10(b), the temperature map at $t = 25$ s was almost uniform at 298 K (room temperature), and no noticeable change was observed until $t = 107$ s (figure 4.10(c)). After that, the temperature in the left side began to increase with time and a temperature gradient was formed in the y -direction as shown in figures 4.10(d)–(f). The temperature distribution reached a steady state at $t = 503$ s and kept nearly constant till the end of the measurements (figures 4.10(g), (h)). In order to obtain further insight into the acquired results, the temporal evolution of the temperature at $y = 0 \mu\text{m}$ is plotted by the filled-dots curve in figure 4.12. Every data point represents the temperature averaged over the x -direction (the averaged area of $688 \times 48 \mu\text{m}^2$ is shown in figure 4.10(b)). For comparison, figure 4.12 also depicts the temporal evolution of the water temperature measured by thermocouples at inlets A and B as dashed lines. In addition, the mean value of these temperatures is plotted as the solid line. It can be observed that the filled dots (i.e., measurement result of the present technique) adequately overlap with the solid line. The standard mean error was calculated to be 0.31 K, which implies the viability of the present technique.

These results clearly demonstrate that the two-wavelength Raman imaging technique which exploits the temperature dependencies of HB and NHB OH stretching modes can be used as an effective means for the measurement of time-evolving, planar temperature distribution in channel flow.

At the end of this section, the possible improvement of the present technique is discussed from the view point of efficient collection of the Raman signal and the extension of the range in applicability. Since this technique probes an inherently weak signal of the spontaneous Raman process, the excitation and detection efficiency is a major concern related to the measurement accuracy and temporal resolution. For higher detection efficiency, the half mirror being used for splitting the Raman signal into two paths in this study can be replaced by a dichroic mirror whose cut-on wavelength coincides with the isosbestic wavelength. The usage of such a dichroic mirror will nearly double the signal strength captured by each camera compared to the combined usage of a half mirror and bandpass filters. In addition, homogenization of the intensity profile of the laser light will lead to the improvement of the excitation efficiency, especially at the edge of the measurement area where measurement results suffer from lower signal intensity compared to the central area. This could result in reducing the non-uniformity of the signal-to-noise ratio over the whole measurement area. Secondly, regarding the versatility of the technique, there is possibility for application to various kinds of solutions used in microfluidic devices although this study treated only pure water. Some Raman spectroscopic studies have already addressed temperature measurements in diluted buffer solutions (Davis *et al.*, 1993) or living cells (Pikov & Siegel, 2010) by measuring the scattering intensity due to vibrational motions of hydroxyl group. In order to extend the applicability of the present technique to more complicated samples containing inorganic ions, organic compounds or biological samples, careful investigations should be carried out in future work to evaluate the influence of the solution composition on the equilibrium of hydrogen bonds.

4.5 Concluding Remarks

A two-wavelength Raman imaging technique was developed for planar, non-intrusive and microscale temperature determination in transient thermal flow field. The major change from the preceding chapter was the development of a two-wavelength imaging system consisting of two bandpass filters and two EM-CCD cameras, which enabled the simultaneous imaging of Raman signals with different wavelengths.

The measurement principle was based on the unique temperature dependence of Raman band arising from OH stretching vibration of H₂O molecules, which could be explained by

the equilibrium shift between hydrogen-bonded (HB) and non-hydrogen-bonded (NHB) states in liquid water. The Raman images of HB and NHB modes were simultaneously captured by utilizing the newly-developed two-wavelength imaging system and the intensity ratio of these modes was calculated. The simultaneous detection removed the need for manual switching of the filters, and enabled to compensate the spatiotemporal fluctuation of the excitation light.

A relay lens system of the two-wavelength imaging system was constructed by combining commercially available C-mount compatible components, an achromatic lens, a half mirror and the bandpass filters which were selected in chapter 3. Using this system, Raman signal arising from water is divided into two paths, spectrally filtered by the filters which transmit the desired signals (HB or NHB modes) and projected onto the two cameras.

A calibration result showed almost linear relationship between the temperature and the intensity ratio of HB to NHB modes in the range 293–343 K with temperature sensitivity of $-0.58\% \text{ K}^{-1}$. The uncertainty associated with the linear regression was calculated to be 1.43 K at a 95% confidence level, which clearly exhibited the advantage of the present ratiometric methodology in reducing the influence of the laser fluctuation on the measurement result, compared to that obtained in chapter 3 (which was approximately 3.7 K) using one-wavelength imaging system. The standard deviation of the intensity ratio within the measurement area was calculated to be 8.15×10^{-3} , which corresponds to 1.46 K according to the temperature sensitivity.

The proposed technique was applied to the unsteady and non-uniform temperature field in a Y-shaped milli-channel. Applying the calibration data, time series temperature distributions were visualized at spatial resolution of $6.0 \times 6.0 \mu\text{m}^2$ (averaging over 4×4 pixels). The temporal evolution of the water temperature measured by the present technique agreed well with that probed by thermocouples with the standard mean error of 0.31 K. The total acquisition time per temperature map was 16.5 s based on averaging over 30 successive Raman images.

Chapter 5

Investigation of Measurement Conditions for Velocity Determination Based on Thermal Tracing by Two-Wavelength Raman Imaging Technique

This chapter proposes a concept of non-intrusive velocity measurement based on thermal tracing by Raman imaging technique, and investigates its possibility focusing on the error in temperature measurement towards the establishment of a fluorescence-free and micro-scale velocimetry. Raman images are acquired at various measurement conditions (such as setting of electron-multiplying gain and measurement area) and the influence of each parameter on measurement error is quantitatively investigated. According to these results, a measurable velocity and a temperature rise required for thermal tracing are roughly estimated in order to discuss the conditions of the flow field which allows the present technique to be applied.

5.1 Concept of Velocity Determination

This section proposes a fluorescence-free methodology for velocity determination based on Raman imaging, whereas the well-established micro-scale velocimetry such as PIV and MTV employ fluorescent particles or caged dyes. The main concept of the present methodology is similar to that reported by Takahashi *et al.* (2012) which has been already referred to in section 1.2.3. They delivered electrolyte solution by drops into flowing water and measured the planar distributions of ion concentration by Raman imaging technique. Subsequently, they calculated the fluid velocity from the displacement of the peak position in time-series concentration distributions. Although they demonstrated velocity measurement based on

Raman imaging, the technique requires an injection of a drop of electrolyte solution as tracer, and thus it has only limited applicability.

In order to enhance the utility of the Raman-based velocity measurement, the present study proposes a more versatile approach using thermal tracing by Raman imaging. This is similar in concept to Takahashi's methodology but it measures temperature instead of concentration for velocity determination. Figure 5.1 illustrates the concept of the present methodology. The top view of the flow field and the time-series temperature distributions in the streamwise direction are shown in figures 5.1(a) and (b), respectively. First, the present technique assumes that an instantaneous heating is provided in the upstream region of a channel flow at $t = t_0$, and consequently the fluid temperature rises by ΔT . Then the heated spot is carried downstream by the fluid flow with decay in peak temperature. The time-series temperature distributions of the passing spot are probed in the downstream area using two-wavelength Raman imaging, which has been introduced in chapter 4. From the obtained temperature distributions, the position of the peak temperature is identified. Finally, the fluid velocity (u) in the x -direction is calculated from the displacement of the peak position (Δx) and the time interval of the image acquisition (Δt), i.e., $u = \Delta x / \Delta t$. In figure 5.1, the flow field has a non-zero velocity component only in the x -direction for ease of explanation, although the technique is potentially applicable to two-component velocity measurement.

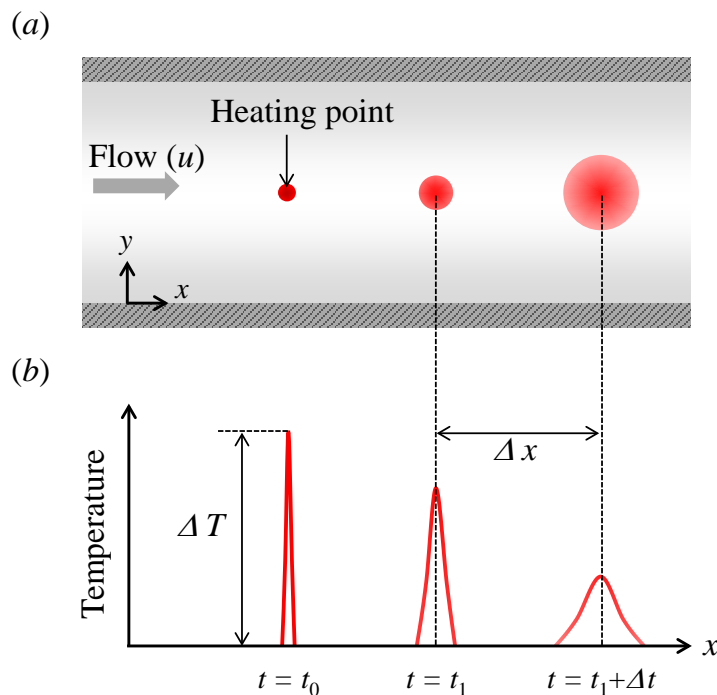


Figure 5.1. Concept of the velocity measurement based on thermal tracing. (a) Top view of the flow field and (b) the time-series temperature distributions in the streamwise direction.

Since this methodology determines the fluid velocity from the temporal evolution of the temperature distribution, a temporal averaging process (such as the integration of successive Raman images employed in the previous chapter) cannot be applied for the purpose of improving signal-to-noise ratio. In this case, the main concern is the increase in error of temperature measurement due to the limited acquisition time, which is considered to be closely related to the application limit of the velocity determination. Therefore, this chapter focuses on the investigation of the measurement error in temperature imaging with short acquisition time and evaluate its applicability to velocity determination.

The principle of the temperature measurement by two-wavelength Raman imaging is detailed in section 4.1. Hence, only the conceptual diagram (figure 5.2) and brief summary are provided here. As shown in figure 5.2(a), the Raman signal from water is divided into two paths by a half mirror, spectrally filtered by optical filters and detected by two cameras simultaneously. Each filter selectively transmits the temperature-sensitive Raman signal, i.e., hydrogen-bonded (HB) or non-hydrogen-bonded (NHB) OH stretching vibration modes in figure 5.3. Using the simultaneously-obtained Raman images (I_{HB} and I_{NHB}), a distribution of the intensity ratio (I_{Ratio}) is calculated as seen in figure 5.2(b). Subsequently, I_{Ratio} is corrected by a reference image (with the method described in section 3.3.3), which yields the corrected intensity ratio (I_{Ratio}^*). Then a planar temperature distribution can be determined by applying previously-obtained calibration data to I_{Ratio}^* .

Note that the proposed methodology can basically measure the fluid velocity integrated in the depthwise direction (i.e., z -direction), since it relies on the result of Raman imaging which provides temperature distributions averaged over the channel height. The methodology is thereby suitable for the case when the flow field is treated as two-dimensional (for example, Hele-Shaw flow).

5.2 Experimental Apparatus

Figure 5.4 shows the experimental setup for temperature measurement by two-wavelength Raman imaging technique. The simultaneous imaging system, temperature controlling system and channel configuration (figure 5.5) were essentially identical to that described in section 4.2.1, but a 488-nm semiconductor laser (Coherent Inc., Sapphire, maximum laser power: 500 mW) was used for excitation instead of the 532-nm laser utilized in chapters 3 and 4. Therefore, bandpass filters were newly selected in order to detect the temperature-sensitive Raman signals effectively. Figure 5.3 shows water Raman spectra in the range 3000–3800 cm^{-1} at three different temperatures. The horizontal axis in the upper side is the wavelength of the scattered light excited by 488 nm. The spectra exhibits the contrasting temperature dependencies of HB and NHB modes as already observed in section 3.1.1. The isosbestic

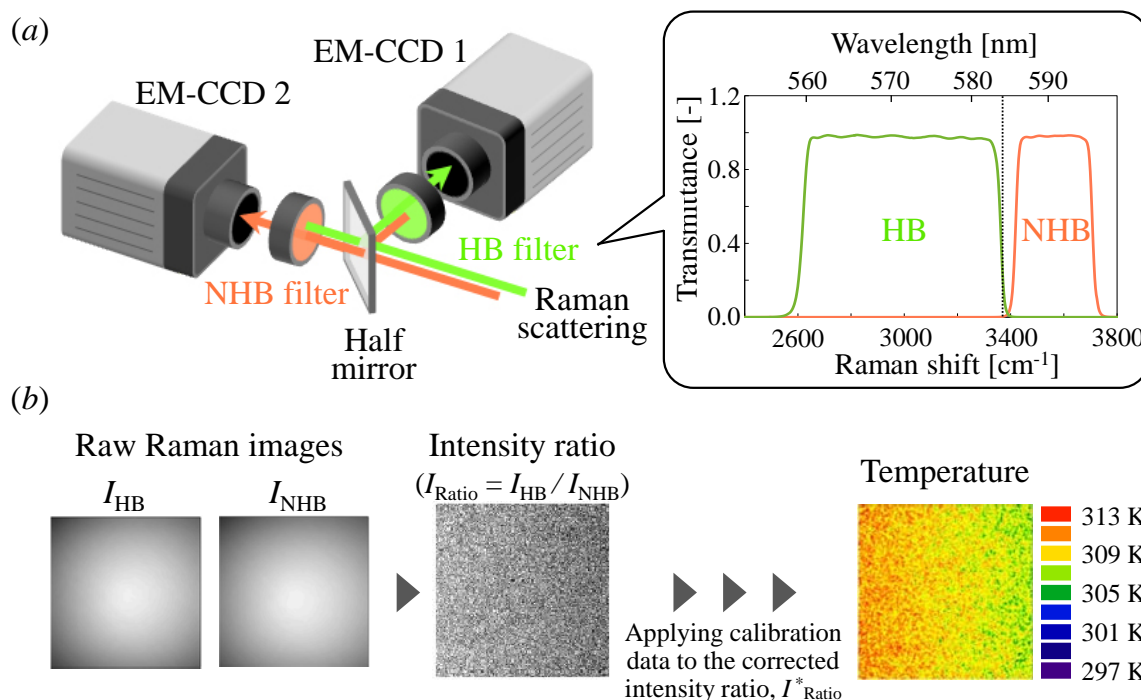


Figure 5.2. Conceptual diagrams of the temperature measurement by two-wavelength Raman imaging. (a) Schematic of the imaging system and the transmittance spectra of the filters. (b) Schematic of the procedure for temperature determination from obtained Raman images.

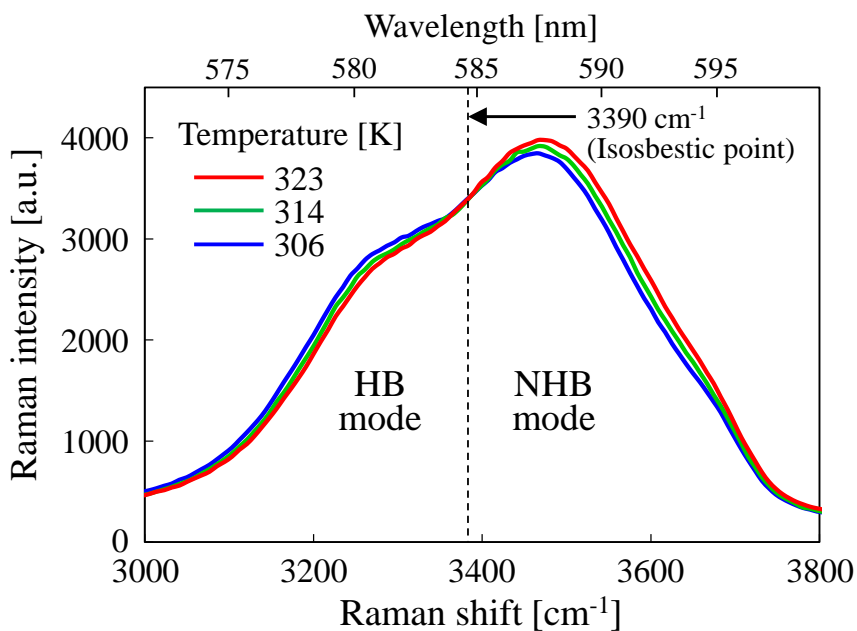


Figure 5.3. Raman spectra arising from OH stretching vibration of liquid H₂O at three different temperatures. The upper horizontal axis represents the wavelength of the scattered light excited by 488 nm.

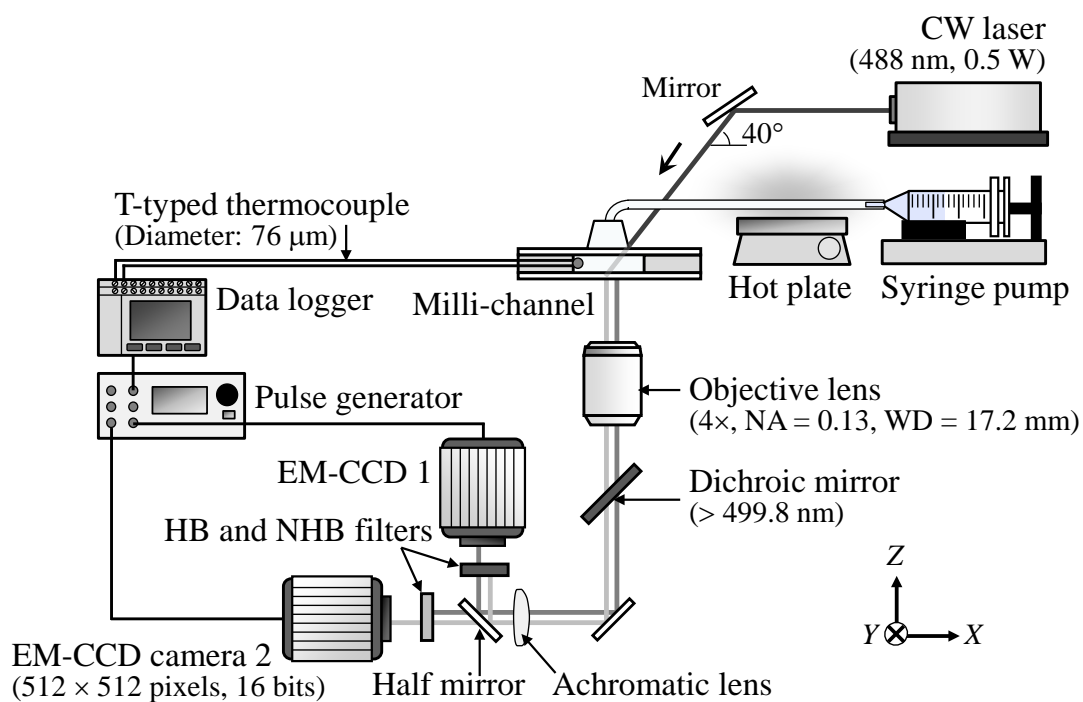


Figure 5.4. Schematic of the experimental apparatus for two-wavelength Raman imaging with an excitation light at 488 nm.

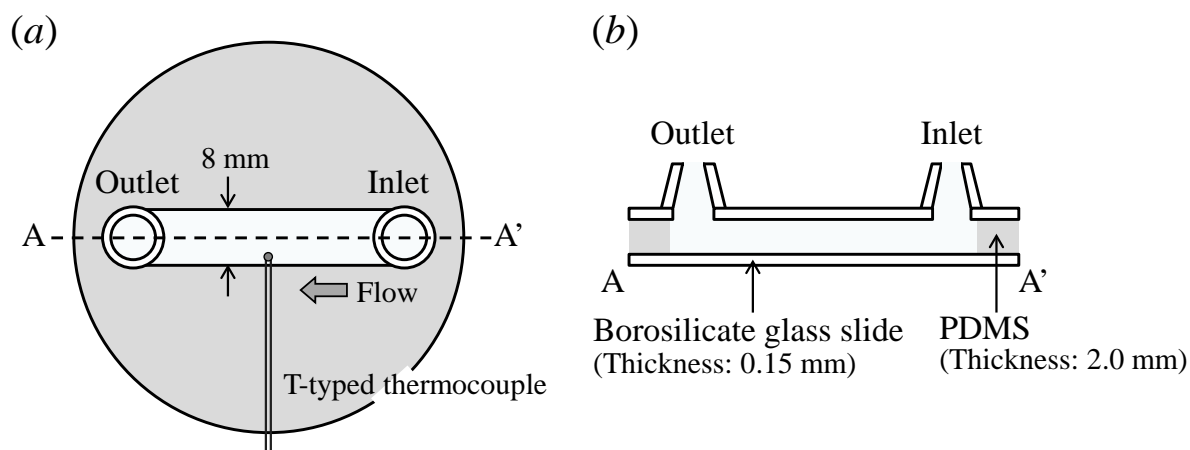


Figure 5.5. (a) Top and (b) cross-sectional views of the I-shaped milli-channel.

point is positioned at lower frequency compared to that in figure 3.2, which is attributed to the difference in the orientation of laser irradiation (including the incident angle and polarization direction) according to the study by Walrafen *et al.* (1986). Based on the measured spectra, two bandpass filters (Semrock Inc., FF01-572/15-25 for HB and FF01-591/6-25 for NHB) were selected. Their spectral properties are shown in figure 5.2(a).

The Raman scattering arising from the irradiated water was collected by an objective lens (Nikon Corp., 4×, NA = 0.13, WD = 17.2 mm), passing thorough the dichroic mirror (Semrock Inc., Di02-R488-25x36, transmittance wavelength: > 499.8 nm), split into two optical paths and simultaneously recorded by the two EM-CCD cameras equipped with the selected bandpass filters. This setup resulted in a total magnification of 4.2, which translate to a whole imaging area of $1.95 \times 1.95 \text{ mm}^2$. The focal plane of the objective lens was set at the center of the channel in the depthwise direction, and the calibration of the camera coordinates was conducted as detailed in section 4.2.3.

5.3 Influence of Measurement Conditions

5.3.1 Temperature Calibration Experiments

Calibration experiments were performed under uniform temperature distribution in order to investigate the relationship between the temperature and the Raman intensity ratio. The experiments were carried out with four different conditions of image acquisition, which were listed in table 5.1. Three parameters (laser power, exposure time and electron-multiplying (EM) gain of the cameras) involved with image acquisitions were varied. The water temperature was controlled from room temperature to around 333 K in the I-shaped milli-channel (figure 5.5), and the flow rate was maintained at 2 mL/min to insure the stability of the temperature field. This corresponds to the bulk velocity of 2.1 mm/s and the Reynolds number of 7.5. For each condition, HB and NHB images were captured simultaneously and a distribution of intensity ratio was calculated as shown in figure 5.2(b). In the present set of experiments, the central region (300×200 pixels) of the obtained distribution was extracted for the calibration and 4×4 pixels were integrated by software binning. Thus, for the measurement area of 300×200 pixels, a smoothed distribution of the intensity ratio with 75×50 binned pixels was newly created.

Figure 5.6 shows the calibration result for each condition. Each data point represents the average intensity ratio over the measurement area. It is obvious that the intensity ratio decreases with water temperature in the range of 293–333 K. According to the result in section 4.3, calibration curves were given by linear least-square fit (not by nonlinear fit) for simplicity and their slopes are listed in table 5.1. All the calibration curves show comparable

Table 5.1. Measurement conditions for calibration experiments

	Laser power [mW]	Exposure time [ms]	EM gain [-]	Slope [K ⁻¹]	Standard deviation [-]	Raman intensity [a.u.]
Condition 1	346	30.5	1000	-0.0136	0.139	27842
Condition 2	447	30.5	330	-0.0133	0.120	10242
Condition 3	496	30.5	120	-0.0135	0.100	4286
Condition 4	496	50.0	120	-0.0129	0.081	7004

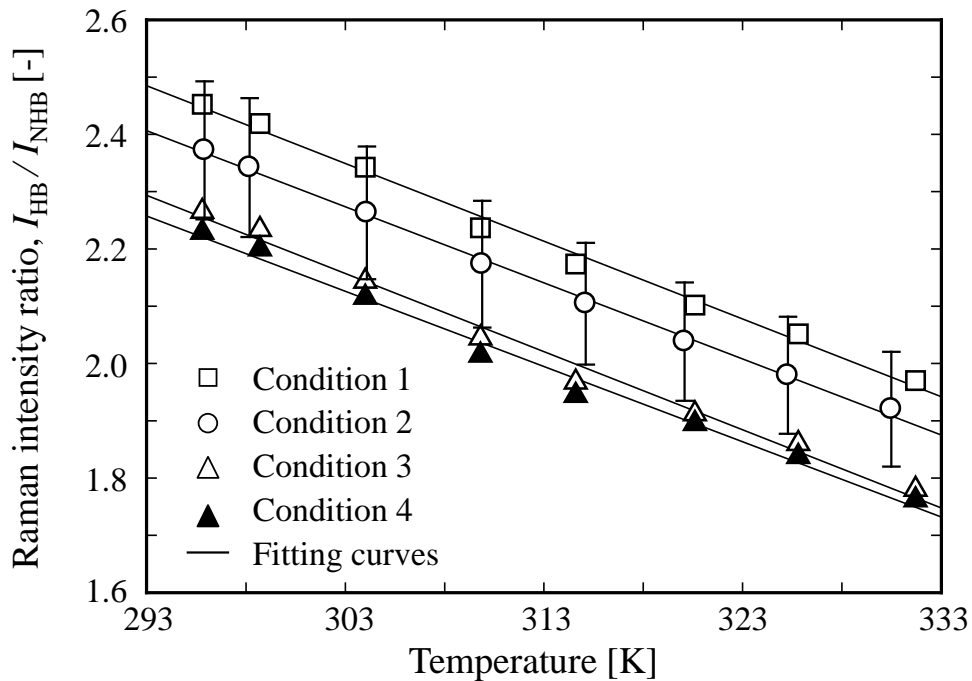


Figure 5.6. Relationship between the temperature and the Raman intensity ratio at four different measurement conditions listed in table 5.1.

magnitude of slope (approximately -0.013 K^{-1}), whereas their intercepts are quite different.

In order to estimate the variation in intensity ratio over the measurement area, the standard deviation of the intensity ratio within the smoothed distribution (75×50 binned pixels) was calculated. (It is noted that these calculations were performed after the correction procedure described in section 3.3.3.) As an example, the calculated standard deviation is indicated as the error bar for Condition 2 in figure 5.6. It can be seen from figure 5.6 that the size of the error bar is a little larger in lower temperature, but the variation coefficient was almost constant at 5.4% for the whole temperature range. The typical value for the standard deviation was 0.120 at 296 K, which corresponds to 9.1 K in temperature according to the slope of the calibration curve (-0.0133 K^{-1}). In the previous chapter, the calibration result showed an almost linear relationship between Raman intensity and temperature in a similar way. However, the typical standard deviation of the intensity ratio was relatively small (equivalent to 1.5 K) compared to the present study due to the long exposure time (500 ms) and temporal averaging process over 30 successive Raman images. This result indicates that the variation in intensity ratio leads to a considerably large temperature error within the measurement area especially when the fast image acquisition is required.

For further insight, the standard deviation of the intensity ratio at room temperature (around 296 K) is listed for each condition in table 5.1. The averaged intensity of the detected Raman image (HB image) is also listed in table 5.1 for reference. When comparing Conditions 3 and 4, it can be seen that the longer exposure time improved the standard deviation as well as the detected signal intensity. On the other hand, focusing on the Conditions 1–3, the standard deviation is the smallest in Condition 3 where the intensity of the Raman image was the smallest due to the lowest EM gain. This result implies that the increase in the EM gain (from 120 to 1000) contributed to the increase in image brightness, but did not have large effect in reducing the standard deviation compared to the effect of the increase in laser power (from 346 mW to 496 mW). The effect of the EM gain will be investigated in detail in section 5.3.2.

5.3.2 Influence of Measurement Conditions

In order to investigate the influence of measurement parameters on the measurement error associated with the spatial variation in intensity ratio, Raman images were acquired with various measurement conditions. The image acquisition was conducted at room temperature and the intensity ratio of the HB to NHB modes was calculated for each pair of images. Afterwards the standard deviation of the intensity ratio was calculated within the measurement area and converted into temperature using the slope of the calibration curve. The slope was assumed to be constant around -0.0133 K^{-1} for all the conditions according to the result in section 5.3.1. The obtained temperature value, which corresponds to the spatial

Table 5.2. Measurement conditions for the investigations of temperature variance

Parameter	Set value
Laser power	496 mW
Exposure time	30.5 ms
EM gain *	120
Measurement area **	$300 \times 200 = 60000$ pixels ($1.14 \times 0.76 \text{ mm}^2$)
Binning factor ***	4×4 pixels ($15.2 \times 15.2 \text{ }\mu\text{m}^2$)

* varied between 8–800 in figure 5.8(a)

** varied between 2400–86400 pixels in figure 5.8(b)

*** varied from 1×1 to 10×10 pixels in figure 5.8(c)

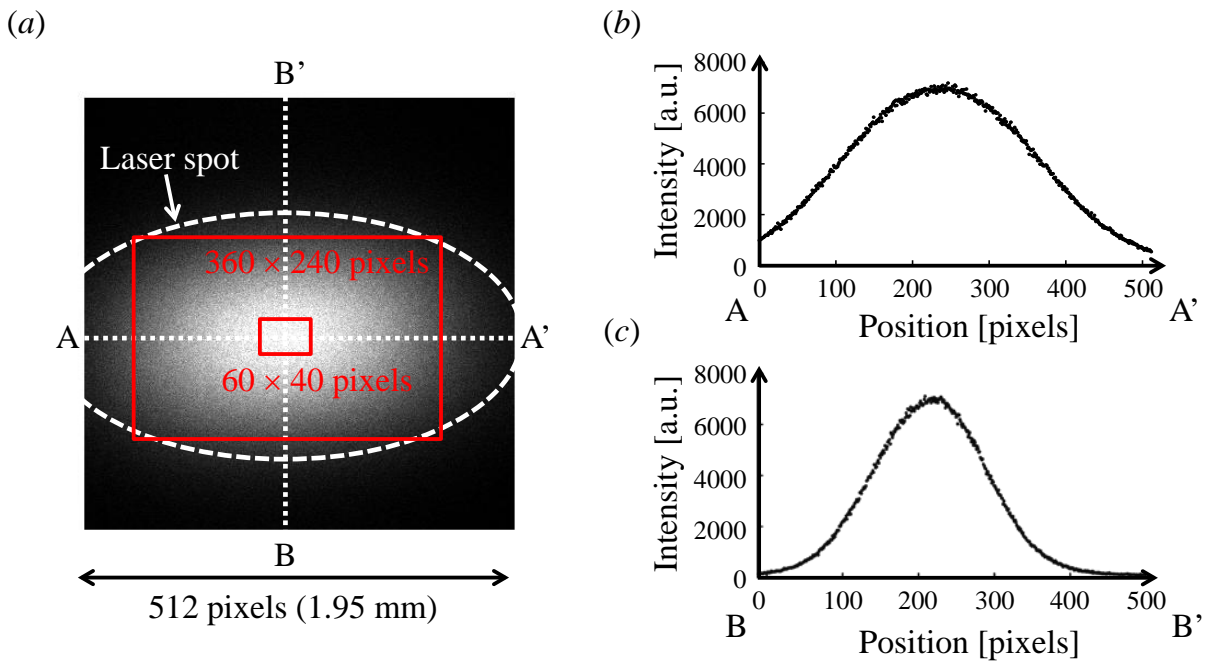


Figure 5.7. (a) Typical Raman image and the measurement area shown as the red rectangles. Intensity profiles of the Raman image (b) in the horizontal direction (A–A') and (c) in the vertical direction (B–B').

variation in intensity ratio, was defined as apparent temperature variance (Θ). By comparing Θ between various conditions, the influences of the following parameters were investigated. The EM gain of the camera, size of the measurement area, and binning factor for spatial averaging were changed, and the other parameters were fixed as listed in table 5.2. The laser power and the exposure time of the camera were set to be the maximum and the minimum values, respectively, within the adjustable range in the present system, envisioning the conditions suitable for velocity measurement. The input photon number (per pixel per frame) in the present experiment was estimated to be approximately 100 from the typical intensity value (6000 counts at the gain of 330), the typical conversion coefficient (5.8 electrons/count) and the quantum efficiency (90%). The value of EM gain was adjusted within the range from 8 to 800 (adjustable range of the camera was from 4 to 1200). This means that the signal intensity was amplified by charge multiplying by a factor of 8–800. The size of the measurement area was defined by the number of the pixels extracted for calculation of the standard deviation of the intensity ratio and varied from 60×40 to 360×240 pixels (i.e., 2400–86400 pixels). The measurement area was arranged in the region illuminated by the excitation laser (major axis: 2.09 mm, minor axis: 1.09 mm) as shown in figure 5.7(a). The binning factor was varied from 1×1 to 10×10 , thus the number of pixels integrated for spatial averaging was 1–100 pixels. With binning of 10×10 pixels, a smoothed distribution with 30×20 binned pixels was newly created for the measurement area of 300×200 pixels.

Figure 5.8(a) shows the relationship between the EM gain and the apparent temperature variance (Θ) calculated from the standard deviation of the Raman intensity ratio. Θ rapidly decreases when the EM gain increases from 8 to 25, while it stays almost constant at approximately 8.0 K when the gain is set at over 40. The minimum value for Θ was calculated to be 7.6 K at the gain of 120. This result indicates that the EM gain has a significant effect on reducing the measurement error by increasing signal-to-noise ratio, though it shows no improvement beyond a certain level. This is almost consistent with the sensor characteristics shown in figure 3.8(b), where the signal-to-noise ratio exhibits almost no improvement at the EM-gain of over 30 with the input photon number of 100. Therefore, the result in figure 5.8(a) is considered to be mainly attributed to the sensor characteristics. From this result, it is experimentally confirmed that the gain should be selected to achieve the minimum temperature variance and need not to be set at higher than that.

Subsequently, Θ is plotted against the total number of pixels which were extracted for measurement area in figure 5.8(b). It shows a quadratic increase in Θ with the number of pixels. The maximum and minimum values for Θ were 9.1 K at 86400 pixels and 5.6 K at 2400 pixels, respectively. This is considered to mainly result from the non-uniform intensity distribution of the excitation light. Figures 5.7(b) and (c) show the intensity profiles of the measured Raman image plotted along the horizontal and vertical axes, respectively. Since the excitation laser beam has a Gaussian intensity profile in this study, measurement results in

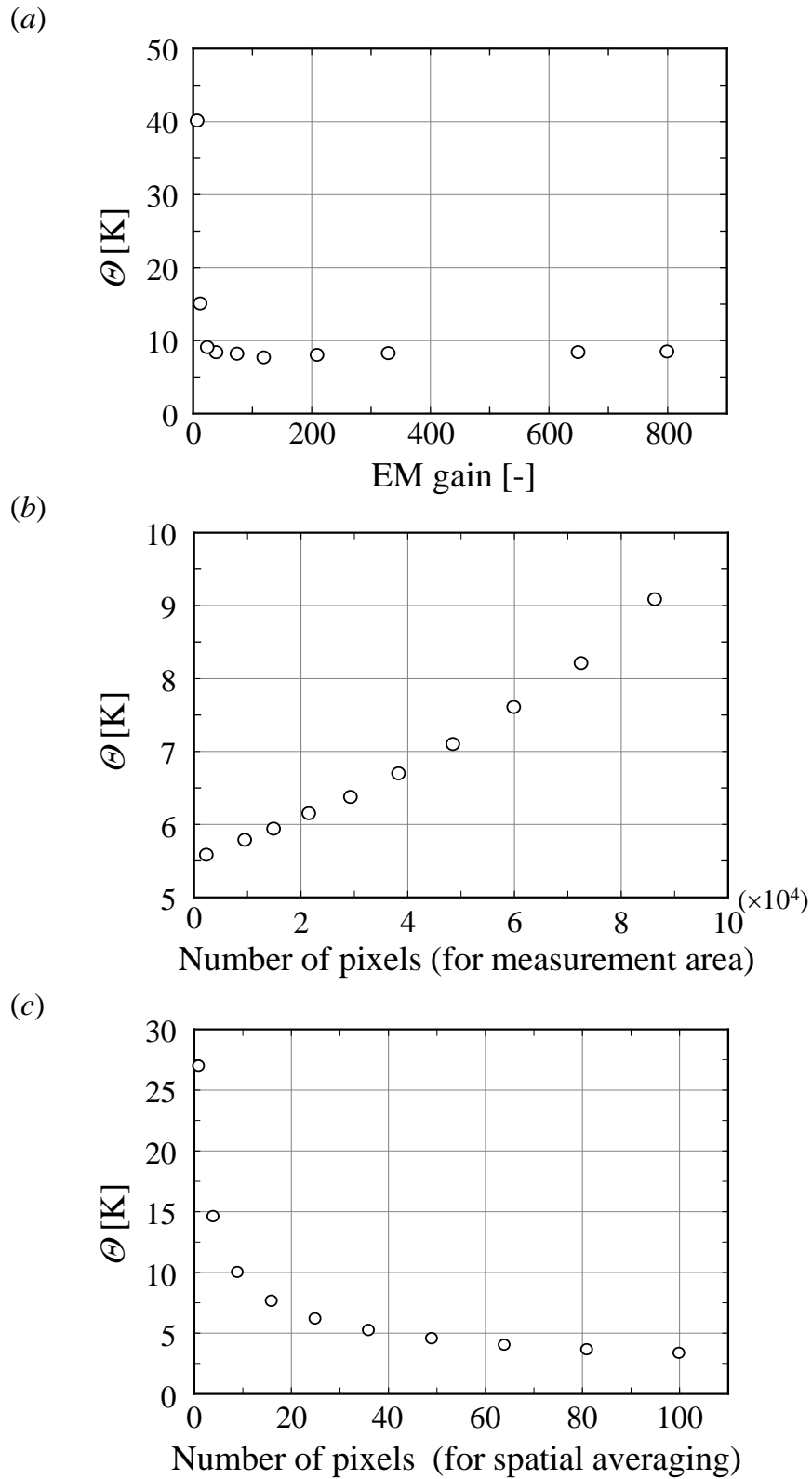


Figure 5.8. (a) Relationship between the EM gain and the apparent temperature variance (θ). (b) Relationship between the number of the pixels extracted for measurement area and θ . (c) Relationship between the number of the pixels integrated for spatial averaging and θ .

the edge region suffer from lower signal level. For example, the Raman intensity at the corner of the measurement area of 300×200 pixels was almost 20% of that at the central region. This non-uniformity in signal level leads to an increase in Θ for a larger measurement area. Hence, homogenizing the intensity profile of the illumination light would be an effective strategy for improving signal-to-noise ratio in the whole measurement area and avoiding an increase in spatial variation in larger measurement area.

Finally, figure 5.8(c) shows the relationship between the apparent temperature variance (Θ) and the number of pixels which were integrated for spatial averaging. It can be seen that Θ decreased with the number of pixels. At the binning factor of 1×1 pixel (i.e., without spatial averaging), Θ was calculated to be 27.0 K, but it decayed to 14.6 K at the factor of 2×2 pixels and 4.0 K at 8×8 pixels. Though the binning process demonstrated powerful effect in reducing the variation, it should be noted that this kind of spatial averaging resulted in lower spatial resolution at the same time (which is also discussed in section 5.3.3).

5.3.3 Discussion of Applicability

In this section, the above measurement results are summarized in terms of future application to velocity determination. Therefore, the concept of the proposed method is briefly reiterated below (see figure 5.1). First, the proposed technique assumes that an instantaneous heating is provided in the upstream region of a channel flow, and at least two successive Raman images are captured in the downstream region during the heated spot passes through the measurement area. The time-series temperature distributions are calculated from the obtained images, and the velocity (u) in the streamwise direction (i.e., x -direction) is derived from the displacement of the peak position (Δx) and the time interval of the image acquisition (Δt).

Under the assumption that a sufficient temperature rise is realized for thermal tracing, the maximum fluid velocity which can be measured by the above procedure was roughly estimated for four different measurement conditions (table 5.3). The laser power and the exposure time were set to be the same as in table 5.2. For calculating the measurable maximum velocity in the streamwise direction, the displacement (Δx) was assumed to be equal to the length of the long side of the measurement area. In addition, the time interval, Δt , was set to be the shortest frame interval of the camera (31.4 ms).

Focusing on Conditions 5 and 6 in table 5.3, the apparent temperature difference (Θ) becomes somewhat larger with an increase in EM gain, which indicates that an optimization of the gain is necessary to minimize the measurement error. Subsequently, the size of the measurement area is discussed by comparing Conditions 6 and 7. A large measurement area is considered to allow velocity measurement of faster flow, but it increases the temperature variance at the same time unless the uniformity of the excitation light is improved. This may result in the requirement for higher energy to produce larger temperature difference, ΔT , in

Table 5.3. Measurable velocity, spatial resolution and Θ calculated for each condition

	Condition 5	Condition 6	Condition 7	Condition 8
EM gain [-]	800	120	120	120
Measurement area [pixels]	300 × 200	300 × 200	150 × 100	300 × 200
Binning factor [pixels]	4 × 4	4 × 4	4 × 4	8 × 8
Measurable maximum velocity in the streamwise direction [mm/s]	36.5	36.5	18.3	36.5
Spatial resolution [μm^2]	15.2 × 15.2	15.2 × 15.2	15.2 × 15.2	30.5 × 30.5
Θ [K]	8.4	7.6	5.9	4.0

order to clearly visualize the heated spot. In addition, from the comparison of Conditions 6 and 8, it is observed that a larger binning factor will require smaller temperature difference (ΔT) for thermal tracing, though the spatial resolution is compromised. It can be concluded from these discussions that the measurable velocity range, the temperature rise required for thermal tracing and spatial resolution can be significantly affected by the measurement conditions of Raman imaging, which suggests that each parameter should be appropriately selected with consideration of the flow condition or the limitation of a heating system.

Finally, the influence of thermal diffusion is mentioned briefly according to previously-reported results. Senga *et al.* (2010) measured the flow velocity in microchannels based on molecular tagging velocimetry, where a caged fluorescent dye was used as a tracer. They determined the fluid velocity from the displacement of the tagged (i.e., fluorescent) region which was identified from the time-series fluorescence images. The important knowledge obtained by their work is summarized below. First, the measurement error was much larger when the fluorescent intensity profile was fitted with Gaussian function than when the displacement was calculated using the intensity peak values of the original profile. Figure 5.9(a) schematically illustrates fluorescent intensity profiles obtained from detected fluorescence images. The fluorescent intensity profile, which initially has a Gaussian-like shape, becomes more distorted with respect to time due to the influence of convective flow. Therefore, the study suggests that the flow velocity should be determined based on the peak values of the original intensity profiles. Secondary, it became more difficult to estimate the accurate flow velocity with the progress in dye dispersion which leads to the distorted intensity profile with attenuated peak intensity. As a result, the calculated velocity values became more scattered with time, as illustrated in figure 5.9(b). According to their experimental result, where a caged fluorescent dye with diffusivity of $5.0 \times 10^{-10} \text{ m}^2/\text{s}$ was used, the ratio of r.m.s. velocity to the mean velocity was 5.8% within 0–40 ms and 7.5%

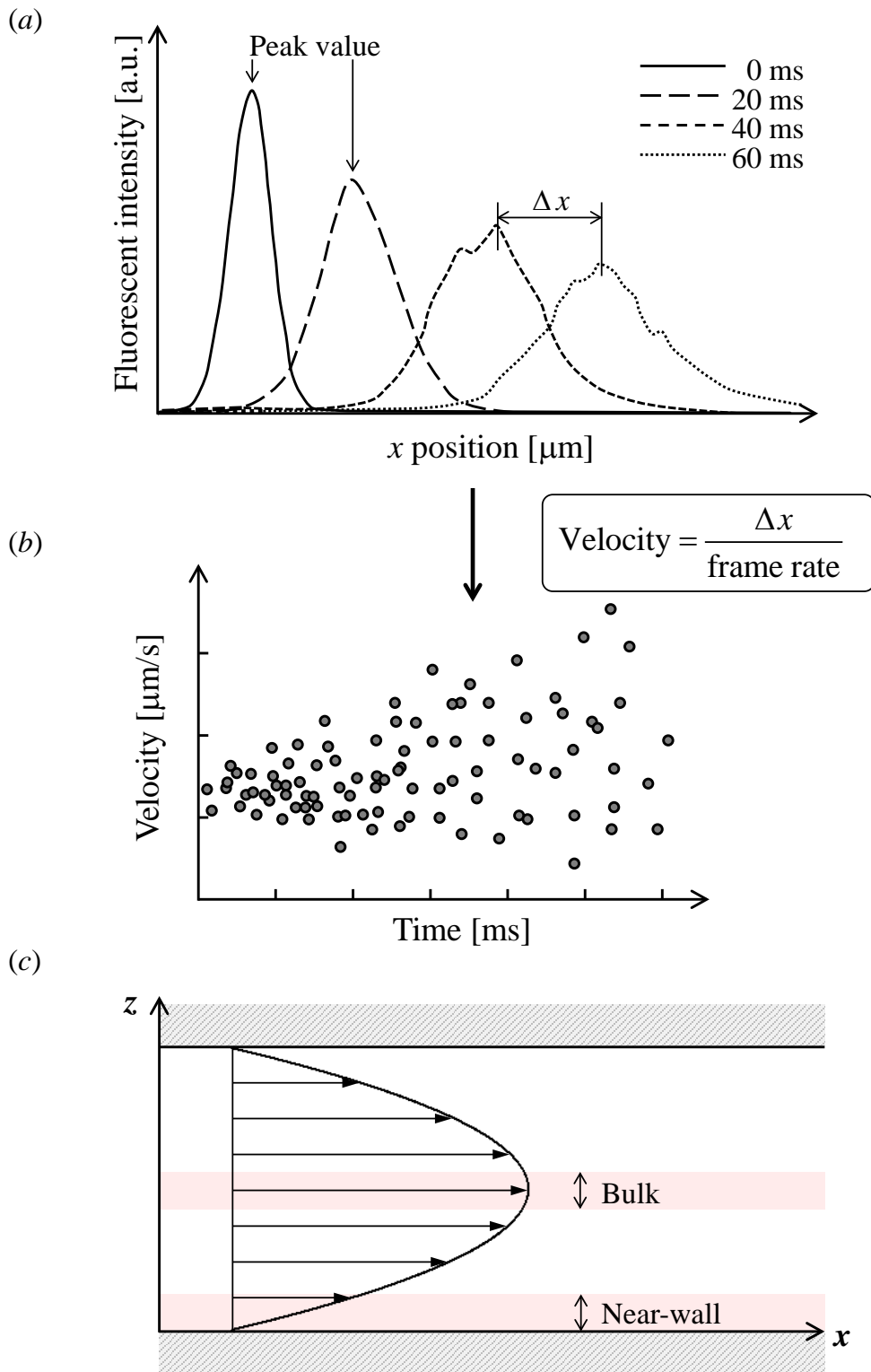


Figure 5.9. Schematic illustrations of (a) the fluorescent intensity profiles in time series obtained by molecular tagging velocimetry, (b) the temporal evolution of the flow velocity calculated from the displacement of the peak intensity values of the measured profiles, and (c) the velocity profile in the depthwise direction.

within 81–120 ms in electroosmotic flow. In addition, the influence of the dye dispersion was more significant in pressure-driven flow than in electroosmotic flow, which resulted in the large measurement error (approximately in 27.2% within 0–60 ms). This might be caused by the large velocity gradient near the wall which is illustrated in figure 5.9(c).

According to these results by Senga *et al.* (2010), the applicability of the proposed method is considered to crucially depend on the influence of dispersion of thermal tracer. The velocity determination should be carefully performed by peak searching method with considering the influence of thermal dispersion including its temporal evolution and relationship with the flow condition.

In order to evaluate the diffusion of thermal tracer, the Peclet number was calculated in bulk region in pressure-driven flow (figure 5.9(a)). The channel height and width were set as 2 mm and 8 mm, respectively, and the flow rate was assumed to be 2.0 mL/min. The thermal diffusivity is $1.4 \times 10^{-7} \text{ m}^2/\text{s}$ in water at 293 K. Using the flow velocity averaged within 200 μm along z -direction, the thermal Peclet number was calculated to be 71. It is much smaller in comparison with the diffusion Peclet number when the same fluorescent dye is used as a tracer (approximately $Pe_D = 19840$), which indicates that the influence of the tracer dispersion is more intensely affects the velocity determination when using the thermal tracer. It should be noted that the above direct comparison between the thermal and the diffusion Peclet number will not be allowed in the near-wall region, except when the adiabatic condition holds at the channel wall.

5.4 Concluding Remarks

A non-intrusive methodology for velocity determination was proposed based on thermal tracing by two-wavelength Raman imaging. Although the proposed method has not yet been demonstrated due to the lack of an appropriate heating system, its applicability was investigated focusing on the error in temperature measurement.

The proposed methodology assumes that a pulsed heating is given in the upstream region in a channel flow and that the heated spot carried downstream by the flow is visualized by time-series temperature measurement using two-wavelength Raman imaging. Then the fluid velocity is calculated from the displacement of the peak temperature and the time interval. In this case, however, the main concern is the increase in error of temperature measurement due to the short acquisition time. Therefore, the investigation was conducted to evaluate the measurement error in temperature imaging.

A two-wavelength Raman imaging system, which was essentially identical to that in chapter 4, was constructed. Thus the system enabled the simultaneous imaging of the Raman

signals with contrasting temperature dependencies, i.e., hydrogen-bonded (HB) and non-hydrogen-bonded (NHB) modes. The intensity ratio of the HB to NHB modes was calculated from obtained Raman images and correlated with water temperature in calibration experiments. Under four different measurement conditions, it was confirmed that the intensity ratios linearly decreased with water temperature in the range 293–333K with almost equivalent slopes. It was also observed that the short acquisition time (30.5 ms) resulted in a large variation in intensity ratio (equivalent to 9.1 K in temperature) even in the uniform temperature condition.

In order to examine the influence of measurement conditions on the variation in intensity ratio (namely, apparent temperature variance within the target area), Raman images were acquired with varying EM gain, size of the measurement area, and binning factor for spatial averaging. It is observed from these measurement results that the measurable velocity range, apparent temperature variance and spatial resolution are mutually related and significantly different depending on the conditions. Using the present imaging system, the measurable maximum velocity in the streamwise direction was roughly estimated to be 36.5 mm/s and the temperature difference required for thermal tracing was estimated to be larger than 7.6 K, when the gain, measurement area, and binning factor were set to be 120, 300×200 pixels, and 4×4 pixels, respectively.

It should be emphasized that the velocity measurement by the proposed methodology has not yet been realized and it is considered to be possible only when the quick heating is achieved. Therefore an appropriately-designed heating system will be required to experimentally validate the technique.

Chapter 6

Visualization of Near-Wall Concentration Distribution by Total Internal Reflection Raman Imaging Technique

This chapter describes the development of a novel measurement technique for near-wall concentration. Total internal reflection (TIR) Raman imaging, which utilizes the Raman scattering excited by an evanescent wave, is proposed in order to realize non-intrusive, surface-selective and two-dimensional concentration measurements. An optical measurement system is newly developed by combining a two-prism-based evanescent wave illumination system with a direct Raman imaging system. Following a calibration experiment, near-wall concentration visualization is demonstrated in a microscale mixing field of H₂O and D₂O.

6.1 Near-Wall Concentration Measurement by Total Internal Reflection Raman Imaging

6.1.1 Measurement Principle for Near-Wall Concentration

For non-intrusive visualization of near-wall concentration, total internal reflection (TIR) Raman imaging technique is proposed for capturing Raman images from liquid molecules in contact with a solid surface. Figure 6.1 illustrates the concept of the technique. The use of an evanescent wave enables the surface-selective excitation of spontaneous Raman process at the solid-liquid interface. The Raman signal arising from near-wall liquid molecules is spectrally filtered by an optical filter and two-dimensionally captured by a camera. The resultant image is a distribution of the TIR Raman intensity integrated over the transmittance wavelength of the filter, as shown in figure 6.1(b). This TIR Raman image can be converted

into the distribution of near-wall concentration (figure 6.1(c)) through the following steps.

According to the equations (2.20) and (2.40), the measured intensity of TIR Raman scattering for the i -species, $I_{i, \text{eva}}$ [photons /s·m²], is defined as,

$$\begin{aligned} I_{i, \text{eva}} &= \int K \cdot I_{\text{eva}}(z) \cdot \Omega \cdot \left(\frac{d\sigma}{d\Omega} \right)_i \cdot N_i(z) dz \\ &= \int K \cdot I_{\text{eva}}(0) \exp(-z/z_p) \cdot \Omega \cdot \left(\frac{d\sigma}{d\Omega} \right)_i \cdot N_i(z) dz \end{aligned} \quad (6.1)$$

where I_{eva} [photons/s·m²] is the evanescent wave intensity, z [m] is the distance from the interface, Ω [sr] is the solid angle of signal detection, $d\sigma/d\Omega$ [cm²/molecule·sr] is the absolute differential Raman cross section, and N_i [molecules/m³] is the number density of i -species molecules being illuminated inside the probe volume. The penetration depth of the of the evanescent wave, z_p [m] is given by (equation (2.41)),

$$z_p = \frac{\lambda}{4\pi\sqrt{n_1^2 \sin^2 \theta_i - n_2^2}} \quad (6.2)$$

When the penetration depth is constant and homogeneous in the measurement area, i.e., the refractive indices of materials (n_1 and n_2) and the incident angle (θ_i) is does not vary spatio-temporally, equation (6.1) can be reduced to:

$$I_{i, \text{eva}} = K \cdot I_0 \cdot \Omega \cdot \left(\frac{d\sigma}{d\Omega} \right)_i \cdot f(N_i) \quad (6.3)$$

where $f(N_i)$ [molecules/m²] is the function determined by the number density (i.e., concentration) of i -species molecules being illuminated. The concentration of i -species (C_i [mol/L]) can be measured by exploiting this dependence of the TIR Raman intensity ($I_{i, \text{eva}}$) on the number density of molecules (N_i [molecules/m³]).

However, it is obvious from equation (6.3) that the TIR Raman intensity ($I_{i, \text{eva}}$) also depends on the excitation intensity I_0 . As a result, the intensity distribution of the raw TIR Raman image (figure 6.1(b)) is affected by the non-uniform distribution of the evanescent intensity due to the Gaussian beam profile. In order to compensate the influence of this non-uniform excitation profile, the detected intensity ($I_{i, \text{eva}}$) is normalized by that at the reference concentration ($I_{i, \text{eva, ref}}$):

$$I_{i, \text{eva}}^* = \frac{I_{i, \text{eva}}}{I_{i, \text{eva, ref}}} = \frac{f(N_i)}{f(N_{i, \text{ref}})} \quad (6.4)$$

By applying previously-obtained calibration data to the calculated intensity ratio ($I_{i, \text{eva}}^*$ [-]), a near-wall concentration distribution can be determined.

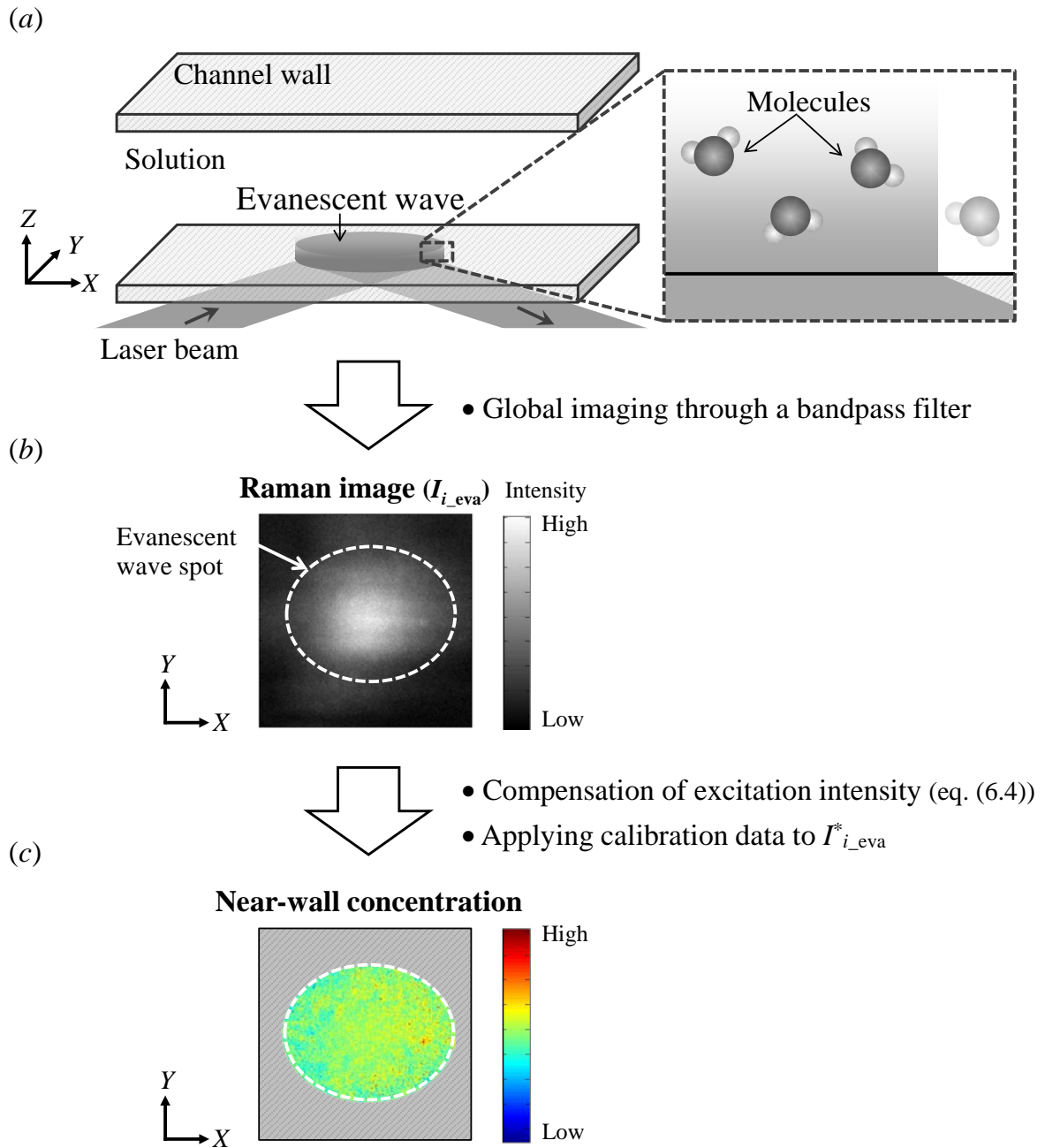


Figure 6.1. Schematic concept of near-wall concentration measurement by TIR Raman imaging. (a) Generation of an evanescent wave in a microchannel by total internal reflection. The enlarged figure illustrates the molecules illuminated by the evanescent wave. (b) Typical example of a raw Raman image and (c) a calculated distribution of near-wall concentration.

6.1.2 Raman Spectra of H₂O/D₂O Mixtures

In the present study, mixture solutions (composed of H₂O and D₂O) were used as sample for TIR Raman imaging in order to demonstrate near-wall concentration measurements for each species in multiple component solutions. Figure 6.2 shows typical Raman spectra from bulk H₂O/D₂O mixtures in the range 1500–4000 cm⁻¹. These were obtained by using the measurement system (in figure 3.1) and a milli-channel (in figure 3.10). These mixtures present distinct spectral shapes depending on their composition. The two broad Raman bands with peak intensities at 2500 cm⁻¹ and 3420 cm⁻¹ can be observed, which originate from O-D and O-H stretching vibration modes, respectively (see table 2.4).

In the present experiments, H₂O/D₂O mixtures were selected for the following reasons: (1) the characteristic Raman bands of O-H and O-D stretching vibrations are well separated (as shown in figure 6.2), which is suitable for demonstrating concentration imaging of each species, (2) the change in solution composition produces large intensity difference, compared to most electrolyte solutions, and (3) they are comparable in refractive indices (as shown in table 2.3), which lead to an equivalent penetration depth of the evanescent wave and enables the application of equation (6.3).

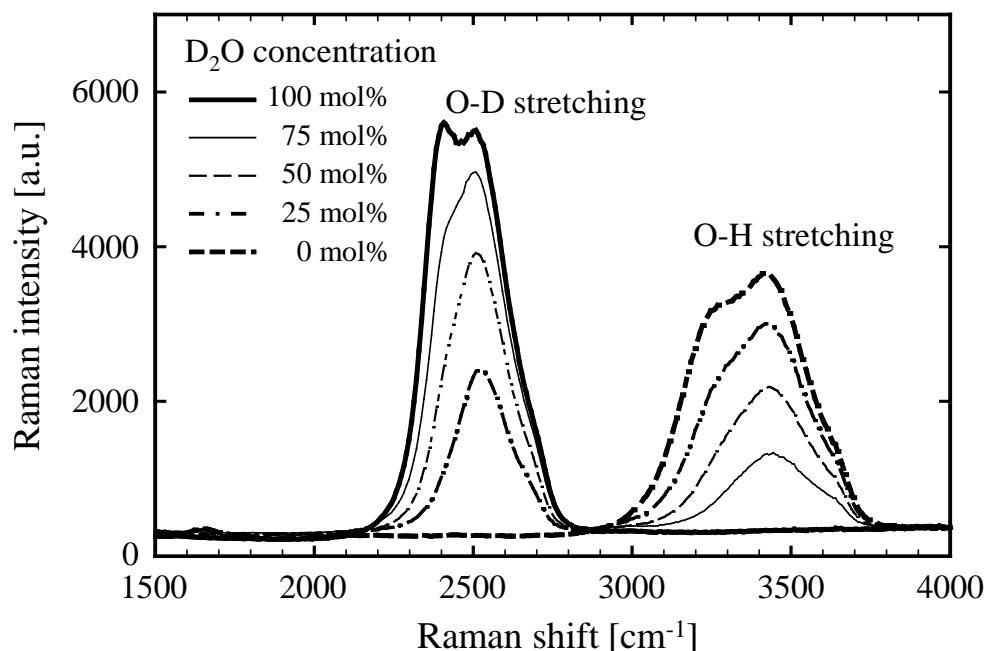


Figure 6.2. Typical Raman spectra of bulk H₂O/D₂O mixtures in the range 1500–4000cm⁻¹, which were measured by the system shown in figure 3.1.

6.2 Measurement System

This section focuses on the development of the measurement system for TIR Raman imaging. The configuration of the illumination system is detailed at the beginning, followed by an explanation of overall structure of the measurement system. Subsequently, the spectroscopic properties of the selected bandpass filters, which are the key components of the system, are described and evaluated based on the measurement result of TIR Raman spectra.

6.2.1 Two-Prism-Based Evanescent Wave Illumination System

To perform surface-selective concentration measurements in microchannels, an evanescent wave illumination system based on two prisms (Kazoe & Sato, 2007) was employed in this study. The configuration of the illumination system is illustrated in figure 6.3. Two prisms which are made of borosilicate glass ($n = n_p$) are attached to the stage of an inverted microscope. One of the prisms is firmly attached, while the other is movable in lateral direction as shown in figure 6.3(a). A microchannel composed of polydimethylsiloxane (PDMS) and a glass slide ($n = n_g$), is located on the prisms with an immersion oil ($n = n_o$). A laser beam is introduced into the prism at an inclined angle, φ [°], internally reflected at a reflection coating, and directed to the glass slide through the immersion oil. The incident angle at the prism-oil interface, θ_p [°], is given by the geometrical optics and the Snell's law (equation (2.38)):

$$\theta_p = \sin^{-1} \left[\frac{\sin(65^\circ - \varphi)}{n_p} \right] + 65^\circ \quad (6.5)$$

After the laser beam is introduced into the glass slide, it travels undergoing total internal reflections with an incident angle of θ_i [°]. As a result, evanescent wave spots are generated at the interface between the glass slide and the solution ($n = n_s$) with the penetration depth given by (equation (2.41)),

$$z_p = \frac{\lambda}{4\pi \sqrt{(n_g \sin \theta_i)^2 - n_s^2}} \quad (6.6)$$

According to the Snell's law, $n_g \sin \theta_i$ in equation (6.6) is expressed as,

$$n_g \sin \theta_i = n_p \sin \theta_p \quad (6.7)$$

Therefore, by substituting equation (6.5) into equation (6.7),

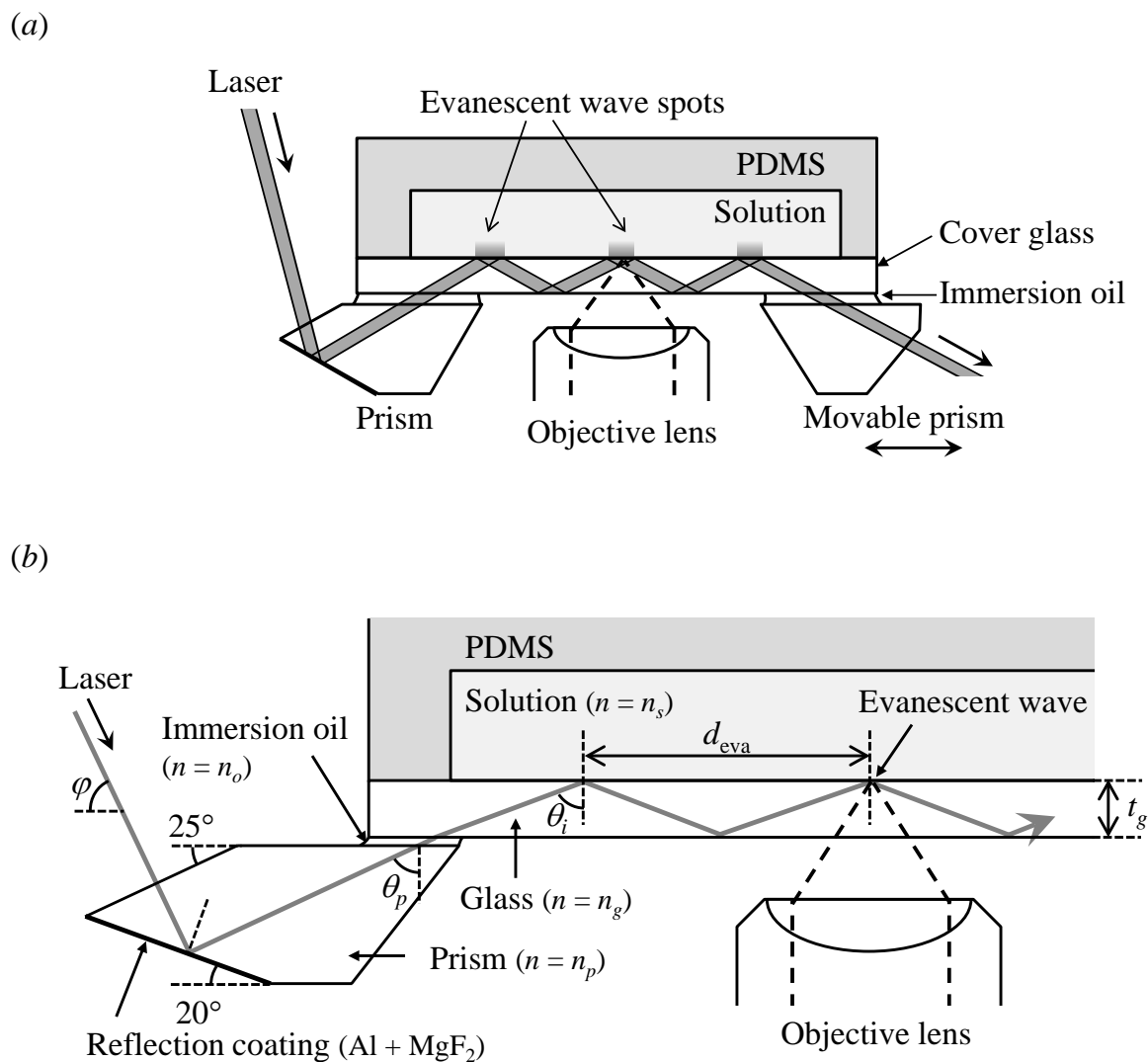


Figure 6.3. Schematics of (a) the two-prism-based optical system for an evanescent wave illumination in a microchannel and (b) the light path of the excitation laser beam which undergoes total internal reflections.

$$n_g \sin \theta_i = n_p \sin \left\{ \sin^{-1} \left[\frac{\sin(65^\circ - \varphi)}{n_p} \right] + 65^\circ \right\} \quad (6.8)$$

From equations (6.6) and (6.8), it is obvious that the penetration depth can be calculated using the inclined angle of the laser beam (φ). The distance between two adjacent evanescent wave spots, d_{eva} [m], is determined by the thickness of the glass slide, t_g [m], and the incident angle θ_i [°]:

$$d_{\text{eva}} = 2t_g \tan \theta_i \quad (6.9)$$

After a certain number of total internal reflections, the beam is finally thrown out from the movable prism, which ensures the beam exit and avoids the light scatter at the glass edge.

There are several advantages of employing the above two-prism-based illumination system compared with conventional total internal reflection microscopy (TIRM), as previously discussed in section 2.3. In comparison with an objective-based TIRM, the two-prism-based system can achieve a larger field of view with low magnification objective lens by using a glass substrate as an optical waveguide. In addition, it has wide selectivity of the thickness and material of channel substrate. Therefore, it offers more choices for channel material which has no strong Raman peaks in the wavelength range of interest. When compared to a conventional prism-based TIRM, the two-prism-based system has an advantage in accessibility to the sample, because the prisms are located in the same side as the objective lens. However, due to the same reason, the signal quality can be deteriorated by the scattering from the adjacent reflections which occurs close to the objective lens. In order to deal with this problem, a thick glass slide is preferable within the limits of the working distance of the objective lens. According to equation (6.9), the usage of a thicker glass slide results in a longer distance between the total internal reflections (d_{eva}) and decreases the number of reflections inside the glass. This leads to a reduction of the background intensity and therefore avoids the decrease in signal-to-noise ratio.

6.2.2 Experimental Apparatus

Figure 6.4 illustrates the experimental setup for total internal reflection Raman imaging. In the present study, a continuous-wave Nd:YVO₄ laser (Coherent Inc., Verdi-V6, $\lambda = 532$ nm) was used for an excitation light source. A convex lens (focal length: 160 mm) was inserted in the laser light path in order to focus the beam and to achieve the desired size of the evanescent wave spot. A microchannel fabricated from PDMS and a silica glass slide ($n_g = 1.461$, $t_g = 1$ mm) was positioned on the prisms with an immersion oil layer ($n_o = 1.515$). The focused laser beam was introduced into the prism with an inclined angle $\varphi = 60^\circ$ and guided towards the silica glass slide, which resulted in total internal reflections with the incident

angle, $\theta_i = 75^\circ$ at the glass-solution interface (from equation (6.8)). Evanescent wave spots were generated at the glass-solution interface and the molecules only in the vicinity of the interface were excited. The penetration depth of the evanescent wave was calculated to be $z_p = 91.4$ nm for silica-water ($n_s = 1.332$) interface by equation (6.6). By changing the position of the convex lens, the size of the evanescent wave spot was adjusted not to exceed the channel width in order to minimize the light scatter at the edge of the PDMS side wall. The interval of the evanescent wave spots were approximately 7.5 mm according to equation (6.9). After undergoing total internal reflections, the beam was finally thrown out from the movable prism in the opposite side.

The Raman scattering was collected through an objective lens (Nikon Corp., 10 \times , $NA = 0.25$, $WD = 7.0$ mm), a dichroic mirror (Semrock, Inc., FF555-Di03, Transmission range: > 562 nm) and an optical bandpass filter, and imaged by an EM-CCD camera (Hamamatsu Photonics K. K., C9100-13, 512×512 pixels, $16 \times 16 \mu\text{m}^2/\text{pixel}$, 16 bits). The optical filter was carefully selected based on spectral measurements in order to transmit only the characteristic Raman signal from sample solutions. The selection of the bandpass filters is detailed in the next section. The imaging region and the spatial resolution were $819 \times 819 \mu\text{m}^2$ and $1.6 \times 1.6 \mu\text{m}^2$, respectively, which were calculated based on the pixel size of the camera ($16 \times 16 \mu\text{m}^2/\text{pixel}$) and the total magnification of the system ($M = 10$). The depth of field of this measurement system was $14.9 \mu\text{m}$, which was derived from equation (2.36). However, the depthwise resolution of TIR Raman imaging is characterized by the penetration depth of the evanescent illumination ($z_p = 91.4$ nm) rather than the optical imaging system.

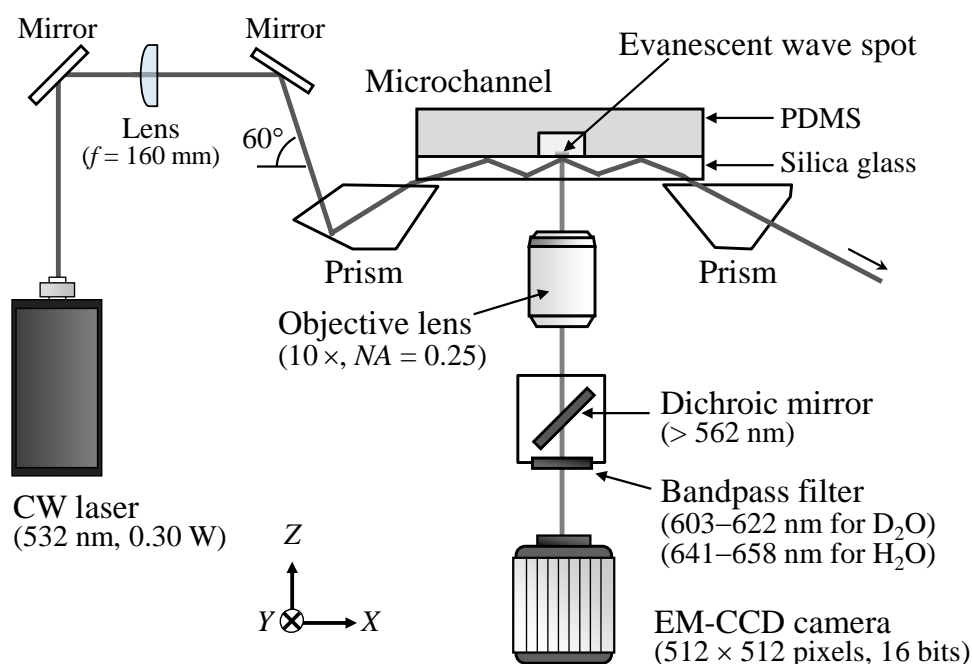


Figure 6.4. Schematic of the experimental setup for total internal reflection Raman imaging.

6.2.3 Filter Selection

Prior to the experiment of TIR Raman imaging, spectroscopic measurements were performed in order to choose the appropriate optical bandpass filters for concentration imaging, because it is important to separate the desired Raman signals (of H₂O and D₂O) from noise. In particular, the Raman scattering from a TIR substrate (a silica glass slide in the present study) can be the major concern in TIR Raman imaging, since the substrate is directly illuminated by the incident laser beam, not like the solution illuminated by the evanescent wave.

The TIR spectra were obtained by using a grating spectrometer (Solar TII Ltd., 400 groove/mm) as shown in figure 6.5. Instead of the dichroic mirror and the bandpass filter in figure 6.4, a dichroic mirror (Semrock, Inc., LPD01-532RU, Transmission range: > 539 nm), a long-pass filter (Semrock, Inc., BLP01-532R-25, Transmission range: > 547 nm) and the spectrometer were set in front of the EM-CCD camera. (The same illumination system, objective lens, and EM-CCD camera were employed.) The sample solutions were introduced into the microchannel and positioned on the prisms. The total acquisition time per spectrum was 100 s and the EM gain was set to be 650. The spectral resolution was less than 0.57 nm, which approximately corresponds to 10 cm⁻¹. The nominal laser power was set to be 0.50 W and it decayed to 0.40 W at the microscope stage. After the measurement, the obtained spectra were smoothed with a 11-points, third-order Savitzky-Golay filter (Savitzky & Golay, 1964) for noise reduction purpose.

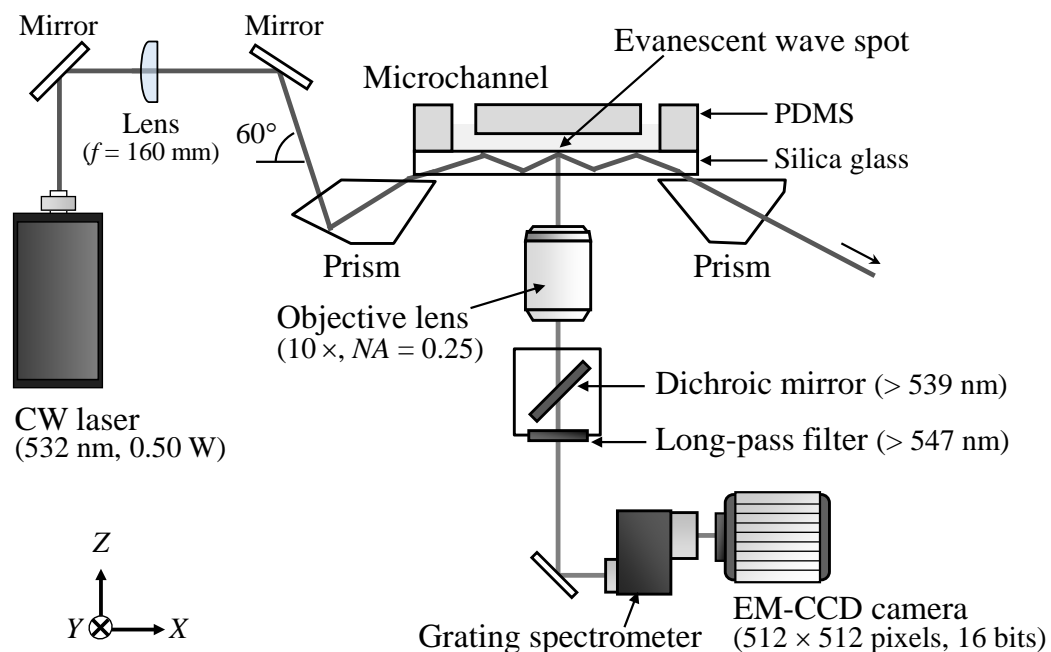


Figure 6.5. Schematic of the Raman spectroscopy system developed for filter selection.

Table 6.1. Properties of H₂O/D₂O mixtures used for the calibration experiment

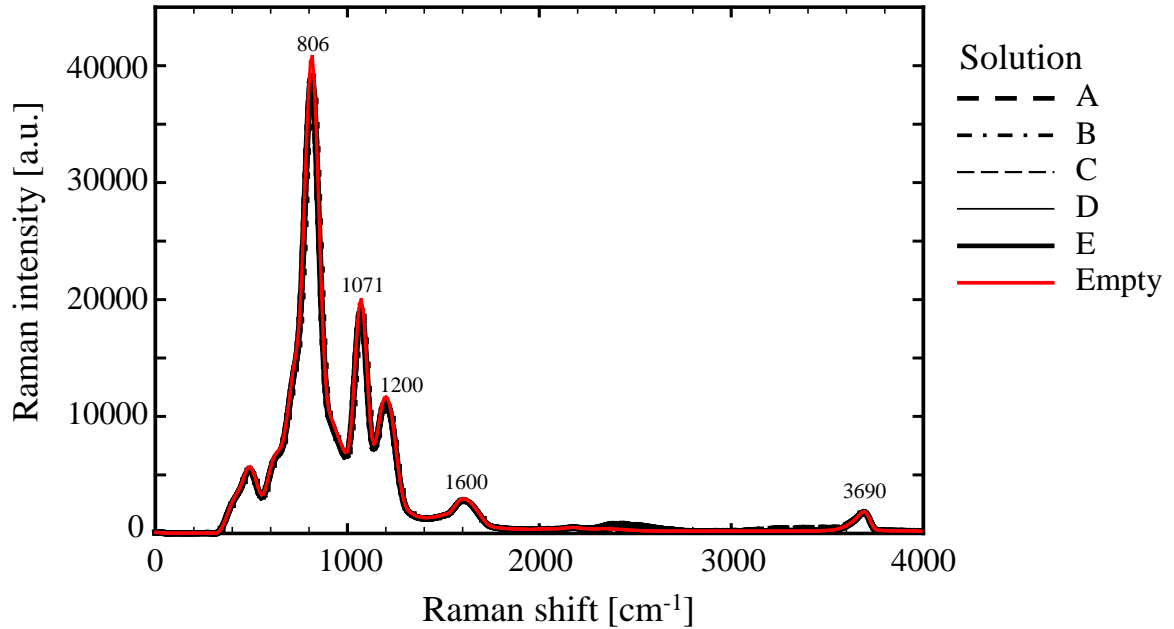
	A	B	C	D	E
H ₂ O concentration [mol%]	100	75	50	25	0
D ₂ O concentration [mol%]	0	25	50	75	100
Refractive index [-]	1.332	1.331	1.330	1.329	1.328
Penetration depth [nm]	91.4	90.8	90.3	89.7	89.2

For the spectral measurements, five different mixture solutions were prepared by mixing pure H₂O and D₂O at different mole fractions, as listed in table 6.1. The penetration depth of the evanescent wave was calculated for each mixture by using its refractive index measured by a refractometer (Atago Co., Ltd., PAL-RI). The refractive index was slightly different depending on the mixture composition, but the penetration depth was calculated to be approximately 90 nm for all the mixtures. Therefore, the following experiments were conducted with the assumption that the difference in the penetration depth has little influence on the detected intensity.

Figure 6.6(a) shows the TIR Raman spectra from the H₂O/D₂O mixtures (in table 6.1) and that from an empty channel (i.e., filled with ambient air) in the spectral range of 0–4000 cm⁻¹. It is noted that the spectral information in the range 0–520 cm⁻¹ is lacked due to the transmission range of the long-pass filter (> 547 nm). All the spectra in figure 6.6(a) exhibit similar spectral shape with strong peaks at 806, 1071, and 1200 cm⁻¹, and relatively weak peaks at 1600 and 3690 cm⁻¹. Since these peaks are observed for the empty channel (shown as red line), they are considered to arise from channel material, prisms, or immersion oil, but not from the content of the microchannel. In addition, most of the above spectral features are consistent with the previously-reported Raman peaks of pure silica glass by Shibata *et al.* (1981) (in table 2.6). Thus the major portion of the spectra in figure 6.6(a) is attributed to the Raman scattering from the silica glass slide being used as a bottom wall of the channel (i.e., the TIR substrate).

Although the Raman signal from silica glass is dominant in the obtained spectra, the TIR Raman scattering from the H₂O/D₂O mixtures inside the channel can be observed in figure 6.6(b), where the enlarged view in the range 1500–4000 cm⁻¹ is shown. In addition to the Raman bands at 1600 and 3690 cm⁻¹, the relatively weak signals from O-H and O-D stretching vibrations can be observed around 3400 cm⁻¹ and 2500 cm⁻¹, respectively. Their band shapes are distorted by the signal from the substrate, but it can be seen that their intensities increase slightly with the concentration of the corresponding species.

(a)



(b)

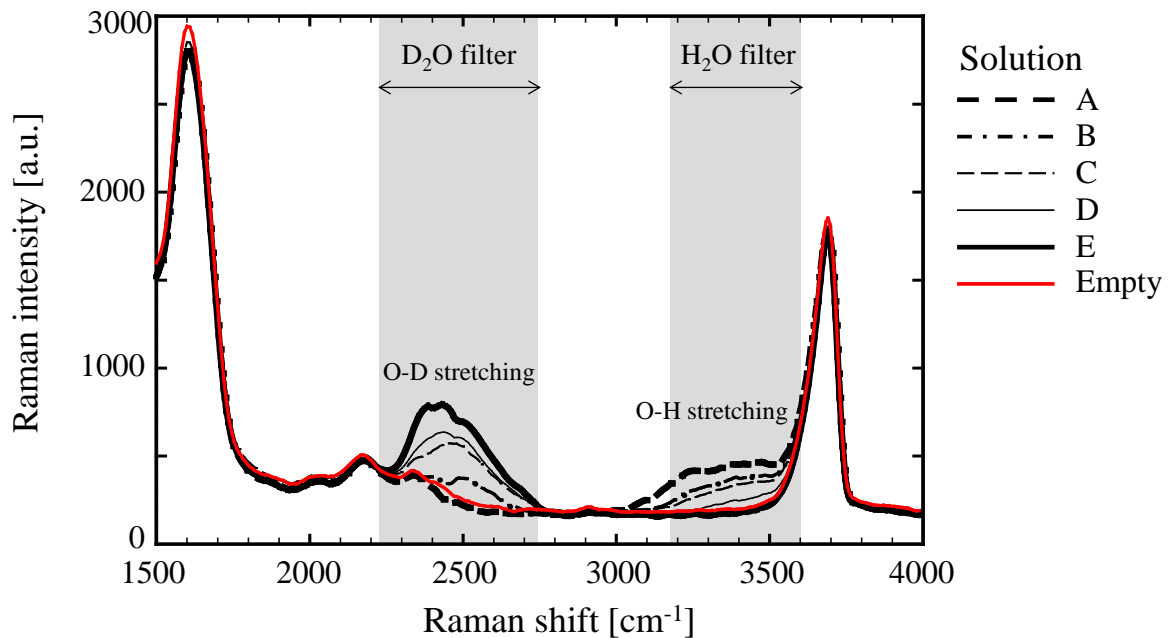


Figure 6.6. Total internal reflection (TIR) Raman spectra from the microchannel filled with the H₂O/D₂O mixtures. The spectrum shown as a red line represents the TIR Raman spectrum from an empty channel (i.e., filled with ambient air). (a) The TIR spectra in the range 0–4000 cm⁻¹ and (b) the enlarged view of the same spectra in the range 1500–4000 cm⁻¹.

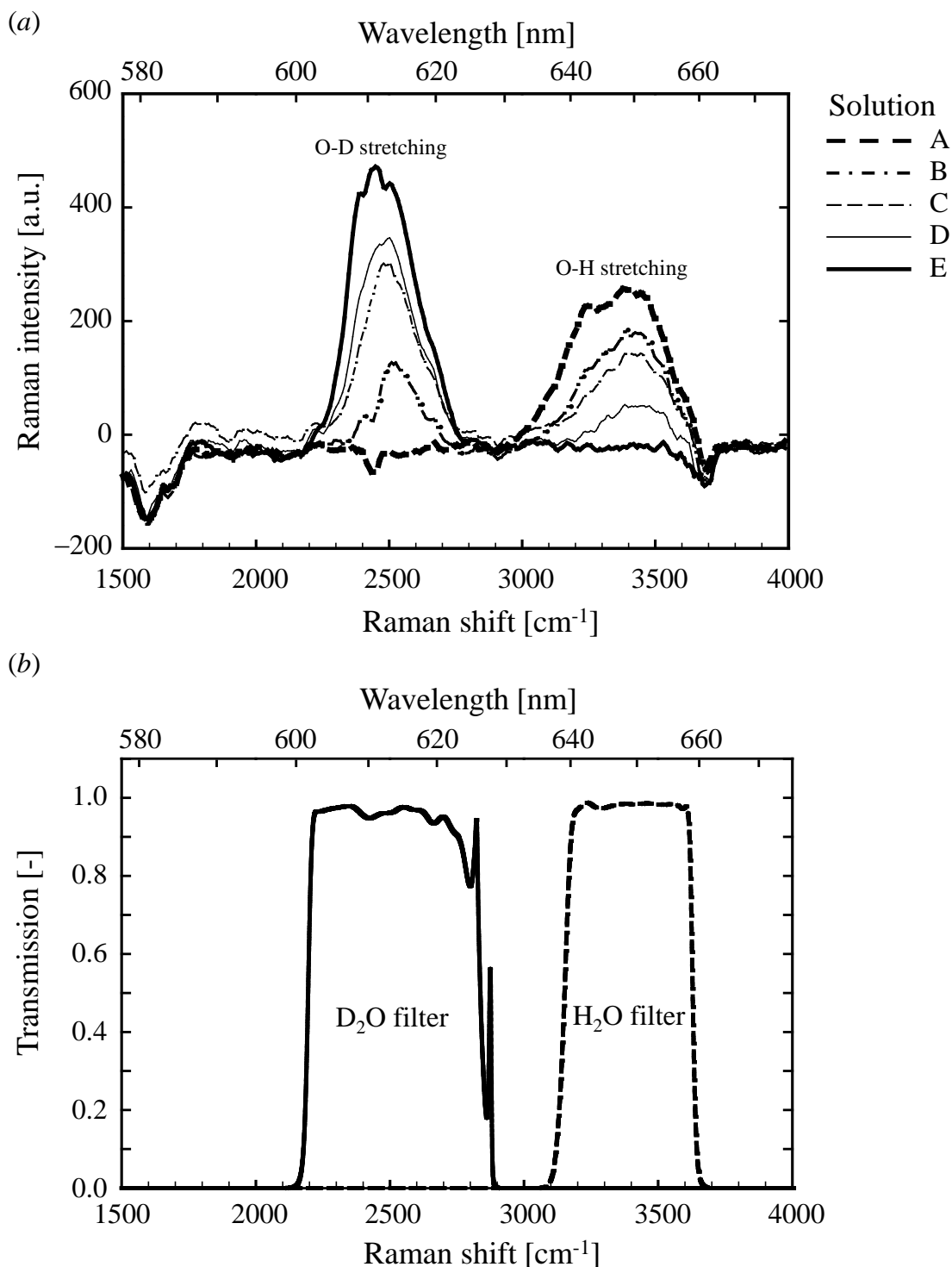


Figure 6.7. (a) Difference Raman spectra of H₂O/D₂O mixtures which were calculated from the TIR spectra (figure 6.6(b)) by subtracting the spectrum obtained with an empty channel as a reference. (b) Spectral transmittance characteristics of H₂O and D₂O filters (Semrock Inc., FF01-650/13-25 (<http://www.semrock.com/FilterDetails.aspx?id=FF01-650/13-25>, December 8, 2014) for H₂O and FF01-615/20-25 (<http://www.semrock.com/FilterDetails.aspx?id=FF01-615/20-25>, December 8, 2014) for D₂O).

In order to remove the background signal from the silica substrate and show the TIR Raman signal from mixtures more clearly, difference spectra were calculated for the solutions by subtracting the reference spectrum of the empty channel depicted as red line in figure 6.6. The obtained spectra are shown in figure 6.7(a). The horizontal axis in the upper side is the wavelength of the scattered light excited at 532 nm. The obtained difference spectra exhibit the characteristic band shapes of O-H and O-D stretching modes as in the bulk spectra (figure 6.3). The intensity change with mixture composition is also clearly confirmed.

According to the above spectral measurement result, two optical filters were selected for concentration imaging; one is for H₂O with transmittance wavelength of 641–658 nm (Semrock, Inc., FF01-650/13-25) and the other is for D₂O with transmittance wavelength of 603–622 nm (Semrock, Inc., FF01-615/20-25). Figure 6.7(b) shows the spectral transmission characteristics of these filters. Their transmittance ranges are also shown in figure 6.6(b) by colored areas and arrows. From these figures, it is confirmed that their transmittance ranges correspond to the O-H and O-D stretching Raman bands, and that there is little overlap with the Raman peaks from TIR substrate.

Finally, the integrated intensity in the transmission band of the selected filter was calculated for each TIR spectrum (shown in figure 6.6), and plotted against the concentration in figure 6.8. It is obvious that the integrated intensity for each filter linearly increased with the concentration of corresponding species. This result implies that the near-wall concentration measurement of desired species can be realized by TIR Raman imaging by utilizing the selected filters.

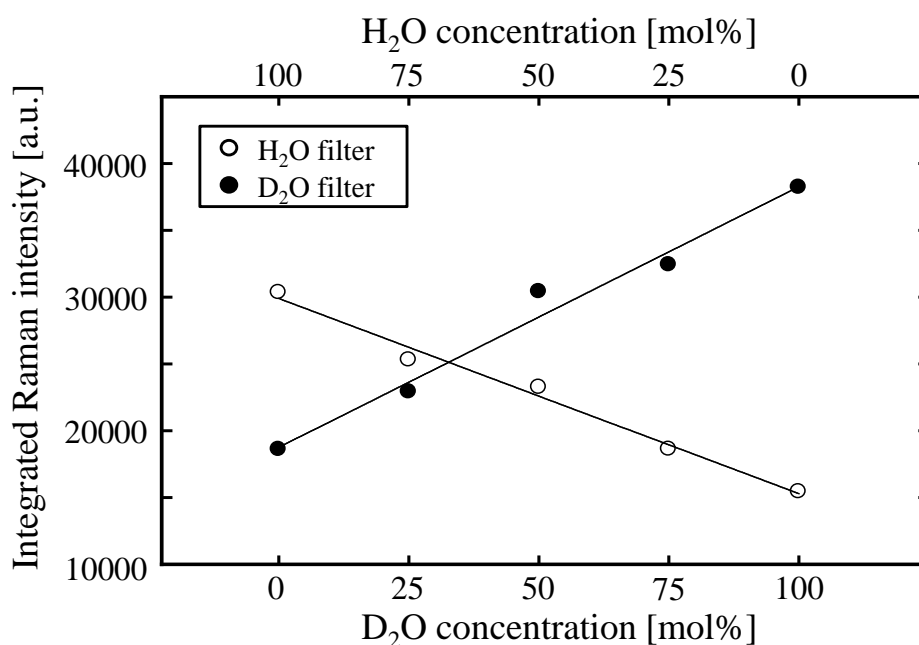


Figure 6.8. The relationship between the concentration and the integrated intensity in the transmission band of the selected filters (calculated from TIR spectrum shown in figure 6.6).

6.3 Calibration Experiment for Total Internal Reflection Raman Imaging

Utilizing the selected filters, a calibration experiment was carried out in order to examine the relationship between the concentration and the Raman intensity excited by the evanescent wave. TIR Raman images were captured under uniform concentration conditions, and the detected intensity was plotted against the concentration.

The H₂O/D₂O mixture solutions whose properties are shown in table 6.1 were used in the calibration experiment. Each mixture was introduced into a microchannel with a height of 50 μm (figure 6.9), whose structure was molded by soft lithography (with the process detailed in section 2.4), and enclosed by a silica glass slide ($t_g = 1$ mm, diameter: 50 mm) by utilizing self-adherence of PDMS. In order to remove the dust attached on the surface, the silica glass slide was previously cleaned in a ultrasonic bath sonicator with methanol and pure water. Since equation (6.6) assumes that the total internal reflection occur at a planar surface, i.e., for the case where the surface roughness is much smaller than the wavelength (Kazoe & Yoda, 2013), the surface roughness of the silica glass slide was examined by an optical surface profiler based on scanning white light interferometry (Zygo Corp., New View TM6200). It was approximately 0.7 nm in arithmetic average roughness. Thus the glass surface was regarded as a flat surface. The penetration depth was calculated to be approximately 90 nm (in Table 6.1), and the thickness of the evanescent wave layer was estimated to be within 210 nm based on the $2.3z_p$ value according to the explanation in section 2.3.2.

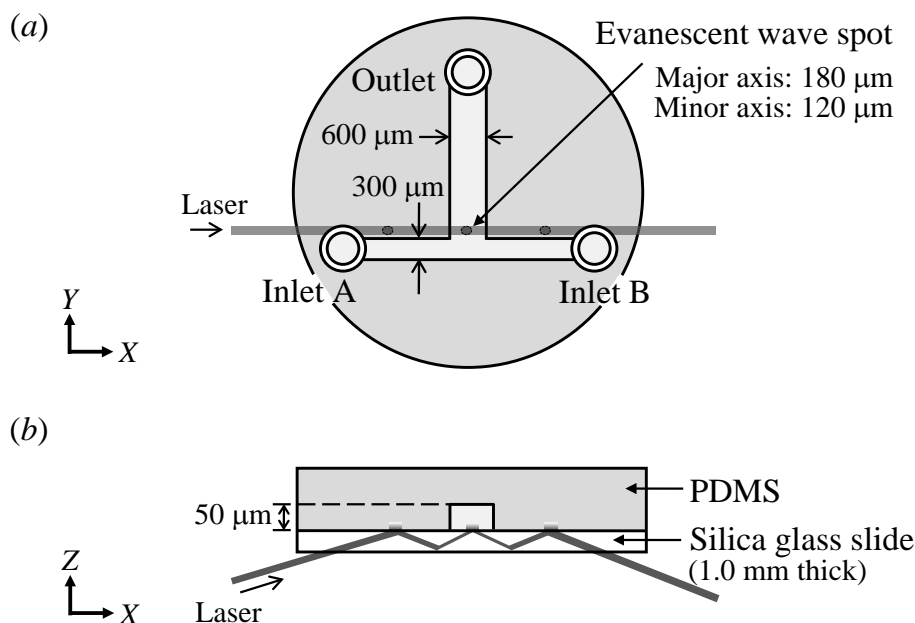


Figure 6.9. (a) Top and (b) cross-sectional views of the T-shaped microchannel.

The solution-filled microchannel (shown in figure 6.9(a)) was positioned on the prisms, and the TIR Raman scattering from the second evanescent wave spot was observed in the experiments. The incident angle of 75° allowed the first and third total internal reflections at silica-PDMS interface as well as silica-solution interface. The laser power was 0.30 W at the sample stage with an ellipsoidal evanescent spot (major axis: $180\ \mu\text{m}$, minor axis: $120\ \mu\text{m}$). The exposure time and the EM gain of the camera were set to be 3 s and 330, respectively, and 10 images were accumulated for each condition.

Figure 6.10 shows the temporally averaged TIR Raman images of three different mixtures (mixtures A, C, and E in table 6.1) obtained through the H_2O and D_2O filters. These images visualize the TIR Raman intensity distributions of 100×100 pixels ($160 \times 160\ \mu\text{m}^2$) in the second evanescent wave spot whose position is indicated by a white dashed line. It is visually apparent that the intensity detected through the H_2O filter decreases with a decrease in H_2O concentration, whereas that obtained through the D_2O filter increased. This result indicates that these two filters are adequate for concentration imaging of the corresponding species. Note that these images represent the distribution of the raw TIR Raman intensity $I_{i, \text{eva}}$, i.e., the influence of the non-uniform excitation intensity is yet to be cancelled out. Therefore, they have intensity distributions due to the ellipsoidal intensity profile of the evanescent wave spot according to equation (6.3), in spite of uniform concentration condition. These images are also considered to be influenced by the scattered light which is arising from dust or bubbles. Subsequently, the relationship between the Raman intensity and the concentration of each species was quantified by using the TIR Raman images in figure 6.10. The intensities at five points in the evanescent wave spot were extracted from each image as shown in figure 6.11, and plotted against the concentration. The Raman intensities at the five locations which were detected through H_2O and D_2O filters were shown in figure 6.12(a) and (b), respectively. The lower horizontal axis is the D_2O concentration of the mixture and the upper axis shows the H_2O concentration. It is confirmed from these figures that the Raman intensities at the five locations increased with the concentration of the corresponding species.

However, as explained above, the raw Raman intensity can vary widely depending on the location due to the Gaussian-like laser profile, which is problematic for the visualization of planar concentration maps. Therefore, in order to compensate the influence of this inhomogeneous intensity profile, the Raman intensities in figure 6.12 were normalized by a reference intensity according to equation (6.4). The intensity values obtained from solution C (i.e., the intensities at 50 mol%) were chosen as the reference value. This yields the relationships between the concentration and the normalized Raman intensities, as shown in figure 6.13. The normalized intensities of H_2O and D_2O filters (which are shown in figures 6.13(a) and (b)) exhibit almost linear increase with H_2O and D_2O concentrations, respectively.

Finally, a linear least-squares fit provides the solid straight lines in figure 6.14, which served as calibration curves for subsequent concentration measurement. The error bars in

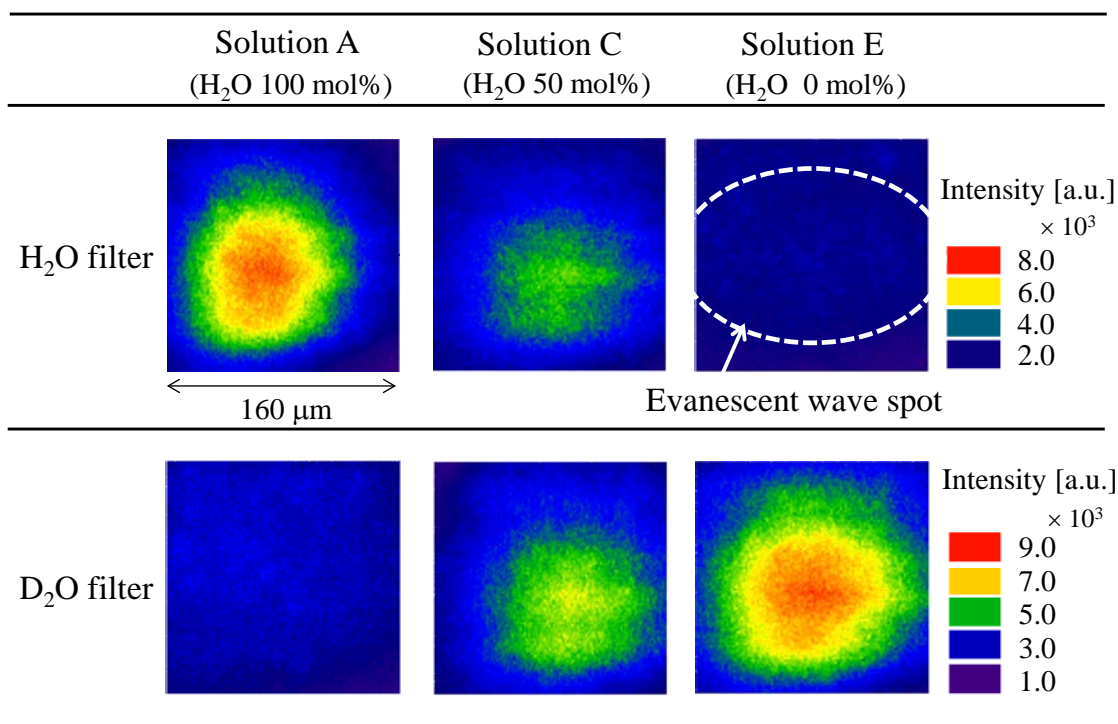


Figure 6.10. Temporally averaged Raman images obtained from mixtures A, C and E through H₂O and D₂O filters. A white dashed line represents the position of the evanescent wave spot.

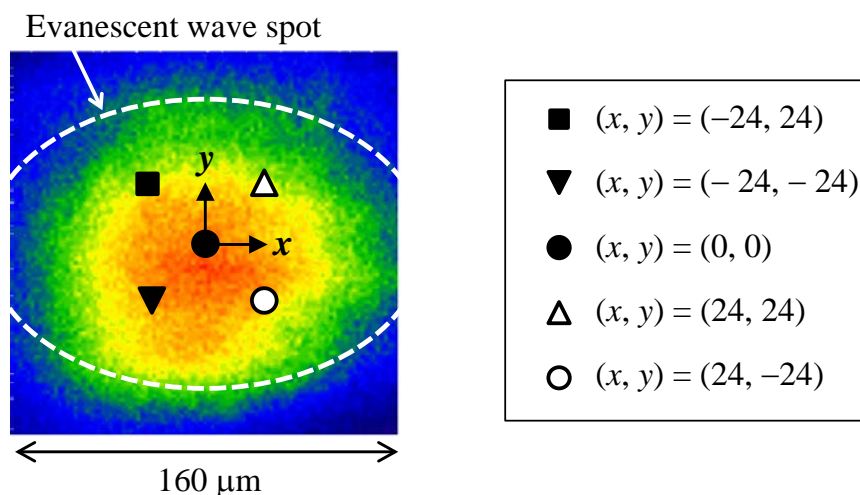


Figure 6.11. Five points in the evanescent wave spot whose intensities were extracted for calibration.

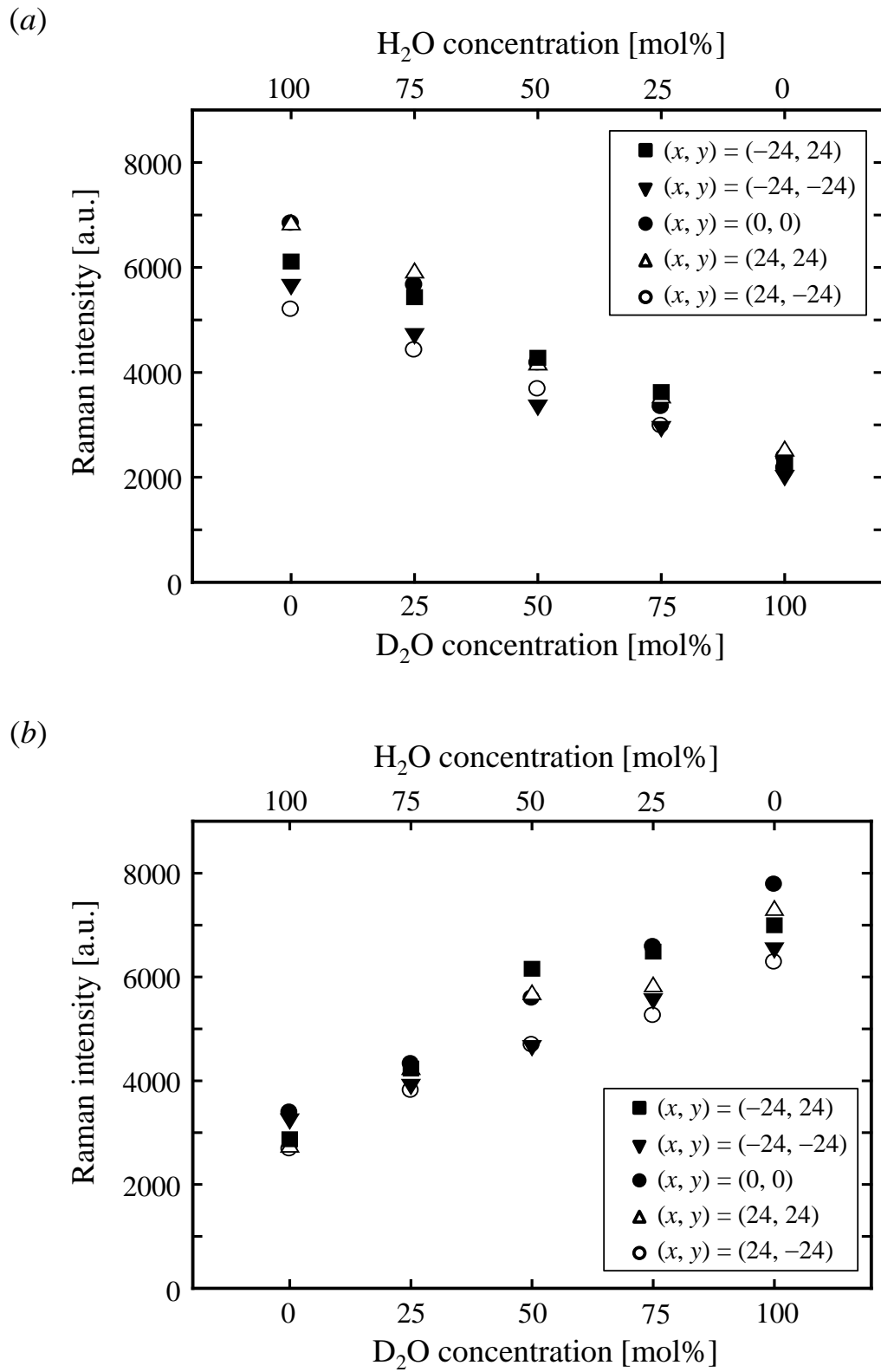


Figure 6.12. Relationship between the concentration and the detected Raman intensity (a) detected through H₂O filter and (b) D₂O filter.

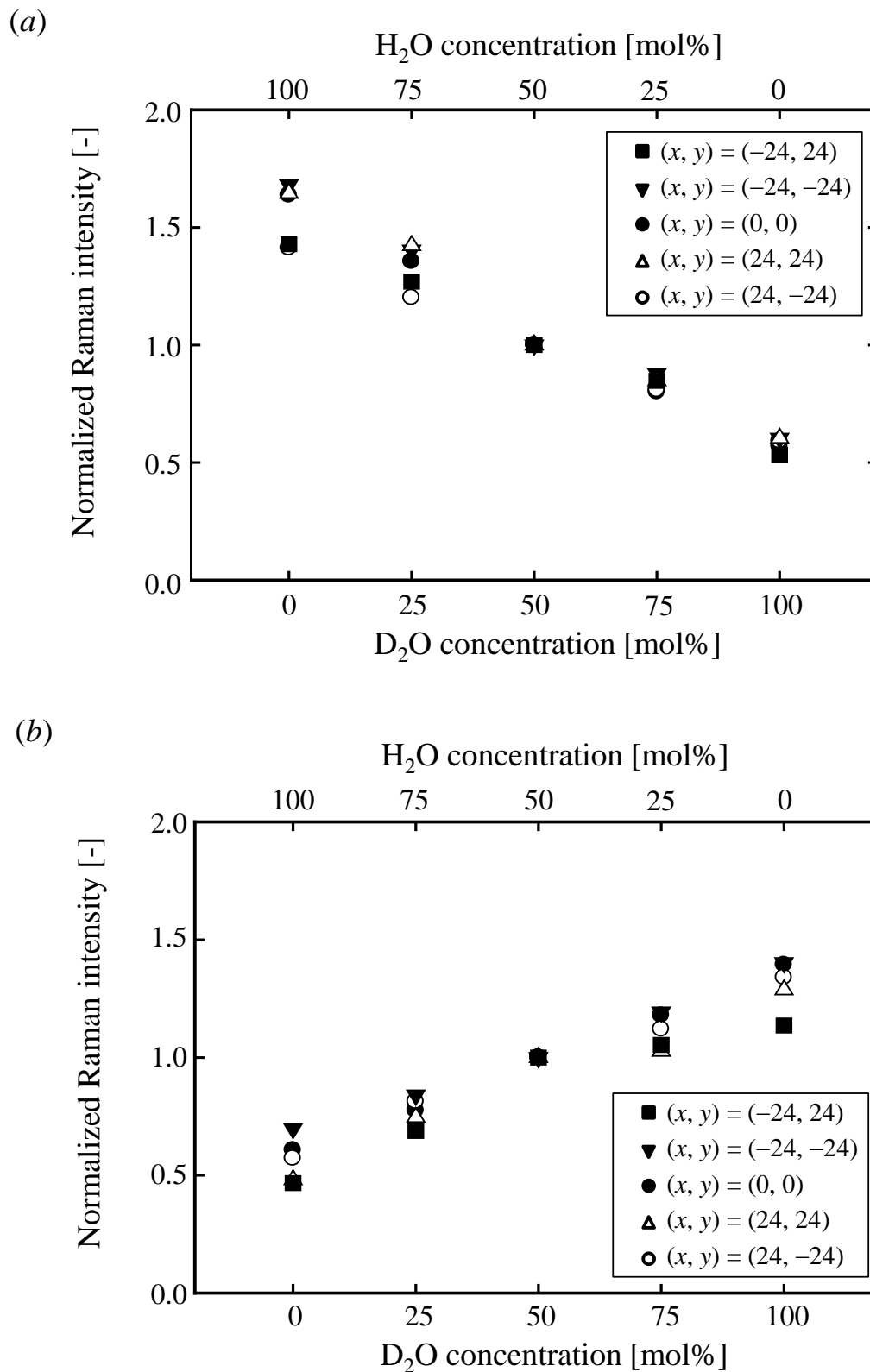


Figure 6.13. Relationship between the concentration and the normalized Raman intensity calculated from (a) the intensities detected through H₂O filter (figure 6.12(a)) and (b) those detected through D₂O filter (figure 6.12(b)).

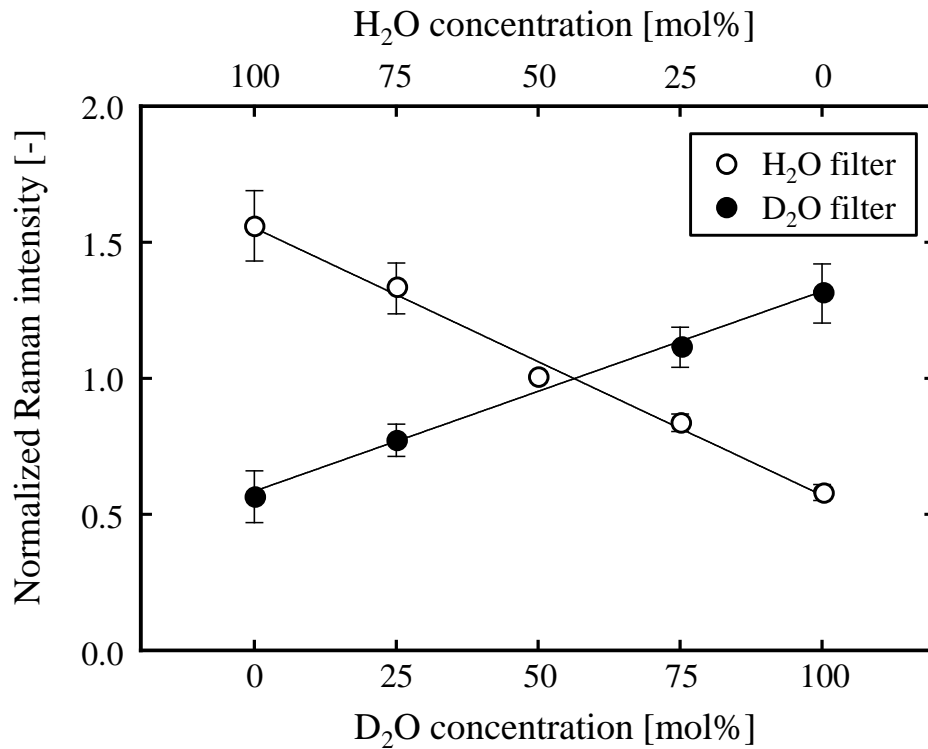


Figure 6.14. Calibration curves between the normalized Raman intensities and the concentration.

figure 6.14 represent the standard deviation of the normalized intensity between the five points. By applying this calibration result, Raman images can be converted into concentration maps of H₂O and D₂O. It is noted that the above the calibration procedure was the same as that employed in work by Sato *et al.* (2003) where planar temperature measurements were performed by LIF technique.

6.4 Visualization of Near-Wall Concentration Distributions

Using the above calibration result, near-wall concentration measurement was performed in the non-uniform mixing flow field in the T-shaped microchannel (figure 6.9). Pure H₂O and D₂O were injected into the channel by using a syringe pump from Inlets A and B, respectively. The flow rate was set at 20 $\mu\text{L}/\text{min}$ for each liquid, and the bulk velocity was calculated to be 22 mm/s in the main channel (width: 600 μm). This corresponds to the Reynolds number of about 2.3. The diffusion Peclet number $Pe_D (= Re \cdot Sc)$ was roughly estimated to be on the order of 10^3 , since the Schmidt number for liquids is typically $Sc \approx 10^3$, as mentioned in

section 2.1. Such a large Schmidt number represents that convection dominates over diffusion in the present experimental condition. The position of the second evanescent wave spot was positioned around the junction area where the two liquids merged (figure 6.15(a)). The conditions for the data acquisition (such as laser power, exposure time, EM-gain, and the frame number of accumulation) were set to be the same as the calibration experiment.

Figures 6.15(b) and (c) give the measurement results for H₂O and D₂O concentrations, respectively, obtained by using the corresponding filters and the calibration curves. The non-uniform concentration distributions were visualized at a spatial resolution of 1.6 × 1.6 μm² in the evanescent wave spot. Although the concentration around the edge of the spot seems to suffer from lower signal level, it is clear that H₂O concentration is generally higher in right-hand side and D₂O concentration was higher in the left-hand.

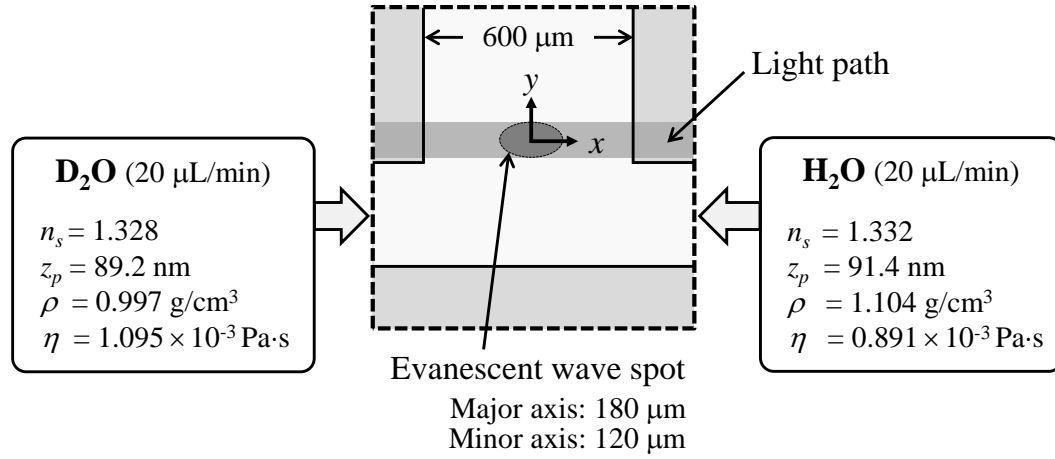
The concentration profile at y = 0 μm is plotted against the x-position for each species in figure 6.16(a). Each plot represents the value which was spatially averaged over 8 pixels along the y-axis (i.e., averaged within the area of 1.6 × 12.8 μm² centered at y = 0 μm). The concentration gradient can be observed at -30 μm ≤ x ≤ 30 μm, which exhibits the mixing behavior of H₂O and D₂O at the junction area. The summation of the measured H₂O and D₂O concentrations were also plotted along the x-axis in figure 6.16(b). It is obvious that the total concentration tends to exceed 100 mol% for most locations, which implies that the measured concentrations are higher than actual concentrations. This may be attributed to the influence of the temporal change in excitation conditions, or in background intensity from channel substrate and some impurities in mixtures. Although further investigations are required for more accurate measurements, these results clearly demonstrate the availability of TIR Raman imaging for chemically-selective visualization of molecular distributions in the vicinity of the channel wall.

Finally it should be noted that the concentration maps in figure 6.15 represent the ‘initial concentration’ without consideration of isotopic exchange reaction between H₂O and D₂O:

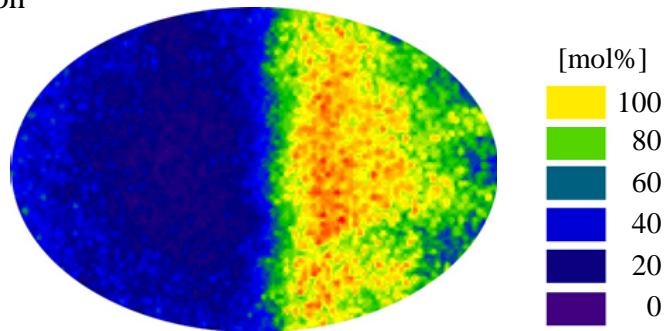


Thus, a mixture of H₂O and D₂O actually contains H₂O, D₂O and HOD in equilibrium and the equilibrium constant K_e [-] can be expressed as $K_e = [\text{HOD}]^2 / ([\text{H}_2\text{O}] \cdot [\text{D}_2\text{O}])$. Since the kinetics of the above reaction is very fast (i.e., diffusion-controlled), the chemical equilibrium is reached instantaneously at each location in a microchannel (Sarrazin *et al.*, 2008). Therefore the local concentration of each component is related to the equilibrium constant K_e through equation (6.10). When the initial concentration (expressed as mole percentage) of D₂O is ψ [mol%], the equilibrium concentration of H₂O, D₂O, and HOD in the H₂O/D₂O mixture are given by (100 - ψ - ϕ /2), (ψ - ϕ /2), and ϕ [mol%], respectively, where ϕ can be derived from,

(a) Measurement area



(b) H_2O concentration



(c) D_2O concentration

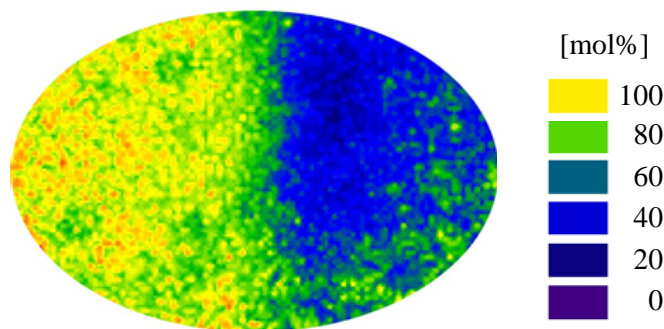


Figure 6.15. (a) Measurement area at the junction of the T-shaped microchannel (shown in figure 6.9), and two-dimensional distributions of (b) H_2O concentration and (c) D_2O concentration. The maps represent the ‘initial concentration’ without consideration of isotopic exchange reaction ($H_2O + D_2O \leftrightarrow 2HOD$).

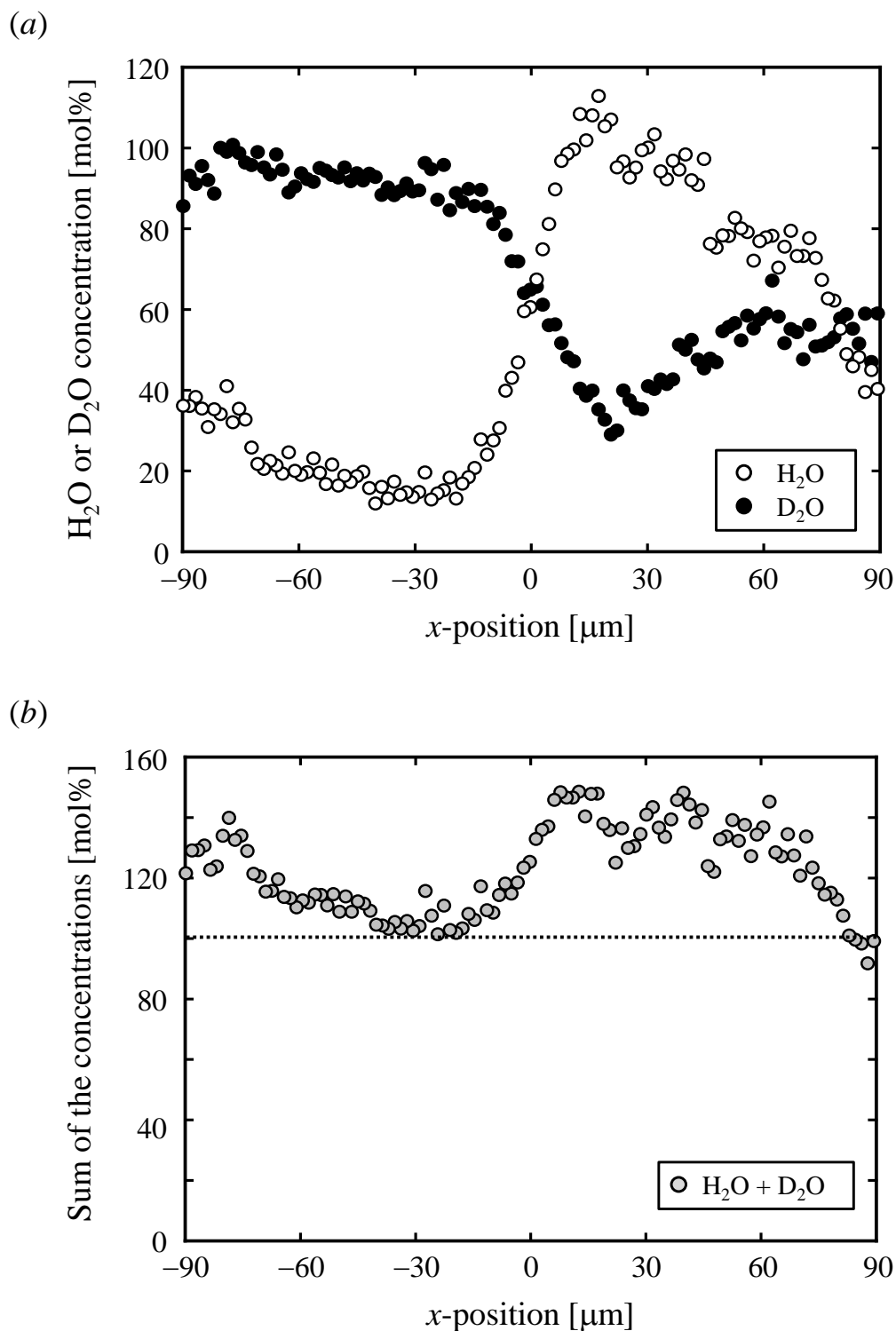


Figure 6.16. (a) X-directional concentration profiles of each species at $y = 0 \mu\text{m}$ (calculated from figures 6.15 (b) and (c)). (b) X-directional profile of the sum of the measured H₂O and D₂O concentrations.

$$K_e = \frac{\phi^2}{(100 - \psi - \phi/2)(\psi - \phi/2)} \quad (6.11)$$

The value of K_e for liquid phase is reported to be $K_e = 3.88$ at room temperature by Libnau *et al.* (1995). Using equation (6.11), the equilibrium concentration maps can be estimated from the initial concentration maps.

6.5 Concluding Remarks

A non-intrusive and surface-sensitive measurement technique utilizing spontaneous Raman scattering excited by an evanescent wave, which is termed total internal reflection (TIR) Raman imaging, was developed for the planar visualization of near-wall concentration in microchannels. The usage of an evanescent wave, which illuminates only the vicinity of the interface with the order of 100 nm, enabled the surface-selective excitation of spontaneous Raman process. Mixture solutions composed of H₂O and D₂O were selected as sample liquid since they have well-separated Raman bands (around 2500 cm⁻¹, 3400 cm⁻¹ respectively) and comparable refractive indices (~ 1.33). The near-wall concentration of each species was obtained from the TIR Raman image exploiting the relationship between the spontaneous Raman intensity and the number of illuminated molecules.

In order to obtain TIR Raman images, a two-prism-based evanescent wave illumination system was coupled to a Raman imaging system. The evanescent wave was generated at the interface between the microchannel wall and the mixture, by using the channel's bottom wall as an optical waveguide. This configuration allowed the measurement with large field of view with low magnification objective lens (10×, NA = 0.25), and the usage of 1-mm-thick silica glass as a channel substrate.

Prior to the experiment, spectroscopic measurements of TIR Raman scattering were conducted to select the appropriate optical bandpass filters. Although the characteristic O-H and O-D stretching Raman bands were partially overlapped with the signal from silica glass which serves as a TIR substrate, the spectral change was clearly observed with change in mixture compositions. Based on the measured spectra, a suitable filter was selected for each component (H₂O and D₂O) from commercially available ones.

Using the selected filters, a calibration experiment was carried out. The calibration result exhibited that the TIR Raman intensity detected through each filter was directly proportional to the concentration of corresponding species. By applying this relationship, the near-wall concentration measurement was demonstrated within an ellipsoidal evanescent wave spot (major axis: 180 μm, minor axis: 120 μm) positioned at the junction area of a T-shaped

Visualization of Near-Wall Concentration Distribution...

microchannel where H₂O and D₂O merged. The concentration map of each component was clearly visualized with lateral spatial resolution of $1.6 \times 1.6 \mu\text{m}^2$ and temporal resolution of 30 s. The penetration depth of the evanescent wave was calculated to be approximately 90 nm. The obtained concentration map for each species successfully visualized the concentration gradient at the junction area, which implies the availability of TIR Raman imaging for chemically-selective measurement of molecular distributions in the vicinity of the channel wall.

Chapter 7

Conclusions and Recommendations

Recent advances in miniaturized fluidic systems have stimulated the development of various measurement techniques for monitoring microscale thermofluid behavior, since it plays a decisive role in enhancing efficiency and functionalities of such systems. Currently, fluorescence-based techniques are most commonly used since they can provide two-dimensional information of vector or scalar fields with high spatiotemporal resolution. However, they have an inherent disadvantage of employing extrinsic fluorescent labels which can potentially alter the sample properties and flow fields due to the electrochemical and toxic influences. Therefore, label-free measurement techniques are required especially for microfluidic systems which deal with electrokinetic phenomena or biological samples. The present study proposed a series of novel methodologies based on spontaneous Raman imaging to realize non-intrusive, chemically-selective, and two-dimensional measurements in microfluidic systems. The conclusions are described below.

7.1 Conclusions

The present study addressed the development of measurement techniques for temperature (in chapters 3 and 4), velocity (in chapter 5), and near-wall concentration (in chapter 6). The conclusions are summarized for each target. The spatial and temporal resolutions achieved in this study are presented and compared with those of the previous studies in figure 7.1. It should be noted that the temporal resolution in figure 7.1 is defined as the time required for obtaining a single Raman image, and the spatial resolution is defined as the size of the area which is imaged onto one binned pixel. However, only for the target of the near-wall concentration measurement in chapter 6, it is defined by that in the depthwise direction which is characterized by the penetration depth of the evanescent illumination.

7.1.1 Development of Non-intrusive Visualization Techniques for Microscale Temperature Field

Non-intrusive planar temperature measurement techniques were developed based on spontaneous Raman imaging both for steady and unsteady temperature fields. The techniques exploited the Raman signal of 3000–3800 cm^{-1} arising from OH stretching vibrations. From the spectral measurement of liquid water, contrasting temperature dependencies of Raman intensity were observed above and below the isosbestic point due to the temperature-related change in hydrogen bonding. These wavenumber ranges were termed hydrogen-bonded (HB) and non-hydrogen-bonded (NHB) modes, and an optical bandpass filter was selected for each mode in order to determine temperature distributions from the ratio of the HB to NHB Raman images. The major advantage of this ratiometric procedure was that the influence of the spatial non-uniformity in excitation intensity can be cancelled out, which enabled the planar temperature determination for any excitation profile.

A fundamental form of a direct Raman imaging system, which consisted of the selected filter and an EM-CCD camera, was initially constructed for the visualization of steady-state temperature. Subsequently it was developed into a two-wavelength Raman imaging system for the measurement of unsteady temperature fields. The two-wavelength imaging system was comprised of two bandpass filters and two EM-CCD cameras, which enabled the simultaneous imaging of Raman signals with different wavelengths, i.e., intensity ratio of HB to NHB images could be obtained with a single measurement without the need for manual switching of the filters. The system also allowed the compensation of the temporal fluctuation of the excitation light.

According to the calibration experiments, it was confirmed for both techniques that the intensity ratio of HB to NHB modes almost linearly decreased with increasing temperature in the range approximately 293–333 K. The temperature sensitivity was calculated to be comparable for the two techniques ($-0.59\% \text{ K}^{-1}$ and $-0.58\% \text{ K}^{-1}$), but the uncertainties associated with the regression were 3.7 K and 1.4 K at a 95% confidence level for the fundamental and the two-wavelength Raman imaging techniques, respectively.

By applying the calibration curves, planar temperature measurements were performed at the junction of milli-channels where warm water and room-temperature water mixed. First, measurements were performed for steady-state temperature fields in a T-shaped milli-channel using the fundamental Raman imaging technique. Non-uniform temperature distributions were quantitatively visualized for all the heating conditions at a spatial resolution of $12.8 \times 12.8 \mu\text{m}^2$ (averaging over 8×8 pixels) with total acquisition time of 30 s. Subsequently, the two-wavelength Raman imaging was applied to unsteady temperature field in a Y-shaped milli-channel. Time-series temperature distributions were visualized at spatial resolution of $6.0 \times 6.0 \mu\text{m}^2$ (averaging over 4×4 pixels) with nearly half acquisition time (16.5 s). The

temporal evolution of the measured temperature agreed well with that probed by thermocouples with the standard mean error of 0.31 K. These results clearly showed the applicability of the Raman imaging techniques to *in-situ* monitoring of two-dimensional temperature distributions in a microscopic thermal flow field.

7.1.2 Investigation of Measurement Conditions of Two-Wavelength Raman Imaging for Velocity Determination

A fluorescence-free methodology for velocity determination was proposed based on thermal tracing by time-series temperature measurement using two-wavelength Raman imaging technique. The proposed method could not be demonstrated in the present study, but its applicability was examined focusing on the error in temperature measurement.

In order to realize velocity determination by using a thermal tracer which is given by a pulsed heating, the position of the tracer must be identified from the time-series temperature measurement. In this case, the main concern is the large error of temperature measurement due to the short acquisition time. According to the calibration result, it was confirmed that the short exposure time (30.5 ms) resulted in a large variation in the Raman intensity ratio (equivalent to 9.1 K in temperature) even in the almost uniform temperature condition. This was significantly larger than the previously-reported value of 1.5 K (which was obtained with a long integration time of approximately 15 s).

In order to examine the influence of measurement conditions on the variation in intensity ratio (i.e., apparent temperature variance within the target area), Raman images were acquired with varying EM gain, size of the measurement area, and binning factor for spatial averaging. From these results, the measurable maximum velocity in the streamwise direction was roughly estimated to be 36.5 mm/s and the temperature rise required for thermal tracing was estimated to be larger than 7.6 K, when the gain, measurement area, and binning factor were set to be 120, 300×200 pixels, and 4×4 pixels, respectively, in the developed system.

Although it should be emphasized that the velocity measurement by the proposed methodology is considered to be possible only when the quick heating is achieved with an appropriately-designed heating system, the present study is expected to contribute to the development of a non-intrusive Raman-based velocimetry in microscale, providing a method for optimizing measurement conditions for a target flow field.

7.1.3 Development of Non-intrusive Visualization Technique for Near-Wall Concentration Field

A non-intrusive and surface-sensitive concentration measurement technique, termed total internal reflection (TIR) Raman imaging, was developed for the visualization of near-wall

Conclusions and Recommendations

molecular distributions in microchannels. A two-prism-based evanescent wave illumination system was coupled to a Raman imaging system in order to selectively excite the near-wall molecules by an evanescent wave.

Mixture solutions composed of H₂O and D₂O were selected as sample liquid, and the near-wall concentration of each species was calculated from the TIR Raman images obtained through the filter which was selected for H₂O or D₂O. The calibration experiments showed that the TIR Raman intensity detected through each filter was directly proportional to the concentration of corresponding species. By applying this relationship, the near-wall concentration measurement was demonstrated within an ellipsoidal evanescent wave spot (major axis: 180 μm, minor axis: 120 μm). The non-uniform concentration map was successfully visualized for each species with lateral spatial resolution of 1.6 × 1.6 μm² and temporal resolution of 30 s. The depthwise resolution was considered to be characterized by the penetration depth of approximately 90 nm. It can be concluded that the results obtained in this study proved the feasibility of the TIR Raman imaging technique for quantitative visualization of near-wall molecular distributions for analyzing surface-related phenomena.

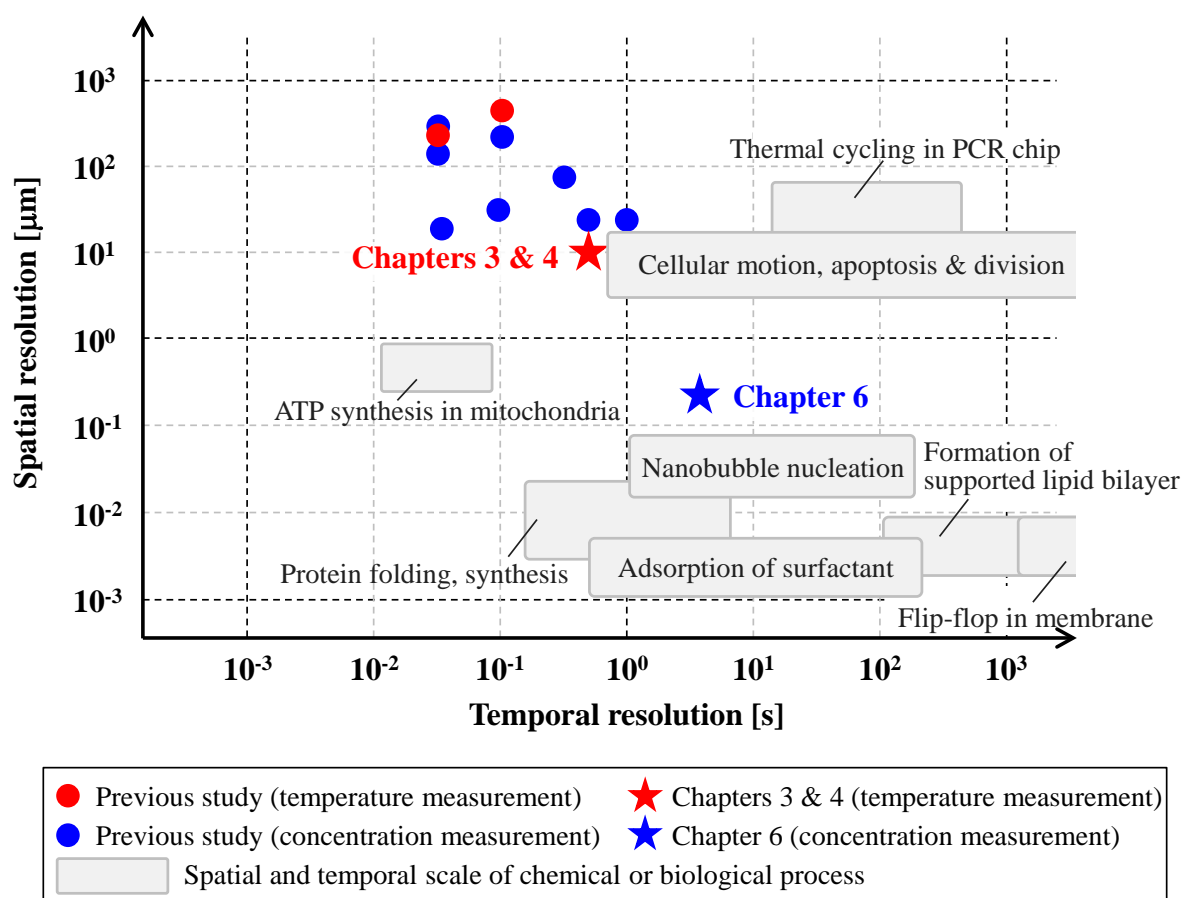


Figure 7.1. Spatiotemporal resolution achieved in the present study and the characteristic scale of various chemical or biological processes.

7.2 Recommendations for Future Research

In order to establish the proposed techniques as practical and versatile approaches for flow analysis or monitoring in various microfluidic systems, there are some technical issues to be addressed in future research. First, this section describes such future issues.

As for the temperature measurement based on Raman imaging, investigations into the composition-related spectral change of OH stretching band in water-based media (such as buffer solutions and living cells) will be required for extending its versatility, although the present study treated only pure water for simplicity. Demonstration of the present technique for more complicated samples containing inorganic ions, organic compounds or biological samples will lead to the future application in various microfluidic systems for the analysis and control of the chemical reactions or biological processes. Moreover, the calibration experiment should be carried out in broader temperature range, which will provide useful information to investigate the limitation of the present technique exploiting the temperature sensitivity of the OH stretching Raman bands. According to the previous study (Walrafen *et al.* 1986), the intensities of HB and NHB modes clearly decreased and increased with temperature, respectively, in the range 276–345 K. The calibration result in the present study exhibited the almost linear temperature dependence of the Raman intensity ratio in the range 293–333 K, but the temperature sensitivity is considered to become much smaller outside a certain temperature range, where the hydrogen bonding is nearly absent or nearly completed.

With respect to the application of Raman imaging technique for velocity determination, the temporally-decaying temperature distributions and velocity data are critical to validate the proposed technique. The present study could not obtain these results due to the lack of a heating system which can realize the local heating and required temperature difference. In order to perform such experiments in future work, a more elaborate heating system (for example, heating by an irradiation of an infrared laser beam) will be required instead of our current method which uses a syringe pump and a hotplate.

For the near-wall concentration measurement, an investigation into the cause of the relatively large measurement error is primarily required. A better approach for the calibration is also required to be examined since the present study used the relationship between the TIR Raman intensity and the bulk concentration of the prepared mixtures, in disregard of the concentration difference between the bulk and the near-wall regions. This may produce the difference in the measured value and the actual near-wall concentration especially in the case the surface-effects have large influence on the near-wall concentration. In addition, TIR Raman imaging should be applied to various concentration fields (such as those at different Reynolds numbers or with unsteady flow), which will be the aid for validating the technique.

Conclusions and Recommendations

Subsequently, the potential applications of the proposed techniques are discussed below. The spatial and temporal scales of some application fields are also shown in figure 7.1 together with the specifications of the developed measurement techniques.

The temperature measurement technique based on Raman imaging is expected to be utilized for controlling chemical or biological processes in microfluidic devices, such as exothermal reaction, polymerase chain reaction, protein synthesis, and cell cultivation. It is also useful for detecting Joule heating induced by electric field. Temperature measurements in such microfluidic systems will aid in maximizing their efficiency, reliability and productivity during the operations, as well as in optimizing their design. Furthermore, if the technique can be applied to biological materials including cells, tissues, and various biological fluids, it might contribute to the biological analyses, for example, investigation into the heat production in brown adipose tissue, researches for thermal therapy, etc.

The velocity measurement technique is expected to be used for controlling fluid transport by affording quantification of supplied amount of sample or reagent, which leads to the optimization of various chemical processes. Moreover, the velocity information is also necessary when quantitatively analyzing the heat and mass transport in microfluidic systems.

TIR Raman imaging technique can be one of effective approaches for investigating various surface-related phenomena, since it selectively probes the region in several tens to hundreds nanometers from the interface. In such vicinity of the solid-liquid interface, interactions between the wall and fluid atoms (typically van der Waals, electrostatic force, structuration and solvation forces) tend to play more prominent and decisive roles (Chakraborty *et al.* (2010)). Consequently, the transport properties can be remarkably different in the near-wall region compared to that in the bulk. Anomalous diffusion in the near-wall region is one example of such phenomena, and has significant importance when focusing on the fluid behaviour close to the wall. According to the result in this study, TIR Raman imaging is considered to have potential to visualize interdiffusion process in the near-wall region. Thus it will provide an effective experimental approach for investigating anomalous diffusion. The technique may also be used for investigating nucleation of surface nanobubbles which is related to slip in microfluidics (Seddon *et al.*, 2012), adsorption and desorption kinetics of surfactants, and fluidity of a supported lipid bilayer which is often used as a model system for cellular membranes. Although the thickness of adsorbed surfactants or lipid bilayer is of the order of few nanometers, the strong C-H Raman signal makes it possible to observe these thin layers (Woods & Bain, 2012).

The spatial domain which can be probed by TIR Raman imaging exists between those of conventional fluidics and molecular dynamics. Therefore, TIR Raman imaging will greatly contribute to combining these separating academic fields as a measurement technique which can provide the experimental data on transport phenomena in such boundary domain.

Acknowledgements

I would like to express my sincere gratitude to my supervisor Professor Yohei Sato for his enthusiastic encouragement, guidance and suggestions throughout the present study.

I would also like to express my appreciation to Professor Koichi Hishida at Keio University for his enthusiastic encouragement, guidance and suggestions and to Professor Kotaro Oka, Associate Professor Yoshihiro Taguchi and Assistant Professor Keita Ando at Keio University for their helpful guidance and suggestions.

I would also like to express my gratitude to Professor Minoru Obara at Keio University, Associate Professor Mitsuhsa Ichianagi at Sophia University, Assistant Professor Yutaka Kazoe at Tokyo University for their enthusiastic guidance and suggestions.

I would also like to thank Mister Harukuni Tsumura at Sankei Co., Ltd. for his helpful advice about optics.

I would also like to thank former and current students Messieurs Konstantinos Zarogoulidis, Yuta Tanaka, Motoyuki Takahashi, Yukihiro Ookuma, Shimon Akiyama, Kota Ozawa, Takeshi Noguchi, Atsushi Ito, Takayuki Ikebe, Kohei Maruyama, Tetsuro Tateishi, Yuki Yamagata, Tsukasa Hattori, and Takayuki Minami. I would also like to thank Mesdames Saki Furuta, Madoka Moriya, and other members in Hishida & Sato laboratory at Keio University.

I would also like to acknowledge to financial supports by Scholarship from Japan Student Services Organization and the Grant-in-Aid for JSPS Fellows from the Japan Society for the Promotion of Science.

Finally, I would like to express special thanks to my father Yoshio Kuriyama and my mother Yuriko Kuriyama for their continuous encouragement and support.

References

- Adar, F., Delhaye, M. & DaSilva, E. 2007 Evolution of instrumentation for detection of the Raman effect as driven by available technologies and by developing applications. *Journal of Chemical Education*, **84** (1), 50–60.
- Ambrose, E. J. 1961 The movements of fibrocytes. *Experimental Cell Research*, **8** Supplement, 54–73.
- Antes, J., Boskovic, D., Krause, H., Loebbecke, S., Lutz, N., Tuercke, T. & Schweikert, W. 2003 Analysis and improvement of strong exothermic. *Transactions of the Institution of Chemical Engineers*, **81**, 760–765.
- Arora, A., Simone, G., Salieb-Beugelaar, G. B., Kim, J. T. & Manz, A. 2010 Latest developments in micro total analysis systems. *Analytical Chemistry*, **82** (12), 4830–4847.
- Asano, K. 2006 *Mass Transfer: From Fundamentals to Modern Industrial Applications*. Weinheim: Wiley-VCH.
- Ashok, P. C., Singh, G. P., Rendall, H. A, Krauss, T. F. & Dholakia, K. 2011 Waveguide confined Raman spectroscopy for microfluidic interrogation. *Lab on a Chip*, **11** (7), 1262–1270.
- Axelrod, D. 1981 Cell-substrate contacts illuminated by total internal reflection fluorescence. *The Journal of Cell Biology*, **89** (1), 141–145.
- Axelrod, D. 2001 Total internal reflection fluorescence microscopy in cell biology. *Traffic*, **2**, 764–774.
- Axelrod, D., Burghardt, T. P. & Thompson, N. L. 1984 Total internal reflection fluorescence. *Annual Review of Biophysics and Bioengineering*, **13**, 247–268.

References

- Bain, C. D. 2001 Motion of liquids on surfaces. *Chemistry and Chemical Physics*, **2**, 580–582.
- Bajaj, V. S., Paulsen, J., Harel, E. & Pines, A. 2010 Zooming in on microscopic flow by remotely detected MRI. *Science*, **330** (6007), 1078–1081.
- Barich, M. V. & Krummel, A. T. 2013 Polymeric infrared compatible microfluidic devices for spectrochemical analysis. *Analytical Chemistry*, **85**, 10000–10003.
- Bart, J., Kolkman, A. J., Vries, A. J. O., Koch, K., Nieuwland, P. J., Janssen, H. J. W. G., Bentum, J. P. J. M. V., Ampt, K. A. M., Rutjes, F. P. J. T., Wijmenga, S. S., Gardeniers, H. J. G. E. & Kentgens, A. P. M. 2009 A microfluidic high-resolution NMR flow probe. *Journal of American Chemical Society*, **131**, 5014–5015.
- Batchelder, D. N., Cheng, C. & Pitt, G. D. 1991 Molecular imaging by Raman microscopy. *Advanced Materials*, **3** (11), 566–568.
- Bayraktar, T. & Pidugu, S. B. 2006 Characterization of liquid flows in microfluidic systems. *International Journal of Heat and Mass Transfer*, **49**, 815–824.
- Braeuer, A., Engel, S. R., Hankel, R. F. & Leipertz, A. 2009 Gas mixing analysis by simultaneous Raman imaging and particle image velocimetry. *Optics Letters*, **34** (20), 3122–3124.
- Braeuer, A. & Leipertz, A. 2009 Two-dimensional Raman mole-fraction and temperature measurements for hydrogen-nitrogen mixture analysis. *Applied Optics*, **48** (4), B57–B64.
- Brody, J. P., Yager, P., Goldstein, R. E. & Austin, R. H. 1996 Biotechnology at low Reynolds numbers. *Biophysical Journal*, **71** (6), 3430–3441.
- Bruus, H. 2008 *Theoretical Microfluidics*. New York: Oxford University Press.
- Carrabba, M. M., Spencer, K. M., Rich, C. & Rauh, D. 1990 The utilization of a holographic bragg diffraction filter for Rayleigh line rejection in Raman spectroscopy. *Applied Spectroscopy*, **44** (9), 1558–1561.

- Carrilho, E., Martinez, A. W. & Whitesides, G. M. 2009 Understanding wax printing: a simple micropatterning process for paper-based microfluidics. *Analytical Chemistry*, **81** (16), 7091–7095.
- Chakraborty, S. (Eds.) 2010 *Microfluidics and Microfabrication*. Boston: Springer.
- Chan, K. L. A. & Kazarian, S. G. 2012 FT-IR spectroscopic imaging of reactions in multiphase flow in microfluidic channels. *Analytical Chemistry*, **84**, 4052–4056.
- Chan, J. W. & Lieu, D. K. 2009 Label-free biochemical characterization of stem cells using vibrational spectroscopy. *Journal of Biophotonics*, **2** (11), 656–668.
- Chrimes, A. F., Khoshmanesh, K., Stoddart, P. R., Mitchell, A. & Kalantar-Zadeh, K. 2013 Microfluidics and Raman microscopy: current applications and future challenges. *Chemical Society Reviews*, **42**, 5880–5906.
- Conibear, P. B. & Bagshaw, C. R. 2000 A comparison of optical geometries for combined flash photolysis and total internal reflection fluorescence microscopy. *Journal of Microscopy*, **200**, 218–229.
- Currie, I. G. 2003 *Fundamental Mechanics of Fluids*, 3rd edn. Boca Raton: Taylor & Francis.
- Davis, K. L., Liu, K. L., Lanan, M. & Morris, M. D. 1993 Spatially resolved temperature measurements in electrophoresis capillaries by Raman thermometry. *Analytical Chemistry*, **65** (3), 293–298.
- Day, J. P. R., Domke, K. F., Rago, G., Kano, H., Hamaguchi, H., Vertiainen, E. M. & Bonn, M. 2011 Quantitative coherent anti-Stokes Raman scattering (CARS) microscopy. *Journal of Physical Chemistry B*, **115**, 7713–7725.
- Delhaye, M. & Dhamelincourt, P. 1975 Raman microprobe and microscope with laser excitation. *Journal of Raman Spectroscopy*, **3**, 33–43.
- Devasenathipathy, S. & Santiago, J. G. 2002 Particle tracking techniques for electrokinetic microchannel flows. *Analytical Chemistry*, **74** (15), 3704–3713.
- Dieing, T., Hollricher, O. & Toporski, J. 2011 *Confocal Raman Microscopy*. Berlin: Springer.

References

- Doremus, R. H. 1994 *Glass Science*, 2nd edn. New York: John Wiley & Sons.
- Dowy, S., Braeuer, A., Reinhold-López, K. & Leipertz, A. 2009a Laser analyses of mixture formation and the influence of solute on particle precipitation in the SAS process. *The Journal of Supercritical Fluids*, **50**, 265–275.
- Dowy, S., Braeuer, A., Schatz, R., Schluecker, E. & Leipertz, A. 2009b CO₂ partial density distribution during high-pressure mixing with ethanol in the supercritical antisolvent process. *The Journal of Supercritical Fluids*, **48**, 195–202.
- Dreier, T., Blaser, S., Kinzelbach, W., Virant, M. & Mass, H.-G. 2000 Simultaneous measurement of particle and fluid velocities in a plane mixing layer with dispersion. *Experiments in Fluids*, **29**, 486–493.
- Erickson, D., Liu, X., Venditti, R., Li, D. & Krull, U. J. 2005 Electrokinetically based approach for single-nucleotide polymorphism discrimination using a microfluidic device. *Analytical Chemistry*, **77** (13), 4000–4007.
- Erickson, D., Sinton, D. & Li, D. 2003 Joule heating and heat transfer in poly(dimethylsiloxane) microfluidic systems. *Lab on a Chip*, **3**, 141–149.
- Ewinger, A., Rinke, G., Urban, A. & Kerschbaum, S. 2013 In situ measurement of the temperature of water in microchannels using laser Raman spectroscopy. *Chemical Engineering Journal*, **223**, 129–134.
- Fei, X. & Gu, Y. 2009 Progress in modifications and applications of fluorescent dye probe. *Progress in Natural Science*, **19**, 1–7.
- Fletcher, P. D. I., Haswell, S. J. & Zhang, X. 2003 Monitoring of chemical reactions within microreactors using an inverted Raman microscopic spectrometer. *Electrophoresis*, **24**, 3239–3245.
- Freeman, S. K. & Landon, D. O. 1969 Small sample handling in laser Raman spectrometry. *Analytical Chemistry*, **41** (2), 398–400.
- Gobie, W. A. & Ivory, C. F. 1990 Thermal model of capillary electrophoresis and a method for counteracting thermal band broadening. *Journal of Chromatography A*, **516**, 191–210.

- Goto, M., Sato, K., Murakami, A., Tokeshi, M. & Kitamori, T. 2005 Development of a microchip-based bioassay system using cultured cells. *Analytical Chemistry*, **77** (7), 2125–2131.
- Greene, P. R. & Bain, C. D. 2004 Total internal reflection Raman spectroscopy. *Spectroscopy Europe*, **16**, 8–15.
- Guo, Z.-Y. & Li, Z.-X. 2003 Size effect on microscale single-phase flow and heat transfer. *International Journal of Heat and Mass Transfer*, **46**, 149–159.
- Haeberle, S. & Zengerle, R. 2007 Microfluidic platforms for lab-on-a-chip applications. *Lab on a Chip*, **7**, 1094–1110.
- Hamaguchi, H. & Hirakawa, A. (Eds.) 1988 *Raman Bunkouhou (Raman Spectroscopy)*. Tokyo: Academy Press Center.
- Harrick, N. J. & Loeb, G. I. 1973 Multiple internal reflection fluorescence spectrometry. *Analytical Chemistry*, **128** (4), 687–691.
- Harrison, D. J., Fluri, K., Seiler, K., Fan, Z., Effenhauser, S. & Manz, A. 1993 Micromachining a miniaturized capillary electrophoresis-based chemical analysis system on a chip. *Science*, **261** (5123), 895–897.
- Hartley, D. L. 1974 Raman Gas Mixing Measurements and Ramanography *Laser Raman Gas Diagnostics*. Lapp, M. & Penny, C. M. (eds.) Schenectady: General Electric Co.
- Hatch, A., Garcia, E. & Yager, P. 2004 Diffusion-based analysis of molecular interactions in microfluidic devices. *Proceedings of the IEEE*, **92** (1), 126–139.
- Ho C.-M. & Tai Y.-C. 1998 Micro-electro-mechanical-systems (MEMS) and fluid flows. *Annual Review of Fluid Mechanics*, **30**, 579–612.
- Hoffmann, M., Schlüter, M. & Rübiger, N. 2006 Experimental investigation of liquid-liquid mixing in T-shaped micro-mixers using μ -LIF and μ -PIV. *Chemical Engineering Science*, **61**, 2968–2976.
- Huang, C.-W. & Lee, G.-B. 2007 A microfluidic system for automatic cell culture. *Journal of Micromechanics and Microengineering*, **17**, 1266–1274.

References

- Ichikawa, N., Hosokawa, K. & Maeda, R. 2004 Interface motion of capillary-driven flow in rectangular microchannel. *Journal of Colloid and Interface Science*, **280** (1), 155–164.
- Ichiyangi, M., Sakai, K., Kidani, S., Kakinuma, Y., Sato, Y. & Hishida, K. 2012a Evaluation methodology of gas permeable characterization in a polymer-based microfluidic device by confocal fluorescence imaging. *Journal of Micromechanics and Microengineering*, **22**, 065023 (8 pp).
- Ichiyangi, M., Sato, Y. & Hishida, K. 2007 Optically sliced measurement of velocity and pH distribution in microchannel. *Experiments in Fluids*, **43**, 425–435.
- Ichiyangi, M., Tsutsui, I., Kakinuma, Y., Sato, Y. & Hishida, K. 2012b Three-dimensional measurement of gas dissolution process in gas–liquid microchannel flow. *International Journal of Heat and Mass Transfer*, **55**, 2872–2878.
- Ikeshoji, T., Ono, Y. & Mizuno, T. 1973 Total reflection Raman spectra; Raman scattering due to the evanescent wave in total reflection. *Applied Optics*, **12** (10), 2236–2237.
- Inoué, S. 1986 *Video Microscopy*. New York: Plenum Press.
- Inoué, S. & Spring, K. 1997 *Video Microscopy: The Fundamentals*, 2nd edn. New York: Plenum Press.
- Iwamoto, K., Miya, M., Ohta, K. & Mima, S. 1980 Total internal reflection Raman spectroscopy as a new tool for surface analysis. *Journal of American Chemical Society*, **102** (3), 1212–1213.
- Iwamoto, K., Ohta, K., Miya, M. & Mima, S. 1981 Total internal reflection Raman spectroscopy at the critical angle for Raman measurements of thin films. *Applied Spectroscopy*, **35** (6), 584–587.
- Izumiya, T. 1984 *Kogaku Glass (Optical Glass)*. Tokyo: Kyoritsu Syuppan.
- Jin, S., Huang, P., Park, J., Yoo, J. Y. & Breuer, K. S. 2004 Near-surface velocimetry using evanescent wave illumination. *Experiments in Fluids*, **37**, 825–833.

- Julián, B., Gervais, C., Cordoncillo, E., Escribano, P., Babonneau, F. & Sanchez, C. 2003 Synthesis and characterization of transparent PDMS-metal-oxo based organic-inorganic nanocomposites. *Chemistry of Materials*, **15** (15), 3026–3034.
- Kazarian, S. G. & Chan, K. L. A. 2006 Applications of ATR-FTIR spectroscopic imaging to biomedical samples. *Biochimica et Biophysica Acta*, **1758**, 858–867.
- Kazoe, Y., Nakamura, T. & Sato, Y. 2010 Evanescent-wave/volume illuminated velocity measurements of transient eletrokinetically driven flow with nonuniform wall electrostatic potential. *Measurement Science and Technology*, **21**, 055401 (10 pp).
- Kazoe, Y. & Sato, Y. 2007 Effect of ion motion on zeta-potential distribution at microchannel wall obtained from nanoscale laser-induced fluorescence. *Analytical Chemistry*, **79** (17), 6727–6733.
- Kazoe, Y. & Yoda, M. 2013 Evanescent wave-based flow diagnostics. *Journal of Fluids Engineering*, **135** (2), 021305 (11 pp).
- Kiefer, J., Seeger, T., Steuer, S., Schorsch, S., Weigl, M. C. & Leipertz, A. 2008 Design and characterization of a Raman-scattering-based sensor system for temporally resolved gas analysis and its application in a gas turbine power plant. *Measurement Science and Technology*, **19** (8), 085408 (9 pp).
- Kim, B.-Y., Hong, L.-Y., Chung, Y.-M., Kim, D.-P. & Lee, C.-S. 2009 Solvent-resistant PDMS microfluidic devices with hybrid inorganic/organic polymer coatings. *Advanced Functional Materials*, **19** (23), 3796–3803.
- Kim, M., Beskok, A. & Kihm, K. D. 2002 Electro-osmosis-driven micro-channel flows: A comparative study of microscopic particle image velocimetry measurements and numerical simulations. *Experiments in Fluids*, **33**, 170–180.
- Kim, M. & Yoda, M. 2010 Dual-tracer fluorescence thermometry measurements in a heated channel. *Experiments in Fluids*, **49**, 257–266.
- Kim, S. H., Noh, J., Jeon, M. K., Kim, K. W., Lee, L. P. & Woo, S. I. 2006 Micro-Raman thermometry for measuring the temperature distribution inside the microchannel of a polymerase chain reaction chip. *Journal of Micromechanics and Microengineering*, **16**, 526–530.

References

- Kirby, B. J. & Hasselbrink, E. F. 2004a Zeta potential of microfluidic substrates: 1. Theory, experimental techniques, and effects on separations. *Electrophoresis*, **25**, 187–202.
- Kirby, B. J. & Hasselbrink, E. F. 2004b Zeta potential of microfluidic substrates: 2. Data for polymers. *Electrophoresis*, **25**, 203–213.
- Kitamori, T., Tokeshi, M., Hibara, A. & Sato, K. 2004 Peer reviewed: thermal lens microscopy and microchip chemistry. *Analytical Chemistry*, **76** (3), 52A–60A.
- Kneipp, K., Kneipp, H., Itzkan, I., Dasari, R. R. & Feld, M. S. 1999 Ultrasensitive chemical analysis by Raman spectroscopy. *Chemical Reviews*, **99** (10), 2957–2975.
- Knox, J. H. & McCormack, K. A. 1994 Temperature effects in capillary electrophoresis. 1: internal capillary temperature and effect upn performance. *Chromatographia*, **38** (3/4), 207–214.
- Konijnendijk, W. L. & Stevels, J. M. 1976 The structure of borosilicate glasses studies by Raman scattering. *Journal of Non-Crystalline Solids*, **20**, 193-224.
- Kovarik, M. L., Gach, P. C., Ornoff, D. M., Wang, Y., Balowski, J., Farrag, L. & Allbritton, N. L. 2012 Micro total analysis systems for cell biology and biochemical assays. *Analytical Chemistry*, **84** (2), 516–540.
- Kumar, A. & Whitesides, G. M. 1993 Features of gold having micrometer to centimeter dimensions can be formed through a combination of stamping with an elastomeric stamp and an alkanethiol “ink” followed by chemical etching. *Applied Physics Letters*, **63** (14), 2002–2004.
- Lee, D.-S., Park, S. H., Yang, H., Chung, K.-H., Yoon, T. H., Kim, S.-J., Kim, K. & Kim, Y. T. 2004 Bulk-micromachined submicroliter-volume PCR chip with very rapid thermal response and low power consumption. *Lab on a Chip*, **4**, 401–407.
- Lee, J. N., Park, C. & Whitesides, G. M. 2003 Solvent compatibility of poly (dimethylsiloxane)-based microfluidic devices. *Analytical Chemistry*, **75** (23), 6544–6554.
- Lee, J. Y., Kim, J. J. & Tai, H. P. 2003 Miniaturization of polymerase chain reaction. *Biotechnology and Bioprocess Engineering*, **8** (4), 213–220.

- Lee, M., Lee, J.-P., Rhee, H., Choo, J., Chai, Y. G. & Lee, E. K. 2003 Applicability of laser-induced Raman microscopy for in situ monitoring of imine formation in a glass microfluidic chip. *Journal of Raman Spectroscopy*, **34**, 737–742.
- Leong, J.-C., Tsai, C.-H., Chang, C.-L., Lin, C.-F. & Fu, L.-M. 2007 Rapid microfluidic mixers utilizing dispersion effect and interactively time-pulsed injection. *Japanese Journal of Applied Physics*, **46** (8A), 5345–5352.
- Leung, S.-A., Winkle, R. F., Wootton, R. C. R. & DeMello, A. J. 2005 A method for rapid reaction optimisation in continuous-flow microfluidic reactors using online Raman spectroscopic detection. *Analyst*, **130**, 46–51.
- Li, X., Tian, J. & Shen, W. 2010 Thread as a versatile material for low-cost microfluidic diagnostics. *Applied Materials and Interfaces*, **2** (1), 1–6.
- Libnau, F. O., Christy, A. A. & Kvalheim, O. M. 1995 Determination of the equilibrium constant and resolution of the HOD spectrum by alternating least-squares and infrared analysis. *Applied Spectroscopy*, **49** (10), 1431–1437.
- Lin, C.-H., Fu, L.-M. & Chien, Y.-S. 2004 Microfluidic T-form mixer utilizing switching electroosmotic flow. *Analytical Chemistry*, **76** (18), 5265–5272.
- Lin, Y., Yu, X., Wang, Z., Tu, S.-T. & Wang, Z. 2010 Measurement of temperature-dependent diffusion coefficients using a confocal Raman microscope with microfluidic chips considering laser-induced heating effect. *Analytica Chimica Acta*, **667**, 103–112.
- Ling, J., Weitman, S. D., Miller, M. A., Moore, R. V. & Bovik, A. C. 2002 Direct Raman imaging techniques for study of the subcellular distribution of a drug. *Applied Optics*, **42** (28), 6006–6017.
- Liu, N., Aymonier, C., Lecoutre, C., Garrabos, Y. & Marre, S. 2012 Microfluidic approach for studying CO₂ solubility in water and brine using confocal Raman spectroscopy. *Chemical Physics Letters*, **551**, 139–143.
- Long, D. A. 1977 *Raman Spectroscopy*. New York: McGraw-Hill.
- Ludwig, R. 2001 Water: from clusters to the bulk. *Angewandte Chemie International Edition*, **40**, 1808–1827.

References

- Maheshwary, S., Patel, N. & Sathysmurthy, N. 2001 Structure and stability of water cluster $(\text{H}_2\text{O})_n$, $n=8-20$: Au Ab initio investigation. *Journal of Physical Chemistry A*, **105**, 10525–10537.
- Maier, J., Panza, J., Drauch, A. & Stewart, S. 2006 Raman molecular imaging of tissue and cell samples using tunable multiconjugate filter. *Proceedings of SPIE*, **6380**, 638009 (12 pp).
- Malarski, A., Egermann, J., Zehnder, J. & Leipertz, A. 2006 Simultaneous application of single-shot Ramanography and particle image velocimetry. *Optics Letters*, **31**(7), 1005–1007.
- Manz, A., Graber, N., & Widmer, H. M. 1990 Miniaturized total chemical analysis systems: a novel concept for chemical sensing. *Sensors and Actuators*, **B1**, 244–248.
- Markwort, L., Kip, B., Silva, E. D. & Roussel, B. 1995 Raman imaging of heterogeneous polymers: a comparison of global versus point illumination. *Applied Spectroscopy*, **49**(10) 1411–1430.
- Matosevic, S., Szita, N. & Baganz, F. 2011 Fundamentals and applications of immobilized microfluidic enzymatic reactors. *Journal of Chemical Technology and Biotechnology*, **86**, 325–334.
- Matsumoto, R., Zadeh, H. F. & Ehrhard, P. 2005 Quantitative measurement of depth-averaged concentration fields in microchannels by means of a fluorescence intensity method. *Experiments in Fluids*, **39**, 722–729.
- Mayer, W., Telaar, J., Branam, R., Schneider, G. & Hussong, J. 2003 Raman measurements of cryogenic injection at supercritical pressure. *Heat and Mass Transfer*, **39**, 709–719.
- McDonald, J. C. & Whitesides, G. M. 2002 Poly(dimethylsiloxane) as a material for fabricating microfluidic devices, *Accounts of Chemical Research*, **35** (7), 491–499.
- Meinhart, C. D., Wereley, S. T. & Gray, M. H. B. 2000 Volume illumination for two-dimensional particle image velocimetry. *Measurement Science and Technology*, **11**, 809–814.

- Meinhart, C. D., Wereley, S. T. & Santiago, J. G. 1999 PIV measurements of a microchannel flow. *Experiments in Fluids*, **27**, 414–419.
- Michaels, C. A. 2010 Surface-sensitive Raman microscopy with total internal reflection illumination. *Journal of Raman Spectroscopy*, **41**, 1670–1677.
- Nakamoto, K. 2009 *Infrared and Raman Spectra of Inorganic and Coordination Compounds*, 6th edn. Hoboken: John Wiley & Sons.
- Natrajan, V. K. & Christensen, K. T. 2009 Two-color laser-induced fluorescent thermometry for microfluidic systems. *Measurement Science and Technology*, **20**, 015401 (11 pp).
- Ng, J. M. K., Giltelin, I., Stroock, A. D. & Whitesides, G. M. 2002 Components for integrated poly(dimethylsiloxane) microfluidic systems. *Electrophoresis*, **23**, 3461–3473.
- Nickolov, Z. S., Earnshaw, J. C. & McGarvey, J. J. 1993 Water structure at interfaces studied by total internal reflection Raman spectroscopy. *Colloids and Surfaces A*, **76**, 41–49.
- Nie, S. & Emory, S. R. 1997 Probing single molecules and single nanoparticles by surface-enhanced Raman scattering. *Science*, **275**, 1102–1106.
- Ohsawa, M., Hashima, K. & Suëtaka, W. 1984 Angular dependence of scattering intensity from thin films in total reflection Raman spectroscopy. *Applications of Surface Science*, **20**, 109–120.
- Otto, C., De Grauw, C. J., Duindam, J. J., Sijtsema, N. M. & Greve, J. 1997 Applications of micro-Raman imaging in biomedical research. *Journal of Raman Spectroscopy*, **28**, 143–150.
- Pan, T., Kelly, R. T., Asplund, M. C. & Woolley, A. T. 2004 Fabrication of calcium fluoride capillary electrophoresis microdevices for on-chip infrared detection. *Journal of Chromatography A*, **1027**, 231–235.
- Park, T., Lee, M., Choo, J., Kim, Y. S., Lee, E. K., Kim, D. J. & Lee, S.-H. 2004 Analysis of passive mixing behavior in a poly(dimethylsiloxane) microfluidic channel using confocal fluorescence and Raman microscopy. *Applied Spectroscopy*, **58** (10), 1172–1179.

References

- Paul, P. H., Garguilo, M. G. & Rakestraw, D. J. 1998 Imaging of pressure- and electrokinetically driven flows through open capillaries. *Analytical Chemistry*, **70** (13), 2459–2467.
- Pikov, V. & Siegel, P. H. 2010 Thermal monitoring: Raman spectrometer system for remote measurement of cellular temperature on a microscopic scale. *IEEE Engineering in Medicine and Biology Magazine*, **29** (1), 63–71.
- Pittman, J. L., Henry, C. S. & Gilman, S. D. 2003 Experimental studies of electroosmotic flow dynamics in microfabricated devices during current monitoring experiments. *Analytical Chemistry*, **75** (3), 361–370.
- Pollack, M. G., Fair, R. B. & Shenderov, A. D. 2000 Electrowetting-based actuation of liquid droplets for microfluidic applications. *Applied Physics Letters*, **77** (11), 1725–1726.
- Polson, N. A. & Hayes, M. A. 2000 Electroosmotic flow control of fluids on a capillary electrophoresis microdevice using an applied external voltage. *Analytical Chemistry*, **72** (5), 1088–1092.
- Port, S. P. S. & Wood, D. L. 1962 Ruby optical maser as a Raman source. *Applied Optics*, **1**, 139–141.
- Prieve, D. C. 1999 Measurement of colloidal forces with TIRM. *Advances in Colloid and Interface Science*, **82**, 93–125.
- Probstein, R. F. 1994 *Physicochemical Hydrodynamics*, 2nd edn. New York: John Wiley & Sons.
- Puppels, G. J., DeMul, F. F. M., Otto, C., Greve, J., Robert-Nicoud, M., Arndt-Jovin, D. J. & Jovin, T. M. 1990 Studying single living cells and chromosomes by confocal Raman microspectroscopy. *Nature*, **347**, 301–303.
- Puppels, G. J., Grond, M. & Greve, J. 1993 Direct imaging Raman microscope based on tunable wavelength excitation and narrow-band emission detection. *Applied Spectroscopy*, **47** (8), 1256–1267.

- Rabenstein, F. & Leipertz, A. 1997 Two-dimensional temperature determination in the exhaust region of a laminar flat-flame burner with linear Raman scattering. *Applied Optics*, **36** (27), 6989–6996.
- Raman, C. V. & Krishnan, K. S. 1928 A new type of secondary radiation. *Nature*, **121** (3048), 501–502.
- Rinke, G., Ewinger, A., Kerschbaum, S. & Rinke, M. 2011 In situ Raman spectroscopy to monitor the hydrolysis of acetal in microreactors. *Microfluidics and Nanofluidics*, **10**, 145–153.
- Rinke, G., Wenka, A., Roetmann, K. & Wackerbarth, H. 2012 In situ Raman imaging combined with computational fluid dynamics for measuring concentration profiles during mixing processes. *Chemical Engineering Journal*, **179**, 338–348.
- Roetmann, K., Schmunk, W., Garbe, C. S. & Beushausen, V. 2008 Micro-flow analysis by molecular tagging velocimetry and planar Raman-scattering. *Experiments in Fluids*, **44**, 419–430.
- Roman, G. T., McDaniel, K. & Culbertson, C. T. 2006 High efficiency micellar electrokinetic chromatography of hydrophobic analytes on poly(dimethylsiloxane) microchips. *Analyst*, **131**, 194–201.
- Rosasco, G. J., Etz, E. S. & Cassatt, W. A. 1975 The analysis of discrete fine particles by Raman spectroscopy. *Applied Spectroscopy*, **29** (5), 396–404.
- Rose, A., Vyas, R. & Gupta, R. 1986 Pulsed photothermal deflection spectroscopy in a flowing medium : a quantitative investigation. *Applied Optics*, **25** (24), 4626–4643.
- Ross, D., Gaitan, M. & Locascio, L. E. 2001 Temperature measurement in microfluidic systems using a temperature-dependent fluorescent dye. *Analytical Chemistry*, **73** (17), 4117–4123.
- Ross, D. & Locascio, L. E. 2003 Effect of caged fluorescent dye on the electroosmotic mobility in microchannels. *Analytical Chemistry*, **75** (5), 1218–1220.
- Russ, J. C. 2007 *The Image Processing Handbook*, 5th edn. Boca Raton: Taylor & Francis.

References

- Sadr, R., Yoda, M., Gnanaprakasam, P. & Conlisk, A. T. 2006 Velocity measurements inside the diffuse electric double layer in electro-osmotic flow. *Applied Physics Letters*, **89**, 044103 (3 pp).
- Salmon, J.-B., Ajdari, A., Tabeling, P., Servant, L., Talaga, D. & Joanicot, M. 2005 In situ Raman imaging of interdiffusion in a microchannel. *Applied Physics Letters*, **86**, 094106 (3 pp).
- Sammarco, T. S. & Burns, M. A. 1999 Thermocapillary pumping of discrete drops in microfabricated analysis devices. *American Institute of Chemical Engineers journal*, **45** (2), 350–366.
- Sammarco, T. S. & Burns, M. A. 2000 Heat-transfer analysis of microfabricated thermocapillary pumping and reaction devices. *Journal of Micromechanics and Microengineering*, **10**, 42–55.
- Samy, R., Glawdel, T. & Ren, C. L. 2008 Method for microfluidic whole-chip temperature measurement using thin-film poly (dimethylsiloxane)/rhodamine B. *Analytical Chemistry*, **80** (2), 369–375.
- Santiago, J. G., Wereley, S. T., Meinhart, C. D., Beebe, D. J. & Adrian, R. J. 1998 A particle image velocimetry system for microfluidics. *Experiments in Fluids*, **25**, 316–319.
- Sarrazin, F., Salmon, J.-B., Talaga, D. & Servant, L. 2008 Chemical reaction imaging within microfluidic devices using confocal Raman spectroscopy : the case of water and deuterium oxide as a model system. *Analytical Chemistry*, **80** (5), 1689–1695.
- Sato, K., Mawatari, K. & Kitamori, T. 2008 Microchip-based cell analysis and clinical diagnosis system. *Lab on a Chip*, **8**, 1992–1998.
- Sato, K., Yamanaka, M., Takahashi, H., Tokeshi, M., Kimura, H. & Kitamori, T. 2002 Microchip-based immunoassay system with branching multichannels for simultaneous determination of interferon- γ . *Electrophoresis*, **23**, 734–739.
- Sato, Y. & Hishida, K. 2006 Electrokinetic effects on motion of submicron particles in microchannel. *Fluid Dynamics Research*, **38**, 787–802.

- Sato, Y., Irisawa, G., Ishizuka, M., Hishida, K. & Maeda, M. 2003 Visualization of convective mixing in microchannel by fluorescence imaging. *Measurement Science and Technology*, **14** (1), 114–121.
- Savitzky, A. & Golay, M. J. E. 1964 Smoothing and differentiation of data by simplified least squares procedures. *Analytical Chemistry*, **36** (8), 1627–1639.
- Schaeberle, M. D., Kalasinsky, V. F., Luke, J. L., Lewis, E. N., Levin, I. W. & Treado, P. J. 1996 Raman chemical imaging: histopathology of inclusions in human breast tissue. *Analytical Chemistry*, **68** (11), 1829–1833.
- Schlücker, S., Schaeberle, M. D., Huffman, S. W. & Levin, I. W. 2003 Raman microspectroscopy: a comparison of point, line, and wide-field imaging methodologies. *Analytical Chemistry*, **75** (16), 4312–4318.
- Seddon, J. R. T., Lohse, D., Ducker, W. A. & Craig, S. J. 2012 A deliberation on nanobubbles at surfaces and in bulk. *A European Journal of Chemical Physics and Physical Chemistry*, **13**, 2179–2187.
- Senga, Y., Nakamura, T., Fukumura, H., Ichianagi, M. & Sato, Y. 2010 Near-wall motion of caged fluorescent dye in microchannel flows obtained from evanescent wave molecular tagging. *Journal of Fluid Science and Technology*, **5** (2), 192–206.
- Shibata, N., Horiguchi, M. & Ehahiro, T. 1981 Raman spectra of binary high-silica glasses and fibers containing GeO₂, P₂O₅ and B₂O₃. *Journal of Non-Crystalline Solids*, **45**, 115–126.
- Shin, Y. S., Cho, K., Lim, S. H., Chung, S., Park, S.-J., Chung, C., Han, D.-C. & Chang, J. K. 2003 PDMS-based micro PCR chip with Parylene coating. *Journal of Micromechanics and Microengineering*, **13**, 768–774.
- Singh, A. K., Cummings, E. B. & Throckmorton, D. J. 2001 Fluorescent liposome flow markers for microscale particle-image velocimetry. *Analytical Chemistry*, **73** (5), 1057–1061.
- Sinton, D. 2004 Microscale flow visualization. *Microfluidics and Nanofluidics*, **1**, 2–21.
- Smekal, A. 1923 Zur quantentheorie der dispersion. *Naturwissenschaften*, **11**, 873–875.

References

- Smith, R. C. & Baker, K. S. 1981 Optical properties of the clearest natural waters (200-800 nm). *Applied Optics*, **20** (2), 177–184.
- Soloff, S. M., Adrian, R. J. & Liu, Z.-C. 1997 Distortion compensation for generalized stereoscopic particle image velocimetry. *Measurement Science and Technology*, **8**, 1441–1454.
- Takahashi, M., Furukawa, T., Sato, Y. & Hishida, K. 2012 Non-intrusive velocity measurement of millichannel flow by spontaneous Raman imaging. *Journal of Thermal Science and Technology*, **7** (3), 406–413.
- Takeuchi, H., Motosuke, M. & Honami, S. 2012 Noncontact bubble manipulation in microchannel by using photothermal Marangoni effect. *Heat Transfer Engineering*, **33** (3), 234–244.
- Taylor, J. B., Carrano, A. L. & Kandlikar, S. G. 2006 Characterization of the effect of surface roughness and texture on fluid flow—past, present, and future. *International Journal of Thermal Sciences*, **45**, 962–968.
- Tian, W.-C. & Finehout, E. (Eds.) 2008 *Microfluidics for Biological Applications*. New York: Springer.
- Tieu, A. K., Mackenzie, M. R. & Li, E. B. 1995 Measurements in microscopic flow with a solid-state LDA. *Experiments in Fluids*, **19**, 293–294.
- Tokeshi, M., Uchida, M., Hibara, A., Sawada, T. & Kitamori, T. 2001 Determination of subyoctomole amounts of nonfluorescent molecules using a thermal lens microscope: subsingle-molecule determination. *Analytical Chemistry*, **73** (9), 2112–2116.
- Török, P. & Kao, F.-J. (Eds.) 2007 *Optical Imaging and Microscopy: Techniques and Advanced Systems*, 2nd edn. Berlin: Springer.
- Tretheway, D. C. & Meinhart, C. D. 2002 Apparent fluid slip at hydrophobic microchannel walls. *Physics of Fluids*, **14** (3), L9–L12.
- Tu, A. 1982 *Raman Spectroscopy in Biology: Principles and Applications*. New York: John Wiley & Sons.

- Tyrode, E., Rutland, M. W. & Bain, C. D. 2008 Adsorption of CTAB on hydrophilic silica studied by linear and nonlinear optical spectroscopy. *Journal of American Chemical Society*, **130**, 17434–17445.
- Viskari, P. J. & Landers, J. P. 2006 Unconventional detection methods for microfluidic devices. *Electrophoresis*, **27**, 1797–1810.
- Voldman, J. 2006 Electrical forces for microscale cell manipulation. *Annual Review of Biomedical Engineering*, **8**, 425–454.
- Vyas, R., Monson, B., Nie, Y. X. & Gupta, R. 1988 Continuous wave photothermal deflection spectroscopy in a flowing medium. *Applied Optics*, **27** (18), 3914–3920.
- Walrafen, G. E. 1962 Raman spectral studies of the effects of electrolytes on water. *The Journal of Chemical Physics*, **36** (4), 1035–1042.
- Walrafen, G. E. 1964 Raman spectral studies of water structure. *The Journal of Chemical Physics*, **40** (11), 3249–3256.
- Walrafen, G. E. 1967 Raman spectral studies of the effects of temperature on water structure. *The Journal of Chemical Physics*, **47** (1), 114–126.
- Walrafen, G. E., Hokmabadi, M. S. & Yang, W. H. 1986 Raman isosbestic points from liquid water. *The Journal of Chemical Physics*, **85** (12), 6964–6969.
- Weigl, B., Domingo, G., LaBarre, P. & Gerlach, J. 2008 Towards non- and minimally instrumented, microfluidics-based diagnostic devices. *Lab on a Chip*, **8**, 1000–2014.
- Wellhausen, M., Rinke, G. & Wackerbarth, H. 2012 Combined measurement of concentration distribution and velocity field of two components in a micromixing process. *Microfluidics and Nanofluidics*, **12**, 917–926.
- Wensink, H., Benito-Lopez, F., Hermes, D. C., Verboom, W., Gardeniers, H. J. G. E., Reinhoudt, D. N. & van den Berg, A. 2005 Measuring reaction kinetics in a lab-on-a-chip by microcoil NMR. *Lab on a Chip*, **5**, 280–284.
- Woods, D. A & Bain, C. D. 2012 Total internal reflection Raman spectroscopy. *Analyst*, **137**, 35–48.

References

- Woods, D. A & Bain, C. D. 2014 Total internal reflection spectroscopy for studying soft matter. *Soft Matter*, **10**, 1071–1096.
- Woods, D. A., Petkov, J. & Bain, C. D. 2011a Surfactant adsorption kinetics by total internal reflection Raman spectroscopy. 1 . Pure Surfactants on Silica. *Journal of Physical Chemistry B*, **115**, 7341–7352.
- Woods, D. A., Petkov, J. & Bain, C. D. 2011b Surfactant adsorption kinetics by total internal reflection Raman spectroscopy. 2 . CTAB and Triton X-100 mixtures on silica. *Journal of Physical Chemistry B*, **115**, 7353–7363.
- Wu, Z., Liu, A. Q. & Hjort, K. 2007 Microfluidic continuous particle/cell separation via electroosmotic-flow-tuned hydrodynamic spreading. *Journal of Micromechanics and Microengineering*, **17**, 1992–1999.
- Xia, Y. & Whitesides, G. M. 1998 Soft lithography. *Annual Review of Materials Science*, **28**, 153–184.
- Yoda, M. & Kim, M. 2013 Studying interfacial transport with evanescent wave-based particle velocimetry and thermometry. *Heat Transfer Engineering*, **34** (2–3), 101–112.
- Zettner, C. M. & Yoda, M. 2003 Particle velocity field measurements in a near-wall flow using evanescent wave illumination. *Experiments in Fluids*, **34**, 115–121.
- Zhang, C. & Xing, D. 2007 Miniaturized PCR chips for nucleic acid amplification and analysis: latest advances and future trends. *Nucleic Acids Research*, **35** (13), 4223–4237.
- Zhao, B., Viernes, N. O. L., Moore, J. S. & Beebe, D. J. 2002 Control and applications of immiscible liquids in microchannels. *Journal of American Chemical Society*, **124**, 5284–5285.
- Ziaie, B., Baldi, A., Lei, M., Gu, Y. & Siegel, R. A. 2004 Hard and soft micromachining for BioMEMS: review of techniques and examples of applications in microfluidics and drug delivery. *Advanced Drug Delivery Reviews*, **56**, 145–172.
- Zoubir, A. (Eds.) 2012 *Raman Imaging: Techniques and Applications*. Berlin: Springer.